Spring 5-15-2015

Correlated NanoSIMS, TEM, and XANES Studies of Presolar Grains

Evan Edward Groopman
Washington University in St. Louis

Follow this and additional works at: https://openscholarship.wustl.edu/art_sci_etds

Part of the Physics Commons

WASHINGTON UNIVERSITY IN ST. LOUIS

Department of Physics

Dissertation Examination Committee:

Thomas J. Bernatowicz, Chair
Ernst K. Zinner, Co-Chair
Ramanath Cowsik
Martin H. Israel
Bradley L. Jolliff
Larry R. Nittler

Correlated NanoSIMS, TEM, and XANES Studies of Presolar Grains

by

Evan Edward Groopman

A dissertation presented to the
Graduate School of Arts and Sciences
of Washington University in
partial fulfillment of the
requirements for the degree
of Doctor of Philosophy

May 2015

Saint Louis, Missouri

.

Contents

8 pyLATTICE: A Program for Electron Diffraction Simulation **181**

9 Conclusions 217

A Appendix 221

Curriculum Vitae 230

List of Figures

List of Tables

Acknowledgments

This thesis is the product of many years of work and would not have been possible without the support and guidance from many family members, dear friends, and colleagues. My advisors, Professors Tom Bernatowicz and Ernst Zinner, have been monumental figures in shaping my scientific career. Tom, your passion for teaching and discovery captivated me from your first Introductory Physics class that I took as a freshman undergraduate. It laid aside any doubt that I wanted to pursue a career in Physics and has shaped my life since. Ernst, all of us can only endeavor to be as tough, relentless, and meticulous in our scientific and personal enterprises as you are every day. Your joy for life, personal energy, and wide-ranging talents are both inspiring and daunting for those of us who wish to follow in your footsteps. The time and dedication that both of you have invested in my career and scientific life is humbling and appreciated beyond measure.

I have had the incredible fortune to pursue my Ph.D. as a member of the 4th floor, the Laboratory for Space Sciences, at Washington University in St. Louis. No one could ask for a more supportive environment to work in. Not only does the lab strive for scientific excellence, but it places the personal side of science as a human enterprise at the forefront of its endeavors. I have received tremendous and invaluable support from so many people

during my tenure and there is more than I can possibly say here about each person. Frank Gyngard, Kevin Croat, Tim Smolar, Christine Floss, and Tyrone Daulton, thank you for all of your tireless mentoring, without which this thesis would not have been possible. Thank you, my officemates, Joben Lewis, Pierre Haenecour, Brendan Haas, and Wei Jia Ong for your great companionship and for helping care for my dog, Rhombus. Larry Nittler, thank you for your tremendous generosity and patience during the course of our collaborations.

Above all, I would not be here without the love, dedication, and incredible generosity of my parents, John and Hilary; my siblings, Alena, Alek, and Ian; my grandmother, Elizabeth; and my wife, Amber. Mommy and Daddy, words can't express my gratitude for your love and support. I can only hope that by endeavoring to emulate your kindness and generosity in my own life I might be able to express my admiration and love for you. Amber, I love you. I am so glad that we could go through this doctoral journey together. You are so talented and thoughtful; I admire you tremendously. I can't wait to continue ours travels through life together.

In memory of Frank Stadermann.

ABSTRACT OF THE DISSERTATION

Correlated NanoSIMS, TEM, and XANES Studies of Presolar Grains

by

Evan Edward Groopman

Doctor of Philosophy in Physics

Washington University in St. Louis, 2015

Professor Thomas J. Bernatowicz, Chair

The objective of this thesis is to describe the correlated study of individual presolar grains via Nano-scale Secondary Ion Mass Spectrometry (NanoSIMS), Transmission Electron Microscopy (TEM), and Scanning Transmission X-ray Microscopy (STXM) utilizing X-ray Absorption Near Edge Structure (XANES), with a focus on connecting these correlated laboratory studies to astrophysical phenomena. The correlated isotopic, chemical, and microstructural studies of individual presolar grains provide the most detailed description of their formation environments, and help to inform astrophysical models and observations of stellar objects.

As a part of this thesis I have developed and improved upon laboratory techniques for micromanipulating presolar grains and embedding them in resin for ultramicrotomy after NanoSIMS analyses and prior to TEM characterization. The new methods have yielded a 100% success rate and allow for the specific correlation of microstructural and isotopic properties of individual grains. Knowing these properties allows for inferences to be made regarding the condensation sequences and the origins of the stellar material that condensed to form these grains.

NanoSIMS studies of ultramicrotomed sections of presolar graphite grains have revealed complex isotopic heterogeneities that appear to be primary products of the grains' formation environments and not secondary processing during the grains' lifetimes. Correlated excesses

in ^{15}N and ^{18}O were identified as being carried by TiC subgrains within presolar graphite grains from supernovae (SNe). These spatially-correlated isotopic anomalies pinpoint the origin of the material that formed these grains: the inner He/C zone. Complex microstructures and isotopic heterogeneities also provide evidence for mixing in globular SN ejecta, which is corroborated by models and telescopic observations. In addition to these significant isotopic discoveries, I have also observed the first reported nanocrystalline core surrounded by turbostratic graphite within a low-density SN graphite grain. Nanocrystalline cores consisting of randomly-oriented 2–4 nm sheets of graphene and surrounded by concentric shells of graphite have been observed in high-density presolar graphite grains from Asymptotic Giant Branch stars, whose grains are typically microstructurally distinct from SN graphite grains. These vastly different stellar environments briefly formed similar nanocrystalline structures before diverging in the structure of their mantling graphite to be typical of AGB and SN grains.

While relatively few correlated NanoSIMS and TEM studies have been performed previously, which this research thesis aims to expand, my collaborators and I also endeavored to add a third correlated technique, STXM/XANES, which had previously not been applied to presolar grains. XANES allows for the investigation of molecular bonds, which we used to help infer physical and chemical properties of stellar ejecta. I investigated the C K-edge and Ti L-edge of molecular bonds in both presolar graphite grains and their TiC subgrains. The presolar graphite grains, while overwhelmingly composed of aromatic C molecules, host a wide variety of minor organic molecules. Considering the large isotopic anomalies in the grains, these minor components are not likely due to contamination. I also investigated the valence state of Ti in Ti-rich subgrains and plan to work towards illuminating the effect that V in solid solution has upon the TiC bonds.

CHAPTER 1

INTRODUCTION

Chapter 1: Introduction

The objective of this thesis is to describe the correlated study of individual presolar grains via Nano-scale Secondary Ion Mass Spectrometry (NanoSIMS), Transmission Electron Microscopy (TEM), and Scanning Transmission X-ray Microscopy (STXM) utilizing X-ray Absorption Near Edge Structure (XANES), with a focus on connecting these correlated laboratory studies to astrophysical phenomena. This chapter provides a brief introduction to the subsequent chapters in this thesis.

Chapter 2: Background

Chapter 2 discusses the history and major discoveries in the fields of stellar nucleosynthesis and laboratory analysis of presolar grains. This discussion of stellar nucleosynthesis covers H burning on the main sequence and He burning for stars ascending the Red Giant branch of the Hertzsprung-Russel diagram. This chapter further discusses nucleosynthesis

along three evolutionary tracks for late-age stars: the Asymptotic Giant Branch (AGB) for low- to intermediate-mass stars, the Born-Again AGB phase, and Type-II (core collapse) supernova (SN) for high-mass stars. These types of late-age stars are the most well studied progenitors for presolar grains. The discussion of presolar grains focuses on presolar graphite and presolar SiC. The isotopic and microstructural differences between high- and low-density presolar graphite grains is discussed along with an overview of type X, AB, and mainstream SiC grains.

Chapter 3: Methods

Chapter 3 contains a discussion of the sample preparation and analysis techniques utilized in this thesis. The instrumental and analysis techniques include NanoSIMS, TEM, and XANES. This chapter also details the sample preparation techniques built upon and developed as a part of this thesis: namely, the micromanipulation and embedding in resin of individual presolar grains, and subsequent ultramicrotoming of the grains in cured resin for TEM study. These microtomed thin sections are also used for XANES and NanoSIMS study.

Chapter 4: C, N, and O isotopic heterogeneities in low-density supernova graphite grains from Orgueil

Chapter 4 is an adaptation of the peer-reviewed journal article, "C, N, and O Isotopic Heterogeneities in Low-Density Supernova Graphite Grains from Orgueil" by Groopman, E.,

Bernatowicz, T., and Zinner, E. (**2012**) The Astrophysical Journal Letters, **754**, L8. This paper details the discovery of spatially-correlated excesses in ^{15}N and ^{18}O that are carried by TiC subgrains in low-density presolar graphite grains. These correlated isotopic anomalies are the signature of the inner He/C zone in models of Type-II SN, pinpointing the location from which material that condensed to form these grains originated.

Chapter 5: NanoSIMS, TEM, and XANES studies of a Unique Presolar Supernova Graphite Grain

Chapter 5 is an adaptation of the peer-reviewed journal article, "NanoSIMS, TEM, and XANES studies of a Unique Presolar Supernova Graphite Grain" by Groopman, E., Nittler, L. R., Bernatowicz, T., and Zinner, E. (**2014**) The Astrophysical Journal, **790**, 9. This paper details the correlated NanoSIMS, TEM, and XANES studies of a unique low-density (LD) presolar graphite grain. This grain's unique microstructure and isotopic heterogeneities have significant import to our understanding of mixing in SNe ejecta and the evolution of the ejecta's physical, chemical, and isotopic composition.

Chapter 6: XANES of Presolar Graphite Grains and their TiC Subgrains

Chapter 6 is an adaptation of two conference abstracts regarding XANES measurements of presolar graphite grains: "Diversity in Carbon K-Edge XANES Among Presolar Graphite Grains" by Groopman, E., Nittler, L. R., Bernatowicz, T. J., Croat, T. K., Zinner, E., and

Kilcoyne, A. L. D. (**2014**) in 45th Lunar and Planetary Science Conference, Abstract #1492 (Lunar and Planetary Institute, Houston); and "Ti-XANES and EELS of Presolar TiC Subgrains Within Low-Density Supernova Graphite Grains" by Groopman, E. E., Daulton, T. L., Nittler, L. R., Bernatowicz, T. J., and Zinner, E. K. (**2012**) Meteoritics and Planetary Science Supplement 75, Abstract #5225. Presolar graphite grains and their constituent subgrains contain a wide variety of XANES spectra, influenced by the chemical bonding properties of the different materials. The ongoing goal of this project is to fully describe the bonding properties of these materials and link these to stellar formation conditions.

Chapter 7: C, Ca, and Ti Isotopes: On the Origins of High- and Low-Density Presolar Graphite Grains

Chapter 7 is an adaptation of the conference abstract "C, Ca, and Ti Isotopes: On the Origins of High- and Low-Density Presolar Graphite Grains" by Groopman, E. E., Zinner, E. K., and Bernatowicz, T. J. (**2013**) in *44th Lunar and Planetary Science Conference*, Abstract #1757 (Lunar and Planetary Institute, Houston). This chapter details new C, Ca, and Ti NanoSIMS measurements of high-density graphite grains and presents a discussion of possible stellar sources.

Chapter 8: pyLATTICE: A Program for Electron Diffraction Simulation

Chapter 8 describes the software **pyLATTICE**, adapted from Thomas Bernatowicz's LATTICE program. This chapter provides background crystallographic information and the **pyLATTICE** software manual.

Chapter 9: Conclusions

Chapter 9 provides concluding remarks regarding the findings and scope of this thesis.

Appendix

The appendix consists of tables containing NanoSIMS bulk-grain isotope data from low- and high-density presolar graphite grains from Orgueil mounts OR1d6m, OR1f4m, OR1g2m.

CHAPTER 2

BACKGROUND

2.1 Preface

In order to study astrophysical objects, astronomers are primarily limited to collecting and analyzing electromagnetic radiation, albeit across a wide range of energies. Roughly 30 years ago, however, small grains of presolar stardust were isolated from primitive meteorites, allowing for the physical study of stellar material in the laboratory. Isotopic analyses of the grains found that they contained isotopic signatures of nucleosynthesis from long-dead parent stars, vastly different than the average isotopic composition of the Solar System, aside from nuclear-specific effects such as radioactive decay and spallation. Such study may be colloquially referred to as performing astrophysics with a microscope in lieu of a telescope.

2.2 Stellar Nucleosynthesis

The majority of the matter in the universe consists of H and He, which currently account for roughly 74% and 24% by mass, respectively. These are primarily primordial, synthesized

during the Big Bang (Alpher *et al.*, 1948), although He is also produced in stars. The heavier elements, from C on up, were synthesized after the Big Bang from nuclear reactions within stars (Burbidge *et al.*, 1957; Cameron, 1957). There are multiple nucleosynthetic processes which result in the synthesis of the heavier elements in stars, each of which yields a specific population of elements and isotopes. The presence of one or more of these processes within a star is determined by the star's initial mass, and metallicity, i.e., the proportion of a star's mass that consists of elements other than H and He.

2.2.1 Hydrogen Burning

For the majority of a star's life it lives on the main sequence (MS), where H burning in the star's core maintains its luminosity (Rose, 1998). On a Hertzsprung-Russel (HR) diagram (Figure 2.1), which plots luminosity versus photospheric temperature, the MS is a narrow band that most observed stars occupy. On the MS line, higher mass correlates with higher luminosities and higher temperatures. Stellar mass is also negatively correlated with stellar lifetime. H burning in stars occurs through the proton-proton chain (p-p) or the CNO cycle. In low-mass MS stars ($0.8 - 1.2$ M$_\odot$) with core temperatures $\geq 10^7$ K, the former process is dominant. The p-p chain starts with the weak interactions

$$p + p \rightarrow {}^2H + e^+ + \nu_e \tag{2.1}$$

$$p + e^- + p \rightarrow {}^2H + \nu_e \tag{2.2}$$

although the second reaction has a much lower probability. ^{2}H further burns with a p to create a ^{3}He plus a γ-ray. From here multiple chains burn ^{3}He into ^{4}He either directly via

$$^3\text{He} + {}^3\text{He} \rightarrow {}^4\text{He} + 2\text{p} \tag{2.3}$$

or indirectly via burning up to ^{8}Be or ^{7}Li, both of which decay into 2 ^{4}He, the latter by fusion with a p. For MS stars with masses M $\gtrsim$ 1.2 M$_\odot$, and for post-MS stars with core temperatures $\gtrsim 1.8 \times 10^7$ K, hydrogen burning is completed via the CNO cycle, which burns H into He using C, N, and O as intermediaries. There exist multiple branches of the CNO cycle which operate in different mass and/or temperature regimes. The basic CNO cycle consists of the reactions and beta decays

$$
\begin{aligned}
^{12}\text{C} + \text{p} &\rightarrow {}^{13}\text{N} + \gamma \\
^{13}\text{N} &\rightarrow {}^{13}\text{C} + \text{e}^+ + \nu_\text{e} \\
^{13}\text{C} + \text{p} &\rightarrow {}^{14}\text{N} + \gamma \\
^{14}\text{N} + \text{p} &\rightarrow {}^{15}\text{O} + \gamma \\
^{15}\text{O} &\rightarrow {}^{15}\text{N} + \text{e}^+ + \nu_\text{e} \\
^{15}\text{N} + \text{p} &\rightarrow {}^{12}\text{C} + {}^4\text{He}
\end{aligned}
\tag{2.4}
$$
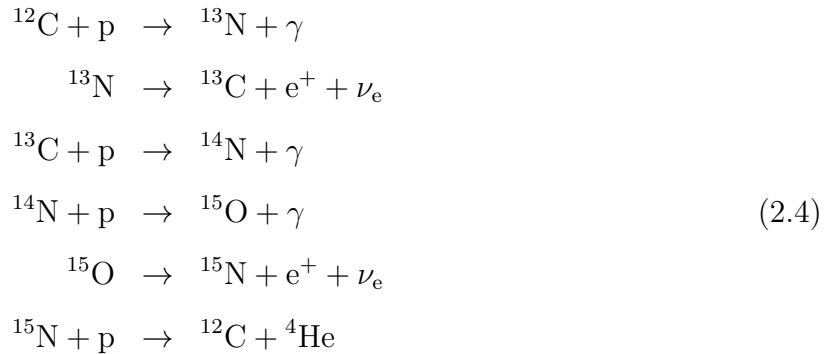
where the ^{12}C consumed in the first reaction is regenerated in the last step of the cycle plus a total of 26.73 MeV.
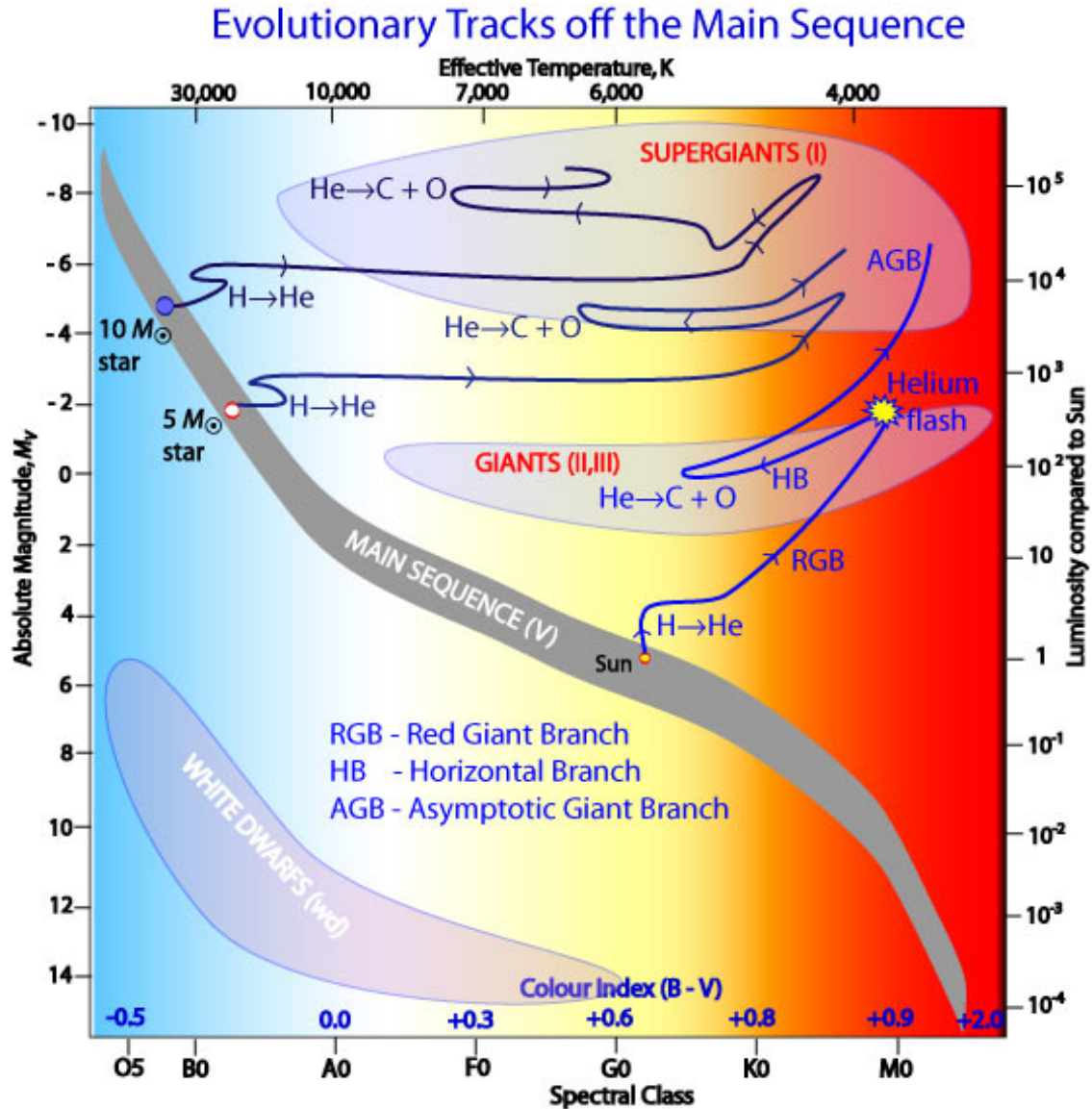
FIGURE 2.1: Hertzsprung-Russel (HR) diagram showing the evolution of late-age stars off of the main sequence (MS). Stars spend the majority of their lives on the MS burning H in their cores into He. More massive stars produce He from H via the CNO cycle, using C, N, and O as intermediaries, whereas in smaller stars the proton-proton chain is dominant. After the H fuel in the star's core has been consumed, the star evolves off of the MS on the HR diagram due to its core contracting and heating, which causes the star's outer envelope to expand and cool. Image source: "Evolutionary Tracks off the Main Sequence" Physics Stage 6 Syllabus ©Copyright 2002 The State of New South Wales Board of Studies.

2.2.2 Helium Burning

When the H in in a star's core is depleted, the star cools and slowly contracts, which eventually increases the core temperature. Abundant H immediately outside of the core ignites when the temperature rises to 10^7 K. This new H-burning shell causes the outer layers of the star to expand and cool, where convective currents are established, transferring heat out of the core more rapidly than via photon radiation, which was previously dominant. At this stage the star's luminosity increases, moving the star along a Reg Giant (RG) trajectory on the HR diagram (Figure 2.1). The He core, however, continues to contract during this time, and when its temperature reaches $\gtrsim 10^8$ K, He burning occurs via triple-α reactions

$$^4\text{He} + {}^4\text{He} \rightleftarrows {}^8\text{Be} + \gamma$$
$$^8\text{Be} + {}^4\text{He} \rightarrow {}^{12}\text{C} + \gamma \tag{2.5}$$

and the reaction

$$^{12}\text{C} + {}^4\text{He} \rightarrow {}^{16}\text{O} + \gamma. \tag{2.6}$$
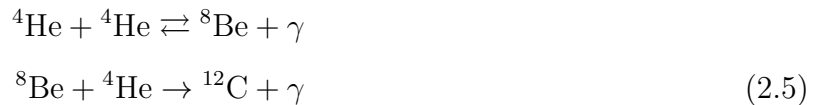
It should be noted that a star's nucleosynthesis and evolution on the HR diagram is heavily dependent upon its initial metallicity – for instance, low-metallicity stars may not experience a RG phase or a first dredge up event (see Section 2.2.3, Figure 2.3) (Karakas & Lattanzio, 2014).

11
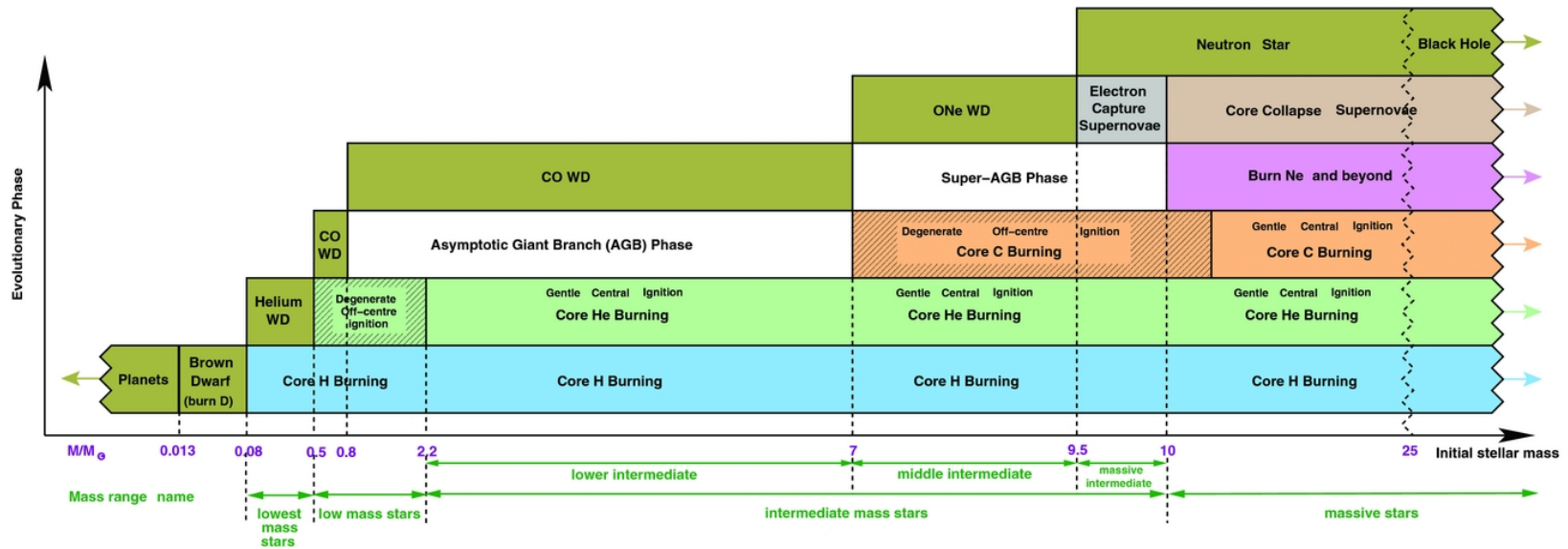
FIGURE 2.2: Figure 1 from Karakas & Lattanzio (2014), a schematic of stellar evolution based upon initial mass at solar metallicity (WD stands for white dwarf). Border regions are not precisely determined theoretically. Low- to intermediate-mass stars transition to the Asymptotic Giant Branch phase after core He burning, while massive stars continue to burn C, Ne, and Si, among other elements, until they become core-collapse (Type-II) supernovae. Lower-than-solar metallicity will shift the borders in the diagram to lower mass.
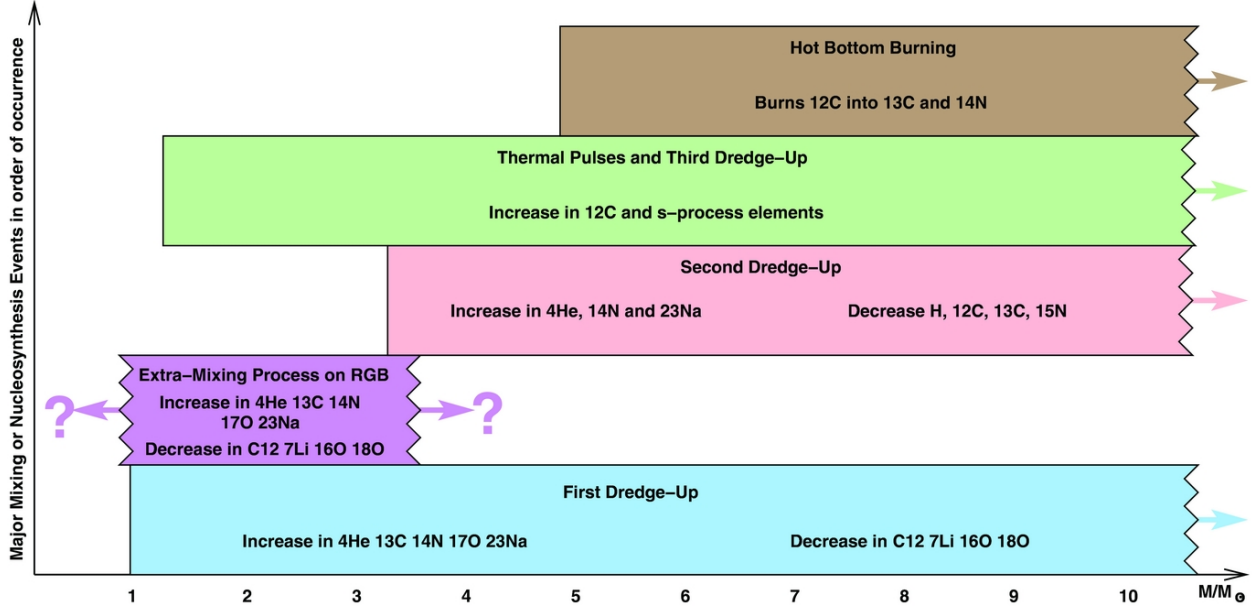
FIGURE 2.3: Figure 4 from Karakas & Lattanzio (2014), a schematic of dredge up, mixing, and nucleosynthetic events in Red Giant and Asymptotic Giant Branch stars (solar metallicity, Z = 0.02). The lower limits of dredge up events and hot bottom burning are sensitive to initial metallicity.

2.2.3 Low- to Intermediate-Mass Stars: The Asymptotic Giant Branch

Low- to intermediate-mass stars (0.8 – 10 M$_\odot$) have contributed nucleosynthetic material to the interstellar medium (ISM) through stellar winds (Karakas & Lattanzio, 2014). During the ascent of the RG branch, convective currents in the envelope dredge up material exposed to partial H burning near the core and mix it with material near the surface in what is called the first dredge up. Following exhaustion of He fuel in the core, the star will begin to ascend the giant branch once more on the HR diagram (Figure 2.1), now called the Asymptotic Giant Branch (AGB), where more massive stars will experience a second dredge up. As before with

H, after core contraction He will ignite in a shell surrounding the core, interior to the H-burning shell. This evolution and structure is schematically shown in Figures 2.2 and 2.4. Instabilities in the He-burning shell, called flashes or thermal pulses, drive nucleosynthesis (mostly C production) and mixing of this material to the surface via convective currents in what are known as third dredge up events. Most stars begin their lives with atmospheres rich in O relative to C, however successive third dredge up events may mix enough C to the star's surface that the number density of C/O $\geq$ 1 in the atmosphere, at which time the star becomes classified as a "carbon star" (C star).

Nucleosynthesis in an AGB star is highly dependent upon the star's initial metallicity and core size. Shells of He and H continue to burn and mix due to convection and thermal pulses. Heat from the thermal pulses allows for proton- and α-capture on C, N, and O, synthesizing small amounts of isotopes of heavier elements such as F, Ne, Na, Mg, and Al. The isotopic compositions of C, N, and O are also strongly affected during this time. Subsequent flashes and dredge up events increase the $^{12}C/^{13}C$ ratio (solar = 89) from roughly $10 - 20$ to between 30 and 100+ (Karakas & Lattanzio, 2014), which matches the observed C isotopic composition of mainstream presolar SiC grains (see Section 2.3.2), whose compositions generally lie in the range $40 \lesssim {}^{12}C/^{13}C \lesssim 100$ (Zinner, 1998). $^{14}N/^{15}N$ ratios are typically $\gtrsim$ 1000 for AGB stars (terrestrial = 272, solar = 459; Marty *et al.* (2011)).

Many of the elements heavier than Fe are synthesized via neutron capture and subsequent beta decay. The two main neutron capture processes are the *s-process* and the *r-process* (see Section 2.2.5), for slow- and rapid-neutron capture, respectively. Slow and rapid are relative terms with the average time for a β-decay as the baseline for each isotope. The *s-process* is
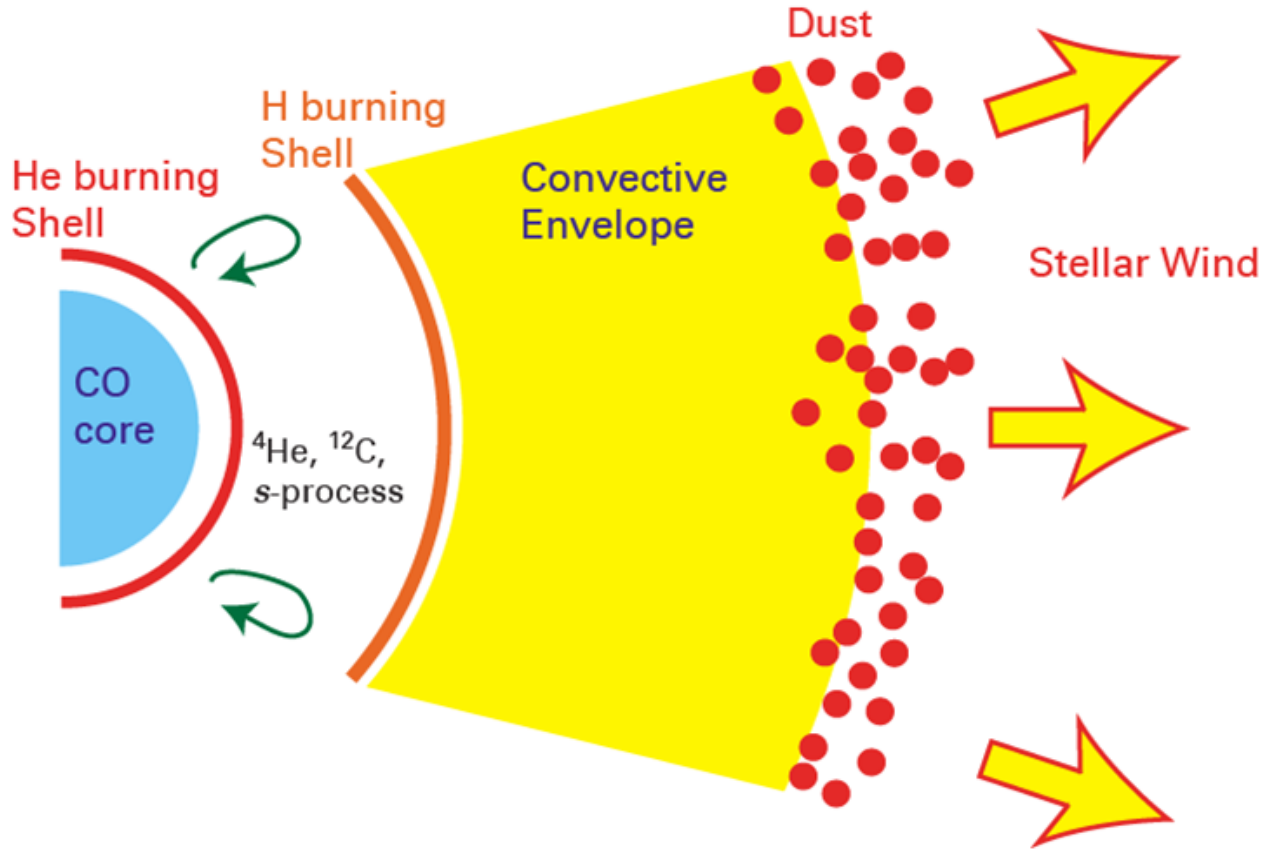
FIGURE 2.4: Schematic structure of an AGB star. Shown is an inert core of C and O surrounded by He- and H- burning shells. Dredge-up events mix material between the burning shells, and a convective currents in the envelope carry material to the star's surface, where it is blown away in the stellar wind, cooling and condensing to dust. (Courtesy of Larry Nittler).

characterized by stellar neutron densities low enough that the average time for a radioactive isotope to β-decay is shorter than the average time to capture another neutron. This leads to the production of isotopes populating the *valley of β-stability*, which accounts for roughly half of isotopes of the elements heavier than Fe. AGB stars are typically associated with heavier elements produced via the *s-process*, where $^{13}C(\alpha, n)^{16}O$ is the major neutron source. While many elements are produced by both the *s-process* and the *r-process*, some isotopes are produced strictly via one process.

15

2.2.4 Born-Again AGB Stars

At the end of the AGB phase, low- to intermediate-mass stars evolve into white dwarfs (WD) by ejecting their envelopes, which become planetary nebulae, leaving behind electron-degenerate cores insufficiently hot for continued fusion, with final compositions reflecting their initial masses (Figure 2.2). Roughly one quarter of AGB stars descending the WD track undergo a *very late thermal pulse* (VLTP) in which the He shell reignites and becomes convective (Herwig *et al.*, 2011). In this scenario, residual H from the star's surface is drawn down by convection and burned in the hot ^{12}C-rich layers, producing ^{13}C via the ^{12}C(p, γ)^{13}N(β^+)^{13}C reaction and lowering the ^{12}C/^{13}C ratio. After a few days, the convection zone is split into a H-burning upper layer and a He-burning lower layer. In the bottom of the He-burning layer, ^{13}C burns via ^{13}C(α, n)^{16}O, generating neutron densities typical of the *i-process* (Cowan & Rose, 1977). H ingestion and *i-process* nucelosynthesis eventually alter the elemental and isotopic composition of the He intershell making it distinct from AGB stars (Herwig *et al.*, 2011). Sakurai's Object is the most well known example of a Born-Again AGB star (Duerbeck *et al.*, 2000).

2.2.5 Massive Stars: Type-II Supernovae

Massive stars (above 8 M$_\odot$) have the chance to become core-collapse (Type-II) supernovae (SNe) at the end of their lives. Their early evolution is quite similar to less massive stars with core H burning and exhaustion ($T \gtrsim 10^7$ K) followed by core He burning and exhaustion ($T \gtrsim 10^8$ K), though on a far shorter timescale. The majority of the *s-process* that takes place

16

in massive stars occurs during core He burning, synthesizing isotopes up to mass $A \approx 88$ using neutrons produced by the reaction $^{22}\text{Ne}(\alpha,\text{n})^{25}\text{Mg}$ (Woosley *et al.*, 2002). Following core He burning, however, core contraction due to the extra mass is enough to heat the core past $\sim 8 \times 10^8$ K, which can ignite C. Subsequent stages of core Ne, O, and Si burning ($T \gtrsim 10^9$ K) yield an inert core of Fe and Ni surrounded by concentric shells of lighter, partially burning elements (Figure 2.5) (Woosley & Weaver, 1995; Woosley *et al.*, 2002).

Simplistically, when the Fe/Ni core of a massive star reaches the Chandrasekhar mass, its electron degeneracy is no longer enough to counter gravitational contraction and it collapses (Woosley *et al.*, 2002). When the density of the core approaches neutron degeneracy levels, infalling material bounces back off of the nuclear core sending a shock wave through the outer layers of infalling material. The shock wave passing through infalling material results in explosive nucleosynthesis of O, Si, Ne, and C, while also generating copious quantities of neutrons. While the precise location(s) where the *r-process* occurs are undetermined, SNe are likely candidates (Woosley *et al.*, 2002).

Mixing in Supernova Ejecta

Many early SN models assumed spherically symmetric explosions based upon 1D models for simplicity, however recent 3D models (Hammer *et al.*, 2010) and observations of SNe and their remnants (e.g., SN 1987A and Cassiopeia A; Wooden *et al.* (1993); Rest *et al.* (2011); Grefenstette *et al.* (2014)) have shown large-scale asymmetries and mixing in SN explosions. In the observations and models, heavy material from deep within the star is ejected in clumps through the lighter outer material, partially inverting the pre-SN concentric-shell
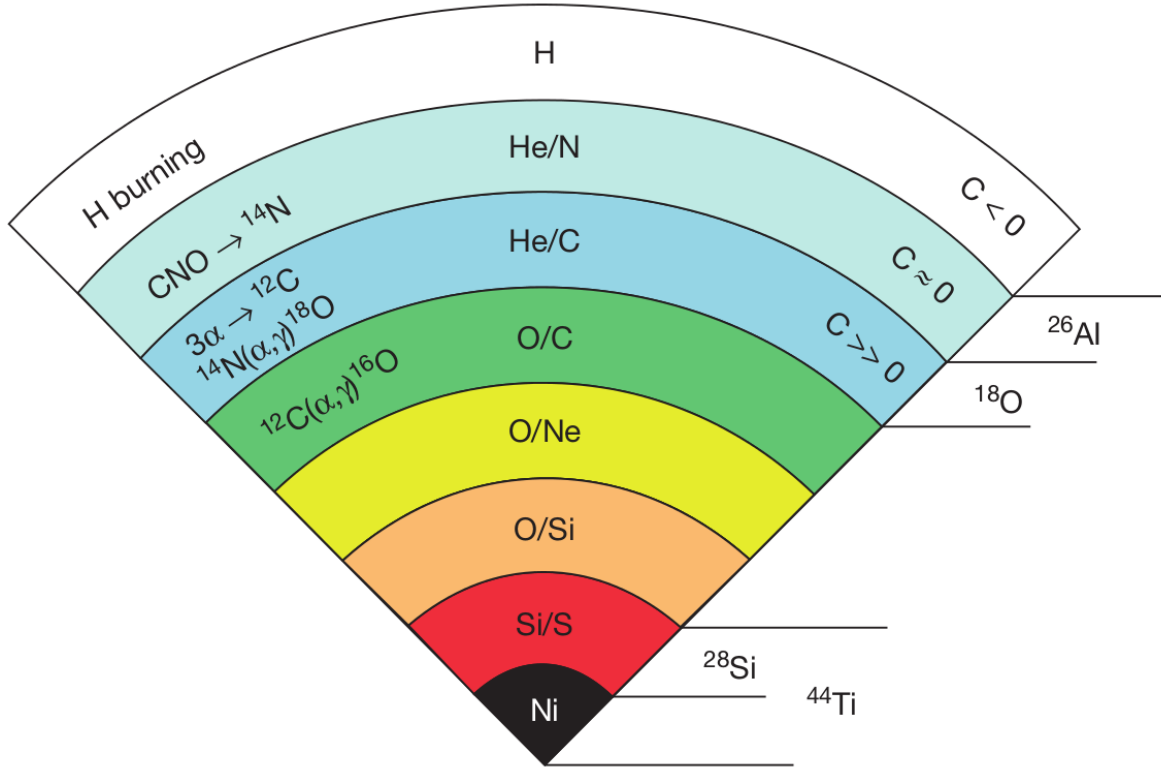
FIGURE 2.5: Figure 9 from Zinner (2014) (source: Woosley & Weaver (1995)). Schematic structure of a pre-SN massive star. Shells are labeled by their most abundant elements. As pressure and temperature rise towards the star's interior and the elemental composition changes, each shell experiences different nucleosynthetic processes. Isotopes listed on the right of the diagram are the primary indicators in presolar grains of a SN origin and are overabundant in their accompanying zones. Presolar grains from SNe contain excesses in many or all of these isotopes, indicating that mixing between non-adjacent zones occurs in the ejecta.

structure. This phenomenon has significant implications for the understanding of presolar grain condensation as presolar grains often contain isotopic signatures from multiple and occasionally non-adjacent SN zones (see Section 5.5.1, Paragraph 4 for a more in-depth discussion).

2.3   Presolar Grains

Presolar grains are the sub-μm-to-μm-sized condensates from the stellar ejecta of late-age stars, such as AGB stars and SNe. These grains formed prior to the Solar System (SS) and survived its formation, becoming entrained in early SS solids, such as asteroids. The majority of presolar grains have been chemically isolated from or studied *in-situ* in primitive meteorites. The more primitive the meteorite (i.e., the lesser the amount of thermal metamorphism or aqueous alteration), the higher the concentration of surviving presolar grains (Huss & Lewis, 1995). Presolar grains have also been found in interplanetary dust particles (IDPs) collected in the upper atmosphere (Messenger *et al.*, 2003) and in cometary samples, e.g., from NASA's STARDUST mission to Comet Wild/2 (Leitner *et al.*, 2010, 2012; Floss *et al.*, 2013).

The first evidence for the existence of presolar material of nucleosynthetic origin within early SS solids (Black, 1972) came from isotopically anomalous noble gas measurements of Ne and Xe (Black & Pepin, 1969; Reynolds & Turner, 1964). Prior to these findings, the SS was believed to be completely isotopically homogenized. Mass-independent O isotopic fractionation had been observed in the first SS solids, Calcium-Aluminum-rich Inclusions (CAIs), though on a far smaller scale. Subsequent tracing of the carriers of these anomalous noble gas measurements led to the discovery of three refractory presolar minerals: nanodiamond (Lewis *et al.*, 1987), SiC (Bernatowicz *et al.*, 1987; Tang & Anders, 1988), and graphite (Amari *et al.*, 1990). Later more presolar minerals were discovered, including the less-refractory silicates (Messenger *et al.*, 2003) and oxides (Hutcheon *et al.*, 1994; Nittler

et al., 1994), in addition to carbide subgrains within parent grains (Bernatowicz *et al.*, 1991), among many others.

2.3.1 Presolar Graphite Grains

Presolar graphite grains were first identified in the Murchison CM2 chondrite by tracing the noble gas component Ne-E(L) through successive acid dissolution steps (Amari *et al.*, 1990). Ne-E(L) is nearly monoisotopic ^{22}Ne resulting from α-capture on ^{18}O and the decay of ^{22}Na ($t_{1/2} = 2.6$ years), which was attributed to nucleosynthesis in novae and AGB stars. A presolar origin for individual graphite grains was confirmed based upon their wide range of C isotopic compositions, with $8 \leq {}^{12}C/{}^{13}C \leq 1500$. Since then, presolar graphite grains isolated in the same manner from both the Murchison CM2 and Orgueil CI1 chondrites have exhibited a wide range of nucleosynthetic signatures indicating a variety of stellar origins including AGB stars, SNe, and Born-Again AGB stars (Hoppe *et al.*, 1995; Zinner *et al.*, 1995; Bernatowicz *et al.*, 1996; Jadhav *et al.*, 2006, 2008, 2013a,b; Amari *et al.*, 2014).

Due to their low abundance (< 2 ppm) compared to SiC (6–9 ppm) or nanodiamond (400 ppm) (Amari *et al.*, 1990), presolar graphite grains have never been found *in-situ* and have only been studied as acid separates. The acid separations were further split into size and density fractions for each meteorite (Amari *et al.*, 1994; Jadhav *et al.*, 2006), though only with sizes > 1 μm. Presolar graphite grains are quasi-spherical, with surface morphologies varying between "vegetable" types: onion and cauliflower (Zinner *et al.*, 1990; Hoppe *et al.*, 1995). Density and surface morphology are intrinsically linked to a graphite grain's presolar progenitor, with low-density (LD; $\rho \lesssim 2.0$ g/cm^3) grains generally containing nucleosynthetic

signatures from SNe and high-density (HD; $2.0 \lesssim \rho \lesssim 2.2$ g/cm^3) grains often containing signatures of an AGB origin (Hoppe *et al.*, 1995; Zinner *et al.*, 1995; Bernatowicz *et al.*, 1996; Jadhav *et al.*, 2006), though small populations of HD grains have been linked to SNe and Born-Again AGB stars (Jadhav *et al.*, 2008, 2013a,b).

In addition to surface morphology, density and stellar origin are also linked to each graphite grain's internal crystal structure and complement of subgrains of different mineral phases. Internal crystal structure can vary from concentric shells of highly-ordered graphite (Bernatowicz *et al.*, 1996; Croat *et al.*, 2005), to more disrupted turbostratic graphite (Croat *et al.*, 2003, 2008), to cores of nanocrystalline C surrounded by highly-ordered or turbostratic graphite (Bernatowicz *et al.*, 1996; Croat *et al.*, 2005; Groopman *et al.*, 2014). Presolar graphite grains appear to readily capture small subgrains of different chemical phases as the graphite condenses; in some cases a subgrain clearly served as a nucleation point for graphite growth (Bernatowicz *et al.*, 1996). As each chemical phase requires a different condensation temperature, pressure, and chemical environment to form, presolar graphite grains and their inferred condensation sequences provide the most detailed picture of the physical and chemical environments in stellar ejecta. These data match well with observations of stellar ejecta from SNe (see Chapter 5; Groopman *et al.* (2014)) and AGB stars (Bernatowicz *et al.*, 2005).

Low-Density (LD) Presolar Graphite Grains

LD presolar graphite grains are those with densities $1.60 \lesssim \rho \lesssim 2.05$ g/cm^3 (Amari *et al.*, 1994; Jadhav *et al.*, 2006). From Murchison this includes the KE size/density fractions ($\rho = 1.6 - 2.05$ g/cm^3) (Amari *et al.*, 1994). From Orgueil this includes the size/density fractions

OR1b ($\rho = 1.59 - 1.67$ g/cm^3), 1c ($\rho = 1.67 - 1.75$ g/cm^3), and 1d ($\rho = 1.75 - 1.92$ g/cm^3) (Jadhav *et al.*, 2006). Most LD graphite grains have been found to contain isotopic signatures of SN nucleosynthesis. As discussed previously, each massive star zone undergoes different pre- and post-SN nucleosynthesis. The majority of material from which the graphite grains and their subgrains condense likely comes from the He/C and He/N zones (Groopman *et al.*, 2012, 2014; Rauscher *et al.*, 2002; Bojazi & Meyer, 2014), with possible smaller contributions from the Si/S zone (^{28}Si excesses; Zinner *et al.* (2006)) and the O/C zone (neutron capture pattern of Ca isotopes; Jadhav *et al.* (2013a)). The isotopic signatures of the He/C and He/N zones observed in LD graphite grains are excesses relative to the SS isotopic composition in ^{15}N and ^{18}O, and large inferred initial ^{26}Al/^{27}Al ratios (Figure 2.6) (Stadermann *et al.*, 2005; Groopman *et al.*, 2012, 2014). The He/C and He/N zones are also among the only zones where the number density of C exceeds that of O (Rauscher *et al.*, 2002), a condition favorable for the condensation of carbonaceous material, as C will otherwise combine with O to form CO until either C or O is depleted.

The crystal structure of LD spherules typically consists of turbostratic graphite, characterized by lateral domain sizes on the order of 10s to 100s of nm (Croat *et al.*, 2008). The d-spacings corresponding to the in-plane hexagonal structure, as determined by electron diffraction, match that of ideal graphite to within 1% (d$^{\text{ideal}}_{(100)} = 2.131$ Å, d$^{\text{ideal}}_{(110)} = 1.231$ Å) (Croat *et al.*, 2008; Groopman *et al.*, 2014). The measured (002) d-spacing for turbostratic graphite, corresponding to the planar stacking direction, is $\sim 5\%$ larger than that of an ideal crystal (d$^{\text{turbo}}_{(002)} = 3.52$ Å; d$^{\text{ideal}}_{(002)} = 3.354$ Å) (Bernatowicz *et al.*, 1996; Croat *et al.*, 2005; Groopman *et al.*, 2014). The increase in bond length is partially due to the presence of O

trapped between sheets, whose concentration has been shown to correlate with the degree of stacking disorder (Joseph & Oberlin, 1983; Croat *et al.*, 2008). Turbostratic graphite in LD grains from the Orgueil meteorite contains a higher concentration of O than their HD cousins, based upon EDXS measurements (Croat *et al.*, 2008). This may not be the case for presolar graphite grains from the Murchison meteorite, however (Ernst Zinner, personal communication).

LD graphite grains typically contain entrained subgrains of various chemical phases such as TiC (25–2500 ppm), SiC ($<$ 100 ppm), Fe-Ni metal ($<$ 100 ppm) (Croat *et al.*, 2003, 2008; Groopman *et al.*, 2014), and rare refractory metal nuggets (Croat *et al.*, 2013). These subgrains are usually primary condensates from the stellar ejecta which formed prior to or concurrently with the condensing graphite parent grain in which they became entrained. Some Fe-Ni subgrains appear to have formed as exsolutions, not from the parent graphite grain, but from a nearby subgrain after capture. The presence of TiC subgrains is nearly ubiquitous in LD presolar graphite grains. While most TiC subgrains are euhedral with well-defined crystal faces, many show evidence of extensive corrosion (Croat *et al.*, 2003). Numerous TiC subgrains are additionally surrounded by partially amorphous rims, likely due to sputtering and structural damage caused by differential speeds of gas and grains in stellar outflows prior to encapsulation within the graphite (Croat *et al.*, 2003; Daulton *et al.*, 2009, 2012). These subgrains clearly formed before the parent graphite grain, which informs our knowledge of the grain's condensation sequence.
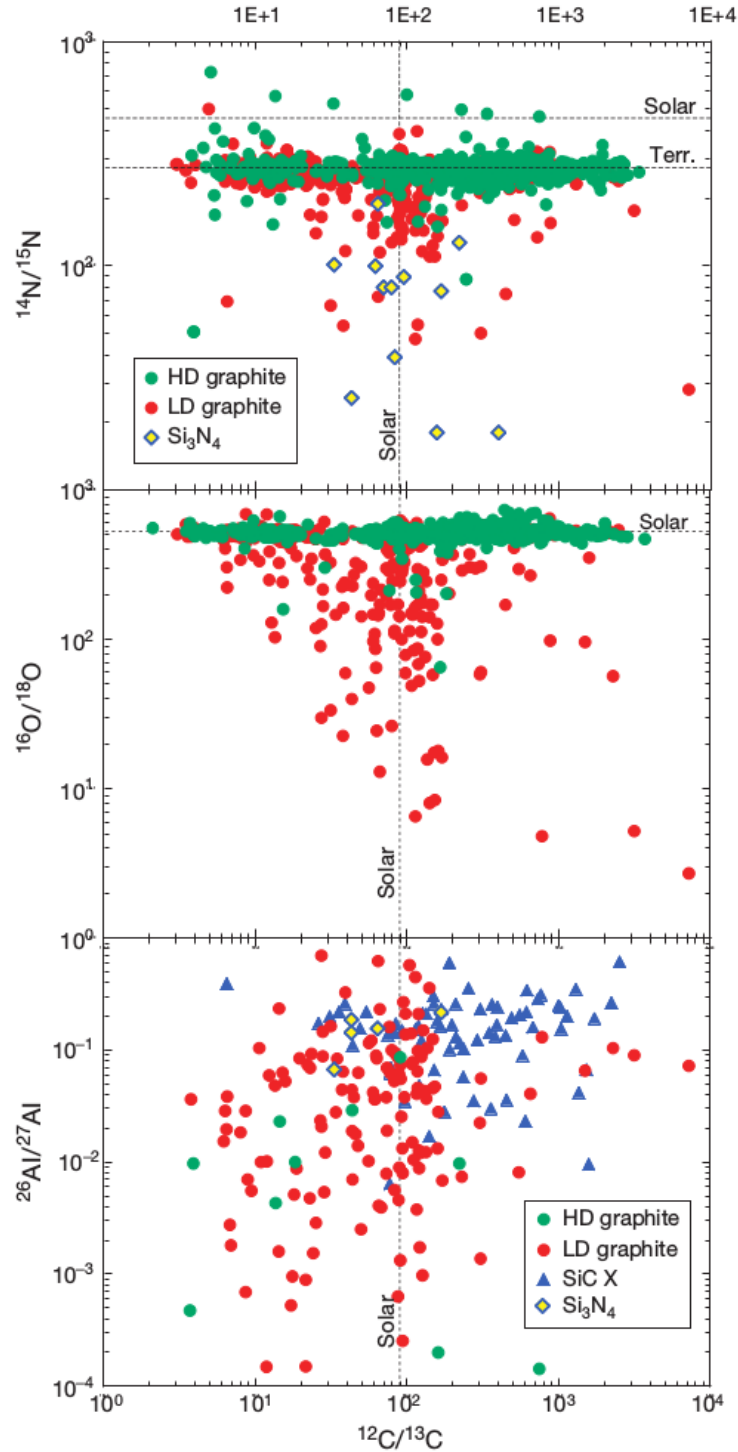
FIGURE 2.6: Adaptation of Figure 12 from Zinner (2014). $^{12}C/^{13}C$ vs. $^{14}N/^{15}N$, $^{16}O/^{18}O$, and inferred initial $^{26}Al/^{27}Al$. LD graphite grains typically exhibit excesses in ^{15}N and ^{18}O, and high inferred initial $^{26}Al/^{27}Al$ ratios, consistent with SN origins and highly similar to SiC X grains (see Section 2.3.2) HD graphite grains (see next subsection) generally exhibit terrestrial N and O ratios, potentially due to isotopic dilution. Source: Presolar Grain Database (Hynes & Gyngard, 2009).
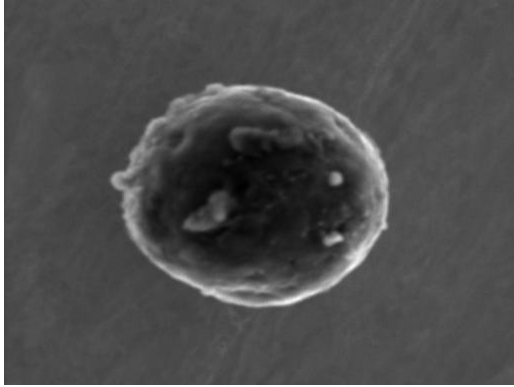
FIGURE 2.7: Secondary electron image of a large LD graphite grain (20 μm).
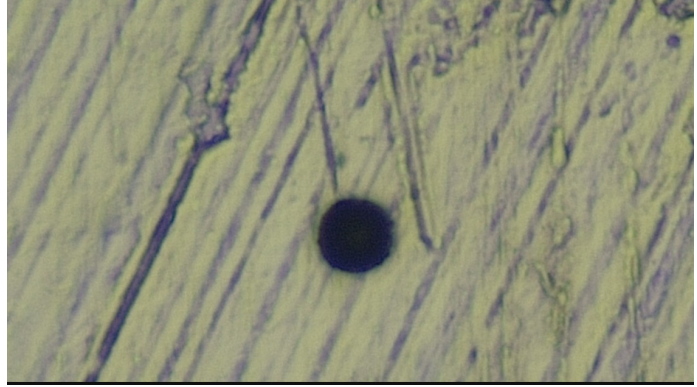
FIGURE 2.8: Optical image of the same grain on a Au foil.
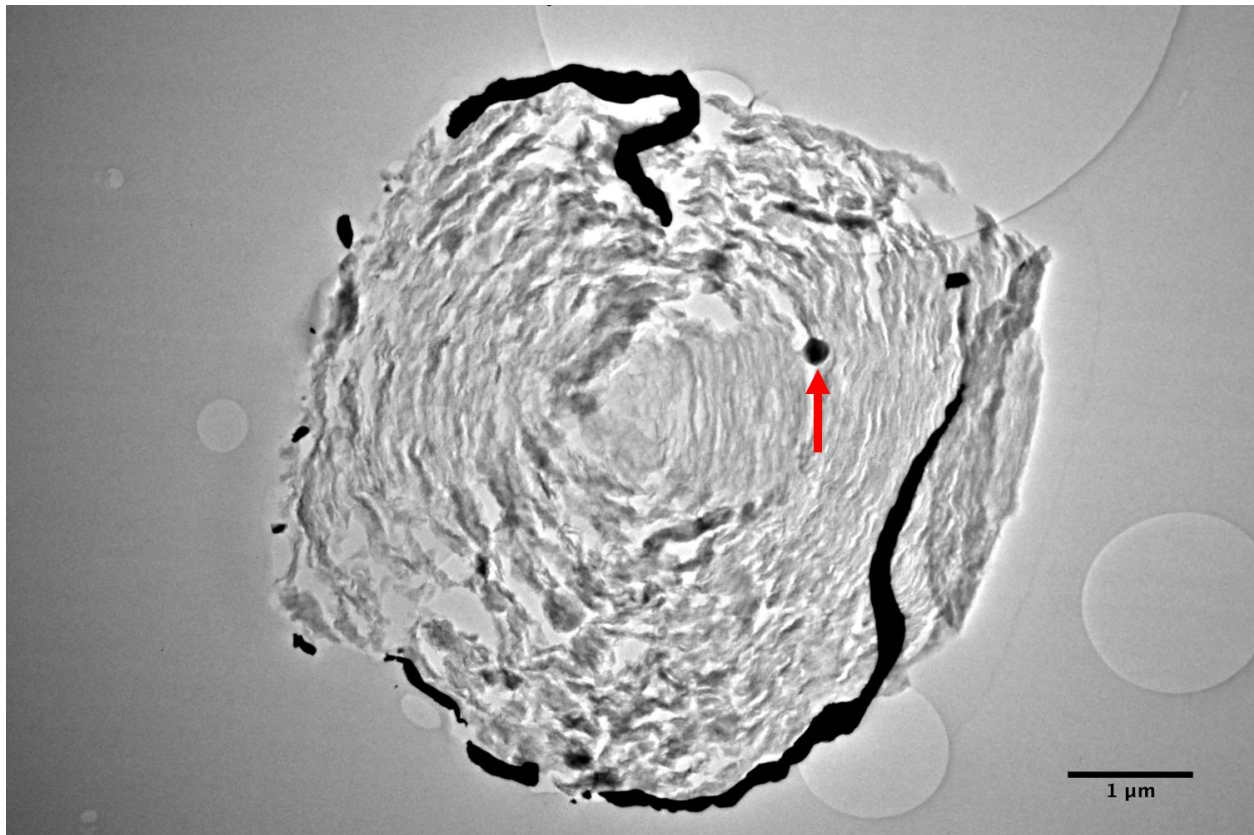
FIGURE 2.9: TEM micrograph of an ultramicrotome section of a LD graphite grain consisting of turbostratic graphite. This is a different grain than shown in the previous images. A TiC subgrain is visible right from center (indicated by arrow). Black "ribbon" is redeposited Au from NanoSIMS measurement.

High-Density (HD) Presolar Graphite Grains

HD graphite grains are those with densities $\rho \gtrsim 2.0$ g/cm^3(ideal graphite $\rho = 2.23$ g/cm^3). From Murchison this includes all of the KF size/density fractions: KFA ($\rho = 2.05 - 2.10$ g/cm^3), KFB ($\rho = 2.10 - 2.15$ g/cm^3), and KFC ($\rho = 2.15 - 2.25$ g/cm^3) (Amari *et al.*, 1994). From Orgueil this includes the size/density fractions OR1f ($\rho = 2.02 - 2.04$ g/cm^3), 1g ($\rho = 2.04 - 2.12$ g/cm^3), 1h ($\rho = 2.12 - 2.16$ g/cm^3), and 1i ($\rho = 2.16 - 2.30$ g/cm^3) (Jadhav *et al.*, 2006). Among the Orgueil fractions, the large majority of presolar graphite grains were isolated from OR1f and OR1g. Most HD graphite grains originate in low-metallicity AGB stars (Hoppe *et al.*, 1995; Zinner *et al.*, 1995; Bernatowicz *et al.*, 1996; Amari *et al.*, 2001; Jadhav *et al.*, 2006), although a portion of them likely form in SNe and Born-Again AGB stars (Jadhav *et al.*, 2008, 2013a,b). HD graphite grains typically have an onion-like internal structure consisting of concentric sheets of well-ordered graphite (Bernatowicz *et al.*, 1996). Approximately one third of HD graphite grains have been found to contain nanocrystalline cores consisting of randomly oriented graphene sheets 3–4 nm in size that are surrounded by mantles of graphite (Bernatowicz *et al.*, 1996; Croat *et al.*, 2005). Bernatowicz *et al.* (1996) suggested that these nanocrystalline cores formed when C was highly supersaturated in the stellar outflows where they formed, and the transition to longer-range order (e.g., mantling graphite) occurred when the number density of condensable C atoms diminished. Since nanocrystalline cores are always found within mantles of well-graphitized carbon, and never vice versa or in an alternating pattern, these grains likely reflect monotonically changing physical and/or chemical environments in AGB outflows.

HD graphite grains generally have lower trace element abundances than LD grains, and in particular, usually have terrestrial N and O isotope compositions (Figure 2.6) (Hoppe *et al.*, 1995; Zinner *et al.*, 1995; Jadhav *et al.*, 2006, 2008, 2013a; Amari *et al.*, 2014). Despite these normal N and O isotopic compositions, HD graphite grains exhibit a wide range of $^{12}C/^{13}C$ ratios. As such, it is unlikely that these N and O isotopic compositions are intrinsic, and are instead due to isotopic dilution with the meteorite parent body or contamination in the laboratory (Zinner, 2014). The puzzle of terrestrial N and O isotopic compositions among HD graphite grains remains an open question. Some HD graphite grains exhibit very low $^{12}C/^{13}C$ ratios coupled with extreme Ca and Ti isotope anomalies whose most likely origin is in the outflows of Born-Again AGB stars, such as Sakurai's Object (see Jadhav *et al.* (2008, 2013a); Herwig *et al.* (2011) and Chapter 7).

Condensation

Subgrains of varied chemical composition within parent presolar grains yield a wealth of information regarding the condensation sequence of these solids and thus the physical and chemical environment in stellar ejecta, as each chemical phase requires a specific range of temperatures, pressures, and chemical environment (e.g., C/O ratio) to form (Lodders & Fegely, 1995). Presolar graphite, with a proclivity for capturing smaller grains as it condenses, provides one of the best testbeds for equilibrium condensation calculations. Lodders & Fegely (1995) calculated the condensation sequence for carbonaceous materials in C-rich stellar atmospheres (see Figure 2.10), which Bernatowicz *et al.* (1996, 2005) subsequently applied to presolar graphite grains from AGB stars. In some presolar graphite grains, Berna-

towicz *et al.* (1996) found that TiC subgrains acted as the nucleation center for subsequent graphite condensation, unambiguously implying that the TiC formed prior to the graphite. Given the range of temperatures and pressures required for such an equilibrium condensation sequence, the graphite grains must have formed in sufficiently dense stellar ejecta, far denser, in fact, than could be accounted for by spherically symmetric stellar winds given the observed mass loss rates in C stars. This was a significant prediction based upon the laboratory analysis of presolar stardust – that stellar outflows from AGB stars are clumpy or jet-like – which was later corroborated by astronomical observations and further simulations (Bernatowicz *et al.*, 2005). As mentioned in Section 2.2.5, SN ejecta have also been observed to be clumpy and have temperature and pressure profiles which lie in the appropriate range for carbonaceous grain condensation (Figure 2.10, see Chapter 5).
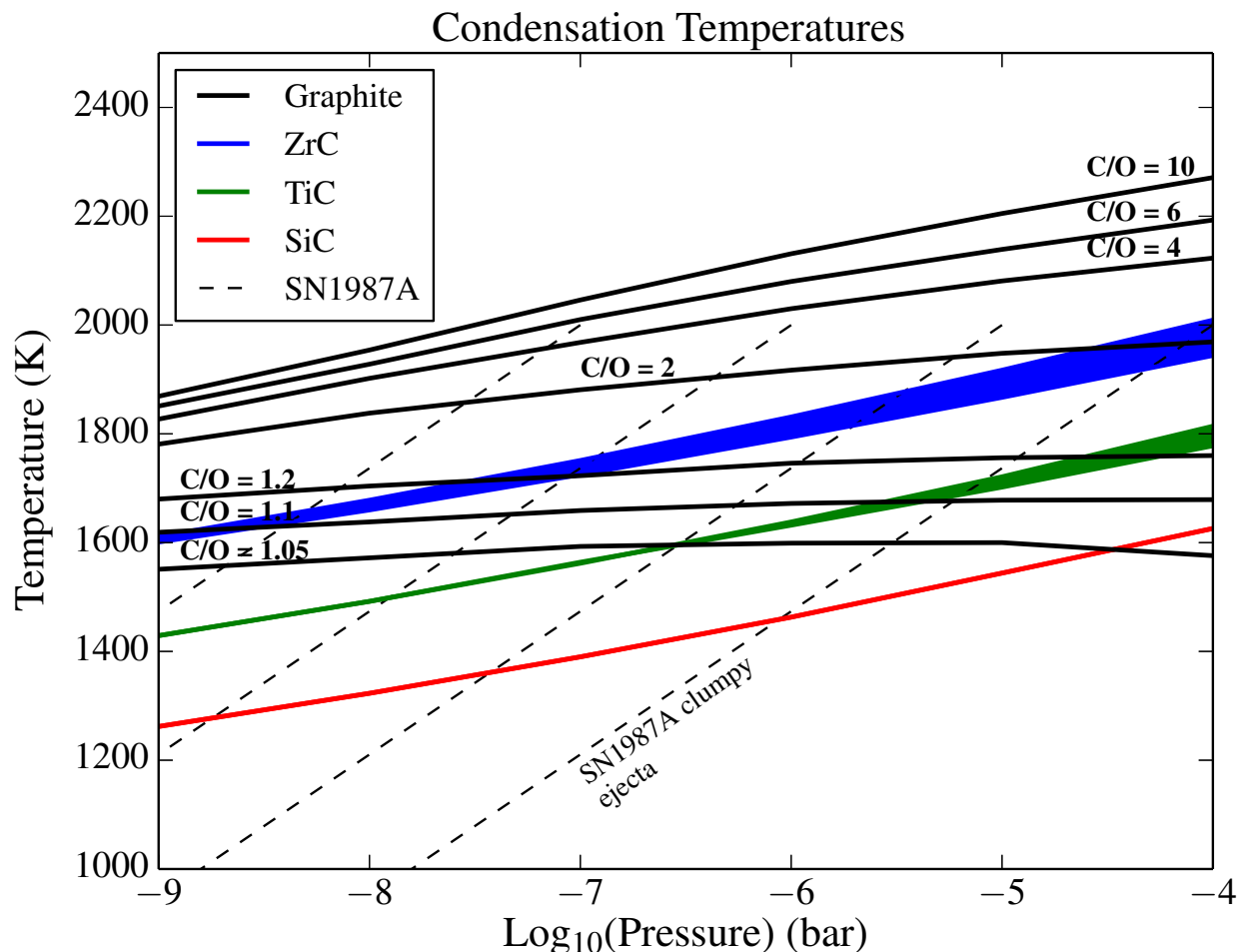
FIGURE 2.10: Figure 9 from Groopman *et al.* (2014), adapted from Bernatowicz *et al.* (1996) and Fedkin *et al.* (2010); condensation data from Lodders & Fegely (1995); SN1987A observations from Wooden *et al.* (1993). Condensation temperatures (T) for carbonaceous materials at different ambient pressures (P) and C/O ratios. The onset T for graphite condensation is highly dependent on the ambient C/O ratio, while the carbides are more sensitive to the ambient P. Envelopes for ZrC (blue) and TiC (green) illustrate the range of T for a range of C/O ratios. At C/O ratios close to 1, TiC condenses prior to graphite for pressures above 10^{-7} bar. SiC (red) can only form prior to graphite at relatively high P. Dashed curves are P-T profiles that Fedkin *et al.* (2010) derived (for mean atomic weight of 16) from Wooden *et al.* (1993) observations of SN1987A's clumpy ejecta by reducing P by factors of 10, 100, and 1000 (right to left). The P of SN1987A's clumpy ejecta dropped from $\sim 10^{-4}$ bar on day 60 to $\sim 8 \times 10^{-9}$ bar on day 777 (T = 500K, not shown). These P-T profiles match well the range of temperatures and pressures required to describe subgrain abundances in presolar graphite grains.

2.3.2   Presolar SiC Grains

Presolar SiC remains the most well-studied type of presolar grain, both isotopically and microstructurally. Presolar SiC was identified as the carrier of the anomalous noble gas components Ne-E(H) and Xe-S (Bernatowicz *et al.*, 1987; Tang & Anders, 1988). The vast majority of presolar SiC ($\sim 93\%$) have an AGB star origin and are classified as mainstream grains (Zinner, 2014). Mainstream SiC grains typically have ^{29}Si and ^{30}Si excesses lying around a line of slope 1.4 on a Si 3-isotope plot (Figure 2.11, Panel 3). Mainstream SiC grains predominantly ^{12}C/^{13}C ratios less than solar (= 89), though ^{12}C/^{13}C ratios range between 10 and 100, with the majority of grains having $50 < {}^{12}$C/^{13}C < 70 (Figure 2.12). Mainstream SiC grains also contain a wide range of ^{14}N/^{15}N ratios, though they are mostly enriched in ^{14}N relative to terrestrial composition (^{14}N/^{15}N $= 272$). All heavy element ratios measured in mainstream SiC grains show signatures of the *s-process*, further confirming their AGB origins.

SiC X grains ($\sim 1\%$ of measured grains) have likely SN origins based upon their large excesses in ^{28}Si (Figure 2.11) and ^{15}N (Figure 2.12), and high inferred initial ^{26}Al/^{27}Al ratios (Figure 2.13). In fact, the similarities in isotopic composition between LD graphite grains and SiC X grains lent credence to the notion that LD graphite grains formed in SNe (Figure 2.6). X grains are typically composed of many small crystal domains, whereas mainstream grains are limited to only a few larger domains (Hynes *et al.*, 2010). These differences likely reflect conditions of greater supersaturation and thus more rapid growth in SN ejecta.

A third population of presolar SiC are the AB grains, primarily defined as those with

^{12}C/^{13}C $\leq$ 10 (Figure 2.12). AB grains have similar Si isotopic compositions to mainstream grains (Figure 2.11), along with a wide range of ^{14}N/^{15}N ratios. AB grains on average also have higher inferred initial ^{26}Al/^{27}Al ratios than mainstream, Y, and Z grains (Figure 2.13). The low ^{12}C/^{13}C ratios are difficult to reconcile with an AGB star origin. The remaining possible progenitor star types include J-stars and Born-Again AGB stars (see Zinner (2014) for a more in-depth discussion).
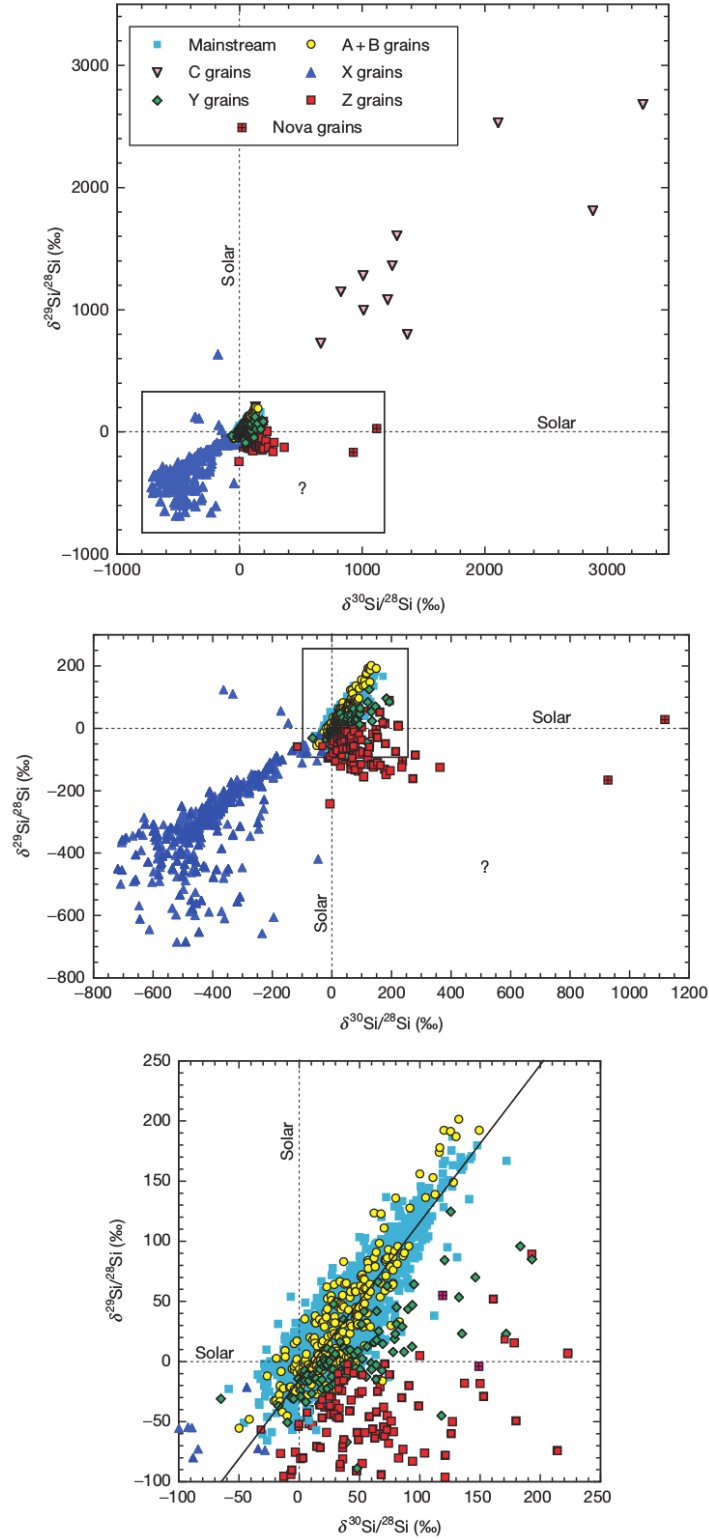
FIGURE 2.11: Figure 4 from Zinner (2014). Si 3-isotope plot showing deviations in permil (‰) from solar composition. $\delta^i\text{Si}/^{28}\text{Si} = 1000 \times \left(\left(\frac{^iSi}{^{28}Si}\right)_{\text{sample}} / \left(\frac{^iSi}{^{28}Si}\right)_{\text{standard}} - 1\right)$. Panel 3 shows the mainstream line, slope 1.4 (solid). Source: Presolar Grain Database (Hynes & Gyngard, 2009).
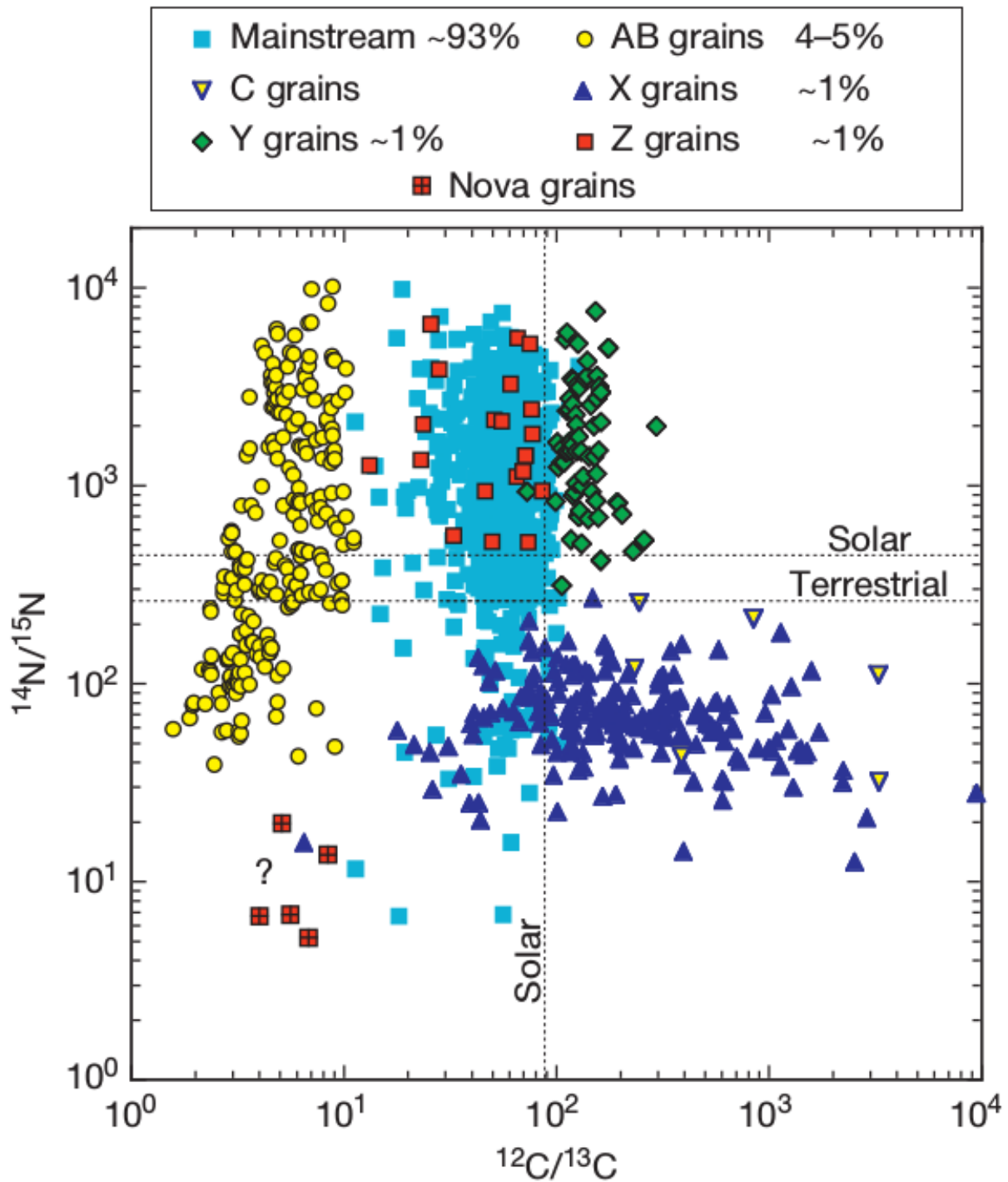
FIGURE 2.12: Figure 3 from Zinner (2014). $^{12}C/^{13}C$ vs. $^{14}N/^{15}N$ for individual presolar SiC grains. One grain is plotted as a question mark as it contains both SN and nova isotopic signatures (Nittler & Hoppe, 2005).
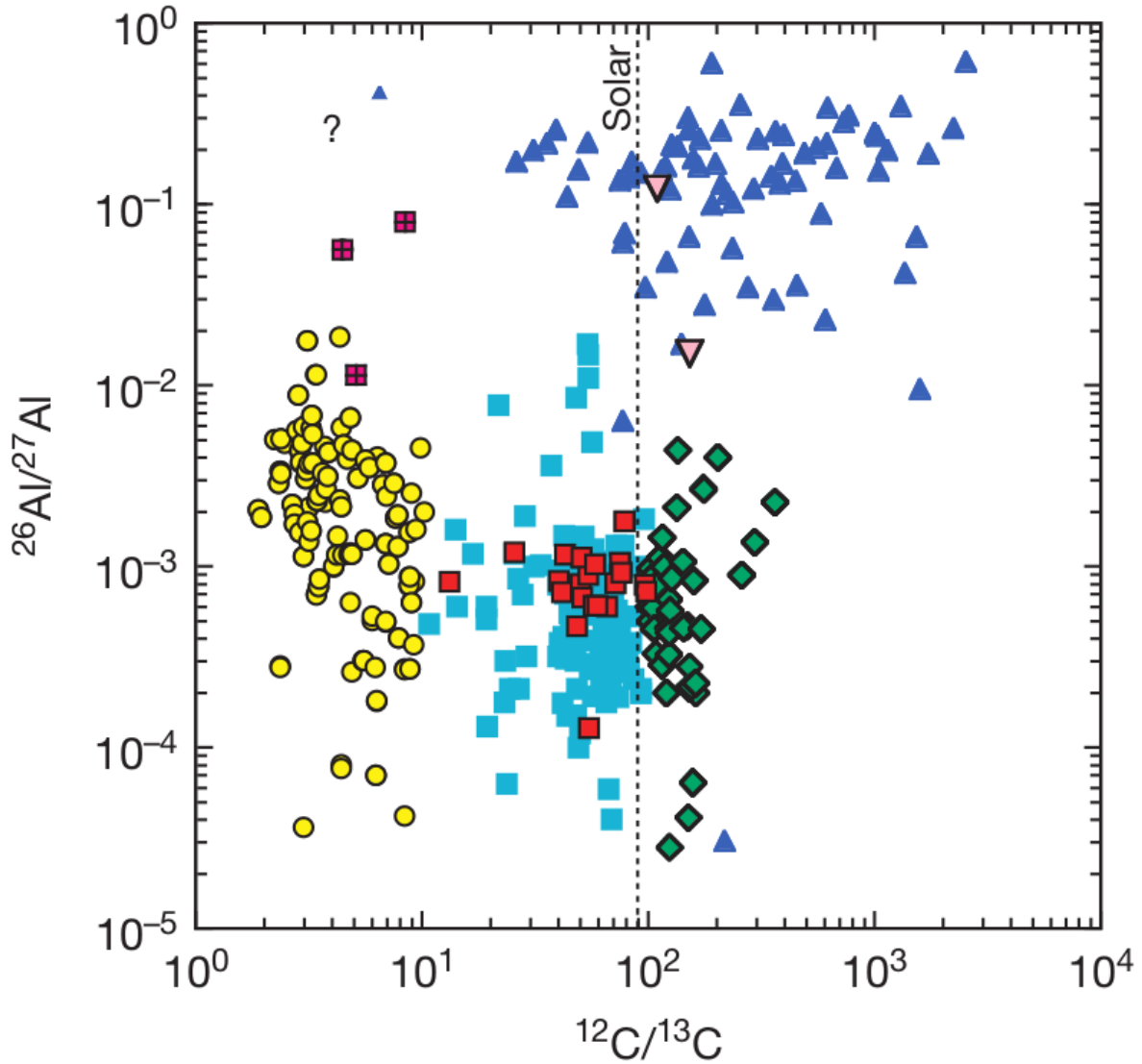
FIGURE 2.13: Figure 5 from Zinner (2014). ^{12}C/^{13}C vs. inferred initial ^{26}Al/^{27}Al. This figure uses the same symbols as Figures 2.11 and 2.12. SiC X grains have the highest initial ^{26}Al/^{27}Al ratio, part of strong evidence for a SN origin. AB grains also have slightly higher Al ratios than those in other grain types.

Bibliography

Alpher, R. A., Bethe, H., & Gamow, G. (**1948**), "The Origin of Chemical Elements", *Physical Review* **73**, 803–804, URL http://dx.doi.org/10.1103/PhysRev.73.803.

Amari, S., Anders, E., Virag, A., & Zinner, E. (**1990**), "Interstellar graphite in meteorites", *Nature* **345**, 238–240, URL http://dx.doi.org/10.1038/345238a0.

Amari, S., Lewis, R. S., & Anders, E. (**1994**), "Interstellar grains in meteorites: I. Isolation of SiC, graphite and diamond; size distributions of SiC and graphite", *Geochimica et Cosmochimica Acta* **58**, 459–470, URL http://dx.doi.org/10.1016/0016-7037(94)90477-4.

Amari, S., Nittler, L. R., Zinner, E., Gallino, R., Lugaro, M., & Lewis, R. S. (**2001**), "Presolar SiC Grains of Type Y: Origin from Low-Metallicity Asymptotic Giant Branch Stars", *The Astrophysical Journal* **546**, 248–266, URL http://stacks.iop.org/0004-637X/546/i=1/a=248.

Amari, S., Zinner, E., & Gallino, R. (**2014**), "Presolar graphite from the Murchison meteorite: An isotopic study", *Geochimica et Cosmochimica Acta* **133**, 479–522, URL http://dx.doi.org/10.1016/j.gca.2014.01.006.

Bernatowicz, T., Fraundorf, G., Ming, T., Anders, E., Wopenka, B., Zinner, E., & Fraundorf, P. (**1987**), "Evidence for interstellar SiC in the Murray carbonaceous meteorite", *Nature* **330**, 728–730, URL http://dx.doi.org/10.1038/330728a0.

Bernatowicz, T. J., Akande, O. W., Croat, T. K., & Cowsik, R. (**2005**), "Constraints On Grain Formation Around Carbon Stars From Laboratory Studies Of Presolar Graphite", *The Astrophysical Journal* **631**, 988–1000, URL http://dx.doi.org/10.1086/432599.

Bernatowicz, T. J., Amari, S., Zinner, E. K., & Lewis, R. S. (**1991**), "Interstellar grains within interstellar grains", *The Astrophysical Journal* **373**, L73–L76, URL http://dx.doi.org/10.1086/186054.

Bernatowicz, T. J., Cowsik, R., Gibbons, P. C. ., Lodders, K., Jr., B. F., Amari, S., & Lewis, R. S. (**1996**), "Constraints On Stellar Grain Formation From Presolar Graphite In The Murchison Meteorite", *The Astrophysical Journal* **472**, 760–782, URL http://dx.doi.org/10.1086/178105.

Black, D. C. (**1972**), "On the origins of trapped helium, neon and argon isotopic variations in meteorites - II. Carbonaceous meteorites", *Geochimica et Cosmochimica Acta* **36**, 377–394, URL http://dx.doi.org/10.1016/0016-7037(72)90029-4.

Black, D. C. & Pepin, R. O. (**1969**), "Trapped neon in meteorites - II", *Earth and Planetary Science Letters* **6**, 395–405, URL http://dx.doi.org/10.1016/0012-821X(69)90190-3.

Bojazi, M. & Meyer, B. (**2014**), "Explosive Nucleosynthesis of 15N in a Massive Star Model", *Physical Review C* **89**, 025807, 1–19, URL http://dx.doi.org/10.1103/PhysRevC.89.025807.

Burbidge, E. M., Burbidge, G. R., Fowler, W. A., & Hoyle, F. (**1957**), "Synthesis of the Elements in Stars", *Reviews of Modern Physics* **29**, 547–650, URL http://dx.doi.org/10.1103/RevModPhys.29.547.

Cameron, A. G. W. (**1957**), "Nuclear Reactions in Stars and Nucleogenesis", *Publications of the Astronomical Society of the Pacific* **69**, 201–222, URL http://dx.doi.org/10.1086/127051.

Cowan, J. J. & Rose, W. K. (**1977**), "An interpretation of galactic observations of CNO isotopes", *The Astrohpysical Journal* **217**, 51–55, URL http://dx.doi.org/10.1086/155551.

Croat, T. K., Berg, T., Bernatowicz, T., Groopman, E., & Jadhav, M. (**2013**), "Refractory metal nuggets within presolar graphite: First condensates from a circumstellar environment", *Meteoritics & Planetary Science* **48**, 686–699, URL http://dx.doi.org/10.1111/maps.12093.

Croat, T. K., Bernatowicz, T., Amari, S., Messenger, S., & Stadermann, F. J. (**2003**), "Structural, chemical, and isotopic microanalytical investigations of graphite from supernovae", *Geochimica et Cosmochimica Acta* **67**, 4705–4725, URL http://dx.doi.org/10.1016/S0016-7037(03)00463-0.

Croat, T. K., Stadermann, F. J., & Bernatowicz, T. J. (**2005**), "Presolar Graphite from AGB Stars: Microstructure and s-Process Enrichment", *The Astrophysical Journal* **631**, 976–987, URL http://dx.doi.org/10.1086/432598.

Croat, T. K., Stadermann, F. J., & Bernatowicz, T. J. (**2008**), "Correlated isotopic and microstructural studies of turbostratic presolar graphite from the Murchison meteorite", *Meteoritics & Planetary Science* **43**, 1497–1516, URL http://dx.doi.org/10.1111/j.1945-5100.2008.tb01024.x.

Daulton, T. L., Bernatowicz, T. J., & Croat, T. K. (**2009**), "Alteration of TiC in Supernovae Outflows: Transmission Electron Microscopy Study of TiC Subgrains in Supernovae Graphite", in "40th Lunar and Planetary Science Conference", Abstract #1996, Lunar and Planetary Institute, Houston, URL http://www.lpi.usra.edu/meetings/lpsc2009/pdf/1996.pdf.

Daulton, T. L., Bernatowicz, T. J., & Croat, T. K. (**2012**), "Electron Energy Loss Spectral Imaging of TiC Formed by Supernovae: A Scanning Transmission Electron Microscopy Study of Grain Formation and Alteration Mechanisms", in "43rd Lunar and Planetary Science Conference", Abstract #2247, Lunar and Planetary Institute, Houston, URL http://www.lpi.usra.edu/meetings/lpsc2012/pdf/2247.pdf.

Duerbeck, H. W., Liller, W., Sterken, C., Benetti, S., van Genderen, A. M., Arts, J., Kurk, J. D., Janson, M., Voskes, T., Brogt, E., Arentoft, T., van der Meer, A., & Dijkstra, R. (**2000**), "The Rise and Fall of V4334 Sagittarii (Sakurai's Object)", *The Astronomical Journal* **119**, 2360–2375, URL http://dx.doi.org/10.1086/301349.

Fedkin, A., Meyer, B., & Grossman, L. (**2010**), "Condensation and mixing in supernova ejecta", *Geochimica et Cosmochimica Acta* **74**, 3642–3658, URL http://dx.doi.org/10.1016/j.gca.2010.03.021.

Floss, C., Stadermann, F. J., Kearsley, A. T., Burchell, M. J., & Ong, W. J. (**2013**), "The Abundance of Presolar Grains in Comet 81P/Wild 2", *The Astrophysical Journal* **763**, 140–150, URL http://stacks.iop.org/0004-637X/763/i=2/a=140.

Grefenstette, B. W., Harrison, F. A., Boggs, S. E., Reynolds, S. P., Fryer, C. L., Madsen, K. K., Wik, D. R., Zoglauer, A., Ellinger, C. I., Alexander, D. M., An, H., Barret, D., Christensen, F. E., Craig, W. W., Forster, K., Giommi, P., Hailey, C. J., Hornstrup, A., Kaspi, V. M., Kitaguchi, T., Koglin, J. E., Mao, P. H., Miyasaka, H., Mori, K., Perri, M., Pivovaroff, M. J., Puccetti, S., Rana, V., Stern, D., Westergaard, N. J., & Zhang, W. W. (**2014**), "Asymmetries in core-collapse supernovae from maps of radioactive 44Ti in Cassiopeia A", *Nature* **506**, 339–342, URL http://dx.doi.org/10.1038/nature12997.

Groopman, E., Bernatowicz, T., & Zinner, E. (**2012**), "C, N, And O Isotopic Heterogeneities In Low-density Supernova Graphite Grains From Orgueil", *The Astrophysical Journal Letters* **754**, L8–L13, URL http://dx.doi.org/10.1088/2041-8205/754/1/L8.

Groopman, E., Nittler, L. R., Bernatowicz, T., & Zinner, E. (**2014**), "NANOSIMS, TEM, and XANES Studies of a Unique Presolar Supernova Graphite Grain", *The Astrophysical Journal* **790**, 9–21, URL http://dx.doi.org/10.1088/0004-637X/790/1/9.

Hammer, N. J., Janka, H.-T., & Müller, E. (**2010**), "Three-Dimensional Simulations of Mixing Instabilities in Supernova Explosions", *The Astrophysical Journal* **714**, 1371–1385, URL http://dx.doi.org/10.1088/0004-637X/714/1371.

Herwig, F., Pignatari, M., Woodward, P. R., Porter, D. H., Rockefeller, G., Fryer, C., Bennett, M., & Hirschi, R. (**2011**), "Convective-reactive Proton-12C Combustion in Sakurai's Object (V4334 Sagittarii) and Implications for the Evolution and Yields from the First Generations of Stars", *The Astrophysical Journal* **727**, 89–103, URL http://stacks.iop.org/0004-637X/727/i=2/a=89.

Hoppe, P., Amari, S., Zinner, E., & Lewis, R. S. (**1995**), "Isotopic compositions of C, N, O, Mg, and Si, trace element abundances, and morphologies of single circumstellar graphite grains in four density fractions from the Murchison meteorite", *Geochimica et Cosmochimica Acta* **59**, 4029–4056, URL http://dx.doi.org/10.1016/0016-7037(95)00280-D.

Huss, G. R. & Lewis, R. S. (**1995**), "Presolar diamond, SiC, and graphite in primitive chondrites: Abundances as a function of meteorite class and petrologic type", *Geochimica et Cosmochimica Acta* **59**, 115–160, URL http://dx.doi.org/10.1016/0016-7037(94)00376-W.

Hutcheon, I. D., Huss, G. R., Fahey, A. J., & Wasserburg, G. J. (**1994**), "Extreme Mg-26 and O-17 enrichments in an Orgueil corundum: Identification of a presolar oxide grain", *The Astrophysical Journal Letters* **425**, L97–L100, URL http://dx.doi.org/10.1086/187319.

Hynes, K. M., Croat, T. K., Amari, S., Mertz, A. F., & Bernatowicz, T. J. (**2010**), "Structural and isotopic microanalysis of presolar SiC from supernovae", *Meteoritics & Planetary Science* **45**, 596–614, URL http://dx.doi.org/10.1111/j.1945-5100.2010.01045.x.

Hynes, K. M. & Gyngard, F. (**2009**), "The Presolar Grain Database: http://presolar.wustl.edu/ pgd", in "40th Lunar and Planetary Science Conference", Abstract #1198, Lunar and Planetary Institute, Houston, URL http://www.lpi.usra.edu/meetings/lpsc2009/pdf/1198.pdf.

Jadhav, M., Amari, S., Marhas, K. K., Zinner, E., Maruoka, T., & Gallino, R. (**2008**), "New stellar sources for high-density, presolar graphite grains", *The Astrophysical Journal* **682**, 1479–1485, URL http://dx.doi.org/10.1086/589139.

Jadhav, M., Amari, S., Zinner, E., & Maruoka, T. (**2006**), "Isotopic analysis of presolar graphite grains from Orgueil", *New Astronomy Review* **50**, 591–595, URL http://dx.doi.org/10.1016/j.newar.2006.06.004.

Jadhav, M., Pignatari, M., Herwig, F., Zinner, E., Gallino, R., & Huss, G. R. (**2013b**), "Relics of Ancient Post-AGB Stars in a Primitive Meteorite", *The Astrophysical Journal Letters* **777**, L27, URL http://dx.doi.org/10.1088/2041-8205/777/2/L27.

Jadhav, M., Zinner, E., Amari, S., Maruoka, T., Marhas, K. K., & Gallino, R. (**2013a**), "Multi-element isotopic analyses of presolar graphite grains from Orgueil", *Geochimica et Cosmochimica Acta* **113**, 193–224, URL http://dx.doi.org/10.1016/j.gca.2013.01.018.

Joseph, D. & Oberlin, A. (**1983**), "Oxidation of Carbonaceous Matter II: X-Ray Diffraction and Transmission Electron Microscopy", *Carbon* **21**, 565–571, URL http://dx.doi.org/10.1016/0008-6223(83)90240-3.

Karakas, A. I. & Lattanzio, J. C. (**2014**), "The Dawes Review 2: Nucleosynthesis and stellar yields of low and intermediate-mass single stars", *ArXiv e-prints* URL http://dx.doi.org/10.1017/pas.2014.xxx.

Leitner, J., Heck, P. R., Hoppe, P., & Huth, J. (**2012**), "The C-, N-, and O-Isotopic Composition of Cometary Dust from Comet 81P/Wild 2", in "Lunar and Planetary Science

Conference", volume 43 of *Lunar and Planetary Science Conference*, Abstract #1839, URL http://adsabs.harvard.edu/abs/2012LPI....43.1839L.

Leitner, J., Hoppe, P., & Heck, P. R. (**2010**), "First Discovery of Presolar Material of Possible Supernova Origin in Impact Residues from Comet 81P/Wild 2", in "Lunar and Planetary Science Conference", volume 41 of *Lunar and Planetary Science Conference*, Abstract #1607, URL http://adsabs.harvard.edu/abs/2010LPI....41.1607L.

Lewis, R. S., Ming, T., Wacker, J. F., Anders, E., & Steel, E. (**1987**), "Interstellar diamonds in meteorites", *Nature* **326**, 160–162, URL http://dx.doi.org/10.1038/326160a0.

Lodders, K. & Fegely, J., B. (**1995**), "The origin of circumstellar silicon carbide grains found in meteorites", *Meteoritics* **30**, 661–687, URL http://adsabs.harvard.edu/abs/1995Metic..30..661L.

Marty, B., Chaussidon, M., Wiens, R. C., Jurewicz, A. J. G., & Burnett, D. S. (**2011**), "A 15N-Poor Isotopic Composition for the Solar System As Shown by Genesis Solar Wind Samples", *Science* **332**, 1533–1536, URL http://dx.doi.org/10.1126/science.1204656.

Messenger, S., Keller, L. P., Stadermann, F. J., Walker, R. M., & Zinner, E. (**2003**), "Samples of stars beyond the solar system: silicate grains in interplanetary dust", *Science* **300**, 105–108, URL http://dx.doi.org/10.1126/science.1080576.

Nittler, L. R., Alexander, C. M. O., Gao, X., Walker, R. M., & Zinner, E. K. (**1994**), "Interstellar oxide grains from the Tieschitz ordinary chondrite.", *Nature* **370**, 443–446, URL http://dx.doi.org/10.1038/370443a0.

Nittler, L. R. & Hoppe, P. (**2005**), "Are Presolar Silicon Carbide Grains from Novae Actually from Supernovae?", *The Astrophysical Journal Letters* **631**, L89–L92, URL http://stacks.iop.org/1538-4357/631/i=1/a=L89.

Rauscher, T., Heger, A., Hoffman, R. D., & Woosley, S. E. (**2002**), "Nucleosynthesis In Massive Stars With Improved Nuclear And Stellar Physics", *The Astrophysical Journal* **576**, 323–348, URL http://dx.doi.org/10.1086/341728.

Rest, A., Foley, R. J., Sinnott, B., Welch, D. L., Badenes, C., Filippenko, A. V., Bergmann, M., Bhatti, W. A., Blondin, S., Challis, P., Damke, G., Finley, H., Huber, M. E., Kasen, D., Kirshner, R. P., Matheson, T., Mazzali, P., Minniti, D., Nakajima, R., Narayan, G., Olsen, K., Sauer, D., Smith, R. C., & Suntzeff, N. B. (**2011**), "Direct Confirmation Of The Asymmetry Of The Cas A Supernova With Light Echoes", *The Astrohpysical Journal* **732**, 3–13, URL http://dx.doi.org/10.1088/0004-637X/732/1/3.

Reynolds, J. H. & Turner, G. (**1964**), "Rare gases in the chondrite Renazzo", *Journal of Geophysical Research* **69**, 3263–3281, URL http://dx.doi.org/10.1029/JZ069i015p03263.

Rose, W. K. (**1998**), *Advanced Stellar Astrophysics*, Cambridge University Press.

Stadermann, F. J., Croat, T. K., Bernatowicz, T. J., Amari, S., Messenger, S., Walker, R. M., & Zinner, E. (**2005**), "Supernova graphite in the NanoSIMS: Carbon, oxygen and titanium isotopic compositions of a spherule and its TiC sub-components", *Geochimica et Cosmochimica Acta* **69**, 177–188, URL http://dx.doi.org/10.1016/j.gca.2004.06.017.

Tang, M. & Anders, E. (**1988**), "Isotopic anomalies of Ne, Xe, and C in meteorites. II. Interstellar diamond and SiC: Carriers of exotic noble gases", *Geochimica et Cosmochimica Acta* **52**, 1235–1244, URL http://dx.doi.org/10.1016/0016-7037(88)90277-3.

Wooden, D. H., Rank, D. M., Bregman, J. D., Witteborn, F. C., Tielens, A. G. G. M., Cohen, M., Pinto, P. A., & Axelrod, T. S. (**1993**), "Airborne spectrophotometry of SN 1987A from 1.7 to 12.6 microns - Time history of the dust continuum and line emission", *Astrophysical Journal Supplement Series* **88**, 477–507, URL http://dx.doi.org/10.1086/191830.

Woosley, S. E., Heger, A., & Weaver, T. A. (**2002**), "The evolution and explosion of massive stars", *Reviews of Modern Physics* **74**, 1015–1071, URL http://dx.doi.org/10.1103/RevModPhys.74.1015.

Woosley, S. E. & Weaver, T. A. (**1995**), "The Evolution and Explosion of Massive Stars. II. Explosive Hydrodynamics and Nucleosynthesis", *The Astrophysical Journal Supplement* **101**, 181–235, URL http://dx.doi.org/10.1086/192237.

Zinner, E. (**1998**), "Stellar nucleosynthesis and the isotopic composition of presolar grains from primitive meteorites", *Annual Review of Earth and Planetary Sciences* **26**, 147–188, URL http://dx.doi.org/10.1146/annurev.earth.26.1.147.

Zinner, E. (**2014**), "Presolar Grains", in K. K. Turekian & H. D. Holland (Eds.), "Treatise on Geochemistry", chapter 1.04, 181–213, Elsevier, 2nd edition, URL http://dx.doi.org/10.1016/B978-0-08-095975-7.00101-7.

Zinner, E., Amari, S., & Jadhav, M. (**2006**), "On the stellar sources of presolar graphite", in "Proceedings of Science (NIC - IX)", 019, URL http://pos.sissa.it/archive/conferences/028/019/NIC-IX_019.pdf.

Zinner, E., Amari, S., Wopenka, B., & Lewis, R. S. (**1995**), "Interstellar graphite in meteorites: Isotopic compositions and structural properties of single graphite grains from Murchison", *Meteoritics* **30**, 209–226, URL http://dx.doi.org/10.1111/j.1945-5100.1995.tb01115.x.

Zinner, E., Wopenka, B., Amari, S., & Anders, E. (**1990**), "Interstellar Graphite and Other Carbonaceous Grains from the Murchison Meteorite: Structure, Composition and Isotopes of C, N, and NE", in "21st Lunar and Planetary Science Conference", Abstract #1700, Lunar and Planetary Institute, Houston, URL http://www.lpi.usra.edu/meetings/lpsc1990/pdf/1700.pdf.

CHAPTER 3

METHODS

3.1 Preface

Due to their small size, rarity, and individual uniqueness, presolar grains are analyzed using a variety of instrumental techniques. The goal of their study is to gain further insight into stellar, interstellar, and nebular processes. Each presolar grain therefore follows a complex multi-stage timeline in the laboratory involving many complementary experimental techniques (see Figure 3.1). This chapter will include a discussion of sample preparation techniques and data analysis methods for Nano-scale Secondary Ion Mass Spectrometry (NanoSIMS), Transmission Electron Microscopy (TEM), and Scanning Transmission X-ray Microscopy (STXM).

3.2 Sample Preparation

This section will describe the sample preparation for presolar grain candidates which were isolated from their parent meteorites via acid dissolution and density separation, such as SiC
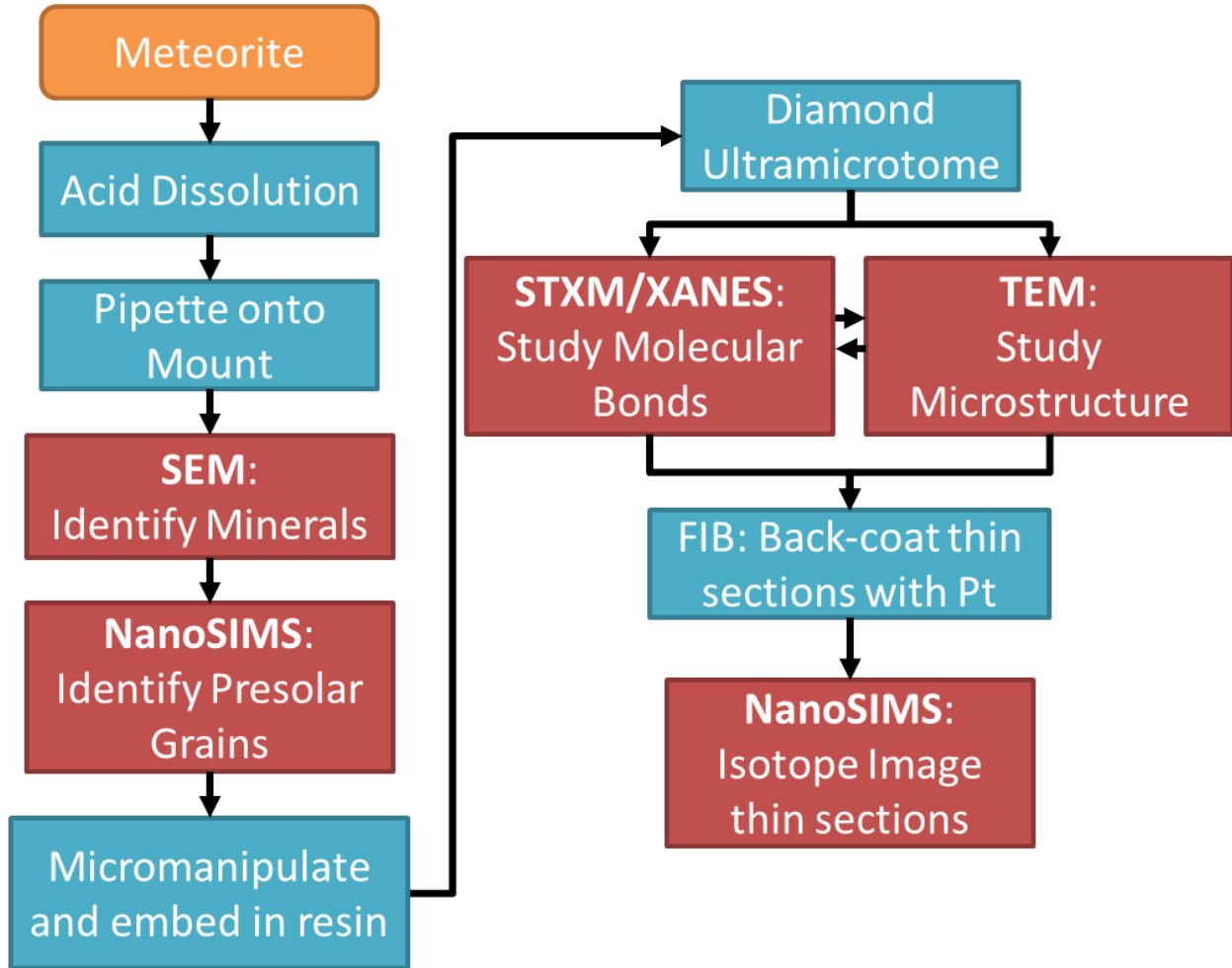
FIGURE 3.1: Flowchart illustrating the timeline of refractory presolar grain analyses in the laboratory. Once a mount of acid-separated meteorite residue is made, the Scanning Electron Microscope (SEM) is used to identify presolar candidates based upon mineral type. Subsequently, isotopes of each grain's major and minor elements are measured in the NanoSIMS. Each presolar grain is identified based upon its isotopic composition. Presolar grains are micromanipulated and embedded in resin prior to diamond ultramicrotomy. Thin sections are deposited on TEM grids after which they are analyzed in the TEM and STXM. The Focused Ion Beam (FIB) is used to back coat individual microtome sections on TEM grids for isotope imaging in the NanoSIMS.

and graphite. Presolar oxide and silicate mineral phases require *in-situ* study and will not be

discussed in this thesis. After the acid dissolution process described in Amari *et al.* (1994),

size/density fractions of the meteorites reside in separate suspensions of a 4:1 mixture of

isopropanol:H_2O by volume. For each sample mount multiple 0.05 μL drops of suspension were deposited using micro-pipettes on a high-purity Au foil pressed into a steel disc. The Orgueil CI1 size/density residues contain copious residual insoluble organic material (IOM). Individual presolar graphite grain candidates were picked with a micromanipulator needle from the original mount and deposited on a clean Au foil to reduce the contribution from the IOM.

3.3   Secondary Ion Mass Spectrometry (SIMS)

The most important development for the study of presolar grains has been the evolution of ion microprobes, from the Cameca IMS-3f, with which the first isotopic measurements on individual presolar grains were made; to its successor, the Cameca NanoSIMS 50(L), which can achieve tens-of-nm spatial resolution. The current generation of NanoSIMS has allowed for *in-situ* study of small presolar grains in meteorites and for investigations into isotopic heterogeneities within individual presolar grains.

SIMS instruments operate on the principle of focusing a primary beam of ions onto the sample, which implants some primary ions and sputters the sample's surface (Figure 3.2). A small fraction (1–2%) of the sputtered atoms and molecules become ionized, allowing for those of the opposite polarity of the primary beam to be extracted via electromagnetic lenses. The NanoSIMS may operate in either positive (Cs^+) or negative (O^-) primary polarities. The beam of secondary ions is focused, collimated, and sent through a double-focusing mass spectrometer consisting of an electrostatic analyzer and a magnet, which splits

the ions based upon their charge-to-mass ratio. The Washington University NanoSIMS can simultaneously measure 5 isotopic or molecular ion species with electromultiplier detectors and/or Faraday cups. The primary beam may be set to either raster across a defined area or remain stationary over one spot during a measurement. In raster mode, the detector counts may either be summed for each cycle (one full raster scan), or counts may be individually summed for each pixel in the scan, resulting in an isotope image. Imaging mode generally requires longer dwell times at each pixel in order to gather enough ion counts for a detailed image. Isotope image analyses are performed using the custom L'Image software (L. R. Nittler, Carnegie Institution).

For carbonaceous presolar grains such as graphite and SiC, a Cs^+ primary beam is used to measure negative secondary ions of $^{12,13}C$ and generally $^{16,18}O$, $^{26,27}CN$ ($^{12}C^{14}N$ and $^{12}C^{15}N$), and $^{28,29,30}Si$. N does not have a stable negative ion, so it must be measured as a molecular CN^- ion. C may be measured as an atomic or a molecular ion (C_2). Atomic and molecular ions have different energy distributions, so atomic C ions are useful when measuring O or Si isotopes simultaneously, while C_2 ions are ideal when measuring N isotopes. The O^- primary beam is used to measure the positive secondary ions of the isotopes of Mg, Al, K, Ca, Ti, V, Cr, and/or Fe (among others).

Following ultramictoromy and/or TEM analyses, isotope images of thin sections of presolar grains may be collected using the NanoSIMS. In this thesis, ~ 10 ultramicrotome sections from each of six presolar graphite grains were deposited on Si wafers, with the remaining sections deposited on TEM grids. The Si wafers provide stable substrates for further NanoSIMS measurements. As an alternative to depositing sections on Si wafers, sections suspended on
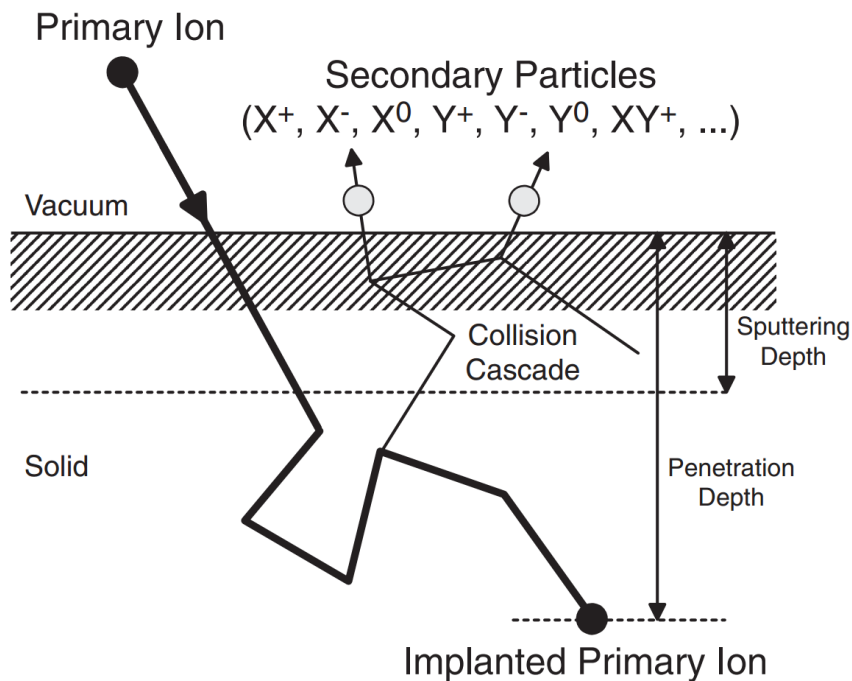
FIGURE 3.2: Figure 1 from Hoppe *et al.* (2013). Physical principle of SIMS: primary ions sputter away surface atoms and molecules from the sample. A fraction of these secondary particles are ionized and are transferred through a mass spectrometer.

film-coated TEM grids may be back-coated with Pt using the Focused Ion Beam Scanning Electron Microscope (FIB-SEM). The coating of Pt results in a more stable substrate for NanoSIMS imaging, leading to longer imaging times for each section. This process involves placing the TEM grid in the FIB-SEM upside-down and injecting a Pt-bearing organo-metallic gas local to a microtome section. The electron beam will slowly crack the organic molecules resulting in Pt deposition onto the backside of the microtome section. After depositing > 10 nm of Pt, the ion beam may be used to more efficiently deposit Pt.

3.4 Grain Picking

After identification of presolar grains in the NanoSIMS, individual grains may be prepared for TEM analyses. This procedure involves picking the grain off of its mount with a micromanipulator needle and embedding the grain in resin prior to ultramicrotomy.

3.4.1 Climate Control

Prior to the picking process, the temperature and humidity in the room should be roughly 70°F and 50%, respectively. The ambient relative humidity is the most important factor for micromanipulation and grain picking. If the humidity is too low ($\lesssim 40\%$) then static charge builds on the micromanipulator needle and grain mount easily during movement and handling, causing grains to jump erratically away from the needle upon approach. Conversely, a high humidity ($\gtrsim 60\%$) will prevent grains from being attracted to the micromanipulator needle, wasting time and increasing the likelihood that the needle will damage or simply dislodge a grain from the mount. It is possible to pick at non-ideal conditions, but there exists a much larger chance of failure. Both humidity and temperature are also important factors for microtoming, as the current SPI diamond knives have fairly shallow water reservoirs (see Section 3.5 and Figure 3.20) where evaporation may become and issue.

3.4.2 Supplies for Grain Picking

- Aluminum block mount (see Section 3.4.2).

- Polyethylene SPI® BEEM 1001 capsule (see Section 3.4.4).

- Carbon fibers (see Section 3.4.6).

- Syringe: 1cc, 31 gauge, filled with LR White™ Hard resin (no air bubbles). The syringe should be filled shortly before picking as the resin has a useful lifetime of roughly 1 day in the syringe.

- 2M NaOH solution.

- Sharpened tungsten micromanipulator needle (see Section 3.4.5).

Al Jig and Capsule Holder

Al mounts are machined to act as capsule holders for embedding grains in resin and to be used as jigs to epoxy hex screws to the cured resin blocks. Figures 3.3 and 3.4 show models and dimensions for the Al blocks. The blocks are cut as $3/4''$-thick pieces from a $7/8'' \times 7/8''$ bar of Al. A through hole in the center of the $7/8'' \times 7/8''$ face is drilled with a #29 ($0.136''$) drill bit. A $1/4''$ deep hole is drilled following the pilot hole with a $3/8''$ drill bit. The pilot hole is threaded using an 8-32 tap. The pilot hole also allows for transmission illumination using an optical microscope, and dislodging stuck capsules.

3.4.3 Equipment

Grain picking with high efficiency requires specialized equipment (e.g., Figure 3.5). The setup includes a Nikon Eclipse E600 optical microscope with super long working distance (SLWD; WD > 20 mm) objectives of $5\times$, $20\times$, and $50\times$ magnification, and an attached high-speed, high-resolution 3CCD camera (1920×1200 pixels; 60 Hz) that is part of an Optronics Microcast HD system. The setup also includes an Eppendorf Patchman NP 2 micromanipulator. All micromanipulator needles are crafted from either prefabricated
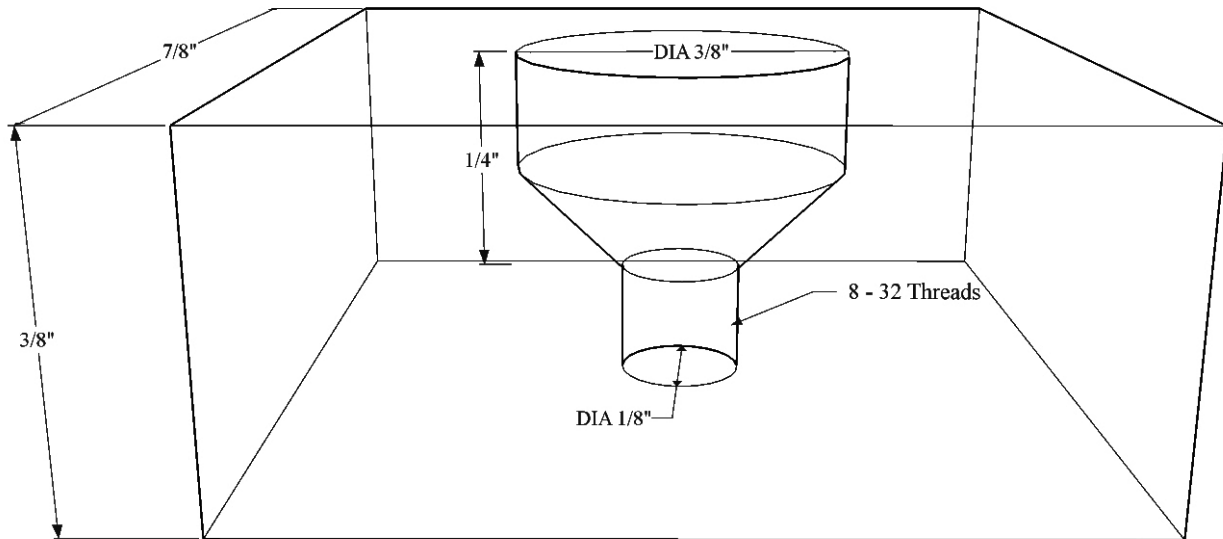
FIGURE 3.3: Side view of a wire frame model of Al jig and capsule holder.

W needles or electrochemically sharpened W wire (see Section 3.4.5), both of which are soldered inside of Cu capillary tubes. The microscope resides on a Kinetic System Benchmate vibration isolation table. Ultramicrotomy is conducted using a Reichert-Jung Ultracut E microtome (Figure 3.17), also on a vibration isolation table. Glass knives are manufactured from $^1/_4''$-thick glass bars using an LKB Knifemaker 7800B.

3.4.4 Capsule Preparation

SPI® BEEM #1001 polyethylene capsules (Figure 3.7) are used for embedding presolar grains in resin. The following procedures detail the required capsule preparation prior to grain picking. *Note: One must be extremely careful to not allow excess static to build up on the plastic capsule, which can deflect grains off of the micromanipulator needle. It is recommended NOT to wear gloves when handling the capsules.*

1. Identify a good capsule. The bottom square face of the capsule should be smooth and free of pock marks (see Figures 3.8 and 3.9).

2. Insert the capsule in an Al jig and use a marker to draw a line on the capsule just above the surface of the Al block.

3. Remove the capsule from the block and using the tip of a razor blade remove the top of the capsule by slowly cutting in a circle around the capsule along the marker line. The resulting capsule will be slightly taller than $1/4''$. It is important to not cut the capsule flush with the block's surface, as the capsule sides are later used to align two Al jigs on top of one another. Conversely, a capsule that is too tall will prevent the micromanipulator needle from reaching the bottom.

4. Label the side of the capsule with a marker.

5. Using a microscope as an aid, place a red dot on the outside of the capsule directly above the center of the interior square face. This will help in locating the center of the capsule when picking grains under the microscope when the capsule's bottom is not in the focal plane. Note: Sometimes the interior square face is not centered within the capsule.

6. Replace the capsule in an Al mount. Remove any dirt from the capsule using compressed N_2 gas.

7. Verify the capsule's cleanliness in the microscope then add one drop of resin from the 31 gauge syringe to the bottom of the capsule. A good way to do this is to place a

Kimwipe™ underneath the block mount, place the first drop from the syringe (squeezing gently) on the wipe, then drop the second into the capsule.

3.4.5   Needle Preparation

1. To shape the needle, you will need approximately 2 cm exposed. Using tweezers, shape the needle so that it is nearly vertical with the tip angled $\sim30°$ from the vertical. The needle needs to be long enough to reach the bottom of the capsule and angled so that the tip is not occluded from view by the shaft.

2. *NaOH is caustic! Gloves and eye protection must be worn while sharpening.*

3. Connect the needle to the circuit through the NaOH. Prior to turning on the 120 V power source, rotate the variable resistor dial back and forth to ensure a good connection. Dip the needle slowly and deeply in and out of the solution with the power supply on and the voltage dial set between 1-5%. Tiny bubbles should form around the needle when dipped.

4. Dip the needle deeply into the NaOH to ensure that the entire needle has been cleaned of dirt up to the Cu shaft. This prevents particles from falling into the resin or onto the sample mount.

5. Repeated dipping in and out of the NaOH solution will result in a long tapered needle, which is optimal for picking and future sharpening. Attempting to sharpen just the tip

will result in a blunt needle. A sharpened needle should only be a few microns thick at the tip.

3.4.6 Preparing and Picking Carbon Fibers

Preparing Carbon Fibers

Making a slide of carbon fibers is relatively straightforward (see Figure 3.10). New slides need to be made when too much dirt and/or condensation has accumulated on the fibers. Locate and clean a new glass microscope slide: first rinse with methanol, then isopropanol, and then distilled water. Dry the slide with compressed N_2 gas. Using tweezers pull a few threads from a woven carbon fiber sheet. Using a razor blade, repeatedly chop the threads on the microscope slide. Repeat until there are a large number of short fibers for picking (25 – 50 μm).

Picking Carbon Fibers

1. Prior to picking the carbon fibers, turn off the room AC unit. Then turn off all of the clean-benches. The airflow may cause carbon fibers or presolar grains to jump off of the micromanipulator needle.

2. Before putting the fiber slide or the mount on the sample stage, find the tip of the needle, center it on the screen and bring it into focus with the 5× objective. [Note: Currently the 5× and 20× objectives are not completely aligned and parfocal. This is not a huge issue except that you may want to have the needle tip slightly above center

on the LCD screen in 5× so that it is centered on 20×.]

3. Bring the needle tip above the plane of focus (roughly 10 seconds on [Fine], middle speed) and set this as [Pos. 1] on the micromanipulator control.

4. Put the mount and fibers on the stage (I usually put the mount in back and the fibers in front because you will have to switch out the fibers for the sample later) and bring the carbon fibers into focus.

5. Search around the slide until you find a good fiber (25 – 50 μm) and bring it to the center of the screen.

6. Move the stage to drop the carbon fiber below focus, using roughly $\frac{3}{4}$ of a minor revolution.

7. Bring the needle tip down into focus.

8. Raise the stage and carbon fiber back up into focus using the minor-z knob until the fiber touches the needle. Move the needle and stage around slightly until the fiber sticks to the needle. The first fiber is always the most stubborn. Ensure that the fiber attaches below the needle and not above.

9. Once the fiber sticks to the needle, move the sample stage below focus. Draw the needle above focus for about 10 seconds on [Fine]. This will give you roughly 3 – 4 seconds of vertical translation of the needle before the resin's surface is reached when you are focused on the bottom of the capsule.

10. Move the sample stage and bring the bottom of the capsule into focus. When the capsule is below focus, center the capsule on the through illumination and the red marker dot drawn on the bottom of the capsule. While moving the stage under the needle, be careful to not get the capsule's edge too close to the needle. Stray electric fields from static charge may dislodge the fiber (or a grain) from the needle. Lower the needle until the tip touches the surface of the resin, then remove the needle. Bring the capsule below focus until you find the carbon fiber and ensure that the fiber is sinking. Check that the fiber reaches the bottom of the capsule then lower the sample stage fully.

11. If the fiber remains at the surface, use the needle to break the surface tension and push the fiber down. Be careful, as the fiber may become reattracted to the needle and become stuck well above the tip.

12. Hit [Pos. 1] to reset the needle and repeat.

13. Once all three fibers have been deposited in the resin, use the needle to rearrange them on the bottom of the capsule. You may have to do this again once the grain is picked. Go slowly and be careful while dropping the needle through the resin until it and the bottom are in focus. The needle will easily gouge the bottom of the capsule, creating places where it is easy to lose the grain.

3.4.7 Picking Grains

This procedure is similar to picking carbon fibers, although EXTREME care should be taken. There are subtle differences between picking grains and fibers.

1. Navigate on mount using $5\times$ objective and then pick grain using $20\times$. I always keep the magnification module set at $1\times$ since the $1.25\times$, $1.5\times$, and $2\times$ can be blurry. With the CCD camera's intrinsic magnification, the microscope can easily approach the diffraction limit, so images will not be improved by using the $50\times$ objective with the CCD camera. Once more, lower the stage below focus before bringing the needle down into focus. Then use the fine-z stage control for all z-movement and the micromanipulator for all xy-movement.

2. Make note of the grain size using the transparency scale. This will help in differentiating the grain once in the capsule from carbon bits or dirt.

3. Make sure no resin is stuck to the needle tip. Lightly touch the tip to a clear area of gold foil, resin (if any) will wick off to the foil. You don't want this to happen as you try to pick your grain otherwise it will never stick to the needle. This also helps reduce excess static on the needle.

4. Always try to pick grain with the underside of the very tip of the needle. If the grain is on top of the needle it may get pushed further up when the needle is dipped in the resin.

5. Once the grain sticks to needle, keep the needle and the grain in focus and lower the sample mount.

6. Move the stage so that the capsule is underneath the needle and grain. Always move the sample stage, NOT the needle. It is best to keep the grain in focus.

7. Raise the sample stage and center needle over the red dot. Continue raising stage until the needle dips into the resin, then lower the stage, exposing the needle. If the grain remains on the needle, repeat. Once the grain is no longer on the needle, raise the needle and focus on the resin surface to find the grain.

8. Grains sink slowly in the resin (may take anywhere from 5 to 20 minutes). If the grain remains on the resin surface, use the needle to break the surface tension in a nearby area. Don't put the needle too close to the grain - you don't want the grain to stick back to the needle.

9. The grain may also need to be coaxed down into the right area. Do this by submerging the needle tip near the grain on the side of the direction you wish to move the grain (again without touching). Moving the needle away will drag the grain in that direction. When you are far enough away, raise the needle and repeat as necessary.

10. When the grain sinks to the bottom of the capsule it is best to position the carbon fibers around the grain in lieu of repositioning the grain with the needle itself. It is too easy for the grain to stick to the needle again, though it will be more difficult to dislodge a second time. Reposition the fibers so that the sample's orientation is easily

determined, e.g., as in Figure 3.12.

3.4.8 Curing

1. After picking the grain and repositioning the carbon fibers, slowly add drops of resin down the side of the capsule until it is $\sim$ ³/₄ full.

2. Check the position of the fibers and grain under the microscope after each drop. If the fibers and grain have moved, you may need to reposition them. Take another picture if things have shifted.

3. Place the capsule and Al block in the vacuum oven for at least 24 hours at $\sim$70°C. Ensure that the threaded hole is over a cavity or a hole in the oven floor. Otherwise the pressure may lift the capsule out of the block, spilling the contents of the capsule inside of the oven. The digital heater/thermometer will read 170°F $\approx$ 77°C, but the analog thermometer will more likely read 66°C. The analog thermometer is more accurate. The roughing pump can achieve a vacuum of $\sim 10^{-3}$ Torr.

3.4.9 Epoxying a Hex Screw to the Resin Block

Always wear latex gloves to prevent getting oils on the hex screw head and to prevent skin exposure to the epoxy.

Supplies: 2 Al jigs, small clamp, weigh paper, 8-32 hex screw, epoxy and popsicle stick, small wooden dowel, razor blade, foil weigh boat.

1. After curing, the resin should fill roughly ¼ to ½ of the cut capsule.

2. With the capsule in one Al jig, thread the hex screw into the other Al jig so that hex screw head sits inside of the jig.

3. Trace the circumference of a blank capsule on the weigh paper and cut out the circle with the razor blade. Place the weigh paper over the Al jig and capsule so that the capsule protrudes through the hole in the weigh paper. This will provide a barrier so that the jigs are not accidentally glued together if the epoxy overflows.

4. Mix epoxy with popsicle stick in foil weigh boat.

5. With end of the small dowel, deposit 1–2 drops of epoxy inside of the capsule capsule. Do not overfill!

6. Nest the jig with the hex screw on top of the capsule and lightly turn screw until it bottoms out on the resin block.

7. Clamp the jigs together and hold for 5+ minutes until the epoxy has set. Epoxy outgasses as it dries so the jigs must be held firmly together.

8. Once the epoxy sets, remove the screw from the jig and place screw/resin block/capsule in the kiln at 60°C for a few hours to complete outgassing.

9. Afterwards, carefully slice away capsule from resin block with a razor blade.

3.4.10   Trimming the Resin Capsule with a Glass Knife

At the microtome station:

1. Fully retract the knife holder and lock it into position. Adjust the knife holder angle to 8° for glass knives.

2. Remove chuck from microtome and secure screw in the chuck.

3. Place the plastic shield on the microtome arm and then secure chuck back to microtome. Level the sample arm. Do not to bump the sample.

4. Select a glass knife and place in the knife holder. Inspect the cutting edge (corner). Corner and edge should be completely flat with no chips or horns (see Figures 3.15 and 3.16). Bad knives should be discarded in a glass recycling or sharps box.

5. Secure a good knife in the knife holder. Unlock the knife holder stage and advance to roughly 0.5 cm from the resin block. Lock the knife holder stage.

6. Focus eyepieces on the knife's edge.

7. Rotate the resin block so that the knife edge is parallel to the lower edge of the resin block's face. Adjust the pitch of the resin block so that its entire top surface is vertically aligned when at the level of the knife's edge. This may take some adjustment after approaching the sample.

8. Locate carbon fibers. Adjust the knife's position as to leave the carbon fibers centered in a 250 μm square (at full magnification this is one square in the reticle).

9. Very slowly advance the knife towards the sample (turn main knob clockwise) while moving the sample up and down in slicing motions. Do not actually advance the

sample! Only move sample up and down in the same plane by rotating sample advance knob back and forth. It is very important that you only advance the knife!

10. When the knife is very close you will see its reflection in the resin block's surface. As you begin trimming, you may need to adjust the pitch of the resin block. Always retract knife before adjusting the sample.

11. Lightly shave off resin from one side of the block, retract knife, and rotate the sample 90°; repeat. Advancing the knife should be done in the smallest steps possible with the most minute adjustment of the advancement knob. Avoid taking a large chunk out of the resin block.

3.5   Ultramicrotomy

In preparation for TEM and X-ray microscopy, presolar grains embedded in resin are sliced with an ultramicrotome into 70 nm-thick sections, which are transparent to 200 keV electrons and to soft X-rays. Using ultramicrotomy to prepare thin sections of presolar grains was not developed as a part of this thesis (Bernatowicz *et al.*, 1996), however this section will detail the full procedure to complement the grain picking procedures above.

An update to the usual microtoming procedures involves using a small steel cylinder with an 8-32 tapped hole through its center, which was fashioned to hold the hex screws centered in the microtome chuck. This is quite useful for trimming and slicing resin blocks, as the block remains centered under rotations, unlike when it is simply clamped in the chuck. An

8-32 nut is also useful for securing the screw; thread the nut onto the hex screw before threading the screw into the holder. Remove any dirt or debris from the sample face and microtome with compressed N_2 gas.

Supplies:

- We use SPI® #9901 MS 2 mm diamond knives
- 1 cc, 31 gauge syringe
- Styrofoam rod
- Isopropanol, a few mL
- Deoinized or distilled water
- Electron Microscopy Sciences Perfect Loop
- Pig's eyelash tool
- TEM grid(s)

3.5.1   Diamond Knife Cleaning and Preparation

The knife is cleaned using a styrofoam rod dipped in isopropanol and is then rinsed with deionized or distilled water. Use a clean razor blade to make a fresh face on the styrofoam rod. After dipping the styrofoam tip in isopropanol, draw the edge of the fresh face across the knife blade 4–5 times, then rinse the blade with water and dry with compressed N. Repeat 4 times. Make sure to rinse both sides of the knife edge.

After the knife has been cleaned, secure it to the microtome with a **tilt of 4°**. Overfill the reservoir with deionized water until the surface tension nearly breaks. Using the syringe, remove water from the reservoir until the meniscus nearly pulls away from the edge of the knife. This will take a good deal of practice at first. One should be able to see the reflection

of the light in the meniscus along the blade's edge, as if it were a mirror. Two dark regions towards the blade's right and left sides will shrink as the central region becomes brighter. One wants these dark regions to be as small as possible without the surface tension along the knife's cutting edge breaking.

3.5.2 Slicing Preparation

Fully retract the microtome arm, then advance one turn. Move the knife towards the sample, leaving roughly 1 mm of space. Set the microtome cuts to be 70 nm thick and the cutting speed to be its slowest. Adjust the microtome cutting window so that the arm begins the cutting sequence with the sample slightly above the knife edge, and finishes the cutting sequence when the sample has cleared the knife blade. One does not want the sample to meet the knife at high speed.

3.5.3 Slicing

Sample sectioning involves ensuring that the sample face is completely vertical through the cutting window. With the sample centered in the microtome chuck, and the sample face perpendicular to the screw axis, this should be nearly achieved already. Slight adjustments to the sample tilt, sample rotation, and/or knife yaw may be necessary. Manually advance the knife as close as possible to the sample. Do this before advancing the sample to avoid having the microtome arm run out of dynamic range during slicing.

Uniformly thick microtome sections will all appear to be the same color under the microscope and/or eyepiece camera. Sections should appear grey on the meniscus near the knife

blade when they are the appropriate thickness. Sections that appear hues of yellow or blue have been sliced too thickly. Sometimes this occurs if the microtome misses a previous cut. These sections will generally still be electron transparent, however they are less than ideal. If section thickness varies often during cutting, there is increased risk of losing the embedded presolar grain.

3.5.4 Collecting Thin Sections

Using an eyelash tool, corral microtomed sections on the water's surface into small groups. Use the Perfect Loop to pick up the sections and deposit them on the coated side of a TEM grid, as shown in Figure 3.21. Repeat as necessary until all sections have been collected. When finished, clean the diamond knife once more, ensuring that no thin sections have adhered to either side of the knife blade.

3.5.5 Supplemental Microtoming Information

- Large SiC grains will often shatter during microtoming. This is not an issue for crystallography, however it often results in loss of central grain material.

- Very large graphite grains may also have this issue, where their cores can be plucked out in a given section. The best way to avoid this is to ensure that the resin has been cured properly and that the slicing is uniform.

3.6 Transmission Electron Microscopy (TEM)

Following ultramicrotomy, microstructural and chemical investigations of the presolar grain thin sections were performed using two instruments, a JEOL high-resolution JEM-2100F TEM equipped with a Bruker QUANTAX energy dispersive X-ray spectrometer (EDXS), and a JEOL 2000FX TEM equipped with a NORAN ultra-thin window EDXS, both operated at 200 keV. The principle of TEM relies on relativistic electrons passing through a mostly transparent - thin - sample and impinging upon a scintillating screen. Electrons scattered during their passage through the sample result in image contrast. Generally, higher-Z elements scatter more electrons over the same distance, and thus result in more darkly contrasting regions. Inelastically scattered electrons also deposit energy into the sample, which eject electrons or promote them to higher energy levels. Characteristic X-rays are thus produced when orbital vacancies are filled by upper-shell electrons, which provide chemical information about the sample. The TEM may also be operated in diffraction mode, where instead of generating an image through the contrast of scattered electrons, the image is de-magnified to such an extent that a bright central spot of direct, mostly unscattered electrons is visible, as are spots and/or regions from scattered electrons. Amorphous media with no preferred scattering direction will exhibit diffusely illuminated diffraction patterns. Diffraction patterns from crystalline materials exhibit strongly preferential scattering (bright spots) along angles that satisfy the Bragg reflection conditions of the crystal's orientation relative to the electron beam. Electron diffraction patterns contain crystallographic and orientational information about the sample. Electron diffraction patterns were captured on

film with both instruments. The JEM-2100F is equipped with a Gatan Imaging Filter (GIF), and both instruments are capable of collecting electron energy loss (EEL) spectra.

3.7   Scanning Transmission X-ray Microscopy (STXM)

Scanning Transmission X-Ray Microscopy (STXM) is a synchrotron-based technique used to collect X-ray absorption spectra from thin samples. Each spectrum's X-ray Absorption Near-Edge Structure (XANES) contains information regarding the sample's coordination chemistry, valence, and composition. Sample preparation for STXM is no different than for the TEM, so the techniques complement each other well. All XANES data for this thesis were collected at Beamline 5.3.2.2 of the Advanced Light Source at Lawrence-Berkeley National Laboratory, which is supported by the Director, Office of Science, Office of Basic Energy Sciences, of the U.S. Department of Energy under Contract No. DE-AC02-05CH11231. The STXM at Beamline 5.3.2.2 has an X-ray energy range between 200 and 800 eV with a selectable energy dispersion down to 0.1 eV (Kilcoyne *et al.*, 2003), which is ideal for probing the C, N, and O K-edges, and the Ti L-edge.

X-rays are absorbed strongly by the thin sample when the X-ray energy is close to an atomic or molecular orbital's characteristic energy. During data collection, the sample is typically rastered across the stationary X-ray beam and the energy is increased after each raster. A photomultiplier counts the total number of photons at each pixel and energy, which when compared to a reference point (e.g., a hole in the sample), yields an absorbance spectrum for each pixel. Molecular bonds can be distinguished based upon their characteristic

energies, which reflect the sample's composition and structure. Each spectrum is therefore a representation of what the average atom "sees" through its molecular bonds and neighboring atoms.

3.8   Summary

Following STXM and TEM analyses, presolar grain thin sections may be isotopically imaged in the NanoSIMS. This allows for the investigation of isotopic heterogeneities within the presolar grains. All of the techniques detailed here provide complementary information regarding each presolar grain's formation history and the properties of its progenitor star. Given the incredibly large physical, chemical, and isotopic parameter space that any star could sample, both in reality and in stellar models, it is of utmost importance to investigate each presolar grain's origin from every possible angle, while balancing the use of destructive and non-destructive techniques.
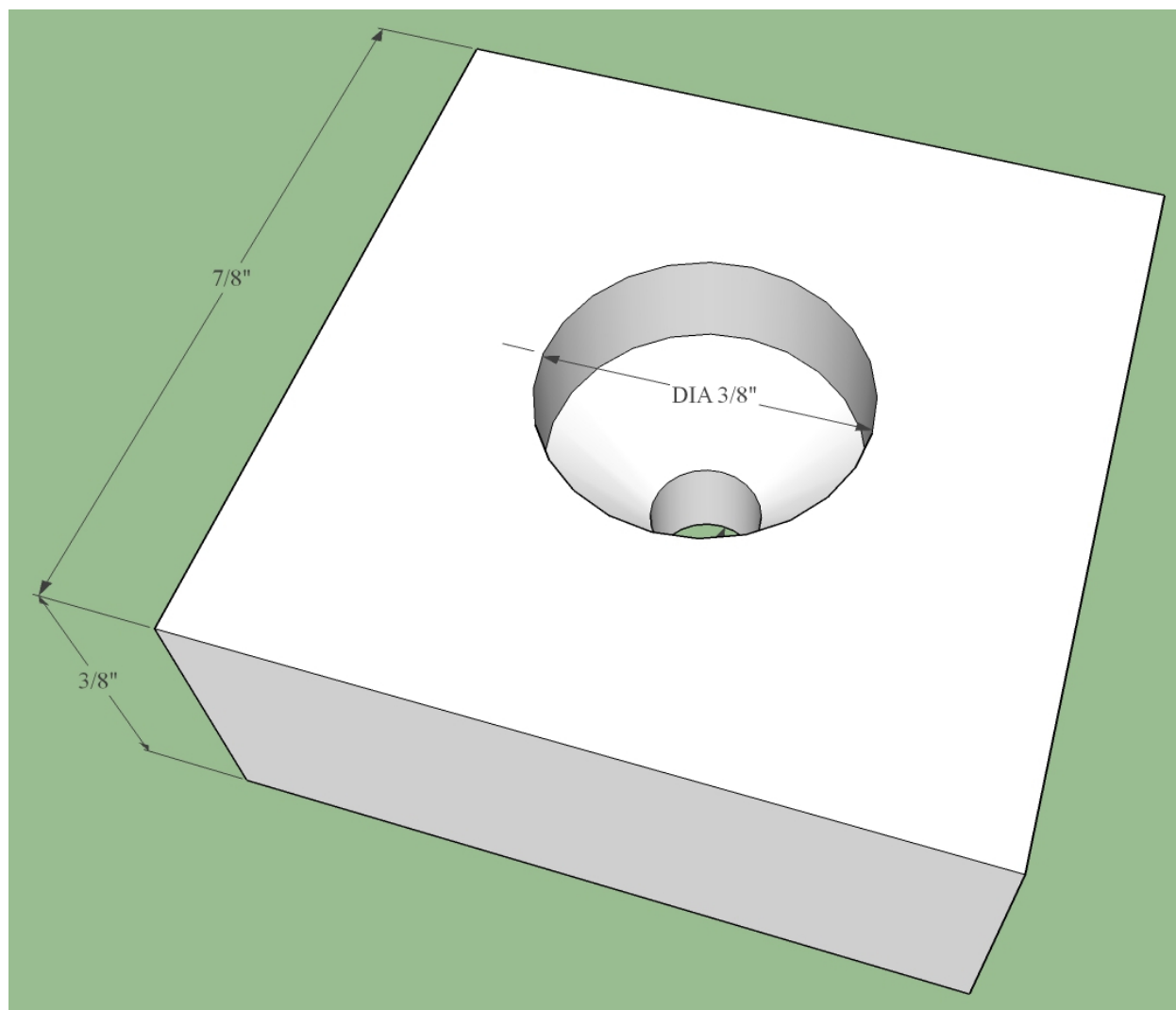
FIGURE 3.4: 3D model view (top and side) of Al jig.
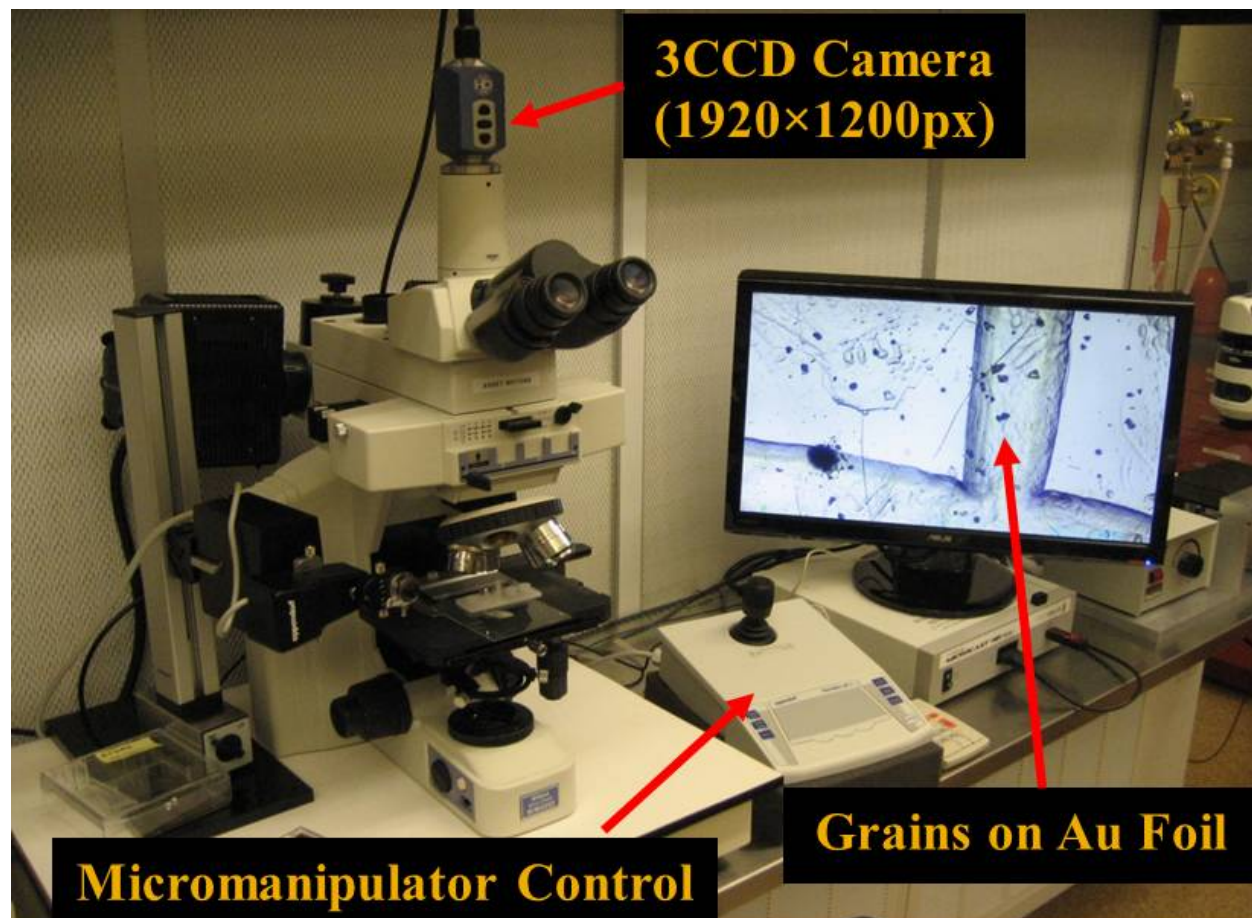
FIGURE 3.5: Grain picking setup with optical microscope, high-resolution and high-speed CCD camera, and micromanipulator. The microscope resides on a vibration isolation table on a laminar flow clean bench.
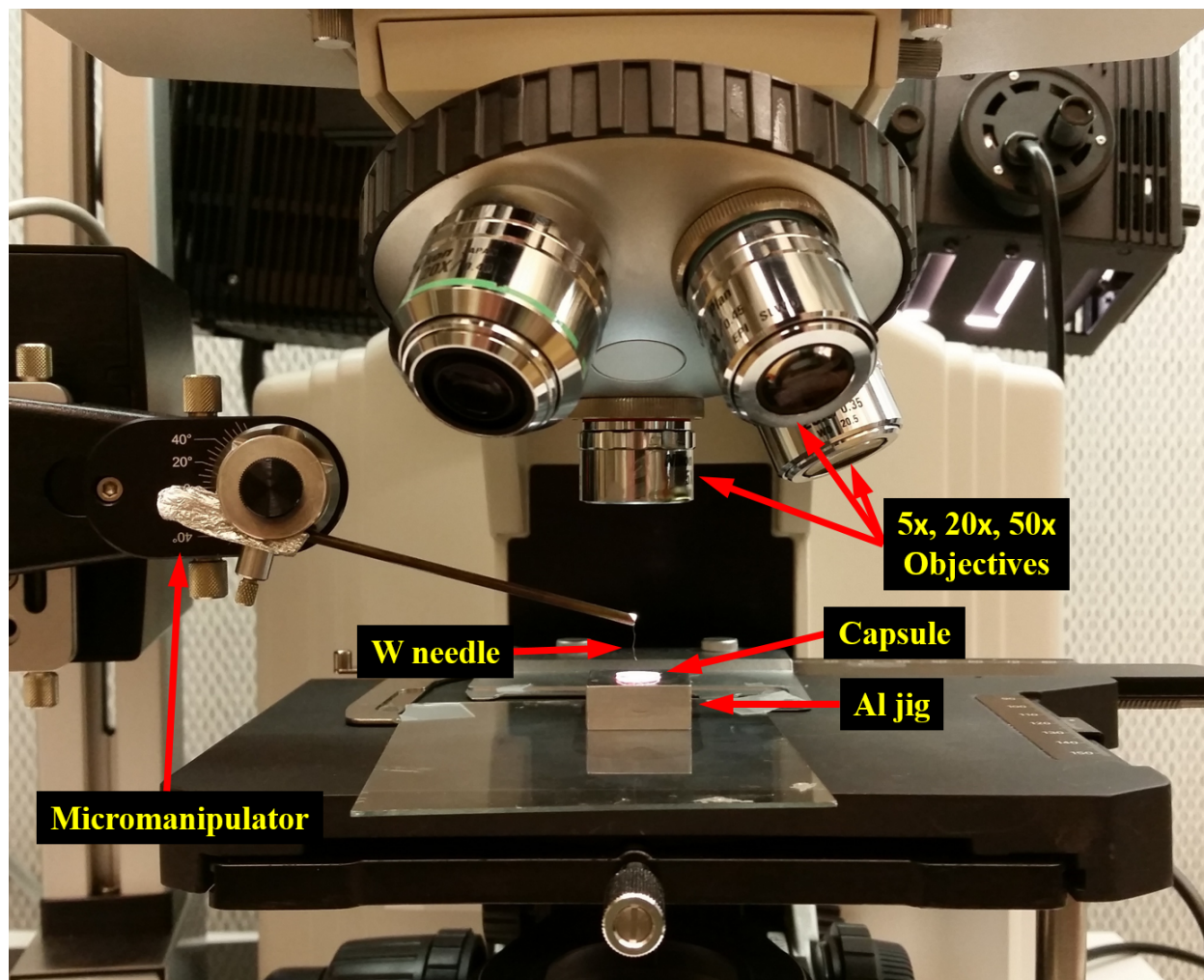
FIGURE 3.6: Side view of optical microscope, micromanipulator, and Al jig with capsule.
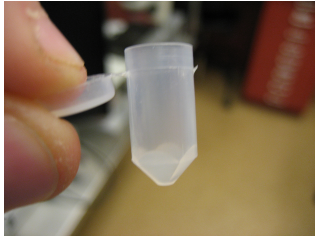
FIGURE 3.7: An SPI⃝R BEEM #1001 polyethylene capsule prior to capsule preparation.
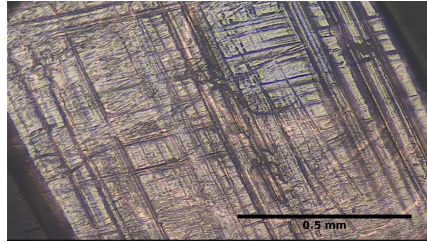
FIGURE 3.8: Example of a poor-quality capsule (interior face). Poor surfaces are characterized by large gouges and irregularities. This capsule is too rough for embedding.
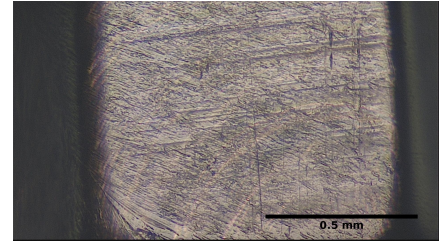
FIGURE 3.9: Example of a higher-quality capsule. Irregular features are fairly small.
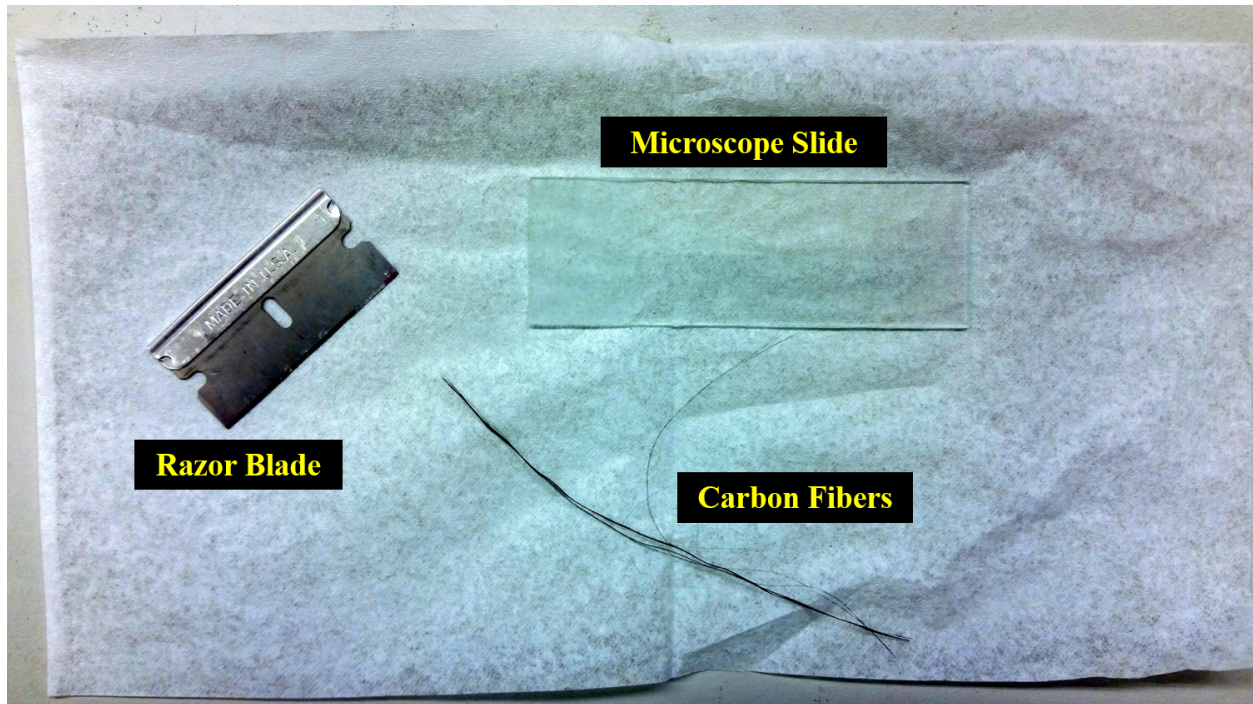
FIGURE 3.10: Supplies for preparing carbon fibers. Use the razor blade to chop the carbon fiber strands on the glass microscope slide. Be careful: carbon fibers will often be attracted to the razor blade.
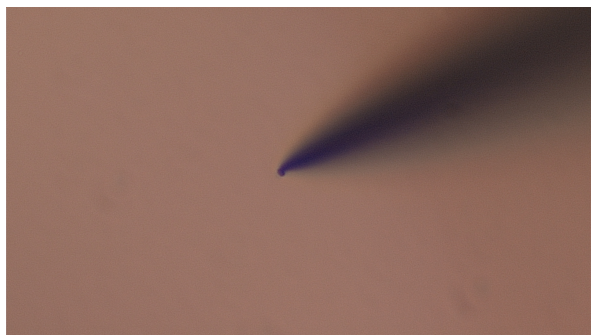
FIGURE 3.11: A 3 μm SiC grain picked with an electrochemically sharpened W micromanipulator needle via electrostatic attraction.
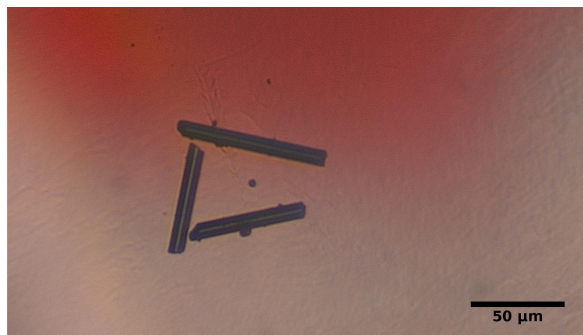
FIGURE 3.12: A 3 μm SiC grain lying on the bottom of a resin-filled capsule. The grain is surrounded by carbon fibers. The red dot on the opposite side of the capsule is visible in the upper middle of the image.
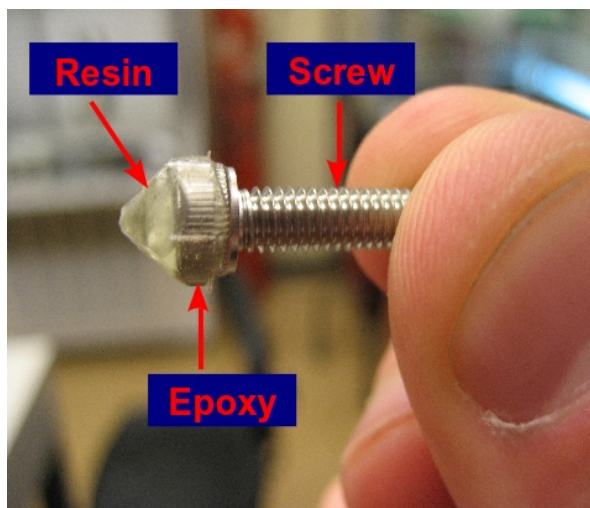
FIGURE 3.13: Resin block epoxied to a hex screw. The tip of this resin block has already been trimmed with a glass knife to form a "Mayan pyramid".
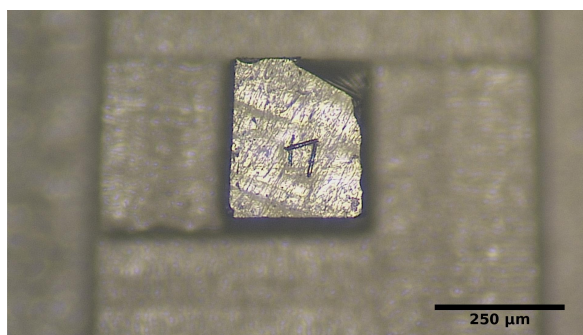
FIGURE 3.14: Top-down view of a trimmed resin block. The top of the pyramid is roughly 250 μm square. Carbon fibers are clearly visible.
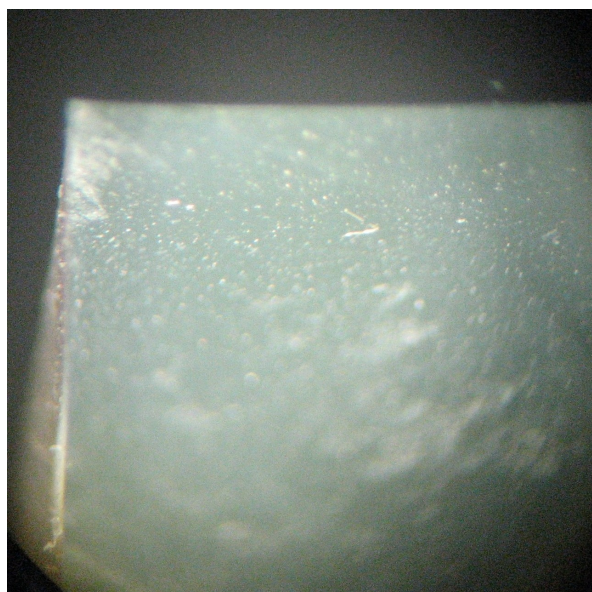
FIGURE 3.15: Example of a high-quality glass knife. Cutting edge is flat and unchipped. Image taken under maximum microtome magnification.
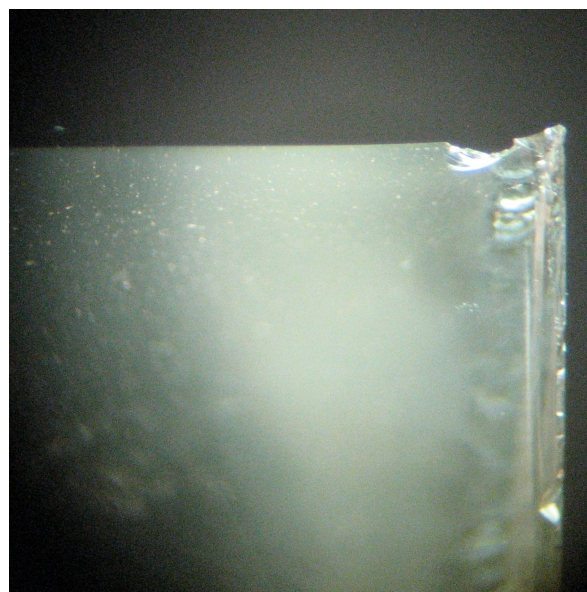
FIGURE 3.16: Example of a poor-quality glass knife. Cutting edge has both a horn and chips out of it.
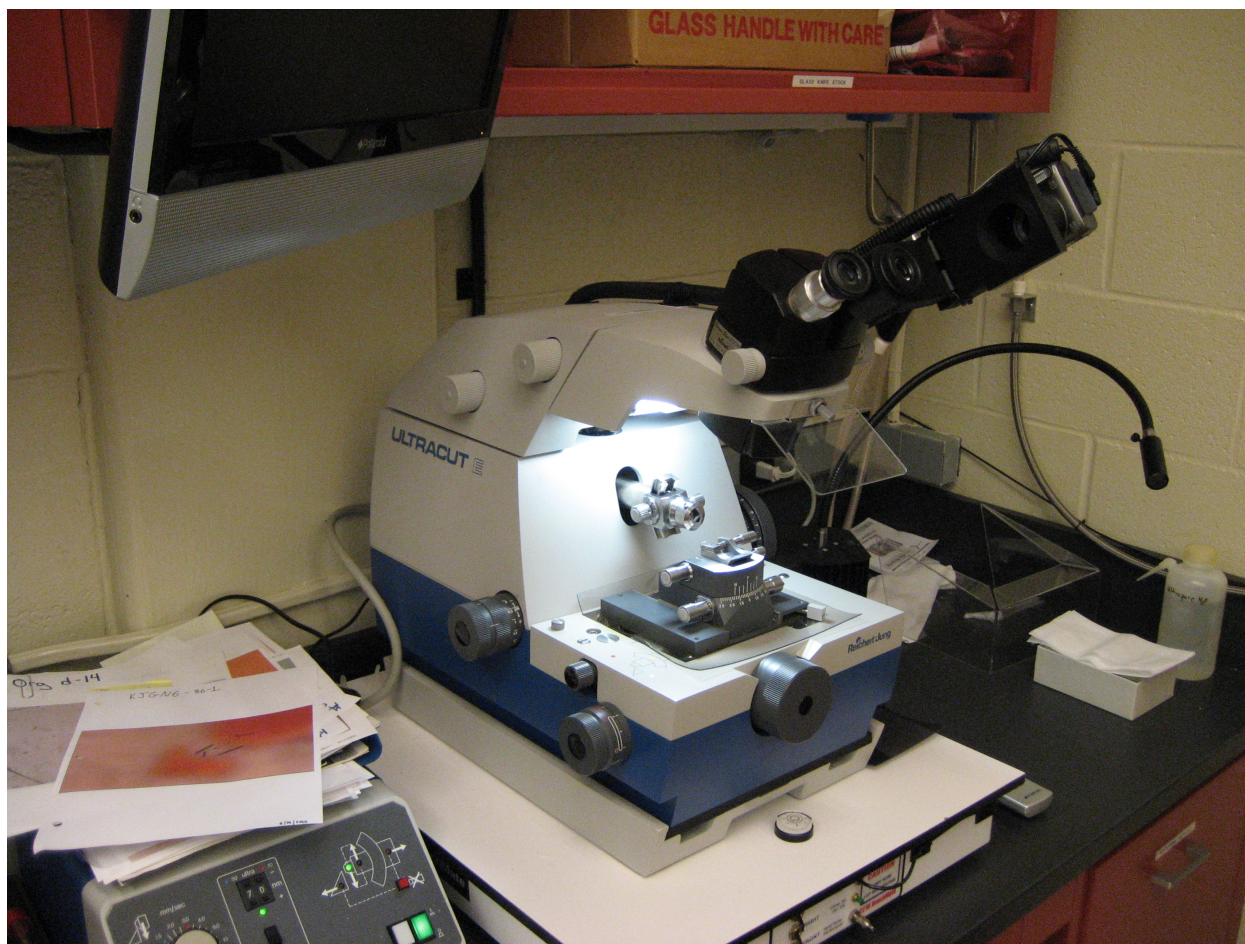
FIGURE 3.17: Reichert-Jung Ultracut-E microtome.
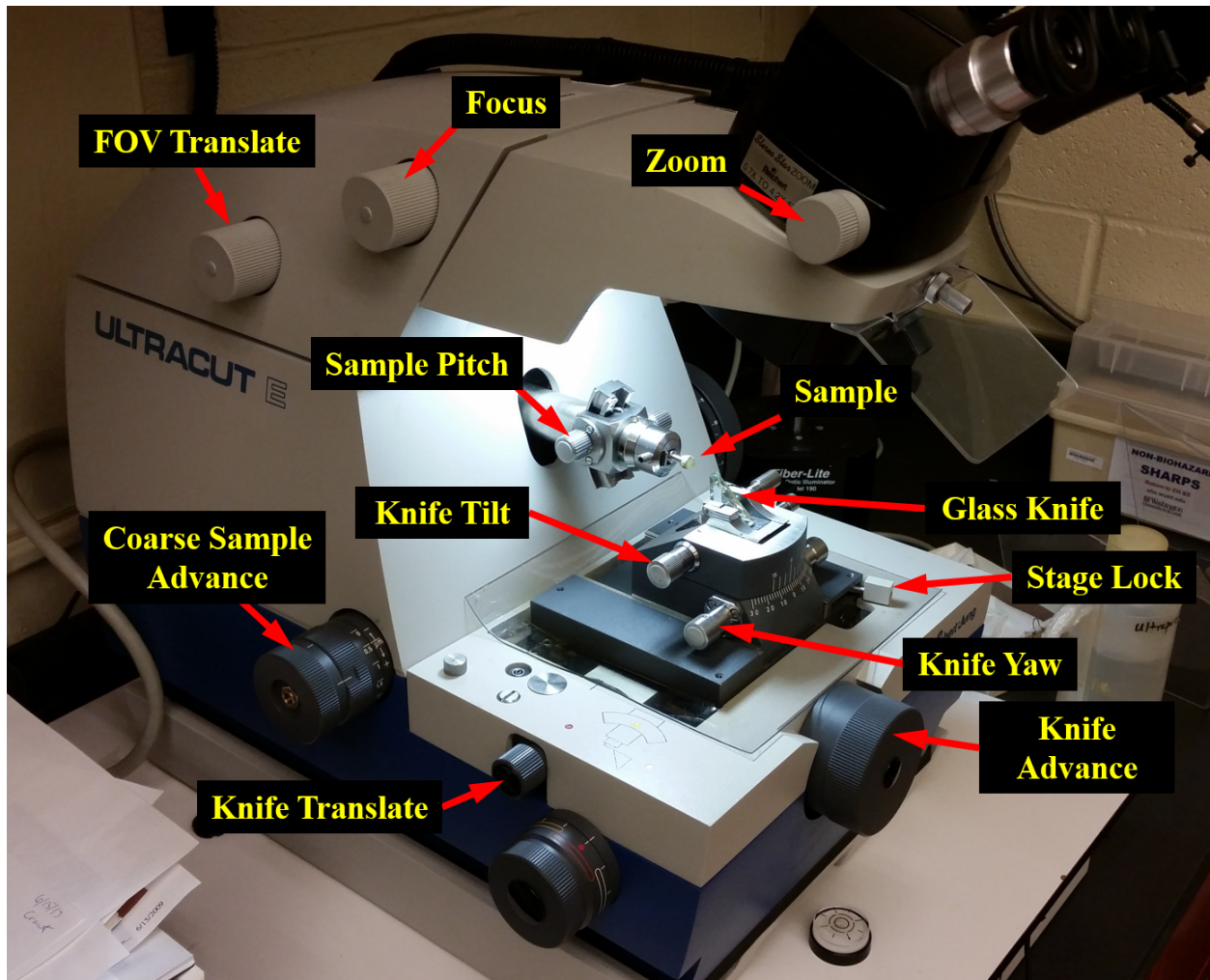
FIGURE 3.18: Reichert-Jung Ultracut-E microtome equipped with a glass knife for resin trimming.
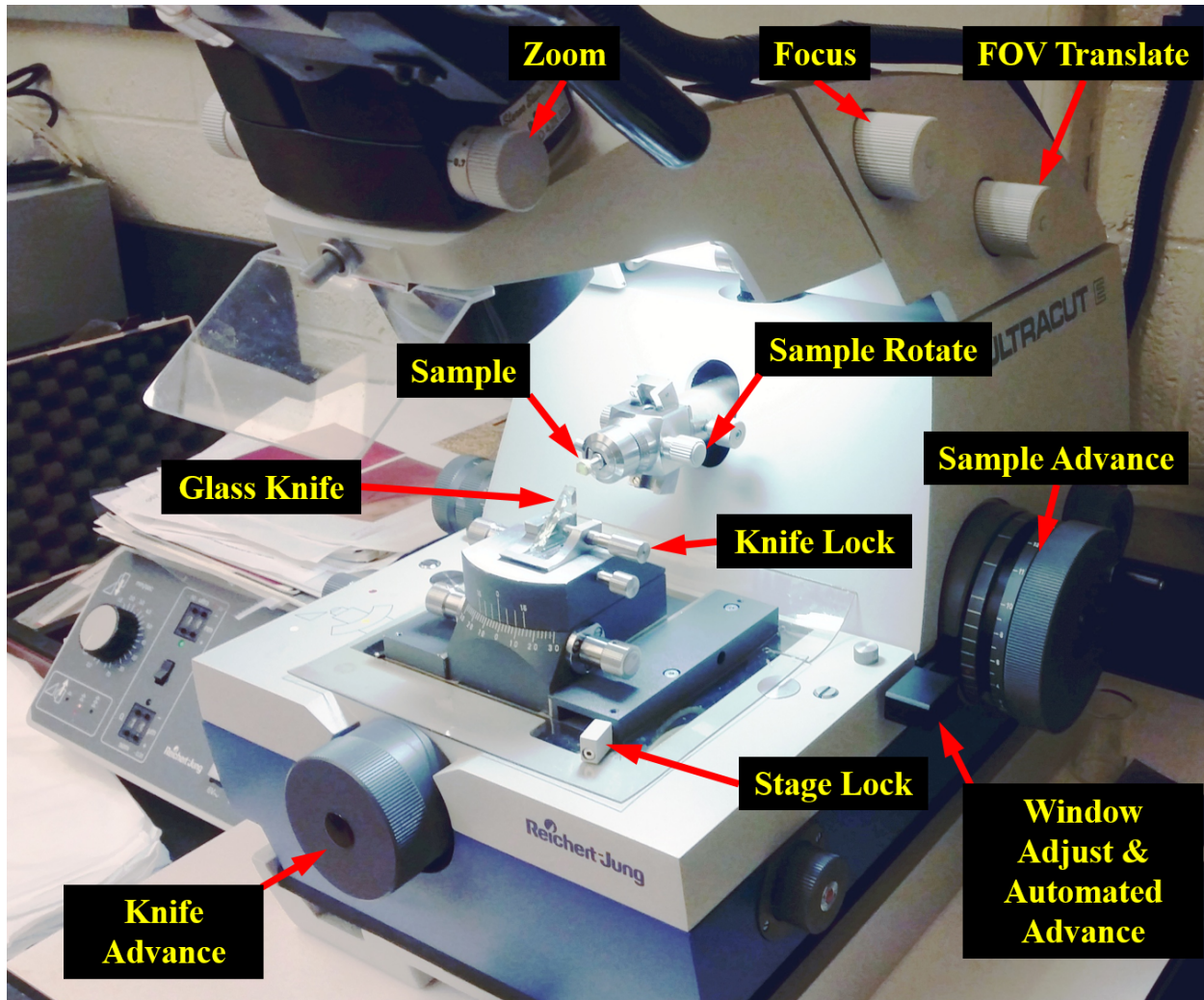
FIGURE 3.19: Reichert-Jung Ultracut-E microtome.
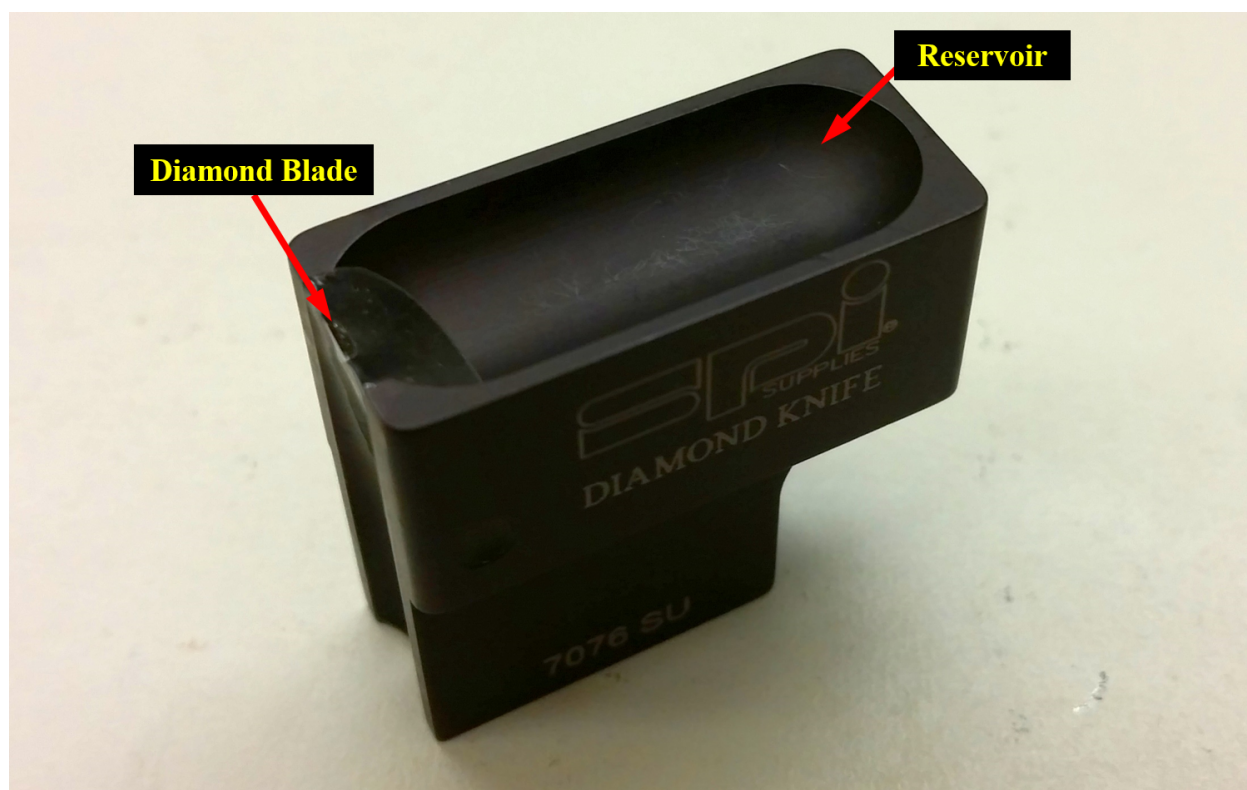
FIGURE 3.20: SPI® #9901 MS 2 mm diamond knife.
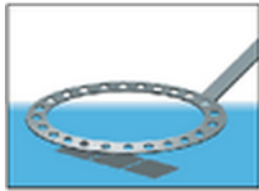
1. Center the loop above the sections
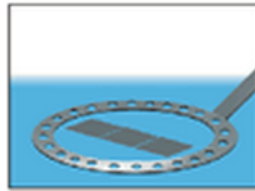
2. Slowly lower the loop over the sections and touch the water
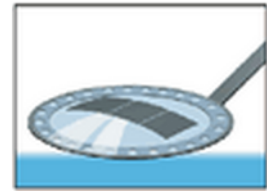
3. Gently lift up the loop with the sections in a droplet of water
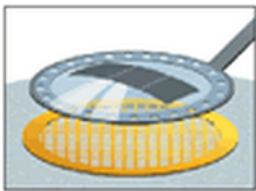
4. Lower the loop onto a grid and lift up again
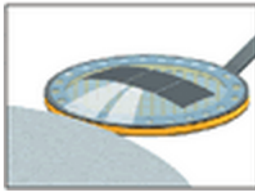
5. For coated grids, touch with filter paper to remove water
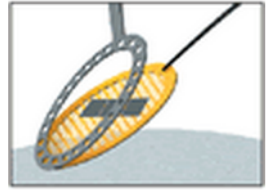
6. Separate the grid from the loop with an eyelash

FIGURE 3.21: Schematic from the Electron Microscopy Sciences website detailing the use of a Perfect Loop to collect microtome thin sections and deposit them on a TEM grid. Adapted from image source: https://www.emsdiasum.com/microscopy/products/preparation/ultramicrotomy.aspx

Bibliography

Amari, S., Lewis, R. S., & Anders, E. (**1994**), "Interstellar grains in meteorites: I. Isolation of SiC, graphite and diamond; size distributions of SiC and graphite", *Geochimica et Cosmochimica Acta* **58**, 459–470, URL http://dx.doi.org/10.1016/0016-7037(94)90477-4.

Bernatowicz, T. J., Cowsik, R., Gibbons, P. C. ., Lodders, K., Jr., B. F., Amari, S., & Lewis, R. S. (**1996**), "Constraints On Stellar Grain Formation From Presolar Graphite In The Murchison Meteorite", *The Astrophysical Journal* **472**, 760–782, URL http://dx.doi.org/10.1086/178105.

Hoppe, P., Cohen, S., & Meibom, A. (**2013**), "NanoSIMS: Technical Aspects and Applications in Cosmochemistry and Biological Geochemistry", *Geostandards and Geoanalytical Research* **37**, 111–154, URL http://dx.doi.org/10.1111/j.1751-908X.2013.00239.x.

Kilcoyne, A. L. D., Fakra, S., Hitchcock, P., Harteneck, B., Hitchcock, A. P., Tyliszczak, T., Rightor, E. G., Yang, L., Steele, W. F., Franck, K., Mitchell, G. E., Warwick, T., Anderson, E., & Ade, H. (**2003**), "Interferometer-controlled scanning transmission X-ray microscopes at the Advanced Light Source", *Journal of Synchrotron Radiation* **10**, 125–136, URL http://dx.doi.org/10.1107/S0909049502017739.

CHAPTER 4

C, N, AND O ISOTOPIC HETEROGENEITIES IN LOW-DENSITY SUPERNOVA GRAPHITE GRAINS FROM ORGUEIL

4.1 Preface

This chapter is based off of the peer-reviewed paper by: Groopman, E., Bernatowicz, T., and Zinner, E. (**2012**). "C, N, and O Isotopic Heterogeneities in Low-Density Supernova Graphite Grains from Orgueil" The Astrophysical Journal Letters, **754**, L8

4.2 Abstract

We report on the results of NanoSIMS isotope imaging of low-density supernova graphite grains from the Orgueil meteorite. 70 nm-thick microtomed sections of three supernova graphite grains were deposited on Si wafers and isotopically imaged in the NanoSIMS. These sections contain hotspots of excesses in ^{18}O and ^{15}N, which are spatially well-correlated, and

are likely carried by internal TiC subgrains. These hotspots are considerably more enriched in ^{18}O and ^{15}N than the host graphite grain. Correlations between ^{18}O and ^{15}N excesses indicate that the grains incorporated material from the He/C supernova zone. Isotope images of the surfaces of some grains show heterogeneities in their N and O isotope compositions, with extreme excesses in ^{15}N and ^{18}O. In the microtome sections we also observe two types of heterogeneities in the grains' C isotopic compositions: smooth, radial gradients in $^{12}C/^{13}C$, with this ratio trending towards solar with increasing radius; and highly anomalous pockets up to 2 μm in size with $^{12}C/^{13}C>>$solar that are located near the centers of the grain sections. Partial isotopic equilibration does not likely explain the C isotopic heterogeneities. These grains and their constituent parts probably formed in a stellar environment with changing isotopic composition.

4.3   Introduction

Low-density graphite grains ($\rho \sim$1.7 g/cm^3) have been isolated from the Murchison CM2 (Amari *et al.*, 1994) and Orgueil CI (Jadhav *et al.*, 2006) carbonaceous chondrites. Isotopic signatures of most low-density graphite grains indicate an origin in Type II supernovae, specifically excesses in ^{15}N, ^{18}O, ^{28}Si, and the inferred presence of ^{26}Al and ^{44}Ti from excesses in ^{26}Mg and ^{44}Ca, respectively, relative to solar composition (Amari *et al.*, 1995; Travaglio *et al.*, 1999; Stadermann *et al.*, 2005; Jadhav *et al.*, 2006). Low-density graphite grains also exhibit a wide range of $^{12}C/^{13}C$ ratios. Stadermann *et al.* (2005) obtained nano-scale secondary ion mass spectrometry (NanoSIMS) isotope images in $^{12,13}C$, $^{16,17,18}O$, and

[46,47,48,49,50]Ti of 9 microtome sections of the graphite spherule KE3e#10 (Croat *et al.*, 2003) from the Murchison low-density KE3 fraction (ρ = 1.65-1.72g/cm^3). These microtomed graphite slices contained gradients in the $^{12}C/^{13}C$ and $^{16}O/^{18}O$ isotopic ratios, with their interiors being more anomalous than their exteriors. It was suggested that these gradients are due to partial isotopic equilibration with the grain's environment during its lifetime. Strong initial O$^-$ secondary ion signals with respect to the "bulk" graphite were found in small regions that contain to internal TiC subgrains. The TiC subgrains are more enriched in ^{18}O than the parent grain, although their C isotopic compositions are indistinguishable from those of the surrounding graphite.

We report on the results of NanoSIMS isotope imaging of low-density supernova graphite grains from the Orgueil meteorite. We acquired isotope images of the surfaces of numerous grains as well as isotope images of microtomed sections of their interiors. Isotopic imaging is a useful tool for investigating the heterogeneous isotopic composition within presolar grains. This study is part of correlated isotopic, chemical, and crystallographic investigations undertaken to characterize individual presolar grains as fully as possible.

4.4 Samples and Experimental Methods

Seven size/density fractions were isolated from the Orgueil CI chondrite (OR1b-OR1h)[1] with densities increasing alphabetically (Jadhav *et al.*, 2006). The OR1d fraction (ρ = 1.75-1.92 g/cm^3) contains considerable insoluble organic matter of solar isotopic composi-

---

[1]OR1b label: OR = Orgueil, 1 = size >1 μm, b = density (ρ = 1.59-1.67 g/cm^3)

tion, which had not been removed during the chemical separation, and which surrounds the graphite grains. A few $\sim0.5\mu$L drops of OR1d suspended in a 4:1 mixture of isopropanol/water were pipetted onto high-purity Au foil and briefly dessicated in a vacuum oven at 70℃ (Groopman *et al.*, 2011). These graphite grains were identified in the scanning electron microscope (SEM) based upon surface morphology and Energy Dispersive X-Ray Spectroscopy (EDXS). Candidate grains were picked with a sharp W micromanipulator needle and were deposited on a clean Au-foil mount to reduce contamination from the insoluble organic matter; some of this material, however, remains stuck to the grains' surfaces. Twenty candidate grains with diameters >5 μm were selected, labeled OR1d6m^2. Raman microprobe spectra with 532 nm excitation and $\sim$1 μm resolution were obtained for all grains (Wopenka *et al.*, 2011).

A several-nanometer-thick coating of Pt was deposited in a sputter coater on the grains to secure them to the Au foil. Whole-grain NanoSIMS measurements of negative secondary ions (^{12,13}C, ^{14,15}N, ^{16,18}O, and ^{28,29,30}Si) were made with a Cs$^+$ primary beam ($\sim$100nm), and measurements of positive secondary ions (^{24,25,26}Mg, ^{27}Al, ^{28,29,30}Si, ^{39,41}K, ^{40,42,43,44}Ca, ^{46,47,48,49,50}Ti, ^{51}V, and ^{52}Cr) were made with an O$^-$ primary beam. To obtain the N isotopic composition we measured ^{12}C^{14}N$^-$ and ^{12}C^{15}N$^-$, as N does not have a stable negative ion. We used sufficiently high mass resolution to separate the isobaric peaks of ^{12}C^{15}N and ^{13}C^{14}N; and ^{12}C^{14}N and ^{13}C^{13}C and ^{12}C^{13}C H. Each grain's bulk isotopic composition was measured by rastering the primary beam over the entire grain's surface and summing the counts for each isotopic species. Additionally, we acquired 256 pixel by 256 pixel isotope images of the

---

^{2}6m = the 6th mount of OR1d

surfaces of grains G6, G13, G17, G21 in ^{12}C, ^{14,15}N, ^{16,18}O and of G24 in ^{12,13}C, ^{28,29,30}Si.

After NanoSIMS analysis, three grains (G17, G18, G24) with sizes 18, 12, and 13 μm were picked from the Au foil mount, embedded in LR White™ hard acrylic resin, and ultramicrotomed into 70nm-thick sections. Grains were selected based upon their isotopic compositions and relatively large sizes, (Table 4.1). Slices of each grain were deposited on Si wafers and on Cu transmission electron microcope (TEM) grids, both SiO and holey-C coated. Due to the grains' large sizes, we were able to obtain hundreds of microtome slices of each grain and distribute these among the 3 different substrates. Each substrate has its own advantage: holey-C substrates are useful for determining Si content and performing EELS over holes; the SiO substrate reduces the C background necessary for C K-edge X-ray absorption near-edge structure (XANES) measurements (Nittler *et al.*, 2011); and the Si wafers, while precluding TEM studies, are a superior heat sink for Raman spectroscopy (high signal-to-noise ratio), and provide a highly stable substrate for NanoSIMS measurements. Due to the large sizes of the grains, many of the slices contain tearing holes from microtoming, shown as grey in the figures. For the slices on Si wafers, isotope images in ^{12}C, ^{14,15}N, ^{16,18}O or ^{12,13}C, ^{28,29,30}Si were obtained with the resin and Si wafer used as isotopic standards. Only one image was obtained for each slice. Each isotope image consists of 20 layers of a 256 pixel by 256 pixel raster area, with a dwell time per pixel per layer of 10ms. Each raster area is chosen to be 1–2 μm wider than the grain slice. While isotope images require much longer measurement times than bulk analyses to gather meaningful statistics, they allow us to investigate heterogeneities in the grains' isotopic compositions.

4.5 Results

4.5 Results

4.5.1 Whole-grain Isotopic Measurements

Whole-grain isotopic measurements are presented in Table 4.1 (Groopman *et al.*, 2011). The majority of grains have signatures of a supernova origin. Six of the 20 grains from OR1d6m are not included, as their isotopic and Raman spectroscopic measurements do not identify them as presolar grains. Each grain's measured bulk composition represents the lower bound of the grain's deviation from solar composition due to surface contamination from insoluble organic material. From isotope images of the grains' surfaces we can locate regions of low contamination and infer a more correct isotopic composition. We must compromise between obtaining accurate isotopic ratios via long measurements during which surface contamination is removed by sputtering and saving as much of the grain as possible for future correlated TEM, XANES, and Raman studies.

4.5.2 Surface Images

Isotopic imaging on the graphite surfaces show heterogeneities in their C, O, and N isotopic ratios. While regions of roughly solar C, O, and N isotopic composition may be explained due to surface contamination, isotopically anomalous regions are found on the grains' surfaces, with extreme excesses in ^{18}O and ^{15}N relative to solar ratios. On G6, G13, and G21 these anomalous regions in have a good spatial correlation. If expressed as delta values (see Figure 4.1 for definition), $\delta^{15}N/^{14}N$ and $\delta^{18}O/^{16}O$, respectively, range up

to 6,400‰ and 98,000‰ (^{15}N/^{14}N=0.03 and ^{18}O/^{16}O=0.20; ^{14}N/^{15}N=37 and ^{16}O/^{18}O=5) in G6; 2,300‰ and 49,000‰ (0.012 and 0.1; 82 and 10) in G13; and 2,300‰ and 98,000‰ (0.012 and 0.20; 82 and 5) in G21. In G17 the anomalous regions on the surface in δ^{15}N/^{14}N and δ^{18}O/^{16}O range up to 15,000‰ and 15,000‰ (.06 and .03; 17 and 31), respectively, but are not spatially correlated. Hotspots on the grains' surfaces vary in size from 110nm to 425nm.
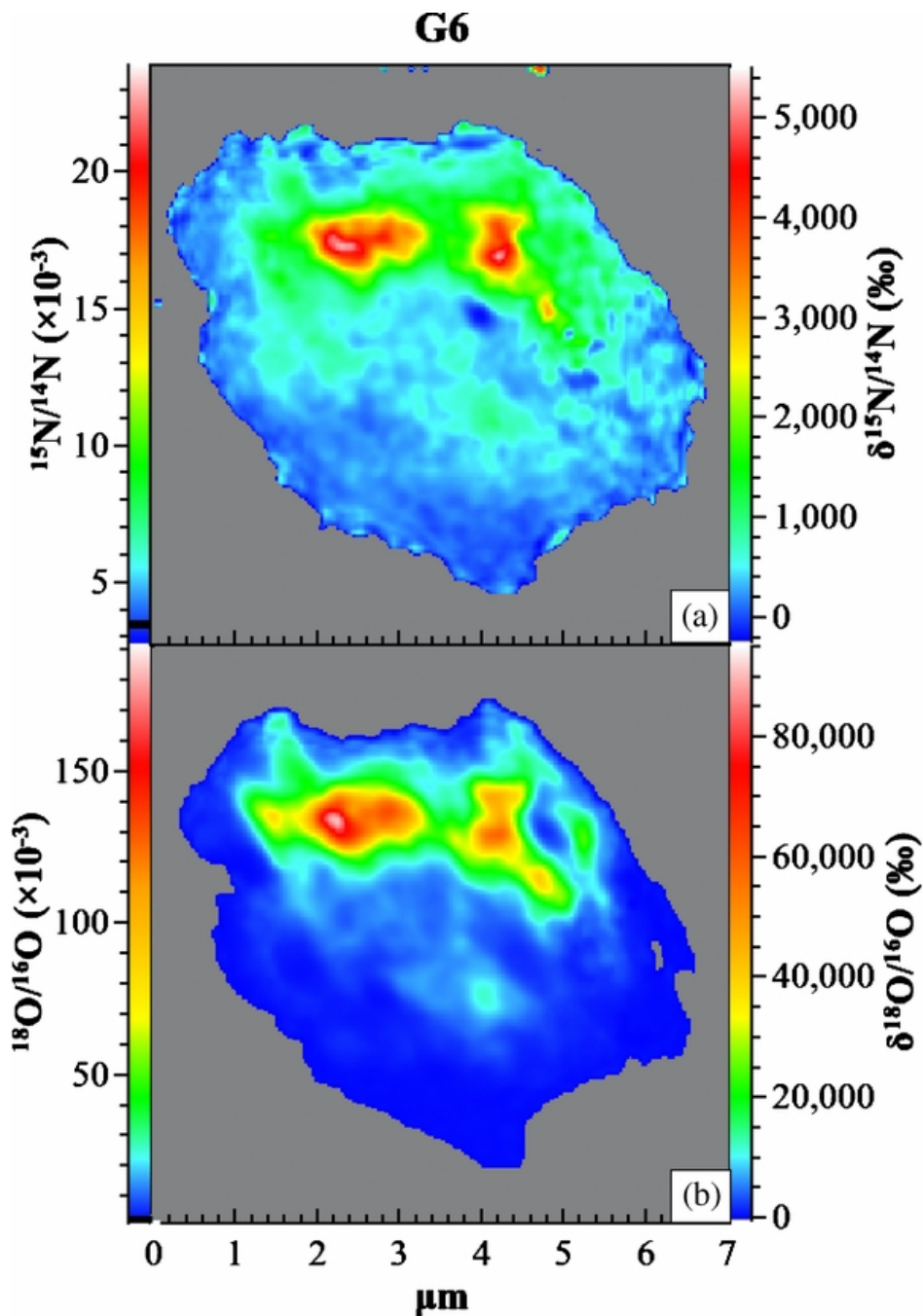
FIGURE 4.1: False-color isotope images of the surface of G6. Images are scaled in absolute ratios (left) and δ-values (right) where $\delta^i X = 1000 \times \left((^i X /^j X)_{\mathrm{sample}} / (^i X /^j X)_{\mathrm{standard}} - 1 \right)$ and $^j X$ is the major isotope ^{14}N or ^{16}O. Black bars on left indicate terrestrial isotopic ratios $(^{15}N/^{14}N_{\mathrm{terrestrial}} \approx 0.004;\ ^{18}O/^{16}O_{\mathrm{terrestrial}} \approx 0.002)$. a) $\delta^{15}N/^{14}N$ isotope image. Deviations from terrestrial range up to 6,400 ‰ $(^{15}N/^{14}N=0.03,\ ^{14}N/^{15}N=37)$. b) $\delta^{18}O/^{16}O$ isotope image. Deviations from terrestrial range up to 98,000 ‰ $(^{18}O/^{16}O=0.20,\ ^{16}O/^{18}O=5)$. There is a good spatial correlation between the hotspots in $\delta^{18}O/^{16}O$ and $\delta^{15}N/^{14}N$.

4.5.3   Microtome Sections

Multiple ultramicrotome sections of G17 and G18 contain highly anomalous and spatially-correlated hotspots of $\delta^{18}O/^{16}O$ and $\delta^{15}N/^{14}N$ [Figs. 4.2,4.3]. Five hotspots were found in 5 slices of G17 and G18 imaged in O and N isotopes. $\delta^{15}N/^{14}N$ and $\delta^{18}O/^{16}O$ in the hotspots range up to 4400‰ and 6100‰ ($^{15}N/^{14}N=0.02$ and $^{18}O/^{16}O=0.01$; $^{14}N/^{15}N=50$ and $^{16}O/^{18}O=70$), respectively. There is a strong spatial correlation between the observed excesses in ^{18}O and ^{15}N. It is likely that internal subgrains, particularly TiC, are the carriers of the isotopic anomalies in O and N within these hotspots. Preliminary TEM studies have confirmed the presence of internal TiC subgrains in other slices of G17, G18, and G24, although no $\delta^{18}O/^{16}O$, $\delta^{15}N/^{14}N$ hotspots were found in the two slices of G24 imaged in O and N isotopes. Auger Nanoprobe scans of slice G18-C after NanoSIMS imaging show a strong Ti signal at the location of the $\delta^{15}N/^{14}N$, $\delta^{18}O/^{16}O$ hotspots (Figure 4.3b). The four other slices with $\delta^{18}O/^{16}O$ and $\delta^{15}N/^{14}N$ hotspots were sputtered away completely during NanoSIMS imaging; we found no elemental Ti traces in Auger scans of these sections. We did not observe differences between the $^{16}O^-$ and $^{12}C^{14}N^-$ signals between any of these hotspots and the surrounding material. Therefore the anomalous δ-value compositions of these hotspots are characterized by excesses in ^{18}O and ^{15}N and not by depletions in the major isotopes, ^{16}O and ^{14}N, respectively. Si isotope images show uniform isotopic distributions within the grains and yield no evidence of internal SiC grains within these slices.

The interiors of the graphite grains contain C isotopic heterogeneities of two forms. Slices M and N of G24 exhibit fairly smooth gradients with $^{12}C/^{13}C$ increasing radially from 8 to

14 (Figures 4.4a–c). Based upon the ^{12}C/^{13}C ratio measured in concentric shells of the slices, there exists a statistically significant gradient in the grain's C isotopic composition. In slices G17-A and G17-B (Figures 4.4d–e) ^{12}C/^{13}C ranges from 400 to 1800, whereas the bulk surface isotopic measurement was 340. The largest anomalies lie in pockets up to $\sim$2 μm in size close to the center of the slice. These pockets have the same Si isotopic composition and ^{28}Si$^-$ count rate as the rest of the graphite grain slice, again yielding no evidence for the presence of internal SiC subgrains.
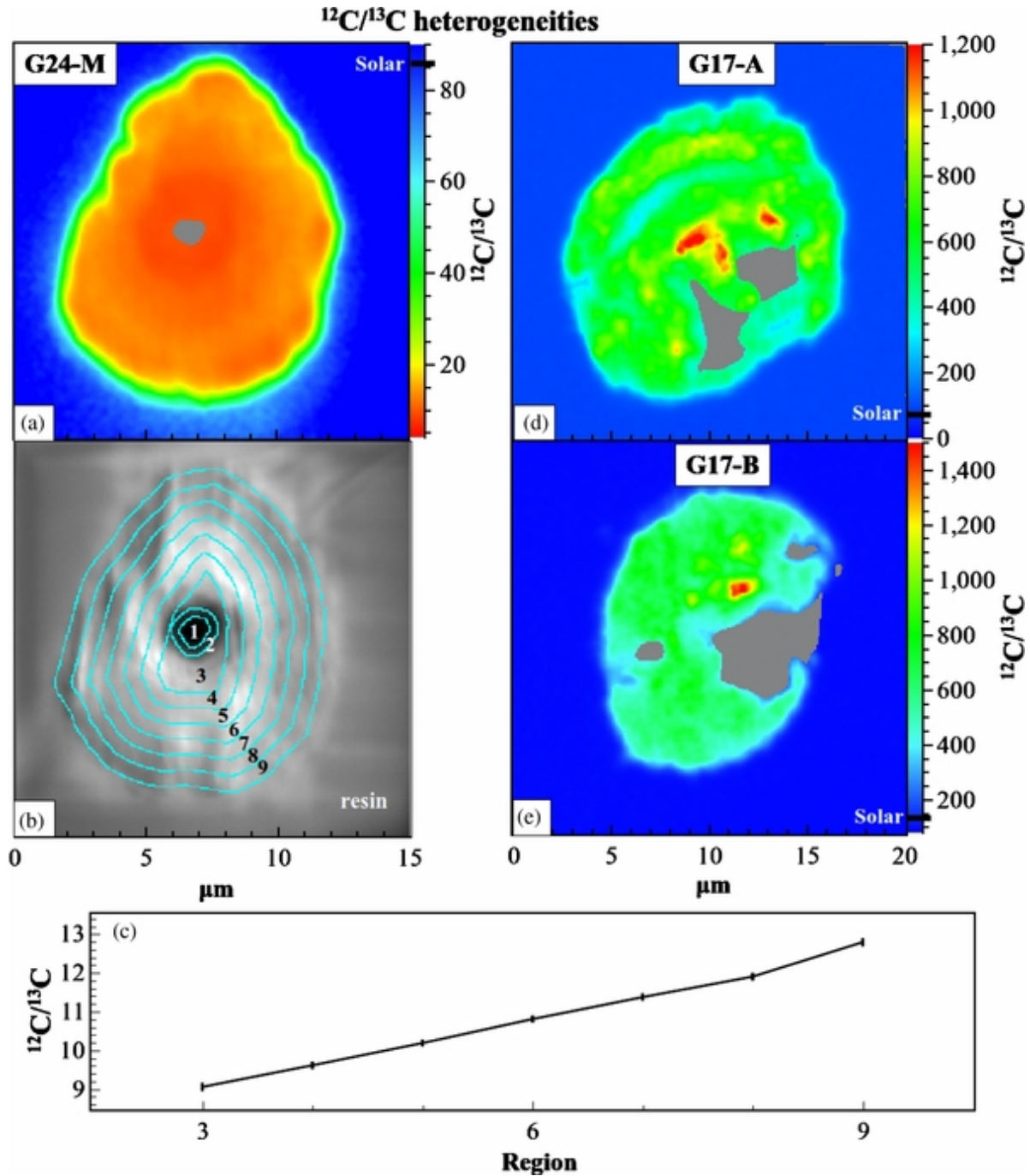
FIGURE 4.4: a) G18 slice M exhibits a radial gradient in $^{12}C/^{13}C$ from 8 to 14. b) Contours used in (c). c) Statistically significant trend in mean $^{12}C/^{13}C$ within concentric regions outlined in (b). All points have 5 σ error bars in $^{12}C/^{13}C$ based on counts. This grain likely formed in an environment where the C isotopic composition was changing on the timescale of grain formation. (d) & (e) G17 slices A and B, respectively. These slices have heterogeneously distributed C isotopic compositions with highly anomalous pockets with sizes up to 2 μm where $^{12}C/^{13}C \gg$ solar. $^{12}C/^{13}C$ varies from 400 to 1800. These pockets are most likely presolar graphites that formed earlier and were incorporated into the host grain.

4.6   Discussion and Conclusions

We have found evidence for heterogeneities in the C, N, and O isotopic compositions of 6 low-density graphite grains. Several of these grains contain bulk excesses of ^{18}O and ^{15}N, evidence of a supernova origin; however, they also contain spatially-correlated isotopic anomalies on their interiors and exteriors that are much more extreme than the bulk graphite measurements. TiC subgrains are a likely carrier of the observed δ^{18}O$/^{16}$O and δ^{15}N$/^{14}$N heterogeneities in the grains' interiors. Previous NanoSIMS studies of microtomed slices of a supernova graphite found that internal TiC subgrains have much larger ^{18}O excesses than the parent grain (Stadermann *et al.*, 2005). Initial ^{16}O$^-$ signals associated with these internal TiCs were also much higher than those in the parent grain. It is unknown whether the higher initial O$^-$ secondary signal is due to intrinsically higher O content in the TiC subgrains or whether O ion yields from TiC are greater than those from graphite. However, recent electron energy loss spectroscopy (EELS) of supernova TiC subgrains has shown that they contain amorphous rims (Daulton *et al.*, 2009) enriched in O up to 20 at. % relative to the interiors of the TiC subgrains (Daulton *et al.*, 2012). These enrichments thus may be due to O-rich amorphous rims around the TiC grains. In the present study, we do not observe higher initial O$^-$ secondary signals from the δ^{18}O$/^{16}$O and δ^{15}N$/^{14}$N hotspots. During our NanoSIMS measurements we presputtered the graphite sections until we achieved a constant ^{12}C$^-$ signal before we began imaging; this may have sputtered away the top surface of any O-rich rims on TiCs in contrast to Stadermann *et al.* (2005), who did not presputter their slices before imaging.

These spatially-correlated $\delta^{18}O/^{16}O$ and $\delta^{15}N/^{14}N$ hotspots suggest that the internal TiC grains in the supernova outflow formed from inner He/C zone material where $^{18}O/^{16}O$ and $^{15}N/^{14}N$ are very high (Rauscher *et al.*, 2002), while the bulk of the host graphite grain formed from a mixture that included material further out in the He/C zone or from other zones, resulting in more modest ^{18}O and ^{15}N excesses. The high $^{12}C/^{13}C$ ratios of G17 and G18 also indicate contributions from the He/C zone, which has $^{12}C/^{13}C \gg$ solar. While it has been proposed that carbonaceous grains form in a supernova environment where the elemental ratio C/O < 1 (Clayton, 2011), all of our observations point to major He/C zone contributions, where C/O > 1. G24 has a very low $^{12}C/^{13}C$ ratio and relatively smaller excesses of ^{18}O and ^{15}N, indicating that it may represent a mixture of material with a significant contribution from the He/N zone, where C/O is still > 1. We did not observe any spatially-correlated hotspots in $\delta^{18}O/^{16}O$ and $\delta^{15}N/^{14}N$ in G24, however TEM investigations have found a large 300 nm TiC grain in another slice on a TEM grid. Since this slice is part of an ongoing TEM study, we will measure the O and N isotopic composition of this TiC in the future.

Isotope images of grain surfaces yield some of the largest excesses in ^{18}O and ^{15}N ever measured in presolar graphite grains. Although TiC abundance has been shown to decrease with radial position in several supernova graphites (Croat *et al.*, 2003), TiC subgrains are not precluded from being the source of the surface $\delta^{18}O/^{16}O$, $\delta^{15}N/^{14}N$ hotspots.

We observed two types of heterogeneities in the C isotopic compositions of microtomed graphites: smooth radial gradients in G18 and G24, and extremely anomalous pockets near the center of grain G17. Both heterogeneities are statistically significant. Radial gradients

in C and O isotope composition have been previously observed (Stadermann *et al.*, 2005). While partial isotopic equilibration with grains' environments may explain the O isotope compositions, gradients in C isotope composition require a different explanation. Since the graphite grains are overwhelmingly composed of carbon, partial isotopic equilibration would require the exchange of a significant portion of the grain's mass over its lifetime in order to reproduce the gradients we observe, which is unlikely. The equilibration of C isotopes would simultaneous have to preserve N and O isotopic anomalies that we observe. Additionally, Zinner & Jadhav (2012) found that the radiogenic components of ^{26}Mg, and ^{41}K within graphite grains from the same Orgueil size/density fraction are spatially correlated with the major isotopes of the parent species in each system, implying that radiogenic daughter isotopes are quantitatively retained and there is no redistribution within the grains. We therefore find it unlikely that significant redistribution or exchange of C has occurred. Instead we suggest that the grains condensed in an environment whose isotopic composition was changing during grain formation. This would likely require small-scale mixing of material in the grains' formation environments on formation timescales and/or movement of the growing grain through regions of changing isotopic composition. Evidence of extinct ^{49}V ($t_{1/2} = 330$ days) in SiC-X grains implies that the timescale of SiC formation in supernova ejecta is on the order of several months (Hoppe & Besmehn, 2002). However, excluding very high pressure environments, graphite is likely to form before SiC from a gas with C/O > 1 and otherwise approximately solar composition (Bernatowicz *et al.*, 1996). Such conditions indicate that formation of the graphite grains occurred within the first few months after the supernova explosion.

The heterogeneous $^{12}C/^{13}C$ anomalies in G17 (Figures 4.2d,e) range up to $^{12}C/^{13}C =$ 1800 and are located in distinct regions within the slices. These anomalous regions are unlikely to be due to the presence of either internal TiC or SiC X grains; their sizes range up to 2 μm, whereas the largest internal TiC found to date was ~500 nm; they lack significant Si and Ti elemental signals with respect to the rest of the graphite slice as measured in the Auger Nanoprobe; and they show no significant enrichments in ^{28}Si with respect to the rest of the graphite in NanoSIMS images. We therefore believe that the pockets are graphite regions that formed from more ^{12}C-enriched material before being incorporated by the parent graphite.
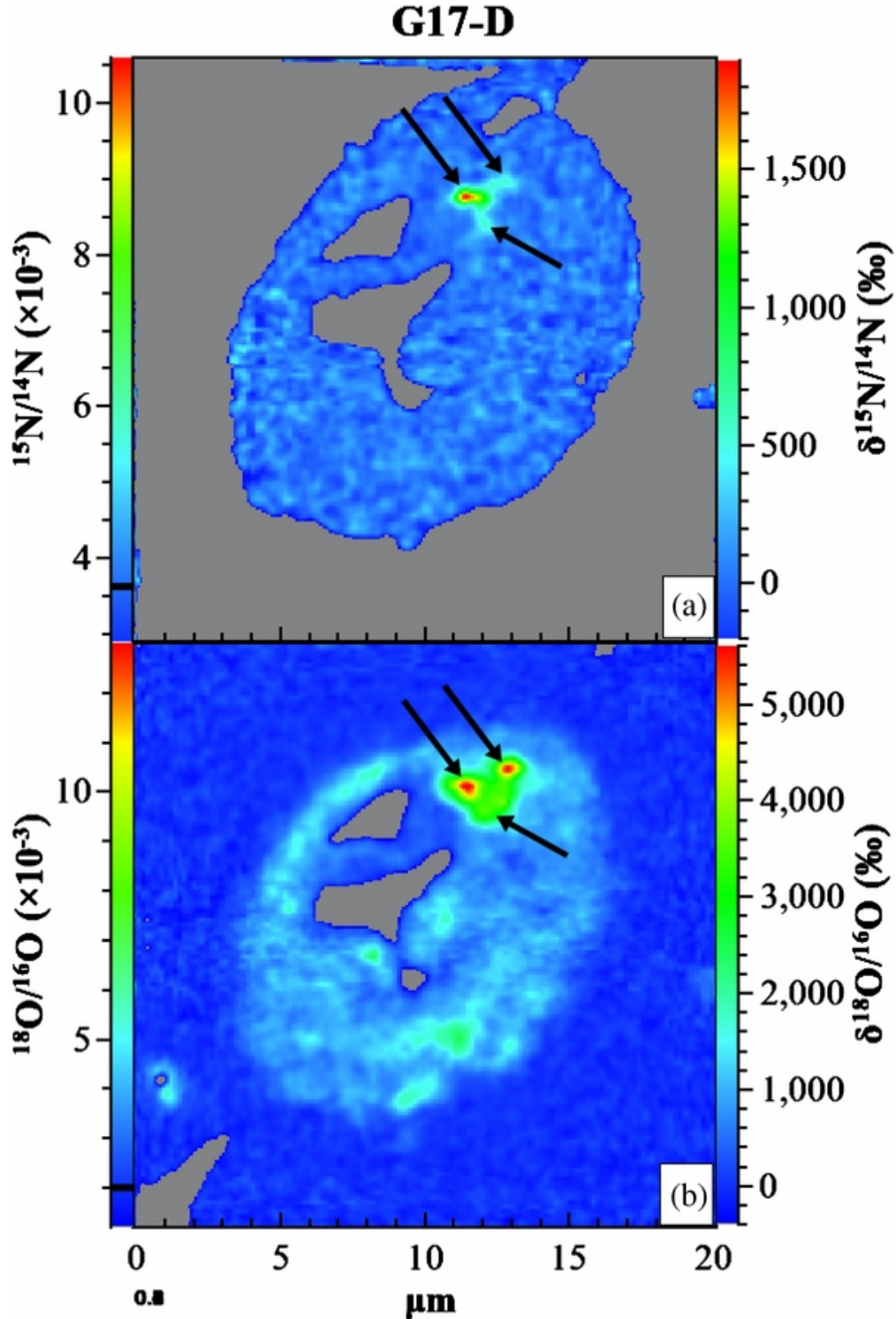
FIGURE 4.2: False color images of grain G17 slice D in $\delta^{15}N/^{14}N$ (a) and $\delta^{18}O/^{16}O$ (b). There is a strong spatial correlation between $\delta^{15}N/^{14}N$ and $\delta^{18}O/^{16}O$ in three hotspots, indicated by arrows. Grey regions indicate holes in the slice from microtoming.

94
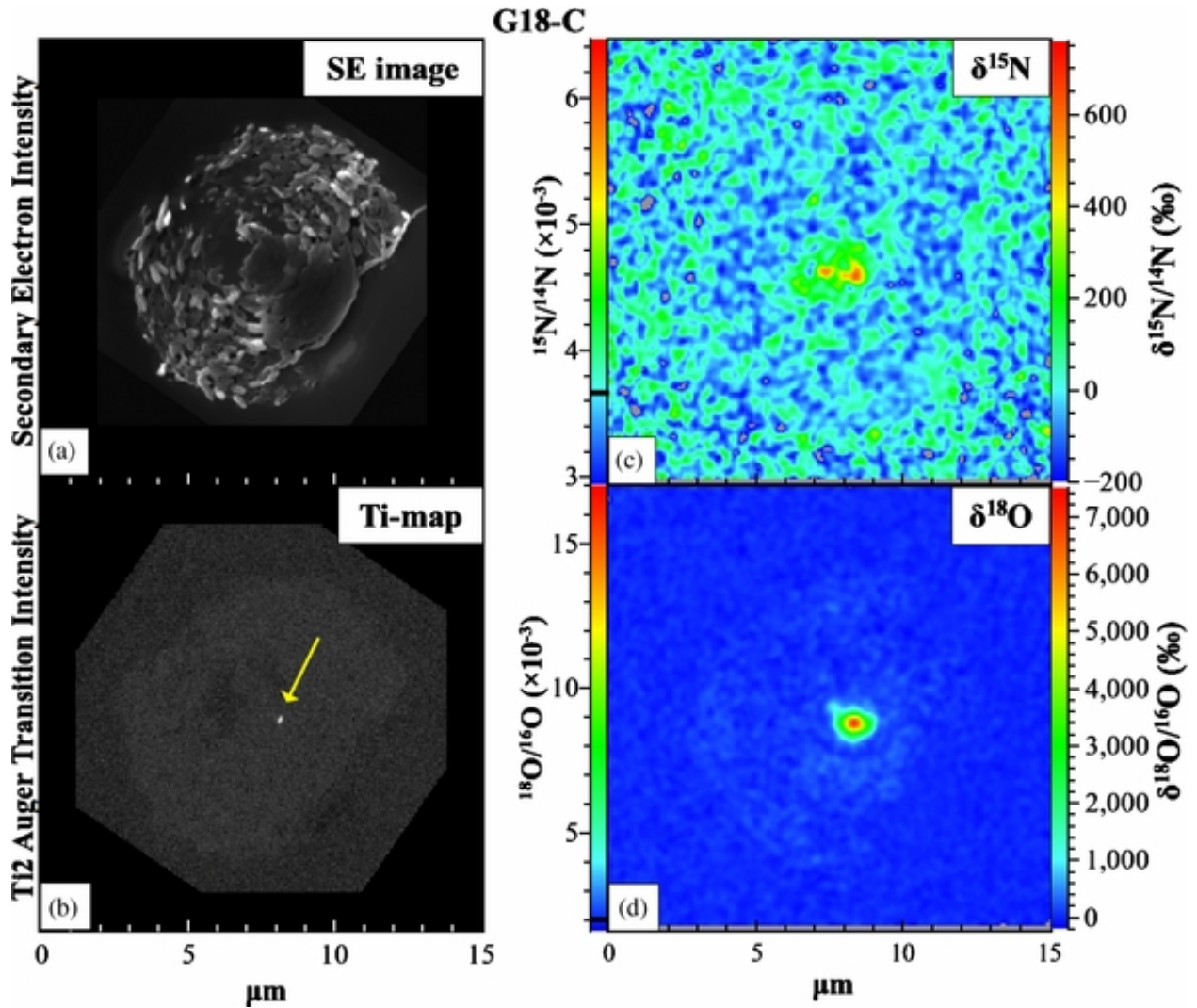
FIGURE 4.3: a) Auger Nanoprobe secondary electron image of G18 slice C after NanoSIMS imaging. b) Auger Ti elemental map. A Ti-rich subgrain is clearly visible in the center of the slice, indicated by arrow. c) False-color N isotope ratio image. $\delta^{15}N/^{14}N$ up to 760‰ ($^{15}N/^{14}N=0.007$, $^{14}N/^{15}N=154$). d) False-color O isotope ratio image. $\delta^{18}O/^{16}O$ up to 7300‰ ($^{18}O/^{16}O=0.017$, $^{16}O/^{18}O=60$). There is a good spatial correlation between hotspots in panels (b)-(d). All images have the same scale and same orientation.

TABLE 4.1: OR1d6m Presolar Graphite: Whole-grain isotopic measurements..

Grain	Size (μm)	^{12}C/^{13}C	^{16}O/^{18}O	^{14}N/^{15}N	δ^{29}Si/^{28}Si (‰)[†]	δ^{30}Si/^{28}Si (‰)	$\left(^{26}\text{Al}/^{27}\text{Al}\right)\times10^3$	$\left(^{44}\text{Ti}/^{48}\text{Ti}\right)\times10^3$
G-4	6	**7.5 ± 0.1**	486.0 ± 9.2	**236.0 ± 18.3**	**-39 ± 11**	**-62 ± 13**	$\cdots$	**106 ±18.7**
G-5	10.5	**45.9 ± 0.3**	**323.5 ± 5.7**	**248.0 ± 10.7**	**-74 ± 12**	**-135 ± 15**	**17.7 ± 0.6**	**5.8 ± 1.0**
G-8	8	**127.8 ± 0.9**	**280.4 ± 5.0**	**145.0 ± 9.3**	**48 ± 10**	**-29 ± 13**	**77.1 ± 0.8**	**27.3 ± 1.7**
G-9	5.5	**8.0 ± 0.1**	**338.5 ± 8.5**	**233.8 ± 12.0**	-37 ± 40	**159 ± 55**	**18.4 ± 0.7**	**109 ± 49**
G-11	7.5	**22.0 ± 0.2**	**297.7 ± 6.0**	**232.2 ± 10.3**	-21 ± 11	**-40 ± 14**	**73.6 ± 0.9**	**3.4 ± 0.8**
G-15	12	**13.4 ± 0.1**	**471.8 ± 10.5**	**240.2 ± 16.4**	-21 ± 24	7 ± 30	$\cdots$	$\cdots$
G-20	4.5	**74.3 ± 0.5**	501.6 ± 10.3	273.9 ± 16.9	**-37 ± 14**	-32± 18	$\cdots$	**46.2 ± 6.1**
G-23	6	**73.7 ± 0.5**	**394.4 ± 7.2**	**214.4 ± 13.1**	**-134 ± 8**	**-168 ± 10**	**68.9 ± 0.7**	**19.5 ± 3.5**
Imaged Grains:								
G-6	4.5	**113.2 ± 0.8**	**163.2 ± 2.8**	**145.3 ± 5.4**	-13 ± 13	**-60 ± 16**	**446 ± 1.5**	**103 ± 6.0**
G-13	5.5	**66.0 ± 0.4**	**170.1 ± 3.2**	263.0 ± 5.8	**-141 ± 17**	**-181 ± 21**	**231 ±2.4**	**349 ± 55.9**
G-17	18	**306.1 ± 2.1**	**306.3 ± 6.4**	**215.1 ± 10.4**	-27 ± 18	**-86 ± 21**	**55.8 ± 2.0**	**130 ± 13.5**
G-18	12	**121.0 ± 0.8**	**432.9 ± 9.2**	**148.8 ± 14.6**	-29 ± 16	-12 ± 20	**12 ± 0.3**	$\cdots$
G-21	7	**140.7 ± 1.0**	**140.1 ± 2.6**	267.6 ± 4.8	**-125 ± 13**	**-165 ± 15**	**271 ±2.7**	$\cdots$
G-24	13	**13.1 ± 0.1**	**479.2 ± 9.4**	**236.3 ± 16.5**	3 ± 11	4 ± 14	$\cdots$	**72.8 ± 15.4**
Terrestrial	-	89	499*	272*	^{29}Si/^{28}Si = .051	^{30}Si/^{28}Si = .034	0.05[††]	0

[†] Delta-value notation, δ^iSi/^{28}Si = $1000\times\left((^i\text{Si}/^{28}\text{Si})_{\text{sample}}/(^i\text{Si}/^{28}\text{Si})_{\text{standard}} - 1\right)$, deviations in permil from standard/terrestrial values.

[††]Inferred ^{26}Al/^{27}Al ratio in Calcium-Aluminum-rich Inclusions, the oldest solar system solids.

* The results of NASA's Genesis mission have shown that terrestrial materials are generally depleted in ^{14}N and ^{16}O relative to the solar wind. Solar wind isotopic ratios were found to be ^{14}N/^{15}N = 441 (Marty *et al.*, 2011) and ^{16}O/^{18}O = 530 (McKeegan *et al.*, 2011).

All values represent whole-grain measurements; anomalies are lower bounds due to surface-adhered insoluble organic material. All errors are 1σ. Bold values indicate $2\sigma+$ deviation from terrestrial. Blank cells indicate no measurable excess in ^{26}Mg or ^{44}Ca.

Bibliography

Amari, S., Lewis, R. S., & Anders, E. (**1994**), "Interstellar grains in meteorites: I. Isolation of SiC, graphite and diamond; size distributions of SiC and graphite", *Geochimica et Cosmochimica Acta* **58**, 459–470, URL http://dx.doi.org/10.1016/0016-7037(94)90477-4.

Amari, S., Zinner, E., & Lewis, R. S. (**1995**), "Large 18O Excesses in Circumstellar Graphite Grains from the Murchison Meteorite: Indication of a Massive-Star Origin", *The Astrophysical Journal Letters* **447**, L147–L150, URL http://stacks.iop.org/1538-4357/447/i=2/a=L147.

Bernatowicz, T. J., Cowsik, R., Gibbons, P. C. ., Lodders, K., Jr., B. F., Amari, S., & Lewis, R. S. (**1996**), "Constraints On Stellar Grain Formation From Presolar Graphite In The Murchison Meteorite", *The Astrophysical Journal* **472**, 760–782, URL http://dx.doi.org/10.1086/178105.

Clayton, D. D. (**2011**), "A new astronomy with radioactivity: Radiogenic carbon chemistry", *New Astronomy Reviews* **55**, 155–165, URL http://dx.doi.org/10.1016/j.newar.2011.08.001.

Croat, T. K., Bernatowicz, T., Amari, S., Messenger, S., & Stadermann, F. J. (**2003**), "Structural, chemical, and isotopic microanalytical investigations of graphite from supernovae", *Geochimica et Cosmochimica Acta* **67**, 4705–4725, URL http://dx.doi.org/10.1016/S0016-7037(03)00463-0.

Daulton, T. L., Bernatowicz, T. J., & Croat, T. K. (**2009**), "Alteration of TiC in Supernovae Outflows: Transmission Electron Microscopy Study of TiC Subgrains in Supernovae Graphite", in "40th Lunar and Planetary Science Conference", Abstract #1996, Lunar and Planetary Institute, Houston, URL http://www.lpi.usra.edu/meetings/lpsc2009/pdf/1996.pdf.

Daulton, T. L., Bernatowicz, T. J., & Croat, T. K. (**2012**), "Electron Energy Loss Spectral Imaging of TiC Formed by Supernovae: A Scanning Transmission Electron Microscopy Study of Grain Formation and Alteration Mechanisms", in "43rd Lunar and Planetary Science Conference", Abstract #2247, Lunar and Planetary Institute, Houston, URL http://www.lpi.usra.edu/meetings/lpsc2012/pdf/2247.pdf.

Groopman, E., Wopenka, B., & Zinner, E. (**2011**), "Isotopic and Raman Analyses of Low-density Orgueil Carbon Grains", in "74th Annual Meeting of the Meteoritical Society, August 812, 2011, London, U.K.", volume 46, A82, Abstract #5031, Blackwell Publishing Ltd, URL http://dx.doi.org/10.1111/j.1945-5100.2011.01221.x.

Hoppe, P. & Besmehn, A. (**2002**), "Evidence for Extinct Vanadium-49 in Presolar Silicon Carbide Grains from Supernovae", *The Astrophysical Journal Letters* **576**, L69–L72, URL http://dx.doi.org/10.1086/342785.

Jadhav, M., Amari, S., Zinner, E., & Maruoka, T. (**2006**), "Isotopic analysis of presolar graphite grains from Orgueil", *New Astronomy Review* **50**, 591–595, URL http://dx.doi.org/10.1016/j.newar.2006.06.004.

Marty, B., Chaussidon, M., Wiens, R. C., Jurewicz, A. J. G., & Burnett, D. S. (**2011**), "A 15N-Poor Isotopic Composition for the Solar System As Shown by Genesis Solar Wind Samples", *Science* **332**, 1533–1536, URL http://dx.doi.org/10.1126/science.1204656.

McKeegan, K. D., Kallio, A. P. A., Heber, V. S., Jarzebinski, G., Mao, P. H., Coath, C. D., Kunihiro, T., Wiens, R. C., Nordholt, J. E., Moses, R. W., Reisenfeld, D. B., Jurewicz, A. J. G., & Burnett, D. S. (**2011**), "The Oxygen Isotopic Composition of the Sun Inferred from Captured Solar Wind", *Science* **332**, 1528–1532, URL http://dx.doi.org/10.1126/science.1204636.

Nittler, L. R., Groopman, E., Bernatowicz, T. J., Croat, T. K., & Zinner, E. (**2011**), "X-ray Absorption Near-Edge Spectroscopy of Supernova Carbonaceous Grains", in "74th Annual Meeting of the Meteoritical Society, August 812, 2011, London, U.K.", volume 46, A178, Abstract #5361, Blackwell Publishing Ltd, URL http://dx.doi.org/10.1111/j.1945-5100.2011.01221.x.

Rauscher, T., Heger, A., Hoffman, R. D., & Woosley, S. E. (**2002**), "Nucleosynthesis In Massive Stars With Improved Nuclear And Stellar Physics", *The Astrophysical Journal* **576**, 323–348, URL http://dx.doi.org/10.1086/341728.

Stadermann, F. J., Croat, T. K., Bernatowicz, T. J., Amari, S., Messenger, S., Walker, R. M., & Zinner, E. (**2005**), "Supernova graphite in the NanoSIMS: Carbon, oxygen and titanium isotopic compositions of a spherule and its TiC sub-components", *Geochimica et Cosmochimica Acta* **69**, 177–188, URL http://dx.doi.org/10.1016/j.gca.2004.06.017.

Travaglio, C., Galli, D., Gallino, R., Busso, M., Ferrini, F., & Straniero, O. (**1999**), "Galactic Chemical Evolution of Heavy Elements: From Barium to Europium", *The Astrophysical Journal* **521**, 691–702, URL http://dx.doi.org/10.1086/307571.

Wopenka, B., Groopman, E., & Zinner, E. (**2011**), "Orgueil Low-Density Presolar Carbon aint Graphite but Glassy Carbon", in "74th Annual Meeting of the Meteoritical Society, August 812, 2011, London, U.K.", volume 46, A252, Abstract #5032, Blackwell Publishing Ltd, URL http://dx.doi.org/10.1111/j.1945-5100.2011.01221.x.

Zinner, E. & Jadhav, M. (**2012**), "Internal "Isochrones" Within Presolar Dust Grains", in "43rd Lunar and Planetary Science Conference", Abstract #1122, Lunar and Planetary Institute, Houston, URL http://www.lpi.usra.edu/meetings/lpsc2012/pdf/1122.pdf.

Chapter 5

NanoSIMS, TEM, and XANES studies of a Unique Presolar Supernova Graphite Grain

5.1 Preface

This chapter is based off of the peer-reviewed paper by: Groopman, E., Nittler, L. R., Bernatowicz, T., and Zinner, E. (**2014**). "NanoSIMS, TEM, and XANES studies of a Unique Presolar Supernova Graphite Grain" The Astrophysical Journal, **790**, 9

5.2 Abstract

We report on isotopic and microstructural investigations of a unique presolar supernova (SN) graphite grain, referred to as G6, isolated from the Orgueil CI chondrite. G6 contains complex heterogeneities in its isotopic composition and in its microstructure. Nano-scale secondary ion mass spectrometer isotope images of ultramicrotome sections reveal hetero-

geneities in its C, N, and O isotopic compositions, including anomalous shell-like structures. Transmission electron microscope studies reveal a nanocrystalline core surrounded by a tur-bostratic graphite mantle, the first reported nanocrystalline core from a low-density SN graphite grain. Electron diffraction analysis shows that the nanocrystalline core consists of randomly oriented 2–4 nm graphene particles, similar to those in cores of high-density (HD) presolar graphite grains from asymptotic giant branch stars. G6's core also exhibits evidence for planar stacking of these graphene nano-sheets with a domain size up to 4.5 nm, which was unobserved in the nanocrystalline cores of HD graphite grains. We also report on X-ray absorption near-edge structure measurements of G6. The complex isotopic- and micro-structure of G6 provides evidence for mixing and/or granular transport in SN ejecta.

5.3 Introduction

Presolar grains condensed in the ejecta of late-stage stellar objects such as asymptotic giant branch (AGB) stars and Type-II supernovae (SNe) prior to the formation of the Solar System. These grains survived travel through the interstellar medium, incorporation into the protosolar nebula, the formation of the Solar System, and entrainment in asteroids and comets. Primitive meteorites preserved this stardust, from where the grains may be isolated and studied in the laboratory. Each presolar grain is a stellar fossil of its progenitor star; microstructural and isotopic study allows for inferences regarding the formation conditions and nucleosynthesis processes in the parent star. Many different species of presolar minerals have been discovered (Zinner, 2014) including: nanodiamond (Lewis *et al.*, 1987), SiC

(Bernatowicz *et al.*, 1987), graphite (Amari *et al.*, 1990), silicates (Messenger *et al.*, 2003), oxides (Hutcheon *et al.*, 1994; Nittler *et al.*, 1994), and carbide subgrains (Bernatowicz *et al.*, 1991), which form in various types and/or outflow regions of stars.

Presolar graphite grains are generally quasi-spherical (Zinner *et al.*, 1990; Amari *et al.*, 1994); their internal crystal structures range from highly-ordered concentric shells of graphite (Bernatowicz *et al.*, 1996; Croat *et al.*, 2005) to more disrupted turbostratic graphite (Croat *et al.*, 2003, 2008). Presolar graphite spherules isolated from the Murchison (CM2) and Orgueil (CI1) carbonaceous chondrite meteorites have been divided into two major populations on the basis of density: high density (HD) ($\rho > 2.05$g/cm^3; $\rho = 2.09$–2.23 g/cm^3 for pure graphite) and low density (LD) ($\rho = 1.60$–2.05 g/cm^3) (Amari *et al.*, 1994; Jadhav *et al.*, 2006). Isotopic studies indicate that HD and LD grains generally formed in the outflows of AGB stars and SNe, respectively (Hoppe *et al.*, 1995; Zinner *et al.*, 1995; Bernatowicz *et al.*, 1996; Jadhav *et al.*, 2006). A relatively small number of HD graphite grains have been identified as having a SN or a Born-Again AGB star origin (Jadhav *et al.*, 2008, 2013a,b), though these grains will not be discussed further here. HD graphite spherules typically have an onion-like internal structure consisting of concentric sheets of well-ordered graphite (Bernatowicz *et al.*, 1996). In contrast, LD graphite grains are typically comprised of turbostratic graphite, with shorter, curved, discontinuous sheets, where the average distance between stacked graphene sheets is up to 5% larger than in ideal graphite (Croat *et al.*, 2008). Increased disorder in presolar graphite grains has been found to correlate with increased O content (Croat *et al.*, 2008). Approximately one third of HD graphite grains have been found to contain nanocrystalline cores consisting of randomly oriented graphene

sheets 3–4 nm in size that are surrounded by mantles of graphite (Bernatowicz *et al.*, 1996; Croat *et al.*, 2005). It has been suggested that these nanocrystalline cores formed when C was highly supersaturated in the stellar outflows where they formed, and the transition to longer-range order (e.g., mantling graphite) occurred when the number density of condensable C atoms diminished (Bernatowicz *et al.*, 1996). Since nanocrystalline cores are always found within mantles of well-graphitized carbon, and never vice versa or in an alternating pattern, these grains likely reflect monotonically changing physical and/or chemical environments in AGB outflows. Prior to the present work, there have been no reported findings of LD SN graphite grains containing nanocrystalline cores.

OR1d6m, described in Groopman *et al.* (2012), is the sixth sample mount of LD presolar graphite grains from the OR1d size/density fraction of the Orgueil CI chondrite ($\rho = 1.75$–1.92g/cm^3) (Jadhav *et al.*, 2006). OR1d6m contains grains with likely SN origins based upon Nano-scale Secondary Ion Mass Spectrometry (NanoSIMS) isotopic measurements. One grain, OR1d6m-6 ($\sim$6.5 μm in diameter, hereafter G6), was selected for further microanalytical and isotopic study in the NanoSIMS, Transmission Electron Microscope (TEM), and Scanning Transmission X-ray Microscope (STXM).

5.4   Methods

After bulk-grain NanoSIMS analysis (Groopman *et al.* (2012), Chapter 4), G6 was electrostatically "picked" off the mount with an electro-chemically-sharpened W needle and deposited in a drop of LR White™ hard resin at the bottom of a polyethylene SPI BEEM

1001 capsule. The capsule tapers pyramidally into a 1 mm × 1 mm square face. Before picking, the face was visually inspected under a microscope to ensure a minimal degree of roughness. Carbon fibers (50 μm × 10 μm) were deposited in the drop of resin and arranged around the grain to aid in locating G6 in the TEM and STXM. The capsule's tapered space was then completely filled with resin and cured for 24 hours in a vacuum oven at 70°C. Following the curing process, a steel screw was glued onto the base of the resin block with epoxy and the polyethylene capsule was removed. A glass knife was used to trim the square face of the resin block to a 250 μm × 250 μm square centered on the grain and fibers. The tip of the resin block was then ultramicrotomed into 70 nm-thick sections. The majority of microtomed sections were deposited on holey-C-coated Cu TEM grids for TEM and STXM analyses, while the remainder sections were deposited on a Si wafer for NanoSIMS isotope imaging (Groopman *et al.*, 2013). The latter were chosen to be from the center region of G6.

5.4.1 Secondary Ion Mass Spectrometry

Isotopic images of the microtome sections on the Si wafer were obtained with the Cameca NanoSIMS 50L at the Department of Terrestrial Magnetism, Carnegie Institution of Washington. Under primary Cs$^+$ bombardment, secondary ions of ^{16}O$^-$, ^{18}O$^-$, ^{12}C^{12}C$^-$, ^{12}C^{13}C$^-$, ^{12}C^{14}N$^-$, ^{12}C^{15}N$^-$, and ^{28}Si$^-$ were collected in multicollection mode. C$_2$ and CN signals were used to determine the ^{12}C/^{13}C and ^{14}N/^{15}N ratios, respectively. Single ions and molecular ions have different energy distributions, so measuring C$_2$ allows for better alignment with the CN secondary ions (DeGregorio *et al.*, 2013), which are commonly used for N-isotopic measurements by SIMS (Zinner *et al.*, 1987). Additionally, carbonaceous materials often

103

yield ion signals where $C_2^-/C^- > 1$, allowing for higher statistical precision. Isotope images were obtained over 5–15 μm raster areas, depending on the cross section size, of 256 pixels $\times$ 256 pixels with a dwell time of 10 ms/px. Typically 10–20 image frames were gathered per measurement or until the microtome section was sputtered away. Images were analyzed with the custom L'image software (L. R. Nittler, Carnegie Institution). The carbon fibers and resin were measured as standards.

5.4.2   TEM

Microtome sections on TEM grids were analyzed with a JEOL high-resolution JEM-2100F TEM, and a JEOL 2000FX TEM equipped with a NORAN ultra-thin window energy dispersive X-ray spectrometer (EDXS). Quantitative EDXS analysis was performed on all internal subgrains using the Cliff-Lorimer method (Cliff & Lorimer, 1975). Electron diffraction patterns were obtained on film in the JEM-2100F and were subsequently digitized. Radial profiles across the digitized diffracted electron intensity images were obtained with a modified version of the open source Diffraction Ring Profiler (Zhang *et al.*, 2011). The code was modified to use a polynomial + Lorentzian profile of the form:

$$c_0 + c_1 x + \frac{A}{2\pi} \times \frac{w}{(x - x_0)^2 + (w/2)^2} \tag{5.1}$$

to model the background diffracted intensity from the central spot, where $c_{0,1}$ are polynomial coefficients, A is the area under the Lorentzian profile, w is the full width at half maximum (FWHM), and x_0 is the median/center position. The user selects points on the

104

background profile, after which the background is fitted and subtracted. The polynomial-Lorentzian model provides a near-perfect match to the background diffraction intensity, substantially better than the Diffraction Ring Profiler's built-in pseudo-Voigt and power-law profiles. Individual diffraction peaks often are not symmetric, having tails toward higher reciprocal spacing. This characteristic is due both to instrumental broadening and to the fact that the patterns are obtained from finite, non-ideal crystals. Individual diffraction peaks were therefore fitted to an asymmetric Lorentzian profile (Eq. 5.4), utilizing nonlinear least-square minimization available through the Python package lmfit (Newville, 2013), where the FWHM, w, was allowed to vary sigmoidally according to an asymmetry parameter, a (Eq. 5.3):

$$L_{sym.} = \frac{A}{2\pi} \times \frac{w}{(x - x_0)^2 + (w/2)^2} \tag{5.2}$$

$$w(x) = \frac{2w_0}{1 + e^{-a(x-x_0)}} \tag{5.3}$$

$$L_{asym.} = \frac{A}{\pi} \times \frac{w_0/(1 + e^{-a(x-x_0)})}{(x - x_0)^2 + (w_0/(1 + e^{-a(x-x_0)}))^2} \tag{5.4}$$

adapted from Stancik & Brauns (2008). Note that when $a \neq 0$, the peak's median reciprocal space location is no longer identical with the location of the peak's maximum intensity. Additionally, w_0 is the full width at half the intensity at the median reciprocal distance, which is larger than the FWHM. To obtain the FWHM, one must substitute the location of the peak maximum into Eq. 5.3 or calculate it numerically from the fit. When $a = 0$, w becomes a constant and the Lorentzian returns to its symmetric form (Eq. 5.2). This form

of asymmetric Lorentzian is advantageous because it models peak tails very well and w is constrained between the values 0 and $2w_0$. Where two or more diffraction intensity peaks overlapped, all were fitted simultaneously, however only the largest peak was modeled as an asymmetric Lorentzian; the other peak(s) were fitted to symmetric Lorentzian profiles to reduce the number of fitting parameters.

Ceylon graphite was used as a calibration standard to determine instrumental broadening of electron diffraction peaks. Flakes of Ceylon graphite were ultrasonically dispersed in distilled water and the suspension was deposited on TEM grids. The invariant in-plane (100) and (110) diffracted intensity peaks were fitted to symmetric Lorentzian profiles to determine the FWHM and d-spacings. Due to the ultrasonic dispersion, most of the deposited Ceylon graphite was actually single- or few-layered graphene, i.e. there is little to no planar stacking. Therefore, in electron diffraction patterns the (002) reflection is nearly nonexistent; in Figure 5.1 this ring profile is labeled as "graphene".

5.4.3   STXM

After TEM analyses, sections of G6 were analyzed with the synchrotron-based STXM at Beamline 5.3.2.2 of the Advanced Light Source, Lawrence-Berkeley National Laboratory (Kilcoyne *et al.*, 2003). Monochromatic X-rays are generated by electrons transmitted through a dedicated bending-magnet, followed by a spherical-grating monochromator that allows for selection of photon energy up to 800 eV in steps as small as 0.1 eV. The beam is focused by Fresnel zone plate optics into a 25–40 nm spot size at the sample. A three-dimensional data "stack" in x × y × eV was generated by using an interferometer-controlled
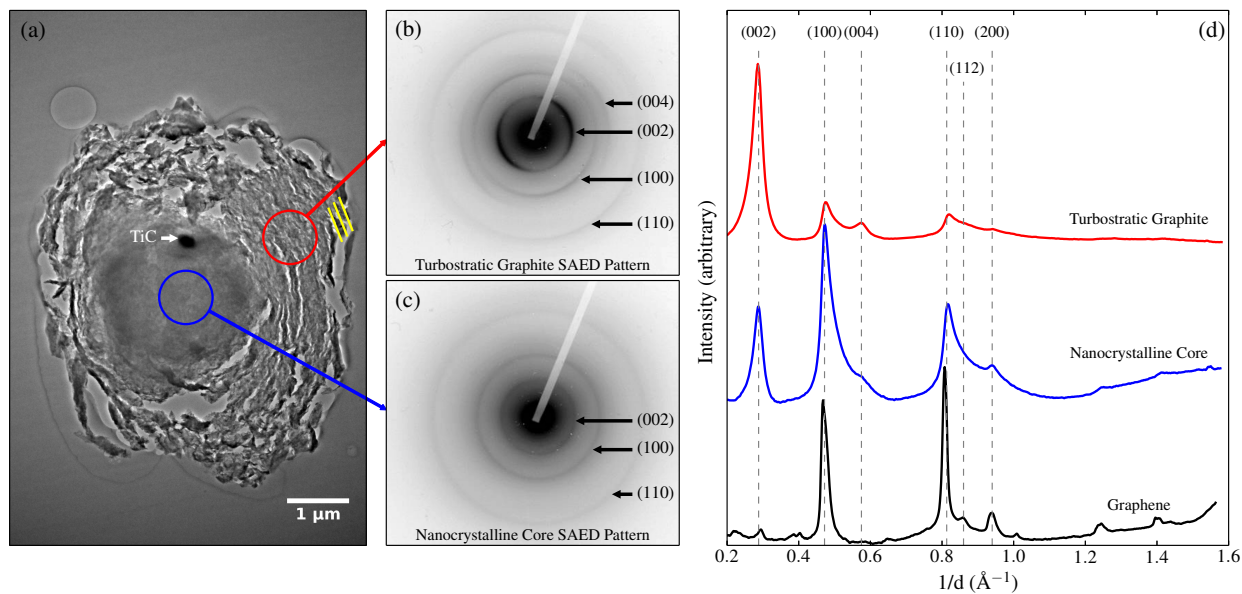
FIGURE 5.1: (a) TEM bright field (BF) micrograph of an ultramicrotome section of presolar graphite grain G6 containing a nanocrystalline core surrounded by turbostratic graphite. It is easy to distinguish between the two regions by visual inspection. A 265 nm TiC subgrain (darkly contrasting) is visible at the edge of the core region. Circles indicate regions where SAED patterns (b–c) were obtained on film with 60s exposures. Parallel lines indicate edge-on orientation of local graphitic planar stacking. (b) SAED pattern of the turbostratic graphite in reverse contrast for easier viewing. Diffracted intensity for (002) and (004) reflections is highest when planar stacking is parallel to the electron beam. Diffracted intensity for in-plane (100) and (110) reflections is largest orthogonal to the largest intensity for planar stacking. (c) SAED pattern of nanocrystalline core. All diffraction rings show no orientational bias, indicating that the core consists of randomly-oriented crystals. SAED pattern includes previously unobserved, but weak (002) reflection, indicating that crystals inside of the core exhibit some degree of planar stacking. (d) Diffraction ring profiles of (b–c), and graphene for calibration (SAED not shown). The graphene was ultrasonically-dispersed from Ceylon graphite and therefore consists of single- and multi-layered regions, hence the presence of a small (002) reflection. Individual profiles are normalized for visual effect; SAED patterns show the absolute intensities. The turbostratic graphite profile is dominated by the strong (002) reflection. The most intense reflection for the nanocrystalline core is the (100) in-plane reflection, comparable in intensity to the (100) reflection from turbostratic graphite (as seen on film), though a weaker (002) reflection is present. Based upon the (100) and (110) peak widths we estimate the average lateral particle size to be 2–4 nm, with a size of ~4.5 nm in the (002) stacking direction.

107

piezoelectric stage to raster the sample across the beam, and by stepping the energy up after each frame. The photon energy was increased in steps of 0.1 eV between 283 eV and 296 eV, across the C K-edge, while 0.5 eV steps were used in the pre- and post-edge regions due to time constraints. The absorbance, or optical density (OD), of the sample was calculated as $-\log(I/I_0)$, where I was the measured intensity through the sample and I_0 was the baseline intensity measured through a hole in the sample. Each pixel within the stack contains an X-ray absorption near-edge structure (XANES) spectrum.

Within the C K-edge region there are three diagnostic absorption features for graphite and aromatic carbon: a peak at 285.2 eV, corresponding to the 1s→2p π^* transition; a sharp peak at 291.5 eV, corresponding to the σ^* exciton; and a broader σ^* peak at 292.5 eV (Brühwiler *et al.*, 1995; Ahuja *et al.*, 1996; Brandes *et al.*, 2008). The π^* peaks were fitted using the same asymmetric Lorentzian profile described above for TEM diffraction patterns, which performs well in modeling the tail present above the peak absorption energy. Prior to fitting the π^* peaks, a linear fit to the pre-edge region between $270 - 282$ eV was subtracted from the spectra. The π^* peaks were fitted without modeling the C K-edge as an arctangent or step function. The aim was to compare the π^* peaks by utilizing as few parameters as possible. Additionally, ionization potentials for the relevant C bonds lie far enough above the aromatic π^* peak (Cody *et al.*, 1995), that they need not be subtracted from the spectrum to quantify the π^* resonance. Peak positions were calibrated using CO_2 gas prior to any measurements on G6.

Spectra from organic carbonaceous materials often contain other minor peaks in the region between the aromatic π^* and σ^* excitons, including those associated with 1s-π^* tran-

sitions in ketones (286.5 eV), aliphatics (287.3 – 288.1 eV), and carboxyl (288.4 – 288.7 eV) (Cody *et al.*, 2008; DeGregorio *et al.*, 2013). To fully deconvolve the spectra and quantify any minor peaks, a continuum step ionization potential for aromatic carbon was subtracted from the spectra. The continuum step was modeled as an error function (erf) of the form:

$$I = H\left[\frac{1}{2} + \frac{1}{2}\text{erf}\left(\frac{E - P}{2\ln(2) \times \Gamma}\right)\right] \tag{5.5}$$

(Stohr, 1992) where E is the energy, H is the height of the step, P is the ionization potential (290.3 eV for aromatic carbon (Cody *et al.*, 1995)), and Γ is the width of the step in eV. At energies higher than the ionization potential, the continuum step decays exponentially (Stohr, 1992), however this does not affect the deconvolution of minor peaks below the ionization potential. Γ is intrinsically linked to the instrumental resolution (Stohr, 1992) and has been chosen to be 1 eV in earlier work (e.g., Cody *et al.* (1995)). Deconvolutions of the nanocrystalline (core) and turbostratic graphite (mantle) spectra (see section 5.5.2) are illustrated in Figures 5.2b-c, where the spectra have been normalized to the area under the σ^* peaks. The asymmetric Lorentzian profiles described above (dashed red in the online version) and continuum steps located at 290.3 eV with widths of 1 eV (dashed black) are subtracted from the absorbance spectra (solid green online). Continuum step heights of 0.21 and 0.25 for the core and mantle, respectively, were chosen so that the residual spectrum (solid blue online) was minimized and non-negative. Graphite is composed of conjugated C, so the π molecular orbitals are delocalized above and below the graphene sheets, which results in a splitting of the main π^* peak into a large component at 285.2 eV (π^*_1) and

a smaller component (π^*_2) $\sim$4 eV higher in energy (Stohr, 1992; Cody *et al.*, 1995). The insets of Figures 5.2b-c show a magnified view of the minor peak region where two Gaussian profiles (dotted green online) were fitted simultaneously (dashed red online) to the residual spectrum. In both insets the smaller of the two peaks at higher energy is the π^*_2 peak. Given the contribution from the tail of the asymmetric Lorentzian profile fit to π^*_1, the areas under the minor peaks can be assumed to be lower limits. The drawback of this method is that the π^* peak and the minor peaks are not fitted simultaneously during the deconvolution, however we do not overestimate the ionization potential's contribution, given the asymmetric model of the π^* peak.
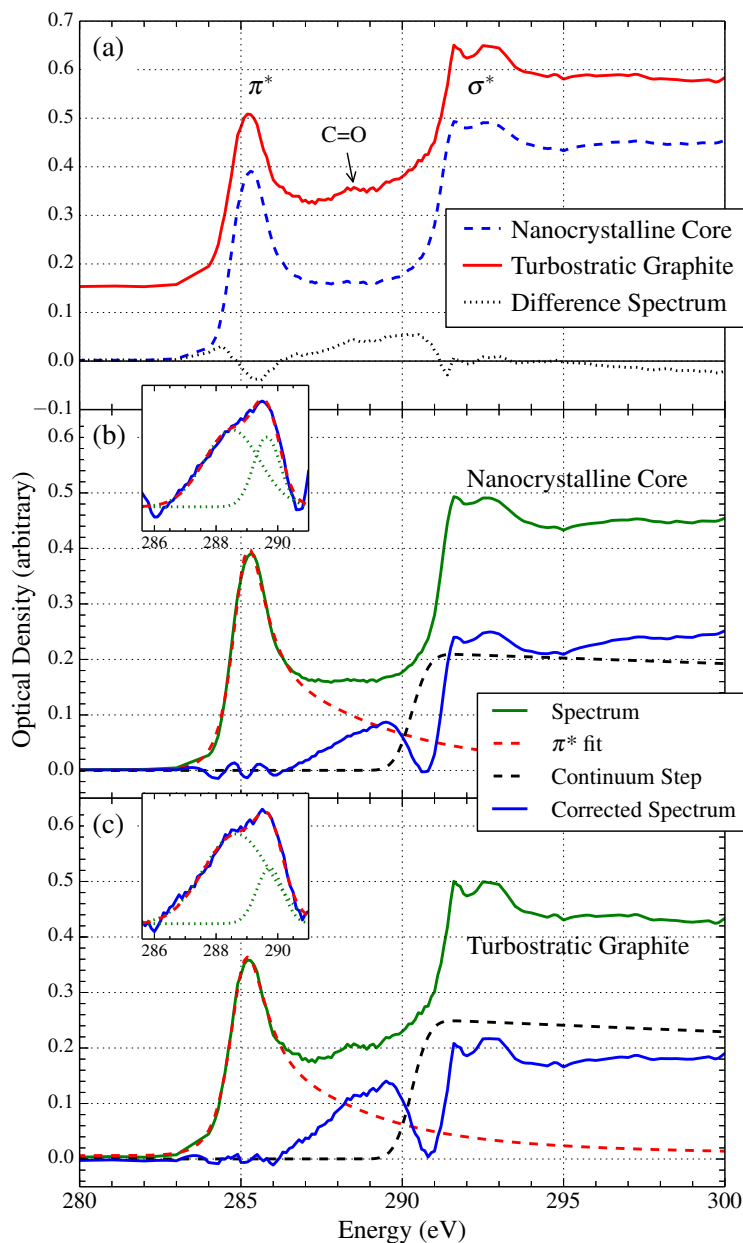
FIGURE 5.2: (a) C K-edge XANES spectra from the nanocrystalline core and mantling turbostratic graphite of presolar grain G6. Both the core and mantle exhibit graphite-like spectra, with aromatic 1s-π^*_1 transitions at 285.3 eV and 285.4 eV, respectively, and σ^* transitions both at 291.5 eV and 292.5 eV. The spectra are normalized to the area under the σ^* peaks. The primary difference between the spectra is the presence of a minor peak matching carboxyl in the turbostratic graphite spectrum. (b-c) Deconvolution of spectra from nanocrystalline core and turbostratic graphite, respectively. Insets show deconvolution of minor peaks into two Gaussian profiles. The smaller, higher-energy peak corresponds to the 1s-π^*_2 transition from conjugated π bonds. The peak at ~288.6 eV is twice as intense in the turbostratic graphite spectrum than in the spectrum from the nanocrystalline core, while the π^*_2 peaks are identical. See the electronic edition for a color version of this figure.

5.5 Results and Discussion

5.5.1 Isotopic Composition

Bulk isotopic measurements of G6 were made as a part of the analysis of the OR1d6m suite of LD graphite grains from Orgueil (Groopman *et al.* (2012), Chapter 4). A SN origin for G6 is indicated by large excesses in ^{12}C, ^{15}N, and ^{18}O relative to solar system isotopic compositions; a small excess in ^{28}Si; and a large ^{26}Mg excess indicating a very high initial abundance of short-lived ($t_{1/2}$ = 7.2E5 yrs.) ^{26}Al (Table 5.1). Presupernova massive stars consist of concentric shells of material defined by their most abundant elements and the different stages of nucleosynthesis which they experience (Woosley & Weaver, 1995) (see Figure 9 of Zinner (2014)). Of particular note to this study are three zones: the He/C zone, characterized by triple-α burning to ^{12}C and the ^{14}N(α,γ)^{18}O reaction; the He/N zone, characterized by the CNO cycle and a prodigious producer of ^{26}Al via hydrogen burning; and the Si/S zone, where ^{28}Si is abundantly produced via α-capture reactions: ^{16}O(α,γ)^{20}Ne(α,γ)^{24}Mg(α,γ)^{28}Si. Presolar grains from SNe, including SiC X grains, silicon nitride (Si$_3$N$_4$) grains, and LD graphite grains, often exhibit nucleosynthetic signatures from multiple zones, which implies that mixing in the ejecta must occur (Travaglio *et al.*, 1999). In isotopic surface images of G6, spatially-correlated extreme excesses in ^{18}O and ^{15}N were found, with δ^{18}O/^{16}O[1] up to 98,000‰ (^{16}O/^{18}O = 5; terrestrial = 499) and δ^{15}N/^{14}N up to 6,400‰ (^{14}N/^{15}N = 37; terrestrial = 272) (see Figure 1 of Groopman *et al.* (2012), Chapter

---

[1] δ^iX/^{j}X = 1000$\times$ $\left(\left(^i\mathrm{X}/^j\mathrm{X}\right)_{\mathrm{sample}}/\left(^i\mathrm{X}/^j\mathrm{X}\right)_{\mathrm{standard}} - 1\right)$

112

4). The extreme O and N isotopic ratios of these surface hotspots are much closer to the ratios of the He/C zone in models of 15–20 $M_\odot$ SNe (Rauscher *et al.*, 2002) than the ratios in the rest of the grain, which likely resulted from a mixture also including material from the overlying He/N zone. Spatially-correlated hotspots of excesses in ^{15}N and ^{18}O have in some cases been found to be carried by internal TiC subgrains (Groopman *et al.* (2012), Chapter 4), which are indicative of material from the inner portion of the He/C zone (Rauscher *et al.*, 2002; Bojazi & Meyer, 2014). In addition to excesses in ^{15}N and ^{18}O, excesses in ^{12}C, ^{42,43,44}Ca, and ^{49,50}Ti are also signatures of the He/C zone in models of 15–20 $M_\odot$ SNe, though once more G6's measured isotopic compositions are less anomalous than those predicted for pure He/C zone material (Table 5.1 and Figure 5.3). The relatively large errors in Ca isotope enrichments are due to the low abundance of Ca in G6. The large error in ^{50}Ti is due to isobaric interference from ^{50}Cr. The Cr$^+$ signal for G6 is large and overwhelmingly due to dichromate contamination from the acid dissolution of the meteorite (Amari *et al.*, 1994; Jadhav *et al.*, 2006). The inferred ^{26}Al/^{27}Al ratio for G6 is one of the highest ever observed in a presolar graphite grain and is indicative of material from the He/N zone, whose ^{26}Al/^{27}Al ratio is 10× higher than that of the He/C zone. G6's ^{26}Al/^{27}Al ratio, however, is even larger than the average predicted ratio in the He/N zone for 15–20 $M_\odot$ SNe. Excess ^{28}Si points to a contribution from the deep Si/S zone, however this excess is marginal in G6. Combined, G6's isotopic composition matches that of a mix of material predominantly from the He/C and He/N zones, which also have C/O > 1, a condition favorable for condensation of carbonaceous grains, with a small contribution from the Si/S zone.

In this work, three different microtome sections (G6A, 4.7 μm; G6C, 5.7 μm; G6I, 5.9
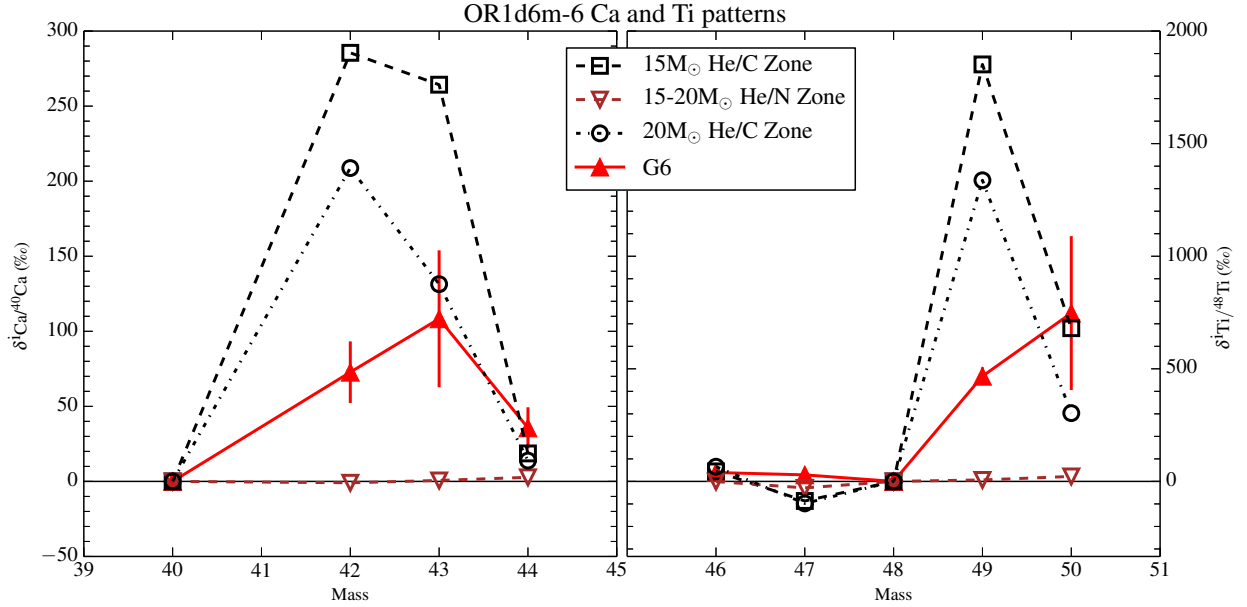
FIGURE 5.3: Ca and Ti isotope patterns (solid triangles, 1-σ errors) for presolar graphite grain G6. Dashed and dotted lines are average compositions from He/C and He/N zones in 15 and 20 M$_\odot$ Type-II SN models (Rauscher *et al.*, 2002). G6 exhibits typical neutron capture patterns in its Ca and Ti isotopic compositions. The relatively large error bars on the Ca δ-values are due to its low abundance. The large error bar on δ^{50}Ti is due to isobaric interference from ^{50}Cr; the Cr signal is dominated by contamination as a result of the acid separation process and resulted in a large correction on ^{50}Ti. The isotope patterns for both elements can be matched by the composition of a mixture of material from the He/C and He/N zones.

μm) on the Si wafer were isotopically imaged in the NanoSIMS. As seen in the prior bulk grain measurement, G6I is highly enriched in ^{18}O and ^{12}C, however this section is only slightly enriched in ^{15}N. The average isotopic compositions of G6A and G6C are slightly less anomalous than those of G6I. All sections are more anomalous in their average C isotopic compositions than the bulk grain, however the reverse is true for their N and O isotopic compositions. G6A, G6C, and G6I also contain large heterogeneities in their C, N, and O isotopic compositions, including regions whose C and N compositions are much more anomalous than in the bulk-grain measurements. These heterogeneities include both radial

114

gradients in the sections' C and O isotopic compositions (Figures 5.4d-e, 5.5a-b), similar to those observed previously in other SN graphite grains (Stadermann *et al.*, 2005; Groopman *et al.*, 2012), as well as small spatially-correlated hotspots of excesses in ^{15}N and ^{18}O likely corresponding to TiC subgrains (Figures 5.4b,c,f). G6A exhibits a smooth radial gradient in ^{12}C/^{13}C and a more irregular gradient in δ^{18}O/^{16}O, with ^{12}C/^{13}C ranging from 162 to 147 and δ^{18}O/^{16}O from 3000 to 510 (^{16}O/^{18}O from 125 to 330) moving from the section's center to its edge (Figure 5.5). G6C and G6I each contain a ~300 nm hotspot of excesses in ^{15}N and ^{18}O (indicated by arrows in Figures 5.4b,c,f and 5.5a), which correspond to the sizes and locations of TiC subgrains identified in the TEM (section 5.5.2). The G6C hotspot has a composition of δ^{18}O/^{16}O = 1840 ± 82‰ (^{16}O/^{18}O = 176 ± 5), and δ^{15}N/^{14}N = 1140 ± 138‰ (^{14}N/^{15}N = 127 ± 9); the G6I hotspot δ^{18}O/^{16}O = 2590 ± 93‰ (^{16}O/^{18}O = 139 ± 5), and δ^{15}N/^{14}N = 430 ± 86‰ (^{14}N/^{15}N = 190 ± 12). All of these values are lower bounds on the isotopic anomalies for the hotspots, as the ion signals for such small regions are diluted by sampling of the surrounding graphite. Groopman *et al.* (2012) showed that the surface of G6 was isotopically heterogeneous, with hotspots in ^{15}N and ^{18}O. These hotspots bias the original bulk grain measurement towards the composition of the presumed TiC subgrains and away from the composition of the less-anomalous graphitic material. Hence, the whole-grain N and O measurements closely match the isotopic composition of the TiC subgrains identified in the microtome sections. The most striking feature of the microtome section isotopic images is the complex O-isotopic heterogeneities in G6C and G6I, notably an ^{18}O-rich ring of material 2.7 μm × 3.3 μm in size (Figures 5.4b,c, 5.5a). This ring lies outside of G6's nanocrystalline core (1.5 μm, section 5.5.2), and is more anomalous than material

at smaller and larger radii. The ring structure has $\delta^{18}O/^{16}O = 2100 \pm 15‰$ ($^{16}O/^{18}O = 161 \pm 1$), with little variation in its C and N isotopic compositions relative to the rest of the section. Since G6A is a smaller section than G6C and G6I, and therefore further from the center of the grain, it is likely that the gradient observed in $^{16}O/^{18}O$ in this section is simply a cross-section of the O-anomalous shell. The ring features in G6C and G6I cover 2.6 and 2.3 μm^2 out of 25.7 and 27.0 μm^2, respectively. The center of microtome section G6C, 1 $\mu m \times$ 1.5 μm in size, is also more ^{18}O-enriched than the outer region of the grain (Figure 5.4c) with $\delta^{18}O/^{16}O = 1585 \pm 17‰$ ($^{16}O/^{18}O = 193 \pm 1$). The dimensions of grain section G6C and of its O-anomalous center are similar to those of the TEM sections which contain a cross section of the nanocrystalline core, though it cannot be unambiguously determined whether the core is present in this particular section. The center of G6I contains a hole near the identified TiC subgrain due to microtome damage, so the O isotopic composition of this region is unknown. It is unknown why the surface hotspots of excesses in ^{15}N and ^{18}O are so much more extreme than those found in G6's interior. In addition, it is interesting that the most ^{18}O-anomalous regions within G6's interior are not carried by TiC subgrains, but are intrinsic features of the graphite structure.

Radial gradients in isotopic composition have been attributed to secondary processes, such as isotopic equilibration with the grain's environment during its lifetime (e.g. in the protosolar nebula or in the meteorite parent body) (Stadermann *et al.*, 2005), and to primary processes, such as the changing isotopic composition of the stellar ejecta during grain formation (Groopman *et al.* (2012), Chapter 4). Changes in the grain's local formation environment could be due either to mixing in the stellar ejecta, and/or to the grain's tra-

jectory through regions with varying isotopic composition (Bernatowicz *et al.*, 2005). While isotopic equilibration of minor elements is a significant issue in HD presolar graphite grains (Hoppe *et al.*, 1995; Jadhav *et al.*, 2006, 2008; Zinner, 2014), LD grains typically retain large anomalies in N and O (Croat *et al.*, 2003; Stadermann *et al.*, 2005; Croat *et al.*, 2008). The observations of radial gradients in the C isotopic compositions of LD graphite grains suggest that isotopic equilibration is less prevalent than the minor isotope dilution observed in HD graphite grains (Groopman *et al.* (2012), Chapter 4). The turbostratic structure of LD graphite grains would presumably have to be disrupted in order to exchange a significant portion of the C with the surrounding environment. Additionally, the complex structure of the O anomalies in G6 suggests that isotopic equilibration is not the root cause, as isotopic diffusion should produce a smooth radial gradient. If a changing local isotopic environment is the cause for the ^{18}O-enriched ring, this would require that the isotopic composition changed non-monotonically.
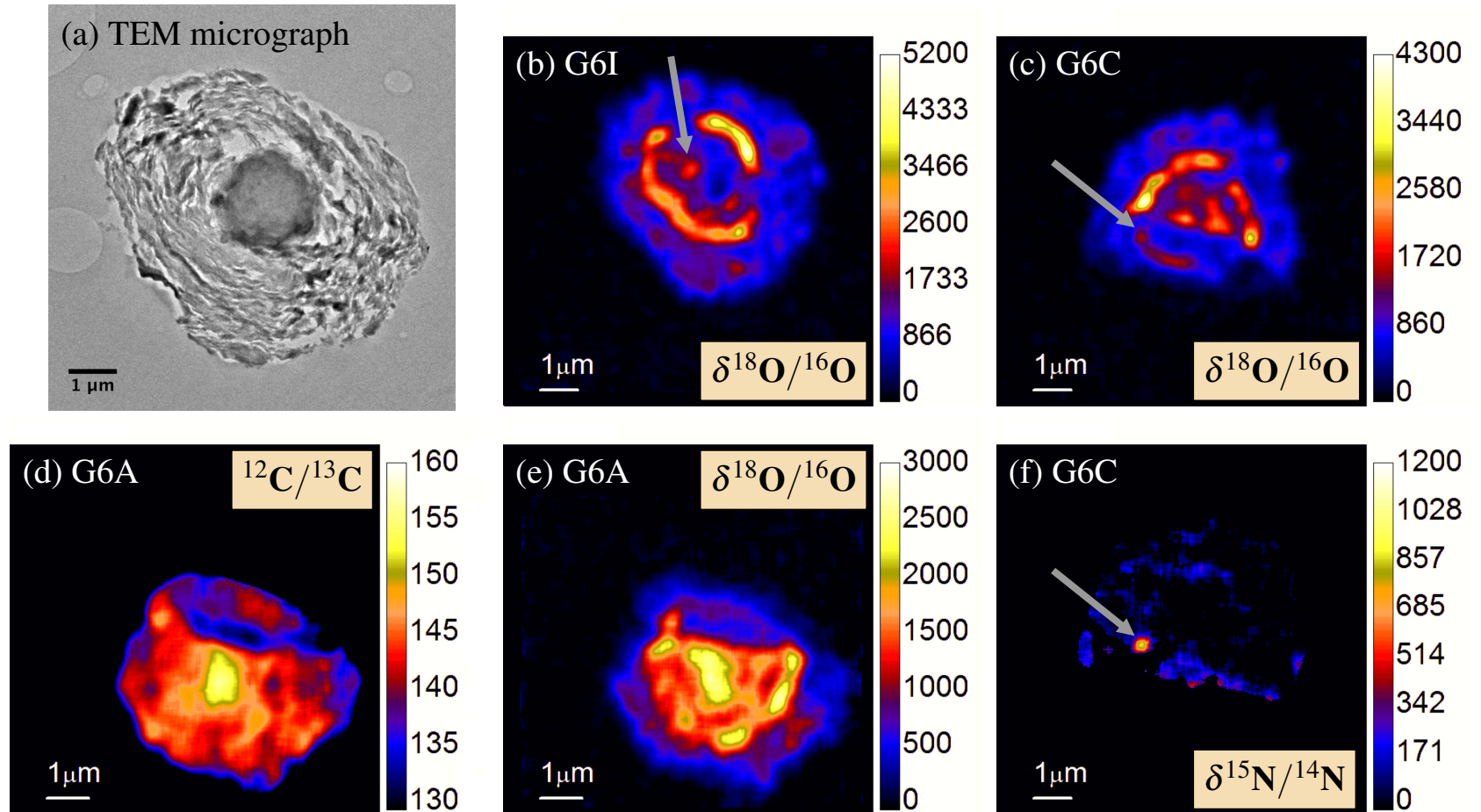
FIGURE 5.4: (a) TEM micrograph of an ultramicrotomed section of G6 containing a nanocrystalline core (1.5 μm) surrounded by turbostratic graphite. (b–f) Isotope ratio images of three different ultramicrotome sections on a Si wafer. Most notable are the complex $\delta^{18}O/^{16}O$ anomalies in (b,c,e), including ring-like structures $\sim$2.5 μm in diameter. The ring-like structures are likely a primary product of a non-monotonically changing formation environment. (b,c,f) Hotspots with correlated excesses in ^{18}O and ^{15}N, indicative of the presence of TiC subgrains (indicated by arrows, see Figure 5.5c for G6I $\delta^{15}N/^{14}N$ data). (d,e) Radial gradients in the C and O isotopic compositions (see Figure 5.5).
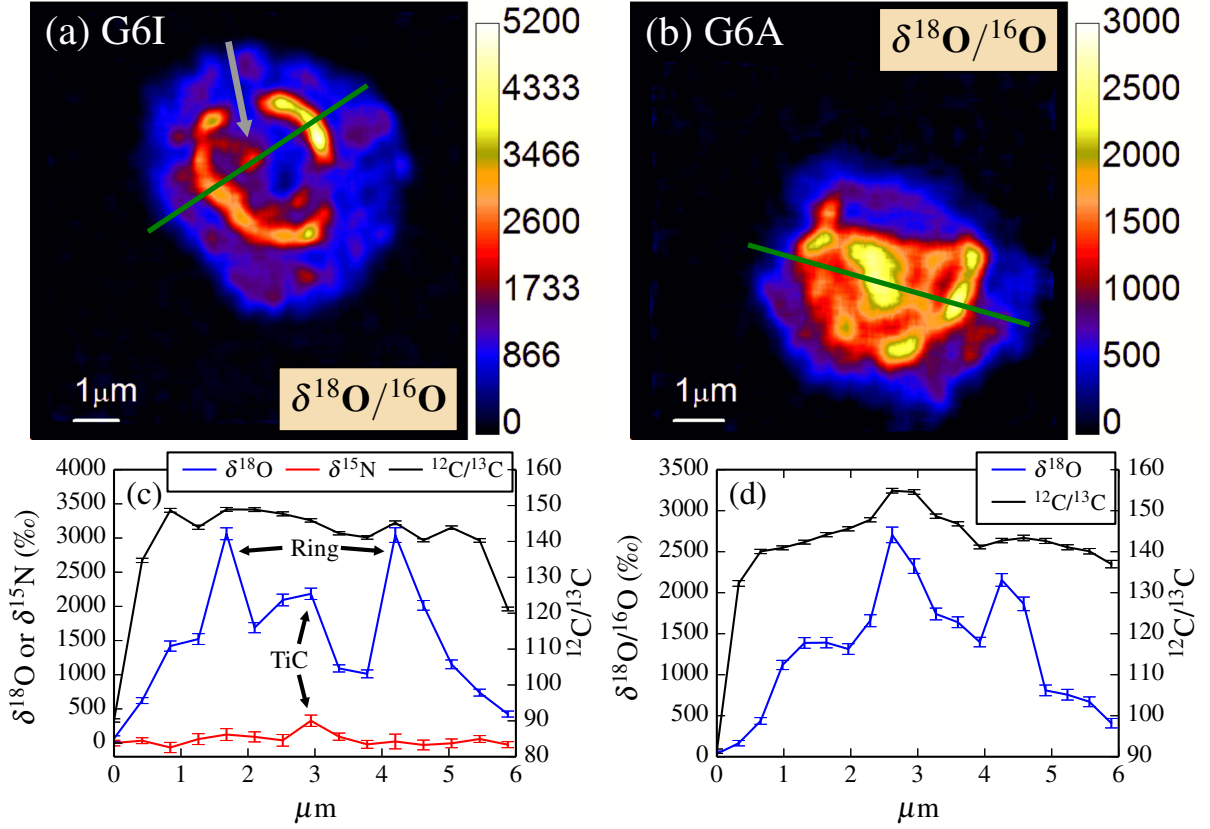
FIGURE 5.5: (a) & (b) O isotope ratio images of microtome sections G6I and G6A, respectively, of presolar graphite grain G6. (c) & (d) Isotopic line profiles of sections in (a) & (b) (green lines). (c) Shows a correlated excesses in ^{18}O and ^{15}N at 2.9 μm corresponding to a TiC subgrain (indicated by arrow in (a)). (d) Radial gradients in C and O isotopic compositions.

Recent three-dimensional simulations of Type-II SN explosions, based upon observations of SN 1987A, provide evidence of the large-scale mixing (fractions of AU) that occurs between inner and outer pre-SN zone material in the ejecta immediately following the explosion (Hammer *et al.*, 2010). In these models, material from inner zones is ejected asymmetrically through the outer zones, carrying with it a mix of heavy elements in addition to 50–70% H and He. There are considerable spatial variations in composition within individual ejecta.

Ni-Fe-Si and O-Ne-Mg "bullets" of material are separately ejected through the C-, He-, and H-rich outer zones, with the heavier knots of Fe-group materials, Ne, and Mg overtaking the O-rich knots, in effect partially inverting the pre-SN concentric shell structure. While such simulations cannot yet provide the resolution required to argue for grain-size-scale mixing, they do provide evidence that stellar ejecta varies spatially in isotopic/chemical composition. The Cassiopeia A SN remnant has also been identified as having resulted from an intrinsically asymmetric explosion, which caused the composition of ejecta to vary spatially (Rest *et al.*, 2011). It has been shown for AGB stars that grains are coupled to the radiation field of the star, which accelerates them through the gas via radiation pressure (Bernatowicz *et al.*, 2005). In effect, the grains act as miniature sails, being propelled faster than the surrounding gas, causing collisions with the gas in front of them. This could also be achieved from the reverse shock wave from a SN. With further simulations and observations of SNe, there exists the possibility for calculating grain condensation parameters - formation times, radii, velocities relative to gas - as done for AGB stars. More simply, these models provide evidence for the mixing of material between adjacent and non-adjacent SN zones. We do, however, remain far from the goal of connecting the isotopic signatures of pre-SN zones with the composition of presolar grains via high-spatial-resolution mixing models.

Isotope ratio images of microtome sections of G6 reveal numerous isotopic heterogeneities. These heterogeneities include spatially-correlated hotspots of excesses in ^{18}O and ^{15}N, which are likely carried by internal TiC subgrains (Stadermann *et al.*, 2005; Groopman *et al.*, 2012). This isotopic signature is indicative of material from the inner He/C zone in Type-II SN (Rauscher *et al.*, 2002; Bojazi & Meyer, 2014), while the bulk grain isotopic composition

is more similar to a mixture of material from the He/C and He/N zones (Rauscher *et al.*, 2002). The presence of radial gradients in ^{12}C/^{13}C, and ^{18}O-anomalous shell-like structures provide evidence for mixing in the SN ejecta. G6 likely condensed from a gas that changed isotopically in a non-monotonic fashion.

5.5.2 Microstructure

The majority of microtomed sections of G6 were deposited on holey-C-coated Cu TEM grids. Some 80% of the grain's volume is visible in the TEM; the remaining sections were deposited on Si wafers, overlie TEM grid bars, or lie outside the TEM's field of view. G6 is primarily composed of turbostratic graphite, characteristic of LD graphite grains from SNe (Croat *et al.*, 2003, 2008).

Nanocrystalline Core

Three sections were found to contain a 1.5 to 2 μm diameter core of nanocrystalline carbon surrounded by a mantle of turbostratic graphite. All other sections are comprised solely of turbostratic graphite. Nanocrystalline cores have only been reported previously from HD onion-type graphite grains from AGB stars (Bernatowicz *et al.*, 1996; Croat *et al.*, 2005).The nanocrystalline and turbostratic regions of G6 are visually distinct in the TEM (e.g., Figs. 5.1a; 5.6a,c,d; 5.8a–d). Selected area electron diffraction (SAED) patterns from the turbostratic graphite mantle (Figure 5.1b) closely match pure graphite. The dominant feature in the patterns is the (002) reflection ($d_{(002)}^{ideal} = 3.354$ Å), which corresponds to planar stacking of graphene sheets. The measured (002) d-spacing for turbostratic graphite is 4.9%

larger than that of an ideal crystal ($d_{(002)}^{turbo}$ = 3.52 Å), similar to previous observations of presolar graphite (Bernatowicz *et al.*, 1996; Croat *et al.*, 2005). This is corroborated by the measured d-spacing of the (004) reflection ($d_{(004)}^{ideal}$ = 1.677 Å; $d_{(004)}^{turbo}$ = 1.75 Å), which is 4.5% larger than ideal. The increase in bond length is partially due to the presence of O trapped between sheets, whose concentration has been shown to correlate with the degree of stacking disorder (Joseph & Oberlin, 1983; Croat *et al.*, 2008). Turbostratic graphite in LD Orgueil grains contains a higher concentration of O than their onion-like HD cousins, based upon EDXS measurements (Croat *et al.*, 2008). Due to the difficulty of quantifying low-Z elements, however, EDXS analysis can only elucidate relative differences in O abundances, not absolute concentrations. Graphane, a hydrogenated form of graphene, is another possible cause of the larger interplanar spacings observed in G6 (Daulton *et al.*, 2010). In graphane, sheets of C atoms are buckled as H bonds to the sheet surfaces, which pulls C atoms out of the plane. However, graphane also exhibits a 5% reduction in the hexagonal edge length relative to pure graphene because of sheet buckling. The other significant features in the SAED patterns are diffracted intensity peaks from the (100) and (110) reflections ($d_{(100)}^{ideal}$ = 2.131 Å, $d_{(110)}^{ideal}$ = 1.231 Å), which correspond to the hexagonal planar structure of graphene sheets. The measured d-spacings for these reflections are within 1% of ideal graphene for both turbostratic and nanocrystalline regions. As we do not observe any edge-length contraction in the turbostratic or nanocrystalline planar structure, we therefore conclude that O, and not H, is most likely responsible for increased interplanar spacings.

The orientation of a crystal structure relative to the electron beam direction will determine whether the Bragg reflection conditions are satisfied, i.e. if the beam is parallel to the

given crystal direction. When many crystals are randomly oriented about the beam axis, such as in powder diffraction, diffraction spots are distributed into rings. In microtomed sections of presolar graphite grains, graphite layers are oriented perpendicular to the section plane, so a SAED pattern will exhibit (002) rings with most of the diffracted intensity oriented in the direction where crystal layers are parallel to the beam (Figure 5.1). Since the (002) crystal direction is orthogonal to both (100) and (110), the direction along which the maximum diffracted intensity lies from these reflections is perpendicular to the maxima in the (002) ring. There is a clear planar stacking direction in the turbostratic graphite, visible upon inspection and inferred from the diffraction patterns. In contrast, the diffracted intensity in the core SAED patterns is isotropic for all reflections (see Figures 5.1c and 5.6c,d), implying that the core consists of small randomly oriented graphene sheets.

Unlike HD onion-type graphite grains with sharp boundaries between graphitic and nanocrystalline regimes, the transition in G6 occurs over a distance of $0.25 - 0.5$ μm. SAED patterns obtained across this transition confirm a weakening (002) peak with decreasing radius. The (002) diffraction peak never disappears in the core, however, in contrast to what was observed in the cores of onion-type graphite grains (Bernatowicz *et al.*, 1996; Croat *et al.*, 2005), though it is less intense than the (100) and (110) reflections (Figure 5.1d). This implies that coherent planar stacking is present among some graphene sheets within the core. The measured (002) d-spacing is 4.9% larger than ideal, similar to that of turbostratic graphite. All three microtome sections containing nanocrystalline material show the same (002) reflection feature, so it is unlikely to be due to a contribution from layers of turbostratic graphite included in the nanocrystalline region. Using the Scherrer formula D

= 1.84λ/2$\Delta\Theta$, where D is the mass-weighted mean particle diameter, λ is the wavelength of the electrons (0.0025 nm at 200 keV), and 2$\Delta\Theta$ is the angular FWHM of the diffraction peak, we estimate the lateral size of the nanocrystals to be 2–4 nm, similar to those obtained by (Bernatowicz *et al.*, 1996; Croat *et al.*, 2005), while the particle size predicted in the planar stacking direction (002) is $\sim$4.5 nm. Dark field (DF) images generated by using the diffracted intensity from the (002) reflection from the turbostratic graphite (Figures 5.6c-d) confirm that there are no large-scale graphitic features within the core which might have contributed to the presence of the small observed (002) reflection. There are, however, small intense spots in the DF images of the core, which may correspond to nanocrystals with planar stacking a few 10s of nm in size. These randomly-oriented "larger" nanocrystals may be responsible for the presence of the isotropic (002) reflection in SAED patterns of the core.

Subgrains

In G6, numerous TiC subgrains (125–265 nm, 2550 ppm) were observed, as well as Fe and Fe-Ni subgrains (15–75 nm, 75 ppm), and one SiC subgrain (70 nm, 30 ppm). The TiC subgrains have V/Ti ratios between 0.098 and 0.104, in general agreement with previous observations of TiC subgrains in SN graphite grains (Croat *et al.*, 2003). TiC and VC are isostructural, allowing for V to exist in solid solution within the TiC structure. Si was the only other trace element observed in the TiC subgrains, with concentrations varying between 0.5 and 6.9 at.%. The Fe-Ni subgrains have varying Ni/Fe ratios, between 0.023 and 0.253. The largest Fe-Ni grain (75 nm) is an intergrowth of two grains, the larger (65 nm) grain with a Ni/Fe ratio of 0.038, and the smaller (10 nm) grain with a Ni/Fe ratio of 0.253. The

larger Fe-Ni grain also contains 1.3 ± 0.2 at.% S, while the smaller grain does not contain any detectable S. The other Fe-Ni grains contain no detectable S, but do contain varying amounts of Si. One 28 nm grain with strong O and Si signals has a Ni/Fe ratio of 0.054 and a (Fe + Ni)/Si ratio of 1.9, resembling fayalitic olivine containing Ni in solid solution with Fe, although we cannot determine the stoichiometry without a quantified O concentration. This grain was too small to index with electron diffraction. Notably, no subgrains were found within the nanocrystalline core; the TiC subgrain shown in Figure 5.1a lies at the core's edge. The SiC subgrain was found near the edge of a microtome section, indicating that it was captured towards the end of G6's condensation. This SiC subgrain is comprised of an intergrowth of 3C and 2H polytypes, the lowest temperature polytypes of SiC (Figure 5.7), such as a SiC X grain described in Hynes *et al.* (2010), Figure 8. 17% of SiC grains studied by Daulton *et al.* (2003) consist of intergrowths of 2H and 3C polytypes, though only one such SiC X grain has been reported.

We also observed two graphite spherule subgrains in G6. The larger one is nearly 1 μm in diameter, with its own distinct nucleation center apparent via visual inspection and in DF images generated from (002) diffracted electron intensity (Figure 5.8). This graphite subgrain became stuck to the larger grain when G6 was only two μm in size and was mostly nanocrystalline. Turbostratic graphite layers continued to grow radially from the two different centers before the layers eventually unified around a common center. Despite the great abundance of metal and carbide subgrains within presolar graphite spherules, agglomerations of individual graphite grains remain quite rare, perhaps due to a low sticking probability between two comparably sized spherules. The second, smaller (300 nm) graphite subgrain

is present at the surface of G6 and was clearly captured by the larger grain. This particular subgrain stands out in DF images formed with diffracted electron intensity from the (100) and (110) reflections (Figure 5.9). The graphite layers of this subgrain are clearly misaligned with the concentric shells of turbostratic graphite which comprise this section of G6. Additionally, this graphite subgrain contains its own 40 nm × 20 nm TiC subgrain at its center (Figure 5.9d).

G6 contains a unique microstructure relative to other presolar graphite grains. To date it remains the only LD SN graphite grain to contain a nanocrystalline core surrounded by a mantle of turbostratic graphite. G6's core is also unique vis-à-vis cores found in HD graphite grains, as it contains evidence for planar stacking of small, otherwise randomly-oriented 2-4 nm sheets of graphene. The microstructural heterogeneities within G6 provide further evidence for a complex and changing formation environment.

5.5.3   Condensation

The lack of subgrains within G6's nanocrystalline core is potentially significant for our understanding of the grain's formation sequence, though it is not statistically rigorous. Metal and carbide subgrains have been found within nanocrystalline cores of HD graphite grains (K. Croat, personal communication, December 2013). Numerical simulations (Cadwell *et al.*, 1994) and laboratory observations (Bernatowicz *et al.*, 1996; Bernatowicz & Walker, 1997) have shown that refractory carbide grains, particularly TiC, can act as the nucleation point for graphite growth, which unambiguously imply that the TiC formed before graphite. The majority of TiC subgrains, however, have been found as inclusions, entrained as the graphite

grain grew. The condensation temperatures, and therefore condensation sequence, for carbonaceous materials including graphite and metal carbides are highly sensitive to the ambient pressures and C/O ratios in stellar ejecta (Lodders & Fegely, 1995; Bernatowicz *et al.*, 1996; Fedkin *et al.*, 2010) (Figure 5.10). As the formation of a nanocrystalline conglomerate in lieu of the formation of graphite purportedly requires a high supersaturation of C (Bernatowicz *et al.*, 1996), the C partial pressure would also be high, yielding a large local C/O ratio. Since the system was out of equilibrium, this does not necessarily translate to a higher formation temperature. Instead, nanocrystalline conglomerates likely formed very quickly once nucleation points became available. As the saturation of C decreased, the system fell into thermodynamic equilibrium where the carbides were able to form, followed by the turbostratic graphite. Recent laboratory investigations into the formation of carbon "soot balls" using PAH seeds (Contreras & Salama, 2013) may be applicable to the formation of nanocrystalline conglomerates. Using various carbonaceous seed molecules and extremely rapid cooling (temperature gradient of 3000K to 100K over a distance of 1.5–2.5 mm), Contreras & Salama (2013) "freeze" the plasma of seed molecules into conglomerates, whose end products can range up to microns in size. It should be noted, however, that this particular setup may not be ideal for the formation of carbonaceous particles with long-range crystalline order (100's of nm to 1 μm), which under stellar conditions can take months (Hoppe & Besmehn, 2002) or years (Bernatowicz *et al.*, 2005) to form.

Graphitization of carbonaceous materials has been found to decrease progressively with increasing oxidation (Joseph & Oberlin, 1983). Therefore, turbostratic graphite in LD grains likely required a higher relative O content in the parent gas than graphite found in HD grains,

and so the C/O ratio ought to be closer to one in the SN ejecta where G6 formed compared to the AGB star ejecta that produced the HD grains. This is corroborated by recent studies of refractory metal nuggets (RMNs) found within HD graphite grains (Croat *et al.*, 2013), which show that HD graphite grains form at higher temperatures than LD grains, which therefore requires a larger C/O ratio (see Figure 5.10). This also implies a large temporal change in the ambient C/O ratio within the SN ejecta, from C supersaturation while the nanocrystalline core forms to C/O $\sim$ 1 when the turbostratic graphite mantle forms. HD grains, with near-ideal onion-like graphite condensing over their nanocrystalline cores, would require higher C/O ratios in order to avoid the crystallographic disruption of entrained O. Alternatively, CO dissociation via UV radiation (Clayton, 2013) might potentially increase the amount of free O available even at larger bulk C/O ratios, which might contribute to the formation of turbostratic graphite in SN ejecta. However, it seems unlikely that UV dissociation of CO molecules would simultaneously not also disrupt C-C bonds. Additionally, the presence of a SiC subgrain near the surface of G6 implies that C/O $\sim$ 1 by the end of condensation.

Figure 5.10 also shows pressure and temperature (P-T) profiles (Fedkin *et al.*, 2010) derived from observations of clumpy ejecta from SN1987A from 60 to 777 days post-explosion (Wooden *et al.*, 1993). The profiles were derived assuming equilibrium thermodynamics and an average atomic mass of 16 in the ejecta (Fedkin *et al.*, 2010). The ejecta's P-T profile evolves from P $\sim 10^{-4}$ bar and T = 2000 K at day 60 to P = 8×10^{-9} bar and T = 500 K at day 777 (not shown in Figure 5.10). Also plotted are P-T profiles for the ejecta with the pressure reduced by factors of 10, 100, and 1000. For clumpy SN ejecta similar to those of

SN1987A, TiC would begin condensing at ∼1715 K and would only do so prior to graphite if the C/O ratio were less than ∼1.15. For lower-density ejecta, this formation sequence would be even more constrained. Based upon these observations and derived P-T profiles, it appears that presolar graphite grains from AGB stars and SNe may form under a similar set of physical conditions. These profiles do not take into account the specific mixture of gas and its effect upon the condensation temperature.

Based upon equilibrium condensation and observations of SN 1987A, SN graphite grains are constrained to form in the first few months to one year post explosion. The interpretation of ^{49}Ti excesses as originating from the decay of short-lived ^{49}V ($t_{1/2} = 330$ days) in some SiC X grains (Hoppe & Besmehn, 2002; Lin *et al.*, 2010) is in general agreement with this picture. Therefore the ejecta's chemical and isotopic changes as recorded in G6 must also have occurred on this timescale.

5.5.4   XANES

XANES spectra from both the turbostratic graphite and nanocrystalline core regions of G6 exhibit graphite-like features (Figure 5.2). The most dominant features include the π^* absorption, located at 285.3 eV and 285.4 eV for the mantle and core, respectively; and the σ^* absorption peaks located at 291.5 eV and 292.5 eV for both materials. The asymmetry parameters of the π^* peak shapes between the mantle and the core are the same. The core FWHM is 1.7 eV and the mantle FWHM is 1.9 eV, while the median energies of the peaks are 285.7 eV and 285.8 eV, respectively. It has been shown for polyaromatic hydrocarbons that as the domain size grows, i.e. as rings are added, discrete π^* resonances around 285 eV begin

to overlap and combine to form a single peak such as that observed in graphite (Brandes *et al.*, 2008; Cody *et al.*, 1995; Schwarz *et al.*, 1987). Additionally, decreasing domain size and amorphization of C smooth out the σ^* peaks and reduce the intensity of the π^* absorption (Gago *et al.*, 2001). The domain sizes of the core's nanocrystalline material, determined by electron diffraction, are large enough to retain strong π^* and σ^* absorbances. The primary difference between spectra of the mantle and core is that the mantle spectrum contains a carboxyl peak (288.6 eV) (Figure 5.2a). This may be attributed to a higher concentration of O in the region where turbostratic graphite formed. From this we can also infer that some portion of the O in the turbostratic region is strongly bonded to the disrupted graphite. From comparison of the carboxyl feature in the turbostratic graphite, which is apparent in all cross sections, to O isotope images detailed above, we can be confident that this peak is not due to a contaminant, as the turbostratic graphite contains the most O-anomalous regions within G6. The peaks at ∼288.6 eV from the deconvolved turbostratic and nanocrystalline spectra differ in magnitude by a factor of two, while the π^*_2 peaks have the same height (Figures 5.2b-c insets).

5.6 Conclusions

Correlated NanoSIMS, TEM, and XANES studies of the Orgueil LD graphite grain G6 have revealed a wonderfully rich and unique SN graphite grain with a complex formation history. Isotopic and structural heterogeneities throughout the grain imply that G6's progenitor ejecta evolved chemically and isotopically over the timescale of months as the grain

130

condensed. The magnitude and structure of isotopic and compositional heterogeneities leave little doubt that they are the product of primary formation and are not caused by secondary alteration or isotopic equilibration. To account for the observed O-anomalous shell, the O isotopic composition of G6's local environment would have had to change by a factor of 3–4 non-monotonically during its formation. These observations may provide evidence for fine-scale mixing in SN ejecta or a mechanism for grain transport through more coarsely mixed ejecta.

Acknowledgements

FIGURE 5.6: (a) TEM bright field (BF) image of slice of presolar graphite grain G6. (b) A schematic electron diffraction pattern (intensities and radii not to scale) from a selected area of turbostratic graphite shown in (a). (c) and (d) are dark field (DF) TEM images generated by diffracted electrons from the (002) reflection, selected by an objective aperture at different angles (circles in (b)). The resulting regions of high intensity in the DF images are those where edge-on planar stacking of graphite is parallel to the selected angle of the electron beam (shown with parallel lines). Regardless of the angle selected for generating DF images, the core region remains uniformly intense, indicating an absence of long-range stacking order. Small bright spots are visible within the core, which may be due to larger nanocrystals (10s of nm) within the core; a distribution of these larger nanocrystals may be responsible for the (002) reflections observed in core diffraction patterns (Figures 5.1c–d). The intensity of the core region is on average greater than that of turbostratic graphite orthogonal to the electron beam, implying that there exists some component of (002) stacking in small particles throughout the core.

132
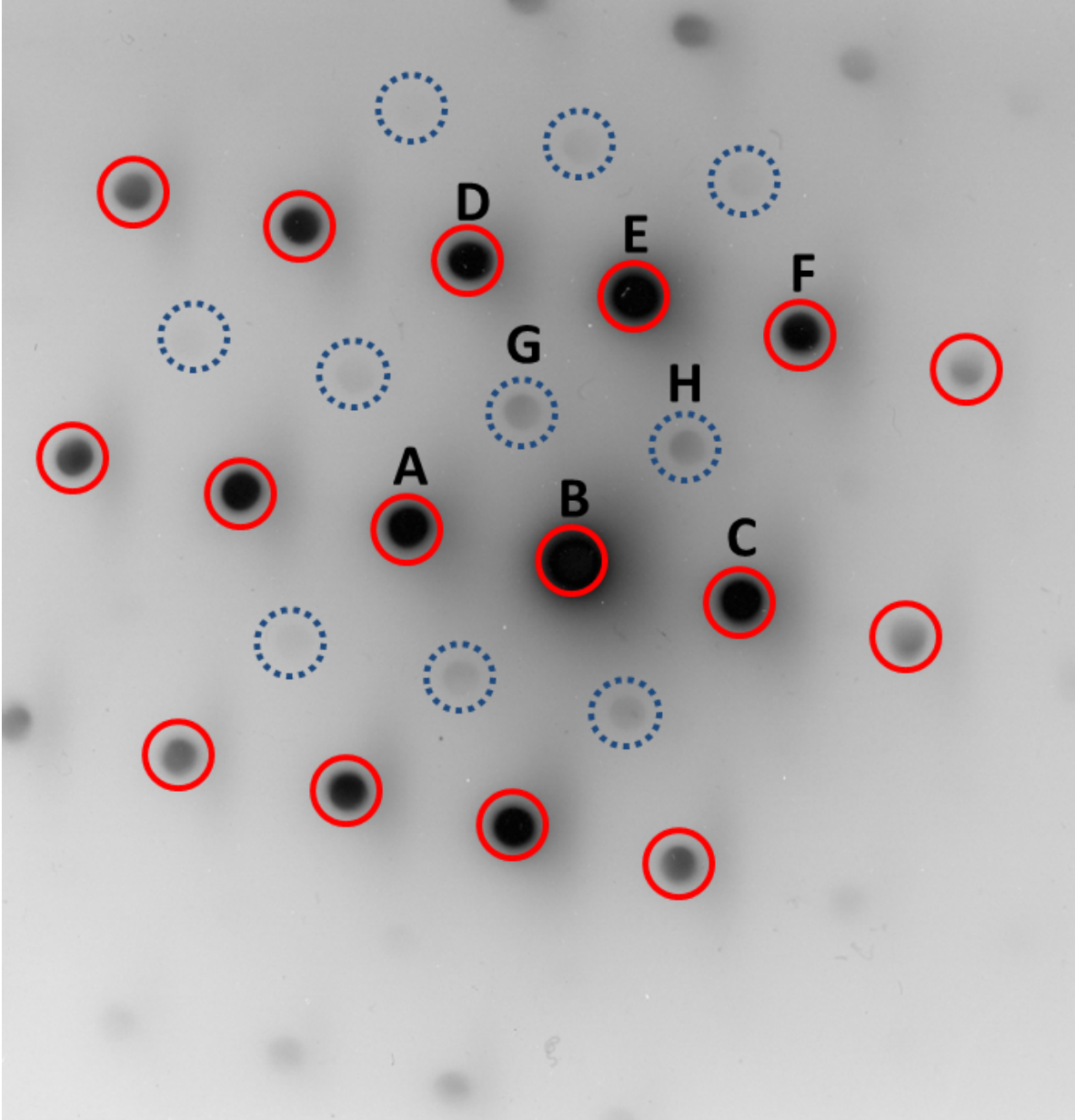
FIGURE 5.7: Diffraction pattern from a SiC subgrain within presolar graphite grain G6 showing an intergrowth between the 3C-SiC and 2H-SiC polytypes. Dark diffraction spots (solid red circles) index to both the [112] zone of 3C-SiC and the [0001] zone of 2H-SiC. These diffraction spots are part of the {11$\bar{1}$} plane of 3C-SiC and the {10$\bar{1}$0} plane of 2H-SiC. As in Hynes *et al.* (2010), the nominal 6% difference in d-spacings expected between the d-spacings of these spots is not apparent. Spots indicated by dashed circles (blue) only index to the [0001] zone axis of 2H-SiC. Letters above certain spots correspond to Miller Indices: A = ($\bar{1}\bar{1}$1)/($\bar{1}$010); B = (000)/(0000); C = (11$\bar{1}$)/(10$\bar{1}$0); D = ($\bar{3}$11)/($\bar{2}$200); E = ($\bar{2}$20)/($\bar{1}$2$\bar{1}$0); F = ($\bar{1}$3$\bar{1}$)/(02$\bar{2}$0); G = ($\bar{1}$100); H = (01$\bar{1}$0). Adapted from Figure 8 of Hynes *et al.* (2010).
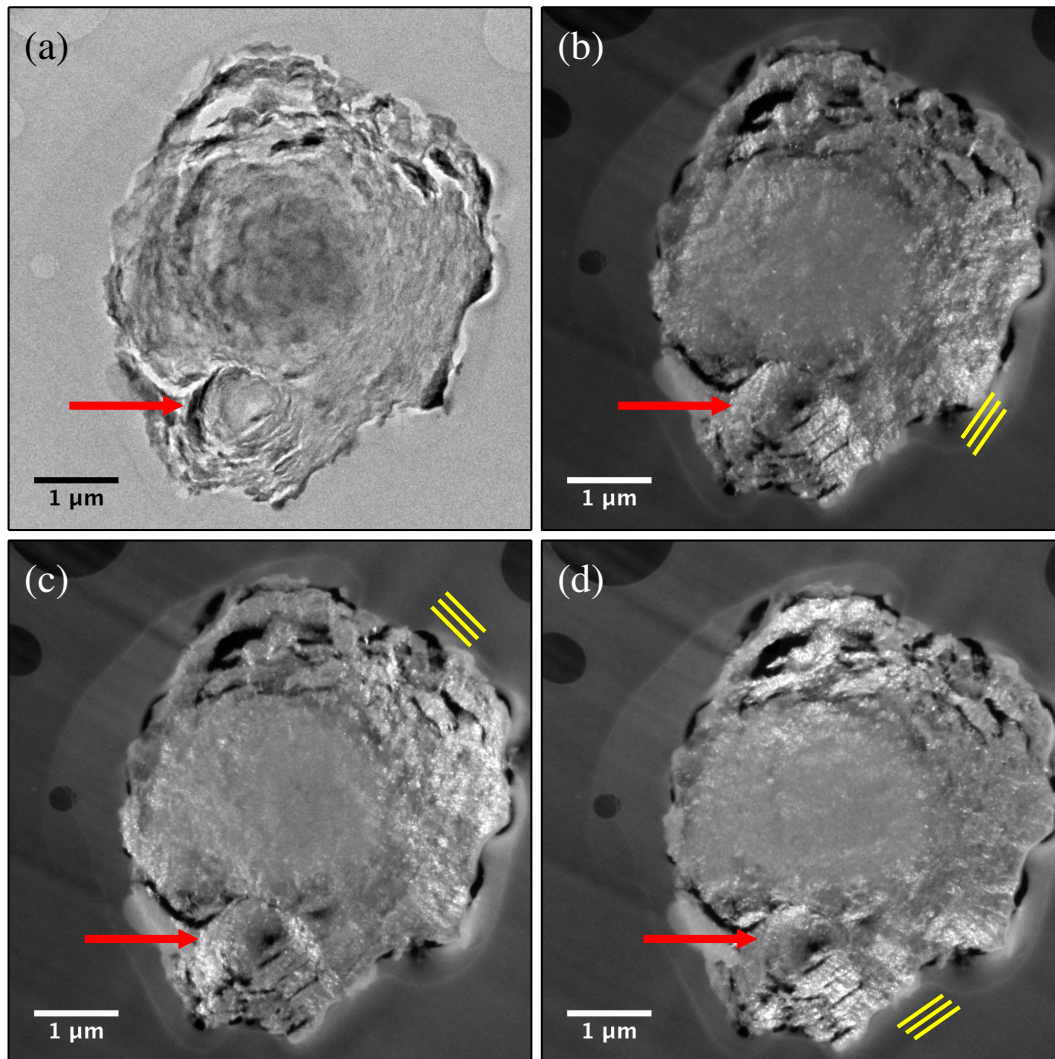
FIGURE 5.8: (a) TEM Bright field (BF) TEM micrograph of a section of presolar graphite grain G6. (b–d) Dark field (DF) images generated with diffracted electrons from the (002) reflection at three different angles (see Figure 5.6). G6's nanocrystalline core is visible in the center-left of the section. Concentric shells of turbostratic graphite, which make up the bulk of G6, clearly have two distinct centers: the largest shells are centered on the nanocrystalline core; directly below the core in the images is a second nucleation center around which smaller shells of turbostratic graphite formed (indicated by arrows). These likely existed as individual carbonaceous grains before they adhered to one another in the stellar ejecta. At the time of cohesion, G6 was predominantly nanocrystalline, while the smaller grain was turbostratic. Subsequently deposited turbostratic graphite grew around the pair. Despite their coevolution, graphite subgrains within larger presolar graphite grains are rare (Croat *et al.*, 2008).
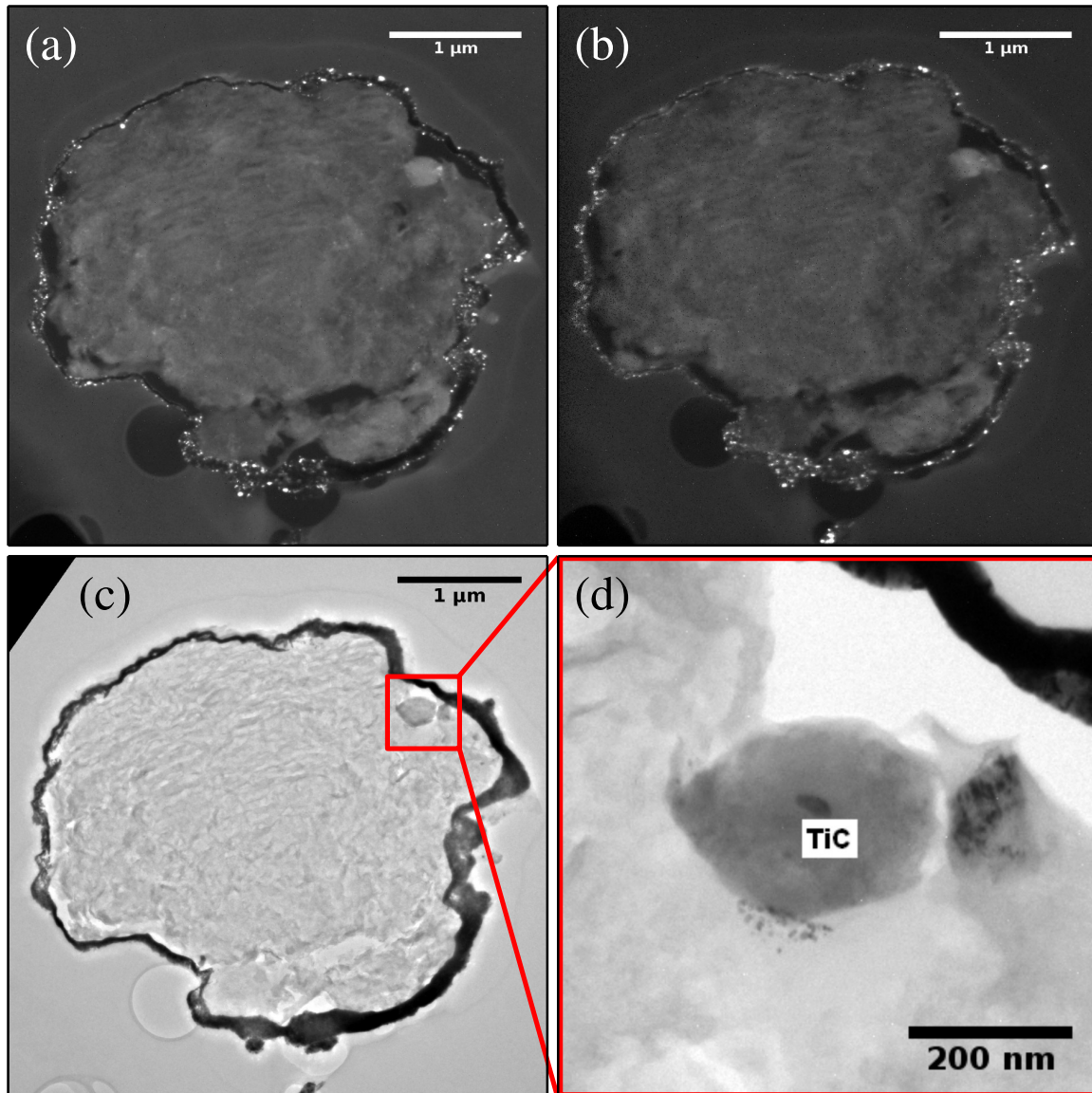
FIGURE 5.9: (a) and (b) Dark field (DF) images generated with diffracted electrons from the (110) and (100) reflections, respectively, of a section of G6, and (c) the corresponding bright field (BF) image. A small graphitic inclusion is clearly visible in the DF images as its stacking direction is misaligned with the parent grain; it is also clearly visible due to diffraction contrast in BF imaging [boxed in (c)]. Upon closer inspection, this graphite subgrain was found to contain a TiC subgrain near its center (d). The black rim around the section is redeposited Au from NanoSIMS analysis.
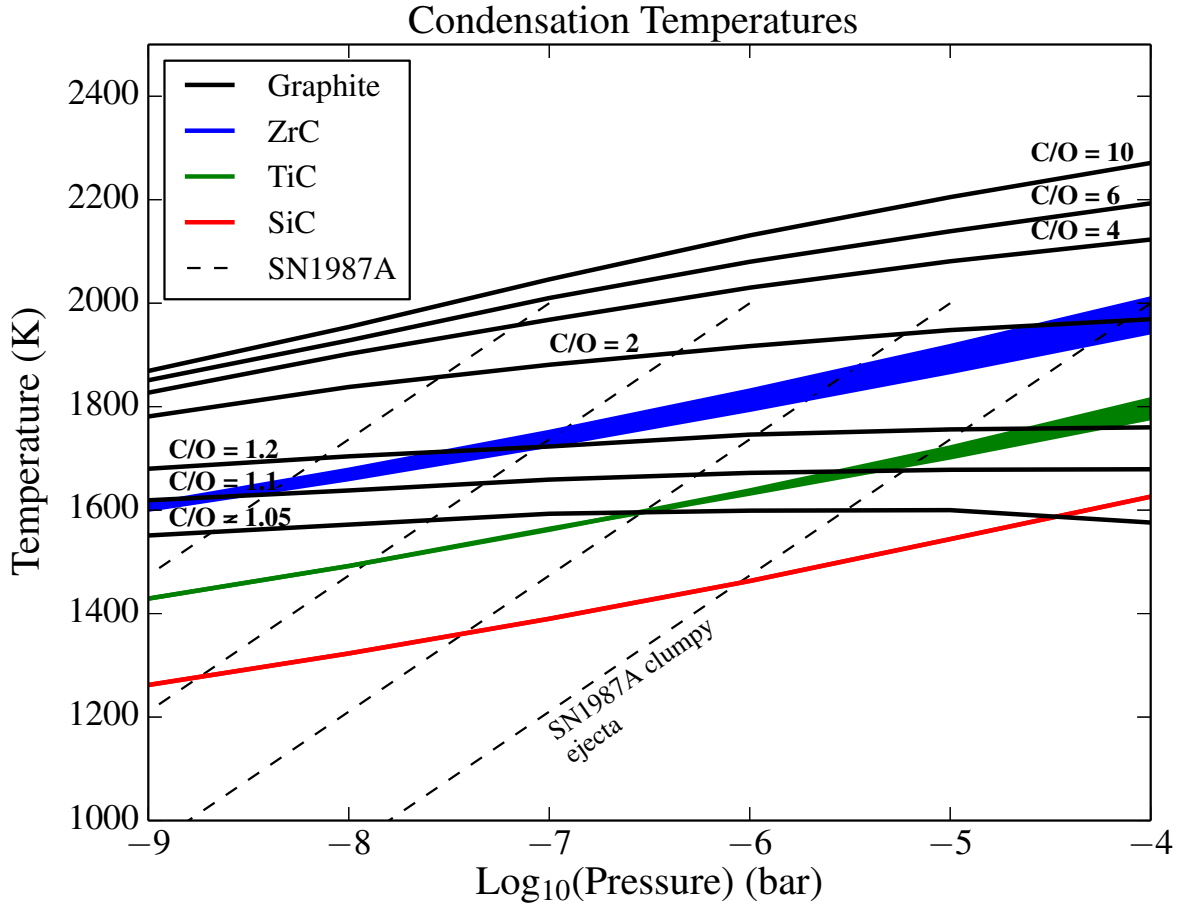
FIGURE 5.10: Adapted from Bernatowicz *et al.* (1996) and Fedkin *et al.* (2010); condensation data from Lodders & Fegely (1995); SN1987A observations from Wooden *et al.* (1993). Condensation temperatures (T) for carbonaceous materials at different ambient pressures (P) and C/O ratios. The onset T for graphite condensation is highly dependent on the ambient C/O ratio, while the carbides are more sensitive to the ambient P. Envelopes for ZrC (blue) and TiC (green) illustrate the range of T for a range of C/O ratios. At C/O ratios close to 1, TiC condenses prior to graphite for pressures above 10^{-7} bar. SiC (red) can only form prior to graphite at relatively high P. Dashed curves are P-T profiles that Fedkin *et al.* (2010) derived (for mean atomic weight of 16) from Wooden *et al.* (1993) observations of SN1987A's clumpy ejecta by reducing P by factors of 10, 100, and 1000 (right to left). The P of SN1987A's clumpy ejecta dropped from $\sim 10^{-4}$ bar on day 60 to $\sim 8 \times 10^{-9}$ bar on day 777 (T = 500K, not shown). These P-T profiles match well the range of temperatures and pressures required to describe subgrain abundances in presolar graphite grains.

TABLE 5.1: OR1d6m-6 isotopic composition.

Ratio	Bulk Grain[†]	Error (1σ)	Average G6I	Error (1σ)	Terrestrial	He/C Zone[††]	He/N Zone[††]
^{12}C/^{13}C	**113**	1	**143**	1	89	35,000	4
δ^{15}N/^{14}N	**872**	171	**38**	18	0	9,100	-990
δ^{18}O/^{16}O	**2057**	74	**1327**	14	0	553,400	-970
δ^{29}Si/^{28}Si	**-60**	16	–	–	0	307	1
δ^{30}Si/^{28}Si	-13	13	–	–	0	342	0
δ^{25}Mg/^{24}Mg	9	19	–	–	0	143	-800
δ^{26}Mg/^{24}Mg	**27,600**	272	–	–	0	893	462
^{26}Al/^{27}Al	**7.66E-01**	1.50E-03	–	–	0	0.02	0.2
δ^{42}Ca/^{40}Ca	**73**	21	–	–	0	286	-1
δ^{43}Ca/^{40}Ca	**108**	46	–	–	0	264	1
δ^{44}Ca/^{40}Ca	**36**	14	–	–	0	19	3
δ^{46}Ti/^{48}Ti	39	26	–	–	0	44	-1
δ^{47}Ti/^{48}Ti	29	28	–	–	0	-87	-29
δ^{49}Ti/^{48}Ti	**467**	40	–	–	0	1,900	7
δ^{50}Ti/^{48}Ti*	**748**	342	–	–	0	680	22

[†] Bold values removed from normal by more than 2σ.
[††]Average zone composition from 15M$_\odot$ SN model (Rauscher *et al.*, 2002)
* 60% correction from ^{50}Cr isobaric interference.

Bibliography

Ahuja, R., Brühwiler, P. A., Wills, J. M., Johansson, B., Mårtensson, N., & Eriksson, O. (**1996**), "Theoretical and experimental study of the graphite 1s x-ray absorption edges", *Physical Review B* **54**, 14396–14404, URL http://journals.aps.org/prb/pdf/10.1103/PhysRevB.54.14396.

Amari, S., Anders, E., Virag, A., & Zinner, E. (**1990**), "Interstellar graphite in meteorites", *Nature* **345**, 238–240, URL http://dx.doi.org/10.1038/345238a0.

Amari, S., Lewis, R. S., & Anders, E. (**1994**), "Interstellar grains in meteorites: I. Isolation of SiC, graphite and diamond; size distributions of SiC and graphite", *Geochimica et Cosmochimica Acta* **58**, 459–470, URL http://dx.doi.org/10.1016/0016-7037(94)90477-4.

Bernatowicz, T., Fraundorf, G., Ming, T., Anders, E., Wopenka, B., Zinner, E., & Fraundorf, P. (**1987**), "Evidence for interstellar SiC in the Murray carbonaceous meteorite", *Nature* **330**, 728–730, URL http://dx.doi.org/10.1038/330728a0.

Bernatowicz, T. & Walker, R. (**1997**), "Ancient Stardust in the Laboratory", *Physics Today* **27**, 26–32, URL http://dx.doi.org/10.1063/1.882049.

Bernatowicz, T. J., Akande, O. W., Croat, T. K., & Cowsik, R. (**2005**), "Constraints On Grain Formation Around Carbon Stars From Laboratory Studies Of Presolar Graphite", *The Astrophysical Journal* **631**, 988–1000, URL http://dx.doi.org/10.1086/432599.

Bernatowicz, T. J., Amari, S., Zinner, E. K., & Lewis, R. S. (**1991**), "Interstellar grains within interstellar grains", *The Astrophysical Journal* **373**, L73–L76, URL http://dx.doi.org/10.1086/186054.

Bernatowicz, T. J., Cowsik, R., Gibbons, P. C. ., Lodders, K., Jr., B. F., Amari, S., & Lewis, R. S. (**1996**), "Constraints On Stellar Grain Formation From Presolar Graphite In The Murchison Meteorite", *The Astrophysical Journal* **472**, 760–782, URL http://dx.doi.org/10.1086/178105.

Bojazi, M. & Meyer, B. (**2014**), "Explosive Nucleosynthesis of 15N in a Massive Star Model", *Physical Review C* **89**, 025807, 1–19, URL http://dx.doi.org/10.1103/PhysRevC.89.025807.

Brandes, J. A., Cody, G. D., Rumble, D., Haberstroh, P., Wirick, S., & Gelinas, Y. (**2008**), "Carbon K-edge XANES spectromicroscopy of natural graphite", *Carbon* **46**, 1424–1434, URL http://dx.doi.org/10.1016/j.carbon.2008.06.020.

Brühwiler, P. A., Maxwell, A. J., Puglia, C., Nilsson, A., Andersson, S., & Mårtensson, N. (**1995**), "Pi-star and sigma-star Exitons in C 1s Absorption of Graphite", *Physical Review Letters* **74**, 614–617, URL http://dx.doi.org/10.1103/PhysRevLett.74.614.

Cadwell, B. J., Wang, H., Feigelson, E. D., & Frenklach, M. (**1994**), "Induced nucleation of carbon dust in red giant stars", *The Astrohpysical Journal* **429**, 285–299, URL http://dx.doi.org/10.1086/174318.

Clayton, D. D. (**2013**), "Analytic Approximation of Carbon Condensation Issues in Type II Supernovae", *The Astrohpysical Journal* **762**, 5–16, URL http://dx.doi.org/10.1088/0004-637X/762/1/5.

Cliff, G. & Lorimer, G. W. (**1975**), "The quantitative analysis of thin specimens", *Journal of Microscopy* **103**, 203–207, URL http://dx.doi.org/10.1111/j.1365-2818.1975.tb03895.x.

Cody, G. D., Ade, H., Alexander, C. M. O., Araki, T., Butterworth, A., Fleckenstein, H., Flynn, G., Gilles, M. K., Jacobsen, C., Kilcoyne, A. L. D., Messenger, K., Sandford, S. A., Tyliszczak, T., Westphal, A. J., Wirick, S., & Yabuta, H. (**2008**), "Quantitative organic and light-element analysis of comet 81P/Wild 2 particles using C-, N-, and O--XANES", *Meteoritics & Planetary Science* **43**, 353–365, URL http://dx.doi.org/10.1111/j.1945-5100.2008.tb00627.x.

Cody, G. D., Botto, R. E., Ade, H., Behal, S., Disko, M., & Wirick, S. (**1995**), "Inner-Shell Spectroscopy and Imaging of a Subbituminous Coal: In-Situ Analysis of ORganic and Inorganic Microstructure Using C(1s)-, Ca(2p)-, and Cl(2s)-NEXAFS", *Energy & Fuels* **9**, 525–533, URL http://dx.doi.org/10.1021/ef00051a018.

Contreras, C. S. & Salama, F. (**2013**), "Laboratory Investigations of Polycyclic Aromatic Hydrocarbon Formation and Destruction in the Circumstellar Outflows of Carbon Stars", *The Astrophysical Journal Supplement Series* **208**, 6–22, URL http://stacks.iop.org/0067-0049/208/i=1/a=6.

Croat, T. K., Berg, T., Bernatowicz, T., Groopman, E., & Jadhav, M. (**2013**), "Refractory metal nuggets within presolar graphite: First condensates from a circumstellar environment", *Meteoritics & Planetary Science* **48**, 686–699, URL http://dx.doi.org/10.1111/maps.12093.

Croat, T. K., Bernatowicz, T., Amari, S., Messenger, S., & Stadermann, F. J. (**2003**), "Structural, chemical, and isotopic microanalytical investigations of graphite from supernovae", *Geochimica et Cosmochimica Acta* **67**, 4705–4725, URL http://dx.doi.org/10.1016/S0016-7037(03)00463-0.

Croat, T. K., Stadermann, F. J., & Bernatowicz, T. J. (**2005**), "Presolar Graphite from AGB Stars: Microstructure and s-Process Enrichment", *The Astrophysical Journal* **631**, 976–987, URL http://dx.doi.org/10.1086/432598.

Croat, T. K., Stadermann, F. J., & Bernatowicz, T. J. (**2008**), "Correlated isotopic and microstructural studies of turbostratic presolar graphite from the Murchison meteorite", *Meteoritics & Planetary Science* **43**, 1497–1516, URL http://dx.doi.org/10.1111/j.1945-5100.2008.tb01024.x.

Daulton, T. L., Bernatowicz, T. J., Lewis, R. S., Messenger, S., Stadermann, F. J., & Amari, S. (**2003**), "Polytype distribution of circumstellar silicon carbide: Microstructural characterization by transmission electron microscopy", *Geochimica et Cosmochimica Acta* **67**, 4743–4767, URL http://dx.doi.org/10.1016/S0016-7037(03)00272-2.

Daulton, T. L., Pinter, N., & Scott, A. C. (**2010**), "No evidence of nanodiamonds in YoungerDryas sediments to support an impact event", *PNAS* **107**, 16043–16047, URL www.pnas.org/cgi/doi/10.1073/pnas.1003904107.

DeGregorio, B. T., Stroud, R. M., Nittler, L. R., Alexander, C. M. O., Bassim, N. D., Cody, G. D., Kilcoyne, A. L. D., Sandford, S. A., Milam, S. N., Nuevo, M., & Zega, T. J. (**2013**), "Isotopic and chemical variation of organic nanoglobules in primitive meteorites", *Meteoritics & Planetary Science* **48**, 904–928, URL http://dx.doi.org/10.1111/maps.12109.

Fedkin, A., Meyer, B., & Grossman, L. (**2010**), "Condensation and mixing in supernova ejecta", *Geochimica et Cosmochimica Acta* **74**, 3642–3658, URL http://dx.doi.org/10.1016/j.gca.2010.03.021.

Gago, R., Jimenez, I., & Albella, J. (**2001**), "Detecting with X-ray Absorption spectroscopy the modifications of the bonding structure of graphitic carbon by amorphisation, hydrogenation, and nitrogenation", *Surface Science* **482**, 530–536, URL http://dx.doi.org/10.1016/S0039-6028(01)00939-6.

Groopman, E., Bernatowicz, T., & Zinner, E. (**2012**), "C, N, And O Isotopic Heterogeneities In Low-density Supernova Graphite Grains From Orgueil", *The Astrophysical Journal Letters* **754**, L8–L13, URL http://dx.doi.org/10.1088/2041-8205/754/1/L8.

Groopman, E., Bernatowicz, T., & Zinner, E. (**2013**), "An Unusual Low-density Supernova Graphite Grain With A Nanocrystalline Core", in "76th Annual Meeting of the Meteoritical Society", volume 48 of *s1*, Abstract #5072, URL http://dx.doi.org/10.1111/maps.12165.

Hammer, N. J., Janka, H.-T., & Müller, E. (**2010**), "Three-Dimensional Simulations of Mixing Instabilities in Supernova Explosions", *The Astrophysical Journal* **714**, 1371–1385, URL http://dx.doi.org/10.1088/0004-637X/714/1371.

Hoppe, P., Amari, S., Zinner, E., & Lewis, R. S. (**1995**), "Isotopic compositions of C, N, O, Mg, and Si, trace element abundances, and morphologies of single circumstellar graphite grains in four density fractions from the Murchison meteorite", *Geochimica et Cosmochimica Acta* **59**, 4029–4056, URL http://dx.doi.org/10.1016/0016-7037(95)00280-D.

Hoppe, P. & Besmehn, A. (**2002**), "Evidence for Extinct Vanadium-49 in Presolar Silicon Carbide Grains from Supernovae", *The Astrophysical Journal Letters* **576**, L69–L72, URL http://dx.doi.org/10.1086/342785.

Hutcheon, I. D., Huss, G. R., Fahey, A. J., & Wasserburg, G. J. (**1994**), "Extreme Mg-26 and O-17 enrichments in an Orgueil corundum: Identification of a presolar oxide grain", *The Astrohpysical Journal Letters* **425**, L97–L100, URL http://dx.doi.org/10.1086/187319.

Hynes, K. M., Croat, T. K., Amari, S., Mertz, A. F., & Bernatowicz, T. J. (**2010**), "Structural and isotopic microanalysis of presolar SiC from supernovae", *Meteoritics & Planetary Science* **45**, 596–614, URL http://dx.doi.org/10.1111/j.1945-5100.2010.01045.x.

Jadhav, M., Amari, S., Marhas, K. K., Zinner, E., Maruoka, T., & Gallino, R. (**2008**), "New stellar sources for high-density, presolar graphite grains", *The Astrophysical Journal* **682**, 1479–1485, URL http://dx.doi.org/10.1086/589139.

Jadhav, M., Amari, S., Zinner, E., & Maruoka, T. (**2006**), "Isotopic analysis of presolar graphite grains from Orgueil", *New Astronomy Review* **50**, 591–595, URL http://dx.doi.org/10.1016/j.newar.2006.06.004.

Jadhav, M., Pignatari, M., Herwig, F., Zinner, E., Gallino, R., & Huss, G. R. (**2013b**), "Relics of Ancient Post-AGB Stars in a Primitive Meteorite", *The Astrohpysical Journal Letters* **777**, L27, URL http://dx.doi.org/10.1088/2041-8205/777/2/L27.

Jadhav, M., Zinner, E., Amari, S., Maruoka, T., Marhas, K. K., & Gallino, R. (**2013a**), "Multi-element isotopic analyses of presolar graphite grains from Orgueil", *Geochimica et Cosmochimica Acta* **113**, 193–224, URL http://dx.doi.org/10.1016/j.gca.2013.01.018.

Joseph, D. & Oberlin, A. (**1983**), "Oxidation of Carbonaceous Matter II: X-Ray Diffraction and Transmission Electron Microscopy", *Carbon* **21**, 565–571, URL http://dx.doi.org/10.1016/0008-6223(83)90240-3.

Kilcoyne, A. L. D., Fakra, S., Hitchcock, P., Harteneck, B., Hitchcock, A. P., Tyliszczak, T., Rightor, E. G., Yang, L., Steele, W. F., Franck, K., Mitchell, G. E., Warwick, T., Anderson, E., & Ade, H. (**2003**), "Interferometer-controlled scanning transmission X-ray microscopes at the Advanced Light Source", *Journal of Synchrotron Radiation* **10**, 125–136, URL http://dx.doi.org/10.1107/S0909049502017739.

Lewis, R. S., Ming, T., Wacker, J. F., Anders, E., & Steel, E. (**1987**), "Interstellar diamonds in meteorites", *Nature* **326**, 160–162, URL http://dx.doi.org/10.1038/326160a0.

Lin, Y., Gyngard, F., & Zinner, E. (**2010**), "Isotopic Analysis of Supernova SiC and Si3N4 Grains from the Qingzhen (EH3) Chondrite", *The Astrohpysical Journal* **709**, 1157–1173, URL http://dx.doi.org/10.1088/0004-637X/709/2/1157.

Lodders, K. & Fegely, J., B. (**1995**), "The origin of circumstellar silicon carbide grains found in meteorites", *Meteoritics* **30**, 661–687, URL http://adsabs.harvard.edu/abs/1995Metic..30..661L.

Messenger, S., Keller, L. P., Stadermann, F. J., Walker, R. M., & Zinner, E. (**2003**), "Samples of stars beyond the solar system: silicate grains in interplanetary dust", *Science* **300**, 105–108, URL http://dx.doi.org/10.1126/science.1080576.

Newville, M. (**2013**), "Non-Linear Least-Square Minimization for Python", URL http://cars9.uchicago.edu/software/python/lmfit/.

Nittler, L. R., Alexander, C. M. O., Gao, X., Walker, R. M., & Zinner, E. K. (**1994**), "Interstellar oxide grains from the Tieschitz ordinary chondrite.", *Nature* **370**, 443–446, URL http://dx.doi.org/10.1038/370443a0.

Rauscher, T., Heger, A., Hoffman, R. D., & Woosley, S. E. (**2002**), "Nucleosynthesis In Massive Stars With Improved Nuclear And Stellar Physics", *The Astrophysical Journal* **576**, 323–348, URL http://dx.doi.org/10.1086/341728.

Rest, A., Foley, R. J., Sinnott, B., Welch, D. L., Badenes, C., Filippenko, A. V., Bergmann, M., Bhatti, W. A., Blondin, S., Challis, P., Damke, G., Finley, H., Huber, M. E., Kasen, D., Kirshner, R. P., Matheson, T., Mazzali, P., Minniti, D., Nakajima, R., Narayan, G., Olsen, K., Sauer, D., Smith, R. C., & Suntzeff, N. B. (**2011**), "Direct Confirmation Of The Asymmetry Of The Cas A Supernova With Light Echoes", *The Astrohpysical Journal* **732**, 3–13, URL http://dx.doi.org/10.1088/0004-637X/732/1/3.

Schwarz, W. H. E., Chang, T. C., Seeger, U., & Huang, K. H. (**1987**), "Core Excitations Of Symmetrical Aromatic Molecules. Specific Correlations In The Valence Shell And Localization In The Core Shells", *Chemical Physics* **117**, 73–89, URL http://dx.doi.org/10.1016/0301-0104(87)80098-8.

Stadermann, F. J., Croat, T. K., Bernatowicz, T. J., Amari, S., Messenger, S., Walker, R. M., & Zinner, E. (**2005**), "Supernova graphite in the NanoSIMS: Carbon, oxygen and titanium isotopic compositions of a spherule and its TiC sub-components", *Geochimica et Cosmochimica Acta* **69**, 177–188, URL http://dx.doi.org/10.1016/j.gca.2004.06.017.

Stancik, A. L. & Brauns, E. B. (**2008**), "A simple asymmetric lineshape for fitting infrared absorption spectra", *Vibrational Spectroscopy* **47**, 66–69, URL http://dx.doi.org/10.1016/j.vibspec.2008.02.009.

Stohr, J. (**1992**), *NEXAFS Spectroscopy*, number 25 in Springer Series in Surface Sciences, Springer-Verlag.

Travaglio, C., Galli, D., Gallino, R., Busso, M., Ferrini, F., & Straniero, O. (**1999**), "Galactic Chemical Evolution of Heavy Elements: From Barium to Europium", *The Astrophysical Journal* **521**, 691–702, URL http://dx.doi.org/10.1086/307571.

Wooden, D. H., Rank, D. M., Bregman, J. D., Witteborn, F. C., Tielens, A. G. G. M., Cohen, M., Pinto, P. A., & Axelrod, T. S. (**1993**), "Airborne spectrophotometry of SN 1987A from

1.7 to 12.6 microns - Time history of the dust continuum and line emission", *Astrophysical Journal Supplement Series* **88**, 477–507, URL http://dx.doi.org/10.1086/191830.

Woosley, S. E. & Weaver, T. A. (**1995**), "The Evolution and Explosion of Massive Stars. II. Explosive Hydrodynamics and Nucleosynthesis", *The Astrophysical Journal Supplement* **101**, 181–235, URL http://dx.doi.org/10.1086/192237.

Zhang, L., Holt, C., Luber, E., Olsen, B., Wang, H., Danaie, M., Cui, X., Tan, X., Lui, V., Kalisvaart, W., & Mitlin, D. (**2011**), "High Rate Electrochemical Capacitors From Three-dimensional Arrays Of Vanadium Nitride-functionalized Carbon Nanotubes", *Journal of Physical Chemistry C* **115**, 24381–24393, URL http://dx.doi.org/10.1021/jp205052f.

Zinner, E. (**2014**), "Presolar Grains", in K. K. Turekian & H. D. Holland (Eds.), "Treatise on Geochemistry", chapter 1.04, 181–213, Elsevier, 2nd edition, URL http://dx.doi.org/10.1016/B978-0-08-095975-7.00101-7.

Zinner, E., Amari, S., Wopenka, B., & Lewis, R. S. (**1995**), "Interstellar graphite in meteorites: Isotopic compositions and structural properties of single graphite grains from Murchison", *Meteoritics* **30**, 209–226, URL http://dx.doi.org/10.1111/j.1945-5100.1995.tb01115.x.

Zinner, E., Ming, T., & Anders, E. (**1987**), "Large isotopic anomalies of Si, C, N and noble gases in interstellar SiC from the Murray meteorite", *Nature* **330**, 730–732, URL http://dx.doi.org/10.1038/330730a0.

Zinner, E., Wopenka, B., Amari, S., & Anders, E. (**1990**), "Interstellar Graphite and Other Carbonaceous Grains from the Murchison Meteorite: Structure, Composition and Isotopes of C, N, and NE", in "21st Lunar and Planetary Science Conference", Abstract #1700, Lunar and Planetary Institute, Houston, URL http://www.lpi.usra.edu/meetings/lpsc1990/pdf/1700.pdf.

CHAPTER 6

XANES of Presolar Graphite Grains and their TiC Subgrains

6.1 Preface

Adapted from the conference abstracts:

Groopman, E., Nittler, L. R., Bernatowicz, T. J., Croat, T. K., Zinner, E., and Kilcoyne, A. L. D. (**2014**). "Diversity in Carbon K-Edge XANES Among Presolar Graphite Grains", in 45th Lunar and Planetary Science Conference, Abstract #1492 (Lunar and Planetary Institute, Houston), URL http://www.lpi.usra.edu/meetings/lpsc2014/pdf/1492.pdf.

Groopman, E. E., Daulton, T. L., Nittler, L. R., Bernatowicz, T. J., and Zinner, E. K. (**2012**). "Ti-XANES and EELS of Presolar TiC Subgrains Within Low-Density Supernova Graphite Grains", Meteoritics and Planetary Science Supplement 75, Abstract #5225.

6.2 Introduction

We report on X-ray absorption near-edge structure (XANES) measurements of 13 presolar graphite grains. High-density (HD) and low-density (LD) graphite grains from the Murchison

and Orgueil meteorites were studied in the NanoSIMS and subsequently ultramicrotomed into 70nm-thick sections, which were deposited on holey-C and SiO coated TEM grids (Croat *et al.*, 2003; Groopman *et al.*, 2012). The LD grains likely originated in Type-II SNe, while the HD grains likely formed in AGB stars, based upon their isotopic compositions (Zinner, 2014).

Presolar graphite grains from SNe often contain 10–100 nm diameter subgrains that are predominantly TiC and rarely include TiO_2. Here, we use XANES (Nittler *et al.*, 2011) and electron energy loss spectroscopy (EELS) to probe the structure of the Ti atomic bonds in presolar TiC subgrains. Since atomic bonds are influenced by sample chemistry (e.g. composition, atom coordination, valence) and lattice defects (affecting atom coordination, bond distances, etc.), the bond structure can provide insight into the formation conditions in the grains' parent stellar outflows.

6.3   Experimental Methods

XANES spectra were acquired at Beamline 5.3.2.2 of the Advanced Light Source at Lawrence-Berkeley National Laboratory. A full description of the instrument is presented in Kilcoyne *et al.* (2003). An interferometer-controlled piezoelectric stage allows for fine-scale x,y rastering of the sample relative to the ∼40 nm stationary soft X-ray beam. By stepping up the monochromated beam energy after each raster, in increments as small as 0.1 eV, one generates a data "stack", a 3-dimensional image in x × y × eV, where each raster point contains a full energy spectrum. Raster areas are set up so that they contain regions
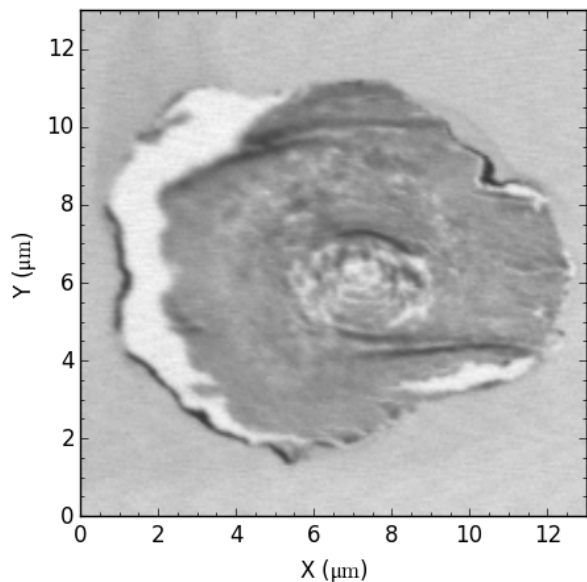
FIGURE 6.1: X-ray absorbance image of a microtomed section of OR1d6m-24 (G24) at 390 eV, above the C K-edge.
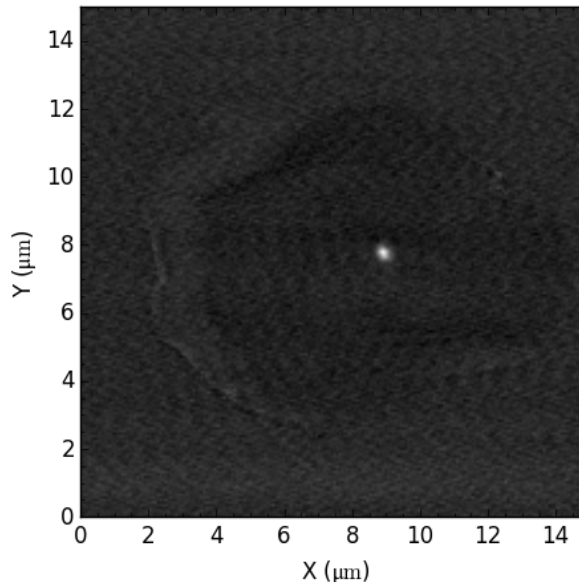
FIGURE 6.2: Ti map of the section in Figure 6.1. Map is a ratio of two images, one above the Ti L-edge (464 eV) and one below the Ti L-edge (440 eV). The resulting high contrast indicates the presence of Ti, in this case a large TiC subgrain.

with holes in the sample to record the baseline intensity, I_0. Absorbance, or the optical density (OD) of the sample, is calculated as OD = -log(I/I_0), where I is the measured intensity through the sample. Reported energies were calibrated using CO_2 gas. Graphite spectra from the literature (e.g., Stohr (1992); Brandes *et al.* (2008)) were used as C K-edge standards. Terrestrial TiC and TiN standards were embedded in resin, microtomed into 70 nm-thick sections, and deposited on SiO-coated TEM grids, similar to the presolar grains. Dhumal *et al.* (2009) and Zega *et al.* (2011) provided data on EELS and XANES TiO standards, respectively.

π^* **Peak Quantification**

For C K-edge spectra, a linear pre-edge fit (270–282 eV) is subtracted from each spectrum.

The major aromatic π^* peaks are fitted to an asymmetric Lorentzian profile of the form:

$$L_{sym.} \;=\; \frac{A}{2\pi} \times \frac{w}{(x - x_0)^2 + (w/2)^2} \tag{6.1}$$

$$w(x) \;=\; \frac{2w_0}{1 + e^{-a(x-x_0)}} \tag{6.2}$$

$$L_{asym.} \;=\; \frac{A}{\pi} \times \frac{w_0/(1 + e^{-a(x-x_0)})}{(x - x_0)^2 + (w_0/(1 + e^{-a(x-x_0)}))^2} \tag{6.3}$$

where A is the amplitude, x_0 is the median (center) energy, a is an asymmetry factor, and w is

the full width at half-maximum (FWHM) (Stancik & Brauns, 2008; Groopman *et al.*, 2014).

w is allowed to vary sigmoidally with energy, $w(x) \to 2 \cdot w_0/[1 + \exp(-a \cdot (x - x_0))]$, which

models peak tails very well. Note that when $a = 0$, L returns to its symmetric Lorentzian

form, but when $a \neq 0$, the peak maximum, p, is no longer equal to x_0. We calculate the

mean peak energy, μ:

$$\mu = \frac{\int_{x_0-5w}^{x_0+5w} x \cdot \mathrm{OD}(x)}{\int_{x_0-5w}^{x_0+5w} \mathrm{OD}(x)} \tag{6.4}$$

where the limits of integration are set widely enough to encompass the entire absorption peak.

The mean of a Lorentzian is otherwise undefined. The standard method for deconvolving

peaks in a XANES spectrum is to model the various ionization edges as arctangent or step

functions and subtract these from the spectrum before fitting peaks as Gaussian profiles

(Cody *et al.*, 1995). This requires assumptions regarding which edges are present in addition to their exact locations and intensities. Here we model only the aromatic C ionization potential, which is the dominant component within our spectra. The continuum step is modeled as an error function (erf) of the form:

$$I = H \left[\frac{1}{2} + \frac{1}{2} \text{erf} \left(\frac{E - P}{2\ln(2) \times \Gamma} \right) \right] \tag{6.5}$$

(Stohr, 1992) where E is the energy, H is the height of the step, P is the ionization potential (290.3 eV for aromatic carbon (Cody *et al.*, 1995)), and Γ is the width of the step in eV (as in Chapter 5). At energies higher than the ionization potential, the continuum step decays exponentially (Stohr, 1992), however this does not affect the deconvolution of minor peaks below the ionization potential. Γ is intrinsically linked to the instrumental resolution (Stohr, 1992) and has been chosen to be 1 eV in earlier work (e.g., Cody *et al.* (1995)). The ionization potentials for minor functional groups in these samples lie at higher energies, so their contribution to the π^* peak fit and minor peak deconvolution is minimal and can be safely ignored. For this reason, the π^* peak can be safely fitted without first subtracting the aromatic C continuum step, minimizing the number of fitting parameters. While the π^* resonances are sensitive to the orientation of the aromatic sheets relative to the beam, this only affects each peak's amplitude and not its FWHM (Brandes *et al.*, 2008). All spectra in the figures are normalized to the area under their σ^* peaks between 291 and 293 eV.

Minor Peak Deconvolution

After the π^* peaks are fitted, the aromatic C continuum step is subtracted from each spectrum, where the height of the step is selected so that the residual spectrum is minimized but non-negative (see Figure 6.3). Aromatic C molecules such as graphite form conjugated π bonds above and below the molecular planes. Conjugated bonds result in delocalized electrons across the graphite sheet's surface, causing a splitting of the π and π^* orbitals (see Figure 6.5; Stohr (1992)). We infer from the strong π^* peak at ~ 285.2 eV (π^*_1) the presence of a weaker π^*_2 peak ~ 4 eV higher in energy (Cody *et al.*, 1995), which must be included in the minor peak deconvolution. The π^*_2 peak and all other minor peaks are modeled as Gaussian profiles and are fitted simultaneously from the residual spectrum (Figure 6.4).

We also collected Ti L-edge XANES spectra from TiC subgrains in 4 presolar SN graphite grains from the Orgueil meteorite (Groopman *et al.*, 2011). These data are compared with previous XANES (Zega *et al.*, 2011) and EELS (Dhumal *et al.*, 2009) measurements of Ti-oxide standards. Following Daulton & Little (2006), the fine structure of L_3 and L_2 edges was parameterized by measuring the L_3/L_2 integrated intensity ratio and the position of the L_3 peak using the custom LAnalysis software (T. Daulton, Washington University). These parameters correlate to Ti valence. For spectra with split L_3 peaks we use the most dominant L_3 peak in our analysis, although for future work we will expand this parameterization to include minor peak positions and heights.
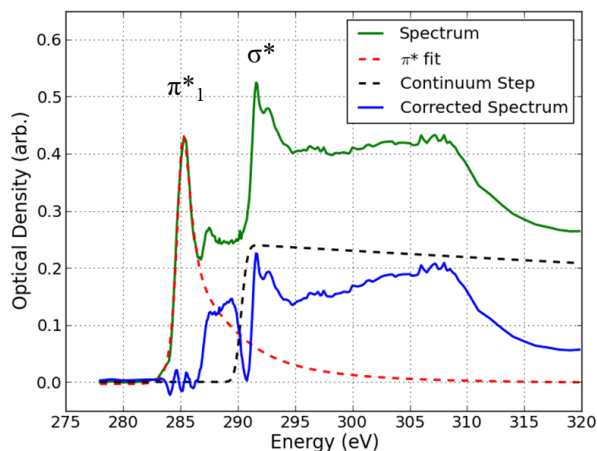
FIGURE 6.3: π^* fit and continuum step subtraction from an optical density spectrum from presolar graphite grain OR1d6m-18 (G18). The height of the continuum step is chosen so that the residual is minimized and non-negative. Graphite is a conjugated molecule, so the π^* oribitals are split in energy.
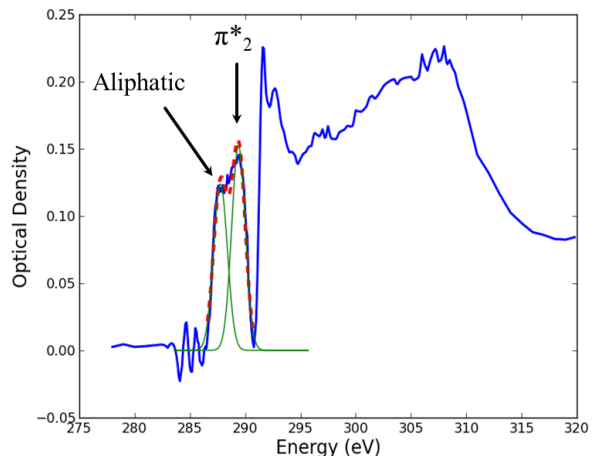
FIGURE 6.4: Gaussian deconvolution of minor peaks. Red dashed profile is the sum of individual Gaussian profiles (green). The π^*_2 peak is inferred from the presence of the strong π^*_1 resonance in Figure 6.3.

6.4   Results

6.4.1   C K-Edge XANES of presolar Graphite

Diversity in C K-Edge Spectra

XANES spectra from pure terrestrial graphite are characterized by strong aromatic π^* (285.2 eV) and σ^* (291.5 & 292.5 eV) excitons from C(1s) transitions (Brandes *et al.*, 2008). All of the presolar grains exhibit graphite-like spectra (Figure 6.6). Many grains' spectra also contain minor peaks corresponding to aliphatic (287.3–288.1 eV, Figure 6.7), ketone (286.5 eV), and carboxyl (288.4–288.7 eV, Figure 6.8) absorptions (Cody *et al.*, 2008; DeGregorio
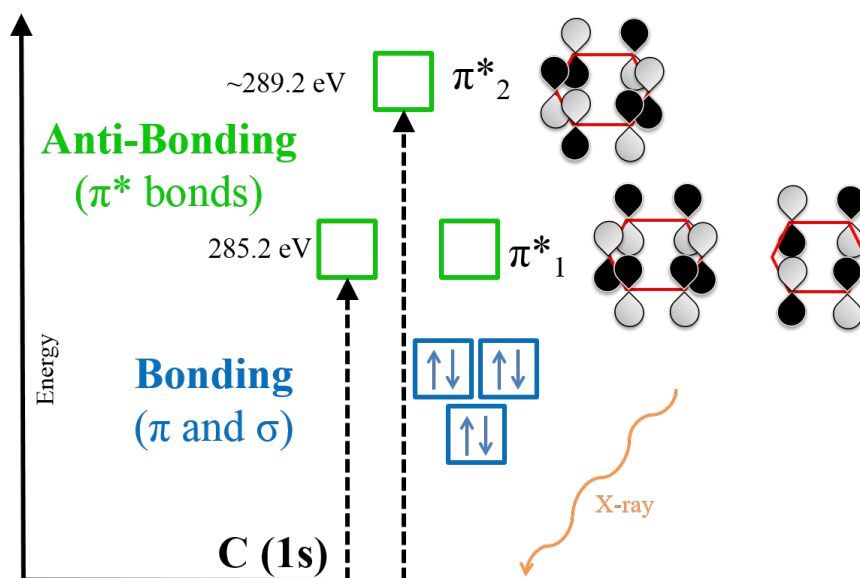
FIGURE 6.5: Schematic diagram of split π^* anti-bonds in conjugated molecules (energy not to scale). π and σ bonding molecular orbitals are filled in the ground state. Incident X-rays excite electrons from the C-1s inner electron shell into vacant anti-bonding orbitals. The splitting in energy of the π^* molecular orbitals arises from the possible configurations of p-orbitals phases (shown in black and gray on the right side) from each C atom in the conjugated molecule.

et al., 2013). Each grain spectrum contains a different combination of minor absorptions. Six grains show aliphatic resonances; two grains ketone resonances; and nine grains carboxyl resonances. The HD grain OR1f3m-38 has a spectrum that is recognizably graphitic, however its π^* peak energy is 285.0 eV, lower than that of terrestrial graphite, and its σ^* absorptions are much broader than in any other graphite grains. As HD graphite grains typically contain less-disrupted graphite than their LD turbostratic cousins (Croat *et al.*, 2008), it is interesting that the spectrum of one of the two HD grains in this study contains multiple minor organic peaks and looks the least like pure graphite.

The peak energies of the aromatic π^* absorptions range from 284.7 to 285.5 eV, with the

majority of grains at 285.2 and 285.3 eV (Figure 6.9). The FWHM range from 1 to 3.5 eV, which, in conjunction with varying degrees of asymmetry, yield median energies from 285 to 286.3 eV. One grain, OR1d6m-6 (G6 in Chapter 5), contains a nanocrystalline core surrounded by a mantle of turbostratic graphite (Groopman *et al.*, 2014). The nanocrystalline core spectrum perfectly matches that of aromatic carbon, which reflects its composition of 2–4 nm sheets of graphene, determined by electron diffraction studies. The turbostratic graphite spectrum contains a small carboxyl peak (288.4 eV) and a longer tail on its π^* resonance. These may reflect the enhanced O content characteristic of turbostratic graphite vis-à-vis pure graphite.
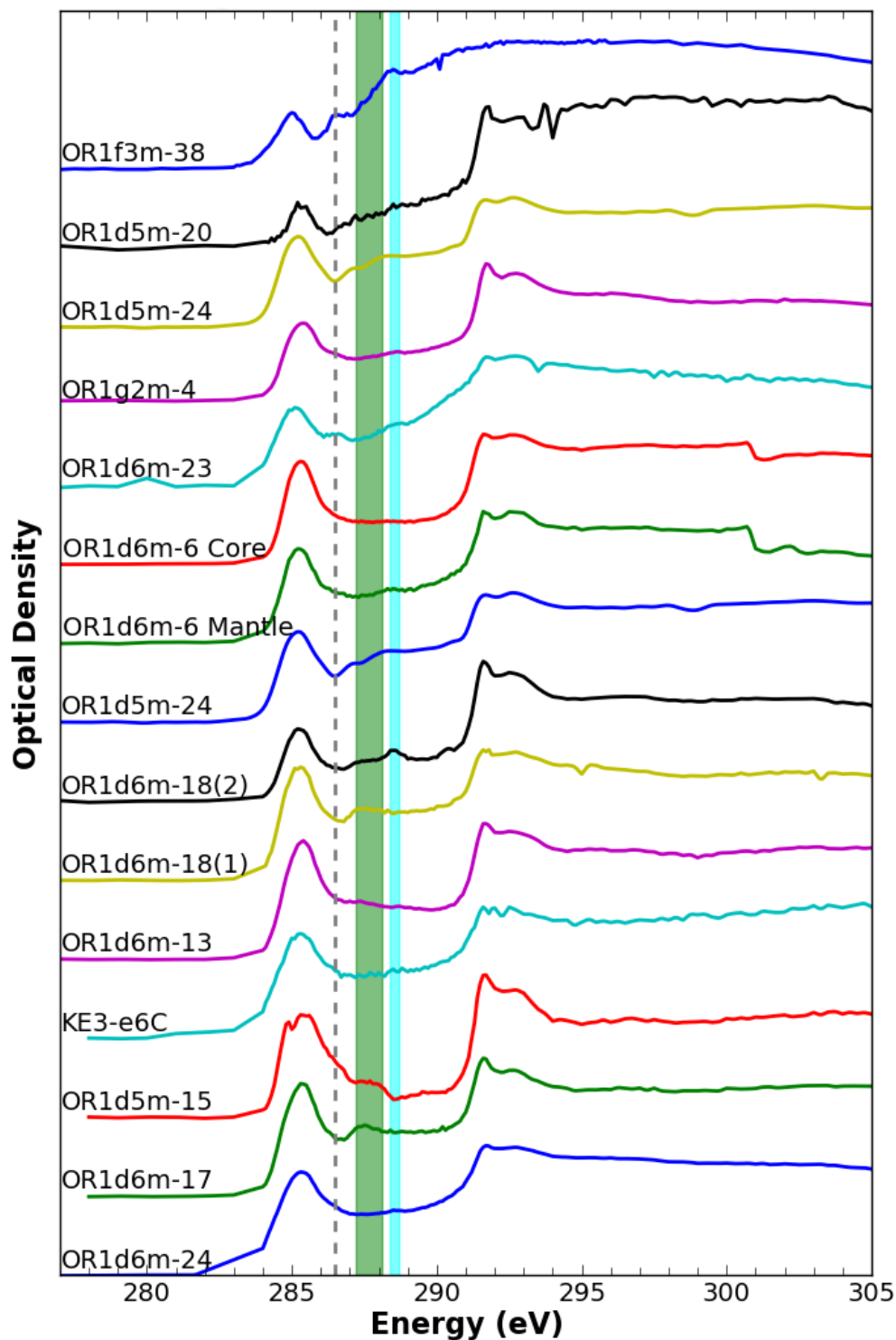
FIGURE 6.6: Presolar graphite XANES spectra exhibiting graphite-like features. Minor peaks are also present in numerous spectra: ketone (dashed, 286.5 eV), aliphatic (green, 287.3–288.1 eV), and carboxyl (cyan, 288.4–288.7 eV), with compositions varying from grain to grain.
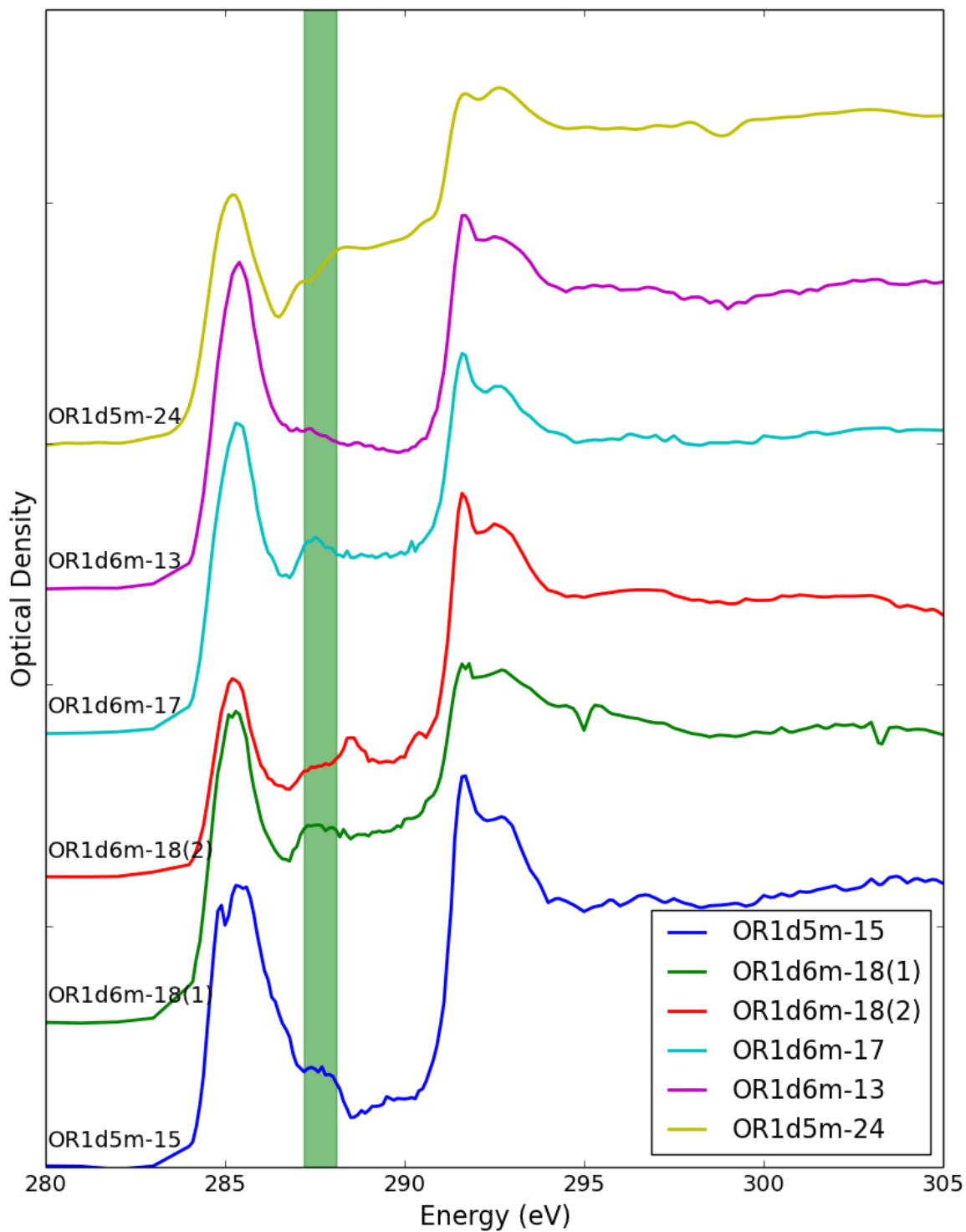
FIGURE 6.7: Spectra from Figure 6.6 that exhibit an absorption resonance in the aliphatic region (287.3–288.1 eV).
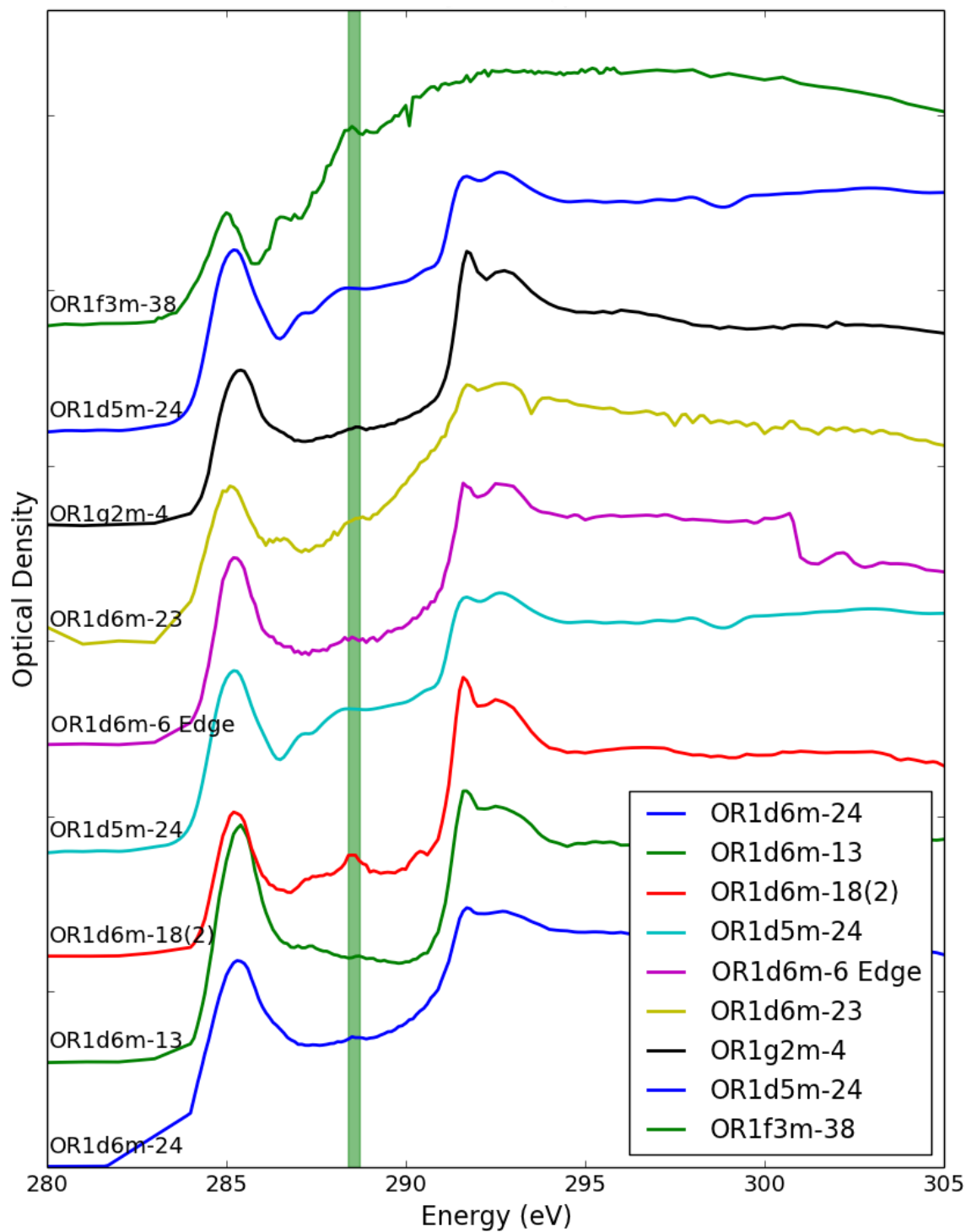
FIGURE 6.8: Spectra from Figure 6.6 that exhibit an absorption resonance in the carboxyl region (288.4–288.7 eV). The two spectra from OR1d6m-18 were collected from different regions of the grain.

156
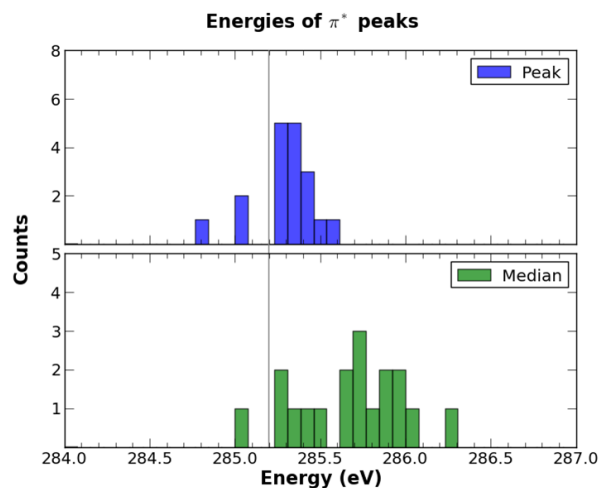
FIGURE 6.9: π^* peak and median energies. Most π^* resonances lie near 285.2 and 285.3 eV. Because the peaks are asymmetric, the median energies tend to be higher than the peak energies. Gray line is the literature π^* peak value of 285.2 eV.
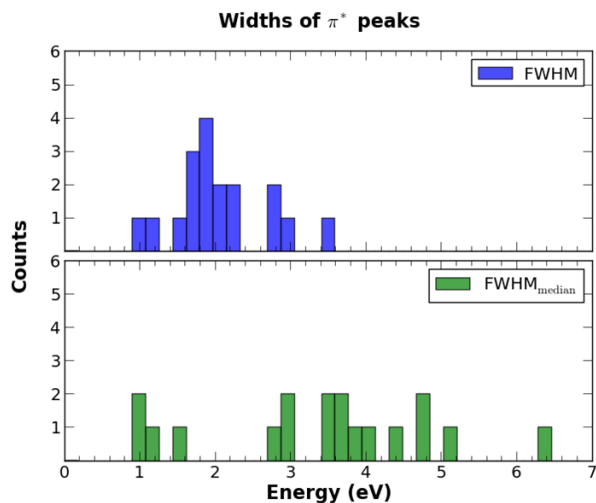
FIGURE 6.10: Widths of π^* peaks. The conventional full width at half-maximum (FWHM) is calculated numerically. The FWHM$_{\mathrm{median}}$ is the w parameter from Equations 6.2 and 6.3, which is the full width of the peak at half of the intensity at the median energy.

6.4.2 Ti L-Edge XANES of presolar TiC subgrains

The L$_3$ peak position and L$_3$/L$_2$ integrated ratio allows us to distinguish between the valence states of our standards which contain minimal peak splitting: TiC, TiN, and TiO. However, the results for the Ti$_x$O$_y$ (x,y > 1) standards overlap considerably and are complicated by significant peak splitting (Figures 6.11 & 6.12). The L$_3$ peak position for most of our presolar TiC subgrains match that of our TiC standard, although their L$_3$/L$_2$ integrated ratios exhibit a larger spread (Figure 6.13). One particularly large TiC subgrain (G24-Aπ, ~300 nm) from a SN graphite grain has an L$_3$/L$_2$ integrated ratio that matches well that of the TiC standard, but its L$_3$ peak position is shifted to a lower energy than any of the

standards. This may be due to V in solid solution within the carbide, which has a V/Ti ratio of 5% based upon EDXS measurements. However, many SN TiC subgrains contain V/Ti up to > 10% (Croat *et al.*, 2003).

6.4.3   C K-Edge XANES of presolar TiC subgrains

We also measured the C K-edge for many of the TiC subgrains, despite the likelihood that the surrounding graphite would interfere. Determining the effects of O in some TiC subgrains' amorphous rims (Daulton *et al.*, 2012) and/or V in solid solution on the C K-edge is a future goal of this project. Due to time constraints at the synchrotron, non-uniform energy dispersion is used during the scan, with smaller energy steps around C and Ti edges, and larger steps in between. Unfortunately, we did not realize that the C K-edge resonances likely due to V lie at a lower energy than those associated with Ti, and so these peaks were truncated during our scans.

6.5   Discussion

The diversity in the variety and abundance of minor organic peaks within the XANES spectra may reflect the varied formation conditions of the presolar graphite grains. All grains exhibit graphite-like spectra, which agree well with TEM observations. The majority of grains in this study originated in SNe and contain significant excesses in ^{18}O relative to terrestrial standards. Minor peaks from O-containing compounds in these grains are therefore most likely indigenous and not due to contamination. Quantification of these minor peaks is

currently not mature enough to report, however these methods appear to work qualitatively.

Further data are required for an in-depth examination of the valence state and bonding characteristic of Ti and C in TiC subgrains, and the bonding characteristics of C in presolar graphite grains. This chapter and the abstracts it is adapted from represent a preliminary investigation into the use of XANES on presolar grains. The next major step is to manufacture higher-quality graphite and Ti mineral standards for comparison to presolar material.
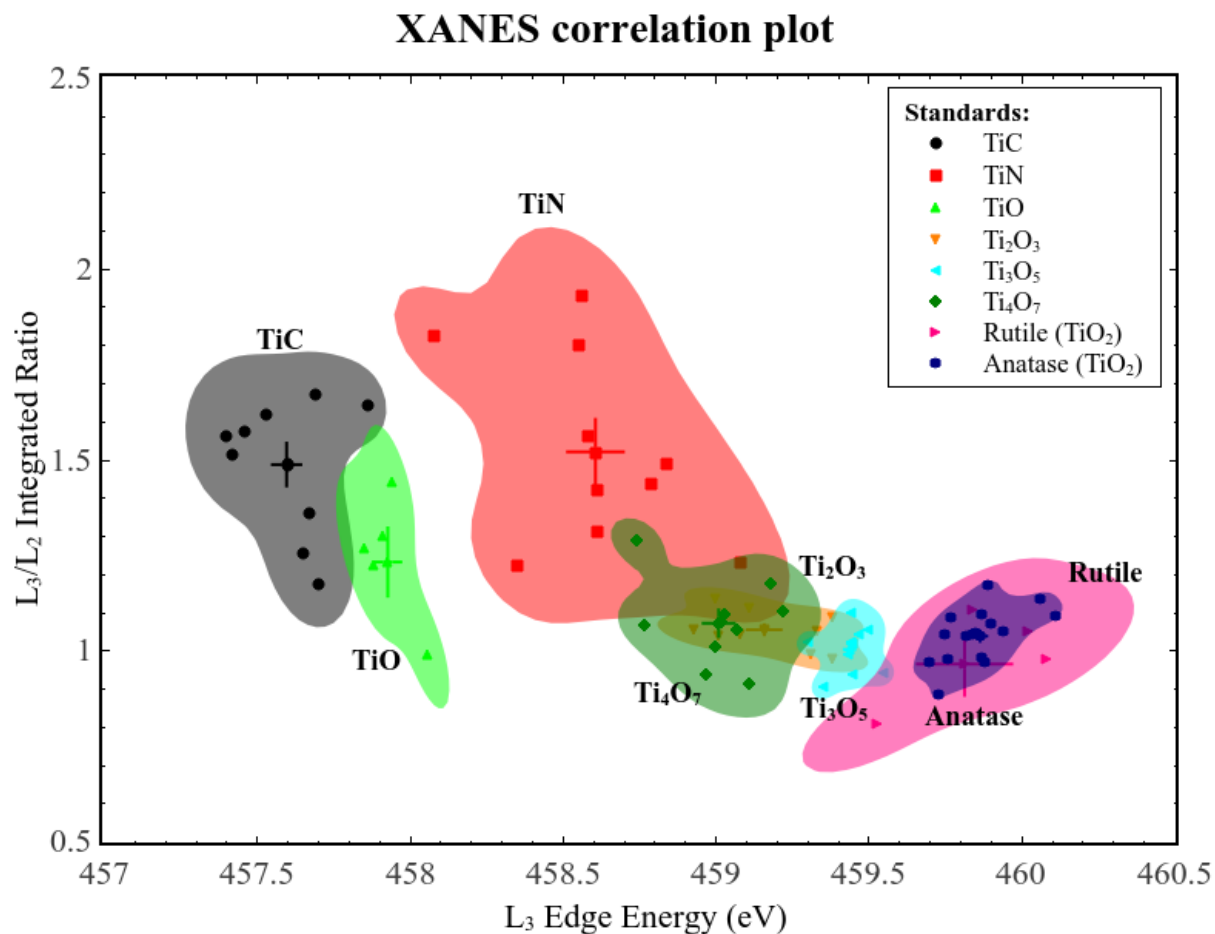
FIGURE 6.11: Correlation plot of L_3 edge energy vs. integrated L_3/L_2. This is one such parameterization that allows for distinguishing between Ti valence states of different materials. Higher L_3 edge energy generally correlates to higher Ti valence. Shaded regions are 2σ boundaries. Error bars are the standard error of the mean.
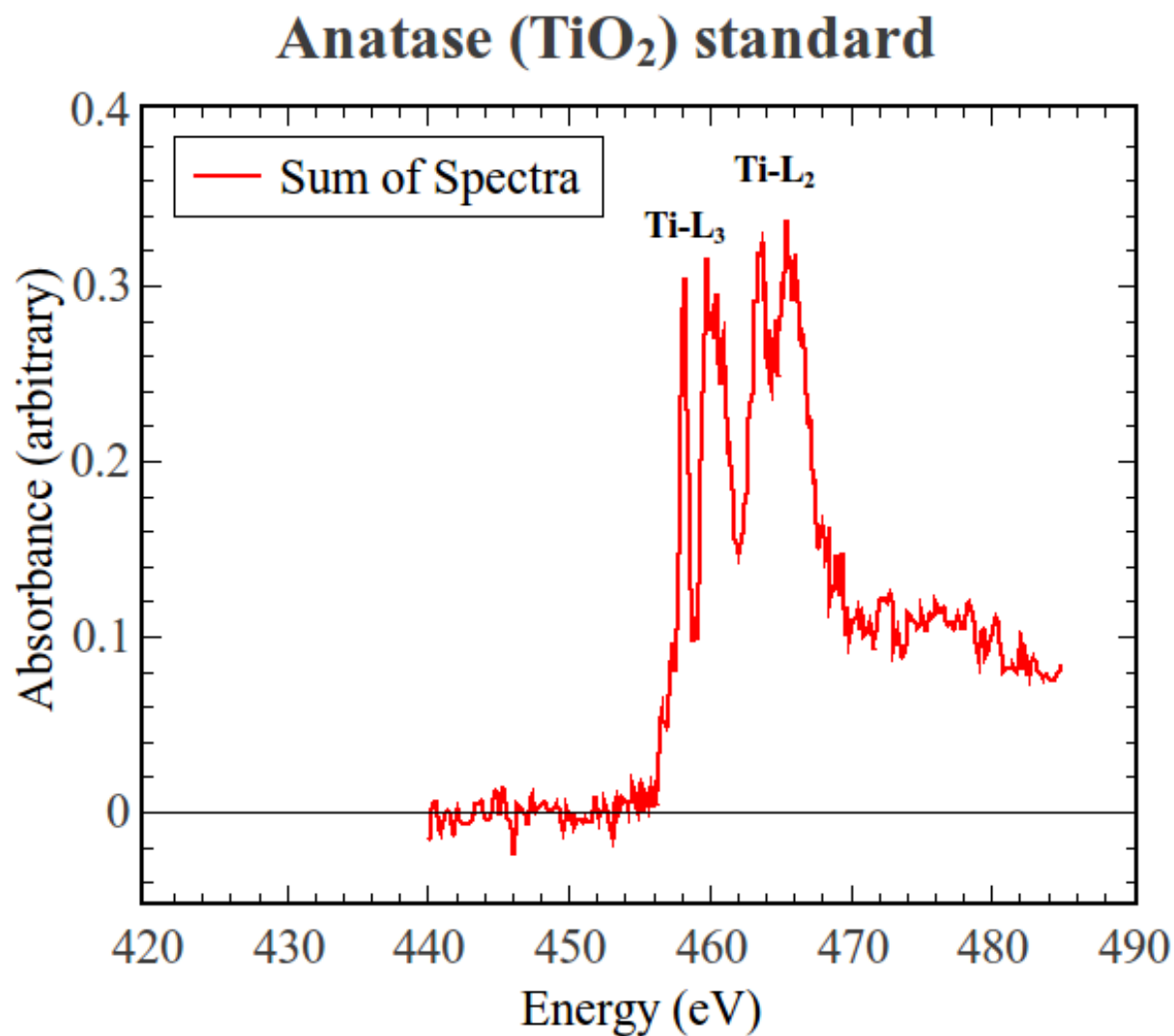
FIGURE 6.12: Example of split Ti-L$_3$ and Ti-L$_2$ peaks in a anatase (TiO$_2$) spectrum summed from all measurements shown in Figure 6.11. The parameterization currently uses only the most dominant peak.
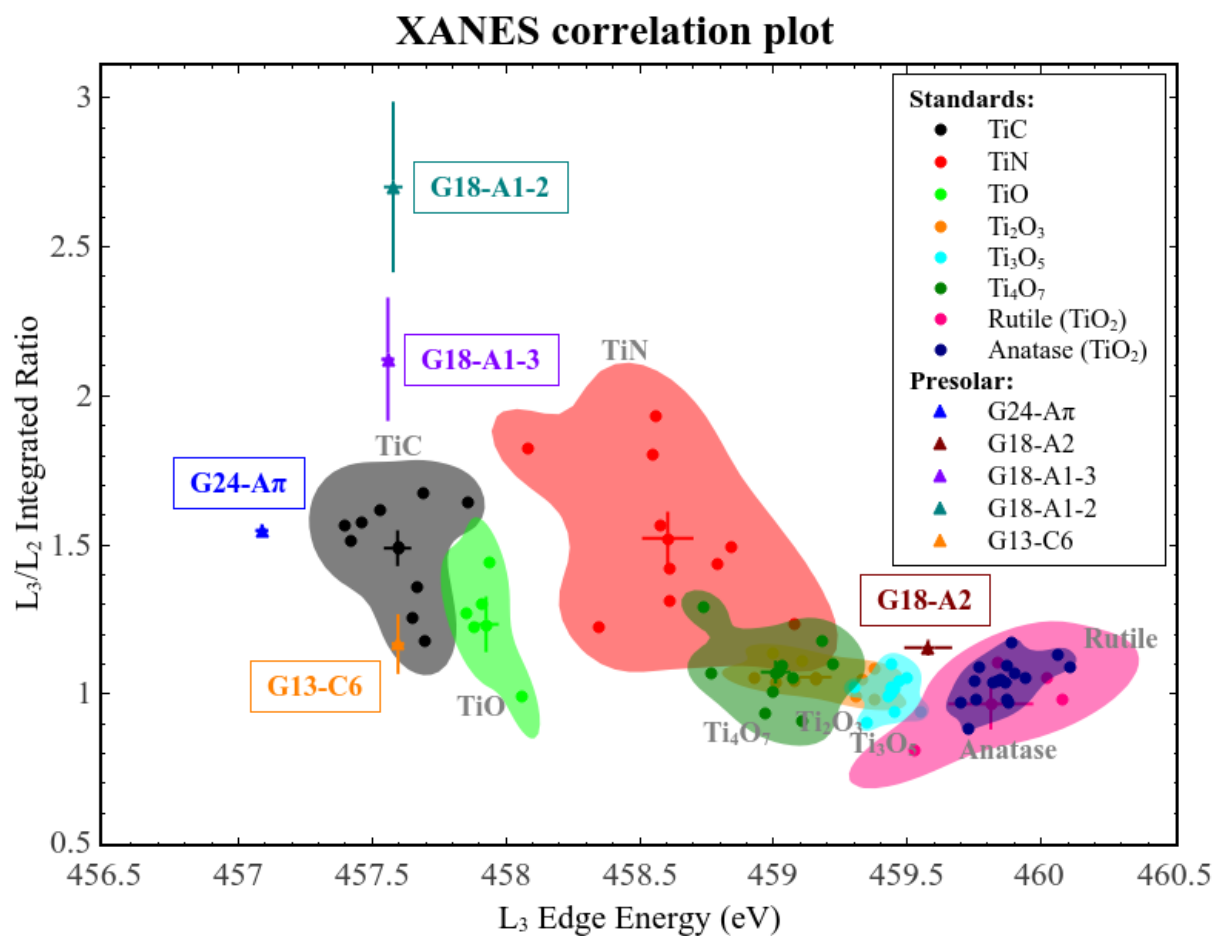
FIGURE 6.13: Same as Figure 6.11, with five presolar Ti-rich subgrains. Three subgrains match well the L_3 edge energy of TiC. Subgrain G24-Aπ has a considerably lower L_3 edge energy, possibly due to V in solid substitution. Subgrain G18-A2 matches the parameterizations of Ti-oxides. This grain was not previously indexed with electron diffraction and was assumed to be a carbide, as the microtome section is on an SiO-coated TEM grid, which always yields an O EDXS signal.

Acknowledgements

Bibliography

Brandes, J. A., Cody, G. D., Rumble, D., Haberstroh, P., Wirick, S., & Gelinas, Y. (**2008**), "Carbon K-edge XANES spectromicroscopy of natural graphite", *Carbon* **46**, 1424–1434, URL http://dx.doi.org/10.1016/j.carbon.2008.06.020.

Cody, G. D., Ade, H., Alexander, C. M. O., Araki, T., Butterworth, A., Fleckenstein, H., Flynn, G., Gilles, M. K., Jacobsen, C., Kilcoyne, A. L. D., Messenger, K., Sandford, S. A., Tyliszczak, T., Westphal, A. J., Wirick, S., & Yabuta, H. (**2008**), "Quantitative organic and light-element analysis of comet 81P/Wild 2 particles using C-, N-, and O--XANES", *Meteoritics & Planetary Science* **43**, 353–365, URL http://dx.doi.org/10.1111/j.1945-5100.2008.tb00627.x.

Cody, G. D., Botto, R. E., Ade, H., Behal, S., Disko, M., & Wirick, S. (**1995**), "Inner-Shell Spectroscopy and Imaging of a Subbituminous Coal: In-Situ Analysis of ORganic and Inorganic Microstructure Using C(1s)-, Ca(2p)-, and Cl(2s)-NEXAFS", *Energy & Fuels* **9**, 525–533, URL http://dx.doi.org/10.1021/ef00051a018.

Croat, T. K., Bernatowicz, T., Amari, S., Messenger, S., & Stadermann, F. J. (**2003**), "Structural, chemical, and isotopic microanalytical investigations of graphite from supernovae", *Geochimica et Cosmochimica Acta* **67**, 4705–4725, URL http://dx.doi.org/10.1016/S0016-7037(03)00463-0.

Croat, T. K., Stadermann, F. J., & Bernatowicz, T. J. (**2008**), "Correlated isotopic and microstructural studies of turbostratic presolar graphite from the Murchison meteorite", *Meteoritics & Planetary Science* **43**, 1497–1516, URL http://dx.doi.org/10.1111/j.1945-5100.2008.tb01024.x.

Daulton, T. L., Bernatowicz, T. J., & Croat, T. K. (**2012**), "Electron Energy Loss Spectral Imaging of TiC Formed by Supernovae: A Scanning Transmission Electron Microscopy Study of Grain Formation and Alteration Mechanisms", in "43rd Lunar and Planetary Science Conference", Abstract #2247, Lunar and Planetary Institute, Houston, URL http://www.lpi.usra.edu/meetings/lpsc2012/pdf/2247.pdf.

Daulton, T. L. & Little, B. J. (**2006**), "Determination of chromium valence over the range Cr(0)Cr(VI) by electron energy loss spectroscopy", *Ultramicroscopy* **106**, 561–573, URL http://dx.doi.org/10.1016/j.ultramic.2006.02.005.

DeGregorio, B. T., Stroud, R. M., Nittler, L. R., Alexander, C. M. O., Bassim, N. D., Cody, G. D., Kilcoyne, A. L. D., Sandford, S. A., Milam, S. N., Nuevo, M., & Zega, T. J. (**2013**), "Isotopic and chemical variation of organic nanoglobules in primitive meteorites", *Meteoritics & Planetary Science* **48**, 904–928, URL http://dx.doi.org/10.1111/maps.12109.

Dhumal, S. Y., Daulton, T. L., Jianga, J., Khomamia, B., & Biswas, P. (**2009**), "Synthesis of visible light-active nanostructured TiOx (x ¡ 2) photocatalysts in a flame aerosol reactor", *Applied Catalysis* **86**, 145–151, URL http://dx.doi.org/10.1016/j.apcatb.2008.08.014.

Groopman, E., Bernatowicz, T., & Zinner, E. (**2012**), "C, N, And O Isotopic Heterogeneities In Low-density Supernova Graphite Grains From Orgueil", *The Astrophysical Journal Letters* **754**, L8–L13, URL http://dx.doi.org/10.1088/2041-8205/754/1/L8.

Groopman, E., Nittler, L. R., Bernatowicz, T., & Zinner, E. (**2014**), "NANOSIMS, TEM, and XANES Studies of a Unique Presolar Supernova Graphite Grain", *The Astrophysical Journal* **790**, 9–21, URL http://dx.doi.org/10.1088/0004-637X/790/1/9.

Groopman, E., Wopenka, B., & Zinner, E. (**2011**), "Isotopic and Raman Analyses of Low-Density Orgueil Carbon Grains", volume 74, Abstract #5031, URL http://adsabs.harvard.edu/abs/2011M%26PSA..74.5031G.

Kilcoyne, A. L. D., Fakra, S., Hitchcock, P., Harteneck, B., Hitchcock, A. P., Tyliszczak, T., Rightor, E. G., Yang, L., Steele, W. F., Franck, K., Mitchell, G. E., Warwick, T., Anderson, E., & Ade, H. (**2003**), "Interferometer-controlled scanning transmission X-ray microscopes at the Advanced Light Source", *Journal of Synchrotron Radiation* **10**, 125–136, URL http://dx.doi.org/10.1107/S0909049502017739.

Nittler, L. R., Groopman, E., Bernatowicz, T. J., Croat, T. K., & Zinner, E. K. (**2011**), "X-Ray Absorption Near-Edge Spectroscopy of Supernova Carbonaceous Grains", *Meteoritics and Planetary Science Supplement* **74**, 5361, URL http://adsabs.harvard.edu/abs/2011M%26PSA..74.5361N.

Stancik, A. L. & Brauns, E. B. (**2008**), "A simple asymmetric lineshape for fitting infrared absorption spectra", *Vibrational Spectroscopy* **47**, 66–69, URL http://dx.doi.org/10.1016/j.vibspec.2008.02.009.

Stohr, J. (**1992**), *NEXAFS Spectroscopy*, number 25 in Springer Series in Surface Sciences, Springer-Verlag.

Zega, T. J., Nittler, L. R., Stroud, R. M., Alexander, C. M. O., & Kilcoyne, A. L. D. (**2011**), "Ti-XANES of Solar and Presolar Hibonite", in "42nd Lunar and Planetary Science Conference", Abstract #1465, Lunar and Planetary Institute, Houston, URL http://www.lpi.usra.edu/meetings/lpsc2011/pdf/1465.pdf.

Zinner, E. (**2014**), "Presolar Grains", in K. K. Turekian & H. D. Holland (Eds.), "Treatise on Geochemistry", chapter 1.04, 181–213, Elsevier, 2nd edition, URL http://dx.doi.org/10.1016/B978-0-08-095975-7.00101-7.

CHAPTER 7

C, CA, AND TI ISOTOPES: ON THE
ORIGINS OF HIGH- AND LOW-DENSITY
PRESOLAR GRAPHITE GRAINS

7.1   Preface

Adapted from the conference abstract:

Groopman, E. E., Zinner, E. K., and Bernatowicz, T. J. (**2013**). "C, Ca, and Ti Isotopes: On the Origins of High- and Low-Density Presolar Graphite Grains", in *44th Lunar and Planetary Science Conference*, Abstract #1757 (Lunar and Planetary Institute, Houston), http://www.lpi.usra.edu/meetings/lpsc2013/pdf/1757.pdf.

7.2   Introduction

We report on NanoSIMS measurements of 27 new high-density (HD) presolar graphite grains (>2 μm) from the OR1f (ρ = 2.02–2.04 g/cm^3; 16 grains) and OR1g (ρ = 2.04–2.12 g/cm^3; 11 grains) size/density fractions from the Orgueil meteorite. We measured ^{12,13}C,

^{28,29,30}Si, ^{39,41}K, ^{40,42,43,44}Ca, ^{46,47,48,49,50}Ti, ^{51}V, and ^{52}Cr; however, we did not measure any O, N, Al, or Mg isotopes, as they are often not diagnostic in HD graphite grains (Jadhav *et al.*, 2013a). These are the first Ca and Ti analyses on OR1g grains. We also report on measurements of Ca and Ti isotopes from the OR1d6m ($\rho = 1.75$–1.92 g/cm^3) low-density (LD) mount (see Groopman *et al.* (2012)).

The origins of presolar graphite grains with extreme anomalies in Ca and Ti isotopes remain enigmatic, although Born-Again AGB stars have been proposed as stellar sources for those with low ^{12}C/^{13}C ratios (< 20) (Jadhav *et al.*, 2008, 2013b). The isotopic compositions of these grains are incompatible with current AGB star models (e.g., Cristallo *et al.* (2009)) and models of supernova (SN) zones where C/O > 1 (Rauscher *et al.*, 2002). O-rich SN zones, however, do reproduce the Ti isotopic patterns. SNe are therefore possible progenitors for HD graphite grains with high ^{12}C/^{13}C ratios (> 100), which are characteristic of the He/C zone, where the plurality of material likely originates (Groopman *et al.*, 2012, 2014) and C/O > 1, a condition favorable for carbonaceous grain condensation.

7.3 Experimental Methods

C and Si measurements were performed using a Cs$^+$ primary beam, while K, Ca, and Ti measurements were performed using an O$^-$ beam. K and Ca positive secondary ions were measured in peak-jumping, multidetection mode using two magnetic fields: ^{12}C, ^{39}K, ^{41}K, ^{43}Ca, and ^{48}Ti (#1); and ^{40}Ca, ^{42}Ca, ^{44}Ca, ^{49}Ti (#2). Ti secondary ions were measured using three fields: ^{12}C, ^{40}Ca, ^{46}Ti, ^{48}Ti, and ^{50}Ti (#1); ^{47}Ti, ^{49}Ti, and ^{51}V (#2); and ^{48}Ti, ^{50}Ti,

and ^{52}Cr (#3). For the Ti isotopes we measured ^{40}Ca to correct for isobaric interferences from ^{46}Ca and ^{48}Ca, assuming solar isotopic abundances, while ^{51}V and ^{52}Cr were used to correct for interferences from ^{50}V and ^{50}Cr. There exists a considerable amount of Cr contamination on the graphite grains due to the dichromate treatment (Jadhav *et al.*, 2006; Amari *et al.*, 1994) used in the meteorite's acid dissolution. This contamination makes it difficult to unambiguously determine ^{50}Ti/^{48}Ti ratios.

7.4 HD Grain Results

7.4.1 C Isotopes

The majority of grains have ^{12}C/^{13}C ratios > solar (=89), ranging up to ^{12}C/^{13}C = 805 (Figure 7.1). Three grains (OR1g2m-5, hereafter g5; OR1f4m-4, f4; OR1f4m-14, f14) fall into the ^{13}C-rich subgroup with ^{12}C/^{13}C < 20. Two grains (f7, g6) have near-solar ^{12}C/^{13}C ratios and minor anomalies, if any, in other isotope systems; these are not unambiguously presolar.

7.4.2 K and Si isotopes

Most grains have normal K isotopic compositions. f2 contains a ^{41}K excess, indicative of the initial presence of ^{41}Ca, which coupled with a small excess in ^{28}Si indicates a SN origin. A number of grains contain small Si anomalies, although they are not unambiguously indicative of a specific stellar origin (Figure 7.2).
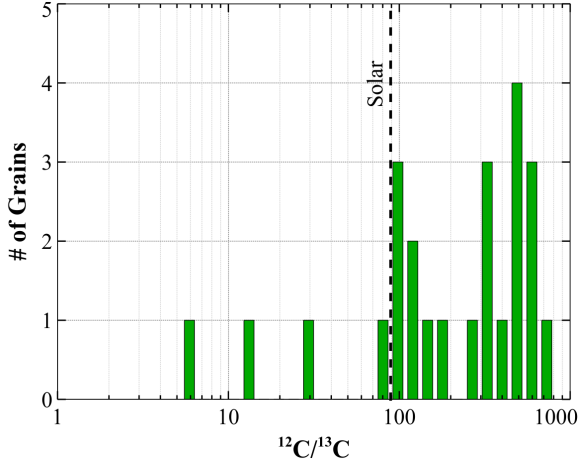
FIGURE 7.1: Distribution of $^{12}C/^{13}C$ ratios for HD graphite grains in this study. The majority of grains contain excesses in ^{12}C relative to solar. The grains with the lowest $^{12}C/^{13}C$ ratios also have extreme Ca and Ti isotope anomalies, indicative of a Born-Again AGB star origin (see Figures 7.3 & 7.7).
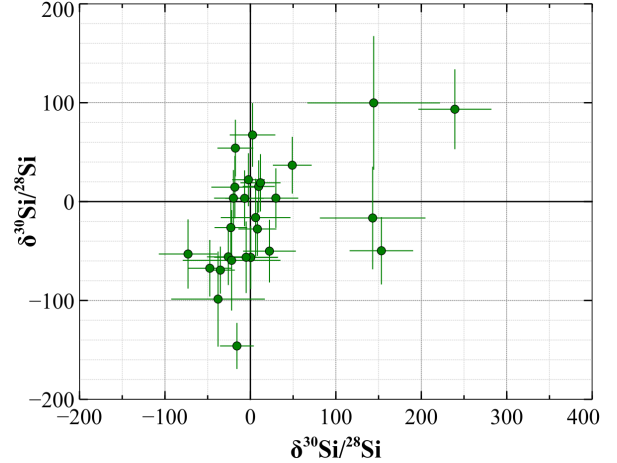
FIGURE 7.2: Si 3-isotope plot. The majority of grains do not have significant Si isotopic anomalies. Error bars are 1σ.

7.4.3 Ti isotopes

Of the three grains in the $^{12}C/^{13}C < 20$ group (f4, f14, g5), f4 and f14 have very large anomalies in their Ti isotopes (Figure 7.3). These patterns are indicative of a Born-Again AGB origin (Jadhav *et al.*, 2008, 2013b). Grain g5, however, with $^{12}C/^{13}C = 5$, contains excesses of $\sim$450 ‰ in $^{46,47}Ti$, but contains a much smaller excess in ^{49}Ti. Cr contamination on g5 was too large to accurately determine its $^{50}Ti/^{48}Ti$ ratio. A SN origin for g5 would require a mix of material predominantly from the He/N zone, where $^{12}C/^{13}C$ is very low, with contributions from an O-rich zone to explain the $^{46,47}Ti$ excesses (Jadhav *et al.*, 2011). A Born-Again AGB origin would also explain the low $^{12}C/^{13}C$ ratio and $^{46,47}Ti$ excesses.

However, it remains difficult to reconcile either of these explanations with its modest ^{49}Ti excess.

Grains f5, f9, f13, and g9, with ^{12}C/^{13}C > 320 (Figure 7.4), also contain large anomalies in their Ti isotopes, which are outside of the range predicted by AGB models (Cristallo *et al.*, 2009), though smaller than those from the ^{12}C/^{13}C < 20 group. f5, f9, and f13 have a relatively small correction to mass 50, thus the measured ^{50}Ti anomalies are not likely artifacts; g9 has a larger correction, although its Ti pattern follows the others. Additionally, these four graphite grains are among the eight from these suites with evidence for internal TiC subgrains, based upon their Ti depth profiles (see e.g. Figure 7.5). f9 contained at least eight peaks in its Ti NanoSIMS depth profile, which are indicative of small subgrains. We will get more conclusive evidence for their origins by examining the graphite grains in the TEM and using EDXS to search for enrichments in *s-process* elements such as Zr and Ru.

7.4.4   Ca Isotopes

Grains f5, f9, and f13 do not contain resolvable Ca isotope anomalies due to large errors from poor counting statistics. Grain f14 contains large excesses in ^{42,43,44}Ca (Figure 7.7), consistent with a possible Born-Again AGB origin (Figure 7.7) (Jadhav *et al.*, 2008). Both f14 and f4 exhibit a classic neutron capture pattern in the Ca isotopes. f14 does not have evidence for any subgrains, based upon its Ti depth profile.
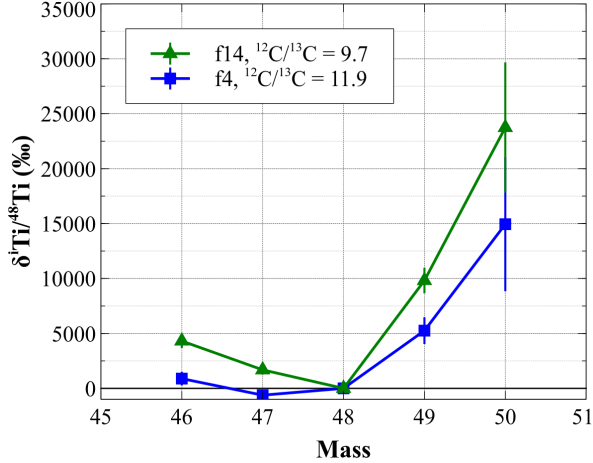
FIGURE 7.3: Extreme Ti isotope anomalies in HD presolar graphite grains with low ^{12}C/^{13}C ratios. These patterns suggest a Born-Again AGB star origin.
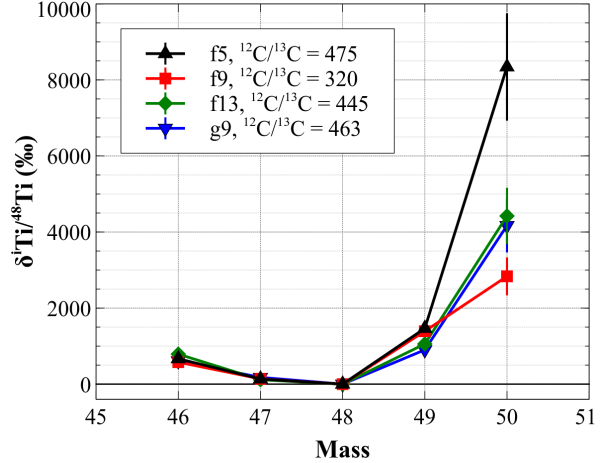
FIGURE 7.4: Large Ti isotope anomalies in HD presolar graphite grains with high ^{12}C/^{13}C ratios. These anomalies are not as extreme as those in Figure 7.3. These patterns suggest a SN origin.

7.5 LD Grain Results

Most of the OR1d6m LD graphite grains contain isotopic signatures of a SN origin, including excesses in ^{15}N, ^{18}O, ^{28}Si, and high inferred initial ^{26}Al/^{27}Al ratios (Groopman *et al.*, 2012). Figure 7.9 shows the Ti isotopic pattern of the LD graphite grains and models of the He/C and He/N zones in 15 and 20 M$_\odot$SNe (Rauscher *et al.*, 2002). A gas mixture of He/C and He/N zone material is thought to be the most likely origin for most of these grains as they are the only SN regions where C/O > 1 (Groopman *et al.*, 2012, 2014). The Ti patterns of the LD graphite grains with resolvable ^{50}Ti/^{48}Ti ratios match the predictions for the He/C zone well and also match those of SiC X grains (Lin *et al.*, 2010). d4 and d24, however, with low ^{12}C/^{13}C ratios, are more consistent with models of the He/N zone, whose
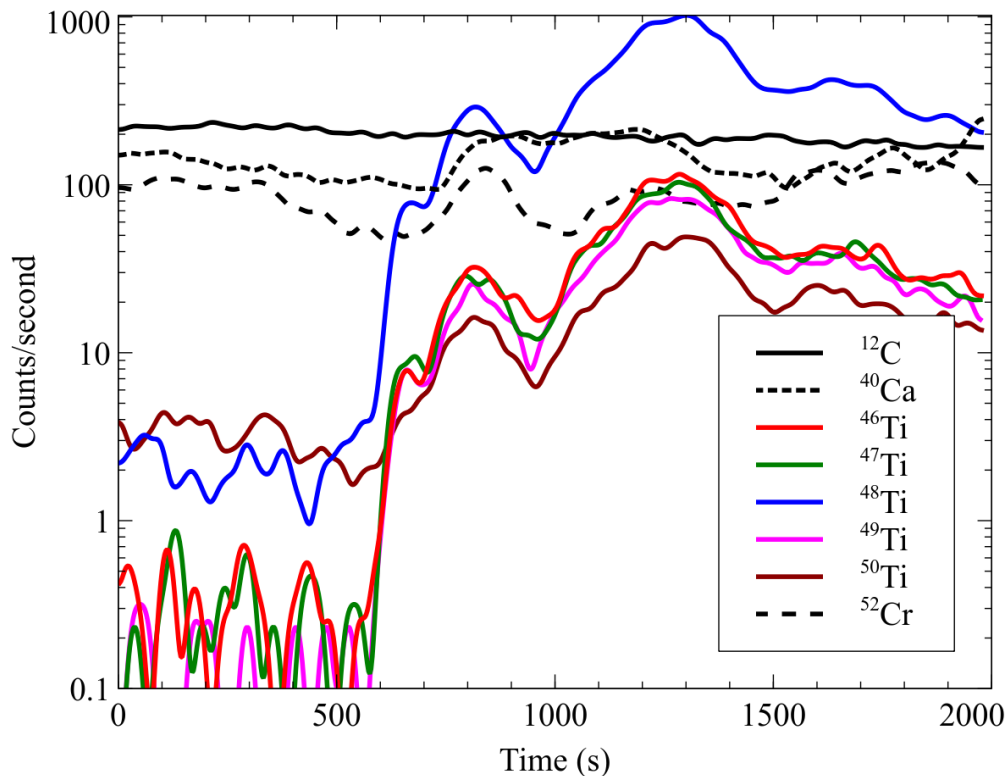
FIGURE 7.5: Ti depth profile of grain OR1f4m-12 (f12). The rise in the Ti signals is due to the sputtering of Ti-rich subgrains, which contain the vast majority of Ti within presolar graphite grains. Ca, on the other hand, is more uniformly distributed throughout the graphite structure. The majority of Cr is contamination from the meteorite's acid dissolution.

Ti isotopic composition is nearly solar.

7.6 Discussion

The isotopic compositions of HD and LD graphite grains are markedly different, suggesting a variety of progenitor environments. LD graphite grains appear to form primarily from various mixtures of SN He/C and He/N zone material, similar to SiC X grains. While most HD graphite grains match the isotopic compositions of low-metallicity AGB stars, it
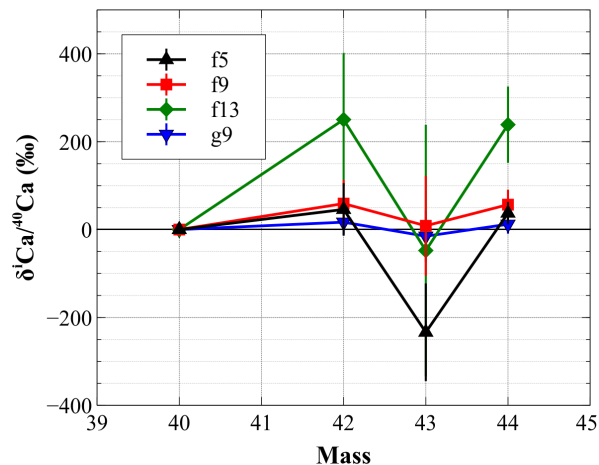
FIGURE 7.6: The grains shown in Figure 7.4 do not contain resolvable Ca isotope anomalies. There is no definitive evidence for extinct ^{44}Ti, which would unambiguously imply a SN origin
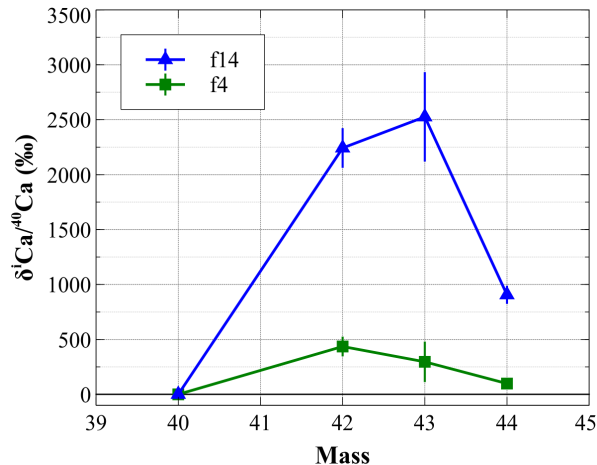
FIGURE 7.7: Large Ca isotope anomalies in a neutron capture pattern in grains from a Born-Again AGB star (see Figure 7.3).

has been suggested that those with large or extreme Ti and Ca anomalies could form either from a mix of He/C, He/N, and O-rich zone material from SNe (those with high ^{12}C/^{13}C) or from Born-Again AGB stars (for both, high and low ^{12}C/^{13}C ratios) (Jadhav *et al.*, 2008, 2013a,b; Amari *et al.*, 2014).

The crystalline structure of presolar graphite grains has been found to be very sensitive to the O content of the surrounding gas; higher O content (with C/O > 1) appears to inhibit the formation of well-ordered graphite, resulting instead in turbostratic layering, characteristic of LD graphite grains (Croat *et al.*, 2008). This appears incompatible with HD graphite grains forming from a mix of O-rich, He/C, and He/N zone material, as HD graphite grains are more highly crystalline than their LD counterparts. The presence of TiC subgrains also requires C/O $\sim$ 1 under reasonable stellar atmospheric pressures (Bernatowicz *et al.*, 1996). The Ti signals for f5, f9, f13, and g9 are dominated by contributions from TiC subgrains,

while the Ca signal is primarily from the host graphite. This would appear to indicate that the TiC subgrains formed from material with a larger contribution from O-rich zones than material that formed the host graphite grain. These grains are similarly difficult to reconcile with a Born-Again AGB origin since a large fraction of C must come from the He intershell (high ^{12}C/^{13}C ratios), yet we do not observe the concomitant Ca anomalies. Future TEM investigations will shed light on the microstructural properties of these grains and the grains' formation conditions.

For more recent peer-reviewed discussions of HD presolar graphite grains from Born-Again AGB stars and SNe, the reader is directed to Jadhav *et al.* (2013a,b).
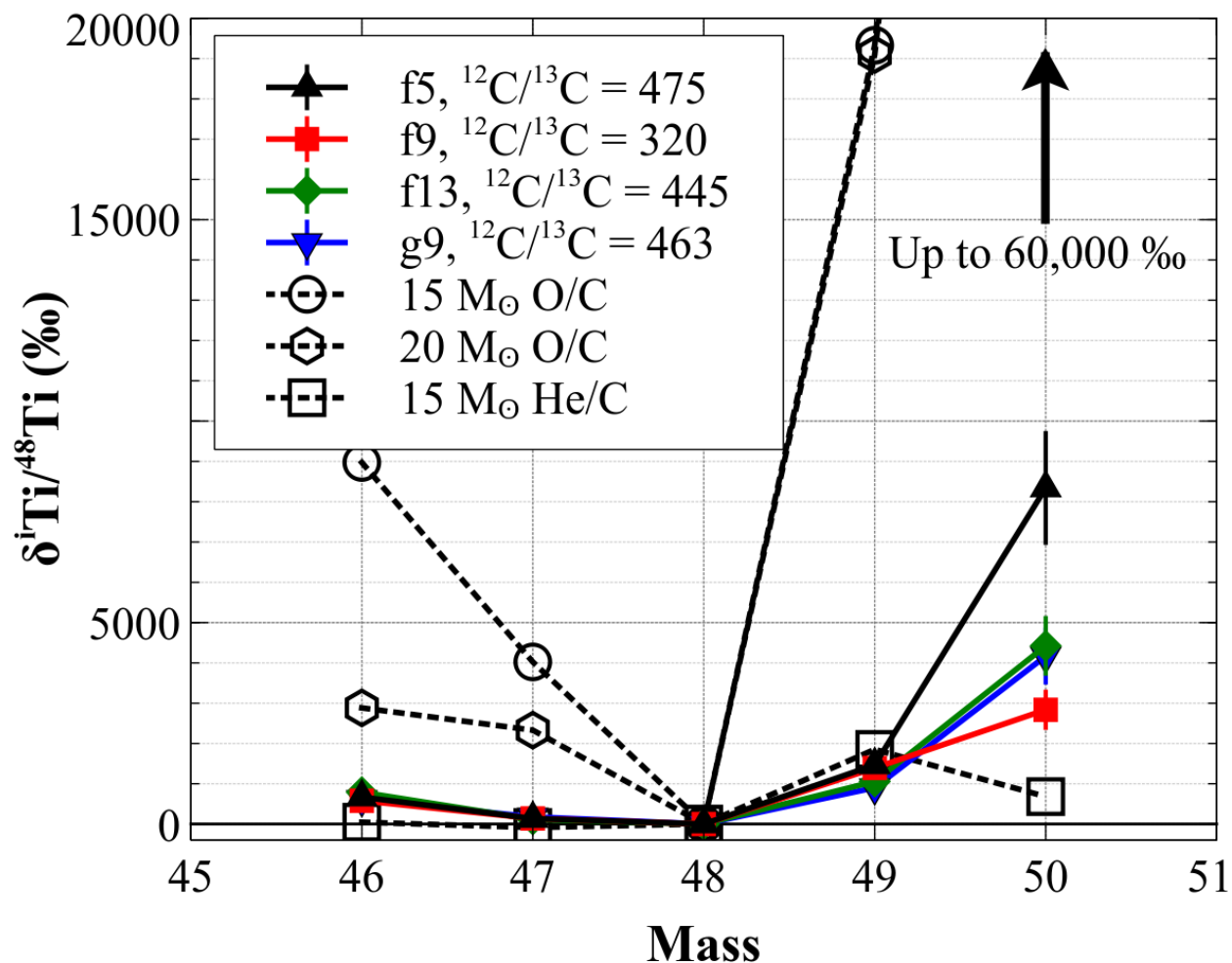
FIGURE 7.8: HD presolar graphite grains from Figure 7.4 with average Ti isotope compositions from the He/C and O/C zones in 15 and 20 M$_\odot$ SN models (Rauscher *et al.*, 2002). A small amount of material from the O/C zone may result in the large observed Ti isotope anomalies in these grains, however the majority of material must still come from zones with C/O > 1, such as the He/C and He/N zones, for carbonaceous condensation to occur.
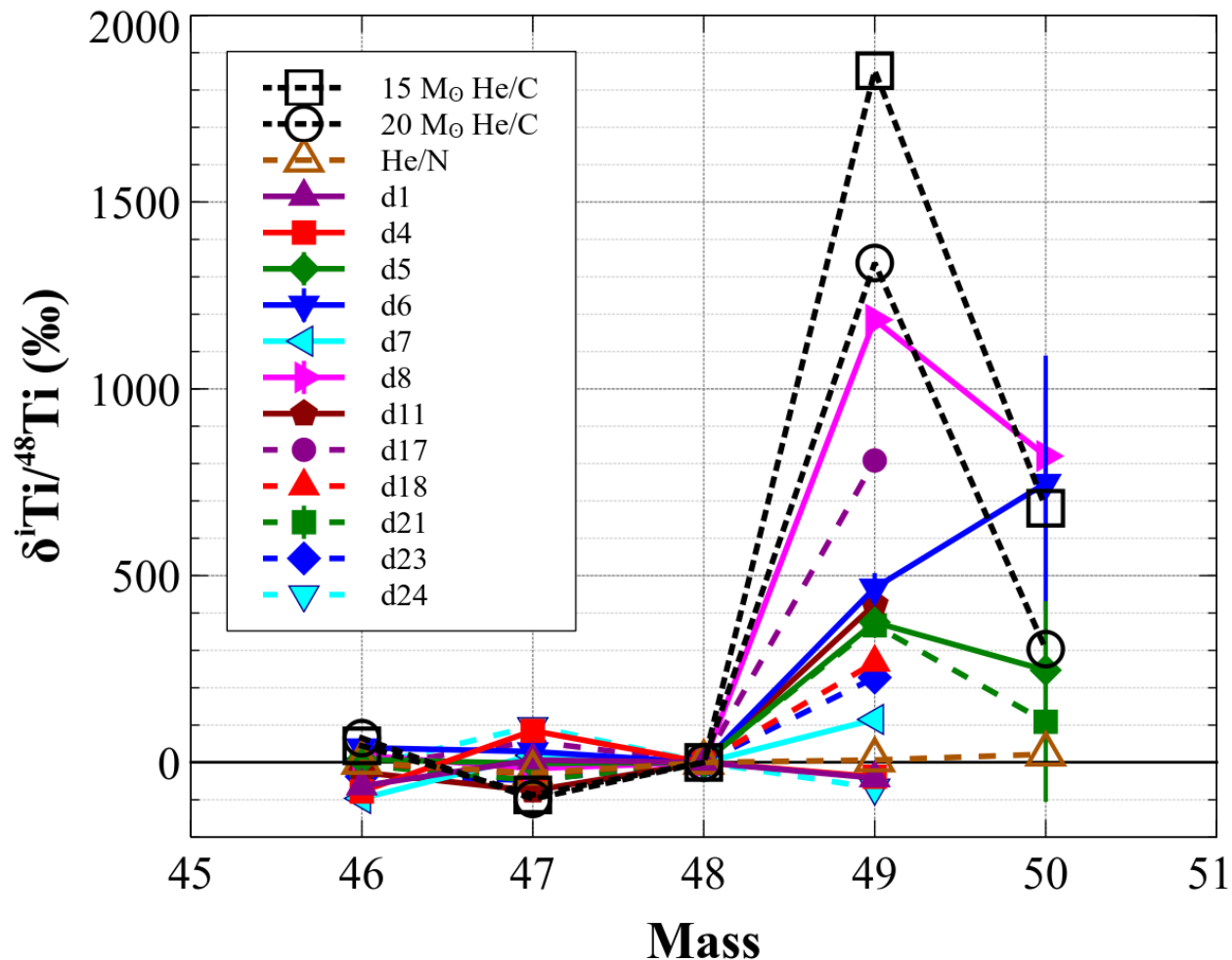
FIGURE 7.9: Ti isotope patterns for LD presolar graphite grains. Many of these grains appear to match the isotopic pattern from a mixture of He/C and He/N zone material, although there are a few discrepancies. The correction for the isobaric interference of ^{50}Cr on ^{50}Ti is high due to the large Cr abundance, so the errors on ^{50}Ti are too large (not shown). Additionally, most grains appear to have lower enrichments in ^{46}Ti and higher enrichments in ^{47}Ti than the calculated patterns for these zones.

Bibliography

Amari, S., Lewis, R. S., & Anders, E. (**1994**), "Interstellar grains in meteorites: I. Isolation of SiC, graphite and diamond; size distributions of SiC and graphite", *Geochimica et Cosmochimica Acta* **58**, 459–470, URL http://dx.doi.org/10.1016/0016-7037(94)90477-4.

Amari, S., Zinner, E., & Gallino, R. (**2014**), "Presolar graphite from the Murchison meteorite: An isotopic study", *Geochimica et Cosmochimica Acta* **133**, 479–522, URL http://dx.doi.org/10.1016/j.gca.2014.01.006.

Bernatowicz, T. J., Cowsik, R., Gibbons, P. C. ., Lodders, K., Jr., B. F., Amari, S., & Lewis, R. S. (**1996**), "Constraints On Stellar Grain Formation From Presolar Graphite In The Murchison Meteorite", *The Astrophysical Journal* **472**, 760–782, URL http://dx.doi.org/10.1086/178105.

Cristallo, S., Straniero, O., Gallino, R., L., P., Domínguez, I., & Lederer, M. T. (**2009**), "Evolution, Nucleosynthesis, and Yields of Low-Mass Asymptotic Giant Branch Stars at Different Metallicities", *The Astrophysical Journal* **696**, 797–820, URL http://dx.doi.org/10.1088/0004-637X/696/1/797.

Croat, T. K., Stadermann, F. J., & Bernatowicz, T. J. (**2008**), "Correlated isotopic and microstructural studies of turbostratic presolar graphite from the Murchison meteorite", *Meteoritics & Planetary Science* **43**, 1497–1516, URL http://dx.doi.org/10.1111/j.1945-5100.2008.tb01024.x.

Groopman, E., Bernatowicz, T., & Zinner, E. (**2012**), "C, N, And O Isotopic Heterogeneities In Low-density Supernova Graphite Grains From Orgueil", *The Astrophysical Journal Letters* **754**, L8–L13, URL http://dx.doi.org/10.1088/2041-8205/754/1/L8.

Groopman, E., Nittler, L. R., Bernatowicz, T., & Zinner, E. (**2014**), "NANOSIMS, TEM, and XANES Studies of a Unique Presolar Supernova Graphite Grain", *The Astrophysical Journal* **790**, 9–21, URL http://dx.doi.org/10.1088/0004-637X/790/1/9.

Jadhav, M., Amari, S., Marhas, K. K., Zinner, E., Maruoka, T., & Gallino, R. (**2008**), "New stellar sources for high-density, presolar graphite grains", *The Astrophysical Journal* **682**, 1479–1485, URL http://dx.doi.org/10.1086/589139.

Jadhav, M., Amari, S., Zinner, E., & Maruoka, T. (**2006**), "Isotopic analysis of presolar graphite grains from Orgueil", *New Astronomy Review* **50**, 591–595, URL http://dx.doi.org/10.1016/j.newar.2006.06.004.

Jadhav, M., Pignatari, M., Herwig, F., Zinner, E., Gallino, R., & Huss, G. R. (**2013b**), "Relics of Ancient Post-AGB Stars in a Primitive Meteorite", *The Astrohpysical Journal Letters* **777**, L27, URL http://dx.doi.org/10.1088/2041-8205/777/2/L27.

Jadhav, M., Zinner, E., Amari, S., & Maruoka, T. (**2011**), "More Ca and Ti Isotopic Ratios in High-Density, Presolar Graphite Grains from Orgueil", in "42nd Lunar and Planetary Science Conference", Abstract #1599, Lunar and Planetary Institute, Houston, URL http://www.lpi.usra.edu/meetings/lpsc2011/pdf/1599.pdf.

Jadhav, M., Zinner, E., Amari, S., Maruoka, T., Marhas, K. K., & Gallino, R. (**2013a**), "Multi-element isotopic analyses of presolar graphite grains from Orgueil", *Geochimica et Cosmochimica Acta* **113**, 193–224, URL http://dx.doi.org/http://dx.doi.org/10.1016/j.gca.2013.01.018.

Lin, Y., Gyngard, F., & Zinner, E. (**2010**), "Isotopic Analysis of Supernova SiC and Si3N4 Grains from the Qingzhen (EH3) Chondrite", *The Astrophysical Journal* **709**, 1157–1173, URL http://stacks.iop.org/0004-637X/709/i=2/a=1157.

Rauscher, T., Heger, A., Hoffman, R. D., & Woosley, S. E. (**2002**), "Nucleosynthesis in Massive Stars with Improved Nuclear and Stellar Physics", *The Astrophysical Journal* **576**, 323–348, URL http://dx.doi.org/10.1086/341728.

Chapter 8

pyLATTICE: A Program for Electron Diffraction Simulation

8.1   Preface

pyLATTICE is a program written to calculate and plot electron diffraction patterns for arbitrary crystals. **pyLATTICE** is written using `Python` and `Qt` and is based upon the program **LATTICE**, written by Prof. Thomas Bernatowicz. The source code and compiled binaries are freely available to use and distribute under the GNU Public License v.2 at https://github.com/eegroopm/pyLATTICE.

8.2   Introduction

The original **LATTICE** program by Bernatowicz (1989) was written to aid in scientific investigations in which crystallographic results play an important role, especially as means to accomplish some other goal. In the field of presolar grain study, crystallographic characteri-

zation of a presolar mineral in not end-goal of the investigation; rather it is an intermediate step in characterizing the physical and chemical conditions present in the presolar grain's progenitor star at the time of grain formation. **LATTICE**'s intent was to make laborious and time-consuming calculations straight-forward and user-friendly, making extensive use of the crystal lattice metric tensor for computations. **LATTICE** was written in `QuickBASIC` and runs on DOS, and is now only usable with a DOS emulator on a modern computer. In keeping with the spirit of the original software, **pyLATTICE** has been rewritten and updated with a graphical user interface (GUI), which does away with linear step-by-step prompts and replaces them with complete user interactivity. **pyLATTICE** is written using the freely available and popular programming languages `Python` and `Qt`, and is designed to be platform-independent, working on Linux, Windows, and Mac OS.

This chapter provides an introduction to crystallography as it applies to **pyLATTICE**'s backend in addition to **pyLATTICE**'s frontend documentation. **pyLATTICE** is also highly extensible, as it comes packaged with a fully-functional `IPython` interpreter (see Section 8.6.4), which allows the user not only to interact via the command line with **pyLATTICE**'s parameters, but also the user's system. If the user has his own local `Python` installation, packages not bundled or required by **pyLATTICE** may be imported and used within the program. Full automation of **pyLATTICE**'s calculations and/or use of user-defined functions are possible via scripting.

8.3 Background and Theory

8.3.1 Crystals: Direct and Reciprocal Lattices

A crystal is any three-dimensional repeating set of atoms on a lattice. A crystal in real space is defined by its unit cell, the simplest repeating unit of atoms, where each atom resides at a specific lattice point. There are seven different geometries for unit cells, including cubic, tetragonal, hexagonal, monoclinic, orthorhombic, rhombohedral, and triclinic. Each unit cell geometry has one or more possible arrangements of atoms (different lattices, e.g., primitive, face centered, body centered), which satisfy the requirement that they may be repeated in three dimensions. There are 14 such Bravais unit cells which define all crystals.

Since all crystals are composed of repeating unit cells in three dimensions, with each unit cell consisting of atoms on a lattice, we may define any point $\vec{p}$ on the crystal lattice in terms of the lattice's basis vectors, $\vec{a}$, $\vec{b}$, $\vec{c}$:

$$\vec{p} = x\vec{a} + y\vec{b} + z\vec{c} \tag{8.1}$$

where x, y, and z are integers. Importantly, the basis vectors for a crystal need not be

orthogonal to each other. The angles between the basis vectors are given by:

$$\alpha = \angle \vec{b}\vec{c} \tag{8.2}$$

$$\beta = \angle \vec{a}\vec{c} \tag{8.3}$$

$$\gamma = \angle \vec{a}\vec{b} \tag{8.4}$$

The metric tensor of this basis, $\mathbf{G}$, contains all of the vector length and angular information:

$$\mathbf{G} = \begin{pmatrix} \vec{a} \cdot \vec{a} & \vec{a} \cdot \vec{b} & \vec{a} \cdot \vec{c} \\ \vec{b} \cdot \vec{a} & \vec{b} \cdot \vec{b} & \vec{b} \cdot \vec{c} \\ \vec{c} \cdot \vec{a} & \vec{c} \cdot \vec{b} & \vec{c} \cdot \vec{c} \end{pmatrix} \tag{8.5}$$

$$= \begin{pmatrix} a^2 & ab\cos(\gamma) & ac\cos(\beta) \\ ba\cos(\gamma) & b^2 & bc\cos(\alpha) \\ ca\cos(\beta) & cb\cos(\alpha) & c^2 \end{pmatrix} \tag{8.6}$$

Calculating and plotting diffraction patterns from crystals involves utilizing the concept of the reciprocal lattice. For a full discussion of this concept and electron diffraction in general, see e.g., Williams & Carter (1996). Just as each crystal has a real (direct) lattice which describes the arrangement of atoms in the crystal's unit cell, each crystal also has a reciprocal lattice, where each point corresponds to a specific set of planes in the crystal. In the reciprocal lattice, any point may similarly be given by the reciprocal lattice vector $\vec{p^*}$:

$$\vec{p^*} = h\vec{a^*} + k\vec{b^*} + \ell\vec{c^*} \tag{8.7}$$

where $\vec{a^*}$, $\vec{b^*}$, and $\vec{c^*}$ are the basis vectors of the reciprocal lattice and h, k, and ℓ are integers. This reciprocal lattice vector is **normal** to the lattice plane $(kh\ell)$ (see Section 8.4 for a brief discussion of crystallographic nomenclature). The reciprocal lattice metric tensor, $\mathbf{G}^*$ is simply the matrix inverse of the real metric tensor: $\mathbf{G}^* = \mathbf{G}^{-1}$. The tensor $\mathbf{G}^*$ is also symmetrical across its diagonal and can be constructed by analogy from $\mathbf{G}$ by replacing all lengths and angles by their starred (*) analogues.

$$\mathbf{G}^* = \begin{pmatrix} (a^*)^2 & a^*b^* \cos(\gamma^*) & a^*c^* \cos(\beta^*) \\ b^*a^* \cos(\gamma^*) & (b^*)^2 & b^*c^* \cos(\alpha^*) \\ c^*a^* \cos(\beta^*) & c^*b^* \cos(\alpha^*) & (c^*)^2 \end{pmatrix} \tag{8.8}$$

After calculating $\mathbf{G}^{-1}$, one may easily solve for the reciprocal lattice basis vector lengths and angles. For instance, $a^* = \sqrt{\mathbf{G}^{-1}[1,1]}$, where $\mathbf{G}^{-1}[1,1]$ is the [1,1] element of the inverse of the real metric tensor. Similarly, α^* may be calculated as either:

$$\alpha^* = \arccos\left(\frac{\mathbf{G}^{-1}[2,3]}{b^*c^*}\right) \text{ OR } \arccos\left(\frac{\mathbf{G}^{-1}[3,2]}{b^*c^*}\right) \tag{8.9}$$

The volume of the direct lattice unit cell is given by the square root of the determinant of $\mathbf{G}$. The volume of the reciprocal lattice unit cell is similarly calculated from the determinant of $\mathbf{G}^*$:

$$\mathcal{V} = \sqrt{|\mathbf{G}|} \tag{8.10}$$

$$\mathcal{V}^* = \frac{1}{\mathcal{V}} = \sqrt{|\mathbf{G}^*|} \tag{8.11}$$

185

8.3.2 Calculating D-spacings

As mentioned above, each crystal contains two lattices: the direct or real lattice, which describes the locations of atoms within a crystal's unit cell; and the reciprocal lattice, which corresponds to planes of atoms in the crystal. Each point in the reciprocal lattice, described by the vector $\vec{q} = h\vec{a^*} + k\vec{b^*} + \ell\vec{c^*}$, corresponds to a <u>plane</u> $(hk\ell)$ in the direct lattice, where h, k, and ℓ are Miller indices. We may calculate q, the magnitude of $\vec{q}$, using the matrix equation

$$q = \sqrt{Q^T \mathbf{G}^* Q} \tag{8.12}$$

where Q is a column matrix with the vector components of $\vec{q}$ as its elements

$$Q = \begin{bmatrix} h \\ k \\ \ell \end{bmatrix} \tag{8.13}$$

and Q^T is its transpose. Therefore

$$q = \left(\begin{bmatrix} h & k & \ell \end{bmatrix} \mathbf{G}^* \begin{bmatrix} h \\ k \\ \ell \end{bmatrix} \right)^{1/2} \tag{8.14}$$

The spacing between adjacent identical planes $(kh\ell)$ is $d_{hk\ell} = 1/q$, which is referred to as the **d-spacing** for the set of equivalent planes $\{kh\ell\}$.

Determining Zone Axes

If we consider two nonparallel planes, $(h_1 k_1 \ell_1)$ and $(h_2 k_2 \ell_2)$, we know that their intersection will form a line. In a crystal, the sets of these identical planes, $\{h_1 k_1 \ell_1\}$ and $\{h_2 k_2 \ell_2\}$, will intersect along parallel lines with a direction [UVW], which is called the zone axis. In order to calculate the zone axis direction between two different lattice planes or sets of planes, we can calculate the cross product of the reciprocal lattice vectors, which are normal to these planes, $\vec{q_1} = h_1 \vec{a^*} + k_1 \vec{b^*} + \ell_1 \vec{c^*}$ and $\vec{q_2} = h_2 \vec{a^*} + k_2 \vec{b^*} + \ell_2 \vec{c^*}$, respectively.

$$
\begin{aligned}
\vec{p} &= \vec{q_1} \times \vec{q_2} & (8.15) \\
&= \mathcal{V}^* \begin{vmatrix} \vec{a} & \vec{b} & \vec{c} \\ h_1 & k_1 & \ell_1 \\ h_2 & k_2 & \ell_2 \end{vmatrix} & (8.16) \\
&= \mathcal{V}^* \left((k_1 \ell_2 - k_2 \ell_1)\vec{a} + (\ell_1 h_2 - h_1 \ell_2)\vec{b} + (h_1 k_2 - h_2 k_1)\vec{c} \right) & (8.17)
\end{aligned}
$$

Notice that the vector $\vec{p}$ is given in terms of the basis vectors of the <u>direct</u> lattice, not the reciprocal lattice. We may therefore observe that the zone axis direction [UVW] is given by:

$$
\begin{aligned}
U &= k_1 \ell_2 - k_2 \ell_1 & (8.18) \\
V &= \ell_1 h_2 - h_1 \ell_2 & (8.19) \\
W &= h_1 k_2 - h_2 k_1 & (8.20)
\end{aligned}
$$

Additionally, since we are only concerned about the zone axis direction, the reciprocal lattice unit cell volume, a constant, is unnecessary. Any zone axes may be reduced to their least common factors, e.g., [220] is reducible to [110], and [633] is reducible to [211].

Note: If we imagine a set of faces on a cubic (isometric) crystal such as (100), (101), (001), (-100) we know that these lie along the same crystal zone, as their intersections are all parallel (in this case parallel to [010]). This zone direction is clearly normal to the (010) plane and thus parallel to its reciprocal lattice vector. One must be careful, however, because real and reciprocal lattice vectors with the same indices, e.g., [010] and (010), are *parallel only in cubic materials.*

Additionally, one may calculate the angle (ϕ) between the two planes by calculating the dot product of their vector normals:

$$|\vec{q_1}||\vec{q_2}|\cos\phi \;\;=\;\; \vec{q_1} \cdot \vec{q_2} \tag{8.21}$$

$$\cos\phi \;\;=\;\; \frac{h_1 h_2 + k_1 k_2 + \ell_1 \ell_2}{\sqrt{h_1^2 + k_1^2 + \ell_1^2}\sqrt{h_2^2 + k_2^2 + \ell_2^2}} \tag{8.22}$$

while one may similarly calculate the angle (ρ) between two directions $[U_1 V_1 W_1]$ and $[U_2 V_2 W_2]$:

$$\cos\rho \;\;=\;\; \frac{U_1 U_2 + V_1 V_2 + W_1 W_2}{\sqrt{U_1^2 + V_1^2 + W_1^2}\sqrt{U_2^2 + V_2^2 + W_2^2}} \tag{8.23}$$

Weiss Zone Law

Due to the multiplicity of planes and vectors in both the real and reciprocal lattices, we must define an origin for our reciprocal lattice. We define the origin to lie in the reciprocal

lattice plane (UVW), which we will call the Zero-Order Laue Zone (ZOLZ; N=0) and which is defined by the direction [UVW]. A zone of any order may similarly be defined by having a reciprocal lattice plane (UVW) with a [UVW] normal vector, however it will be the Nth such plane from the reciprocal lattice origin. For a reciprocal lattice point $(kh\ell)$ representing a direct lattice plane to lie in the Nth order reciprocal lattice plane (UVW), it must satisfy:

$$hU + kV + \ell W = N \qquad (8.24)$$

While it is possible to calculate d-spacings for reciprocal lattice points in any order Laue zone, we will focus on the N=0 reciprocal lattice plane (UVW), which contains the origin, from here on. In order to generate graphics in **pyLATTICE**, this condition must be applied.

Hexagonal Crystals

Hexagonal close-packed (hcp) crystal systems require special attention when calculating distances and angles (Frank, 1965). In a hexagonal crystal the base plane contains three crystallographically-equivalent directions, which are not mutually orthogonal, and a fourth axial direction normal to the basal plane. If the direction [UVTW] lies in the plane (hkil), it satisfies the Weiss Zone Law:

$$hU + kV + iT + \ell W = 0 \qquad (8.25)$$

Critically, the vector normal to the plane $(khi\ell)$ is actually $[h, k, i, \ell/\lambda]$ and the direction $[UVTW]$ is actually $[U, V, T, \lambda W]$ in the Cartesian coordinate system. In 4-vector notation,

Equation 8.25 becomes:

$$[U, V, T, \lambda W] \cdot [h, k, i, \ell/\lambda] = 0 \tag{8.26}$$

By geometry λ can be shown to be

$$\lambda^2 = \left(\frac{2}{3}\right)\left(\frac{c}{a}\right)^2 \tag{8.27}$$

where a is the basal plane lattice parameter and c is the lattice parameter normal to the basal plane. Because the three basal directions are not mutually orthogonal, they can be represented as a 2-vector with the condition that $i = -(h + k)$, so $(1\bar{1}02)$ is equivalent to $(1\bar{1}2)$ and $(11\bar{2}1)$ is equivalent to (111). When calculating the angles between hcp planes, however, it is important to use the 4-vector dot product, which is $\underline{\text{NOT}}$ equivalent to the dot product of 3-vectors. The angle between two planes $(h_1 k_1 i_1 \ell_1)$ and $(h_2 k_2 i_2 \ell_2)$ is

$$\cos\phi = \frac{h_1 h_2 + k_1 k_2 + \frac{1}{2}(h_1 k_2 + k_1 h_2) + \frac{3}{4}\ell_1\ell_2\left(\frac{a}{c}\right)^2}{\left(h_1^2 + k_1^2 + h_1 k_1 + \frac{3}{4}(\ell_1)^2\left(\frac{a}{c}\right)^2\right)^{1/2}\left(h_2^2 + k_2^2 + h_2 k_2 + \frac{3}{4}(\ell_2)^2\left(\frac{a}{c}\right)^2\right)^{1/2}} \tag{8.28}$$

once the substitution $i = -(h+k)$ has been made. Compared to the 3-vector angle (Equation 8.22) one can see that aside from a few specific conditions, the angles between two hcp planes and two cubic planes with the same 3-vector indices will be different.

8.4   Nomenclature and Notation

The various symbols used in conjunction with Miller Indices (h, k, and ℓ) and crystallographic directions (U, V, and W) can be somewhat confusing to a beginner. Negative numbers are conventionally written with bars, so $\overline{1} = \text{-}1$ or $\overline{h} = \text{-}h$. A vector in either lattice will be written in terms of its basis vectors, e.g., $\vec{q} = h\vec{a} + k\vec{b} + \ell\vec{c}$, or in shorthand notation $[h,k,\ell]$, where commas separate the implicit basis vector directions.

- $(kh\ell)$ is a family of real lattice planes such that it is orthogonal to the direction $[h,k,\ell]$ in the reciprocal lattice. So $(kh\ell)$ is also shorthand for the direction in the reciprocal lattice.

- $\{kh\ell\}$ is the set of all planes equivalent to $(kh\ell)$ by the lattice symmetry. For instance, in a cubic crystal, (100), (010), (001), and their negative analogs are all equivalent under symmetry operations so $\{100\}$ would denote this entire set.

- $[UVW]$ denotes a particular direction in the real lattice and a particular plane in the reciprocal lattice. This reciprocal lattice plane may contain numerous $\{kh\ell\}$ points in which case the real lattice direction is the zone axis for $\{kh\ell\}$ real-space planes.

- $\langle UVW \rangle$ is the set of equivalent directions in the real lattice under symmetry operations.

- Often when denoting an indexed spot (real plane) from a diffraction pattern the brackets will be dropped. This is the case in **pyLATTICE**'s graphing window (see Figures 8.4 and 8.5).

191

The notation for planes, directions, and reflections are summarized in Table 8.1.

TABLE 8.1: Notation for Planes, Directions, and Reflections. Reproduced from Williams & Carter (1996) Table 12.1.

Real Space	Reciprocal Space	Indices
Particular Direction	Particular Plane	$[UVW]$
General Direction	General Plane	$\langle UVW \rangle$
Particular Plane	Particular Direction	$(kh\ell)$
General Plane	General Direction	$\{kh\ell\}$
Diffracting Plane	Indexed reflection	$kh\ell$

8.5 pyLATTICE Code

8.5.1 Packages

pyLATTICE is built on `Python` and `Qt`. **pyLATTICE** relies on the following package versions to run correctly (some of these are implicit dependencies of other listed packages). Other versions may work but have not been tested.

- `Python 3.4`
- `PyQt 4.10.4`
- `sip 4.15.5`
- `NumPy 1.8.1`

- `Pandas 0.14.0`
- `Matplotlib 1.3.1`
- `h5py 0.2.3`
- `IPython 2.1.0`

- openpyxl 2.0.3
- xlrd 0.9.3
- tables 3.1.1

At the time of this writing, **pyLATTICE** is compatible with `Python 2.7`, however **pyLAT-TICE**'s continued development will focus on `Python 3`, and so future compatibility is not guaranteed. <u>Important</u>: `Python 3` serializes (pickles) data differently from `Python 2` and the two methods are completely incompatible. This is important for **pyLATTICE** because HDF (.h5) files (e.g., mineral databases, space group conditions, d-space lists) saved from **pyLATTICE** running on `Python 3` cannot be read by **pyLATTICE** running on `Python 2`, and vice versa. Upon upgrading/downgrading your version of `Python`, this must be kept in mind. An easy way to convert serialized data from one `Python` version to another is to use an intermediate file format that can be read by both versions, such as CSV (.csv) or Excel (.xls).

8.5.2 Calculating D-spacings

pyLATTICE calculates d-spacings using the following matrix equation, as shown in Section 8.3,

$$d_{hkl} = \left(\begin{bmatrix} h & k & \ell \end{bmatrix} \mathbf{G}^* \begin{bmatrix} h \\ k \\ \ell \end{bmatrix} \right)^{-1/2} \tag{8.29}$$

In the process of calculating each d-spacing, **pyLATTICE** first checks whether the appropriate space group conditions and the Weiss Zone Law (Equation 8.24, $N=0$) are satisfied for the given $[UVW]$ zone axis. This implementation does not currently take advantage

of `NumPy`'s vectorization, and so can be somewhat slow. To remedy this, the routine for d-space calculations is written in `Cython`, a C extension for Python, which vastly improves the execution time of "for loops". This extension, `_dspace.pyx`, must be compiled on each independent platform and for each Python version prior to running **pyLATTICE** from source, although this is taken care of on the fly during **pyLATTICE**'s import stage with the package `pyximport`:

```python
try:
    from resources.dspace import DSpace
    print('Importing compiled "DSpace"')
except ImportError as error:
    # Attempt autocompilation.
    import pyximport
    pyximport.install()
    from resources._dspace import DSpace
    print('Building "DSpace"')
```

When running **pyLATTICE** from source the user must also pay careful attention to the system's installed `Python` version (e.g., 2+, 3+) *and* architecture (e.g., 32-bit, 64-bit). Because **pyLATTICE** requires compiled `Cython` modules to run, the user must have the appropriate tools present on the system for compilation. Additionally, the compiled module must be built with a compiler that matches the installed `Python`'s architecture. Firstly, `Python` (implying `CPython`, which is simply an implementation of `Python` written in `C` and the most common installation, not e.g., `IronPython` or `Jython`) is compiled using Microsoft's Visual C++. `Python 2` uses Microsoft Visual C++ 2008 while `Python 3` uses Microsoft Visual C++ 2010. Microsoft Visual C++ Express versions can usually be obtained from Microsoft's website free of charge. There also exist alternative C++ compilers which can be

used, such as MinGW, however as of this writing the 64-bit MinGW compiler does NOT work. The Microsoft Visual C++ Express version also do not natively come with 64-bit support, which requires locating the correct software developer kit (SDK) packages. Therefore, there are fewer options for 64-bit `Python` installations, especially on Windows. On Linux there are many more options for open-source 64-bit compilers.

In order to build one of the `Cython` extensions manually at the command line, using the Csetup.py file in the resources directory, one should type:

`$ python Csetup.py build_ext --inplace` or

`$ python Csetup.py build_ext --inplace -c mingw32`

if you are using the alternative compiler MinGW32. Each `Cython` module will only need to be compiled once. Alternatively, pre-compiled binaries are available for each operating system, though these are not updated as regularly as the source code; each binary must currently be compiled on the platform it will run on, so a Windows binary must be compiled on Windows, a Linux binary on Linux, etc. This is because the compilation process currently "freezes" the user's `Python` installation, including platform-specific compiled routines such as .dll's (Windows) or .so files (Linux). The source code does come with a setup.py script that utilizes the package `Cx_Freeze` to compile a binary on the user's current platform, which will work if all of the `Python` dependencies are installed. The user may then compile a portable copy for personal use.

8.6 Using pyLATTICE

8.6.1 Calculating D-Spacings: Input Parameters

Crystal Type
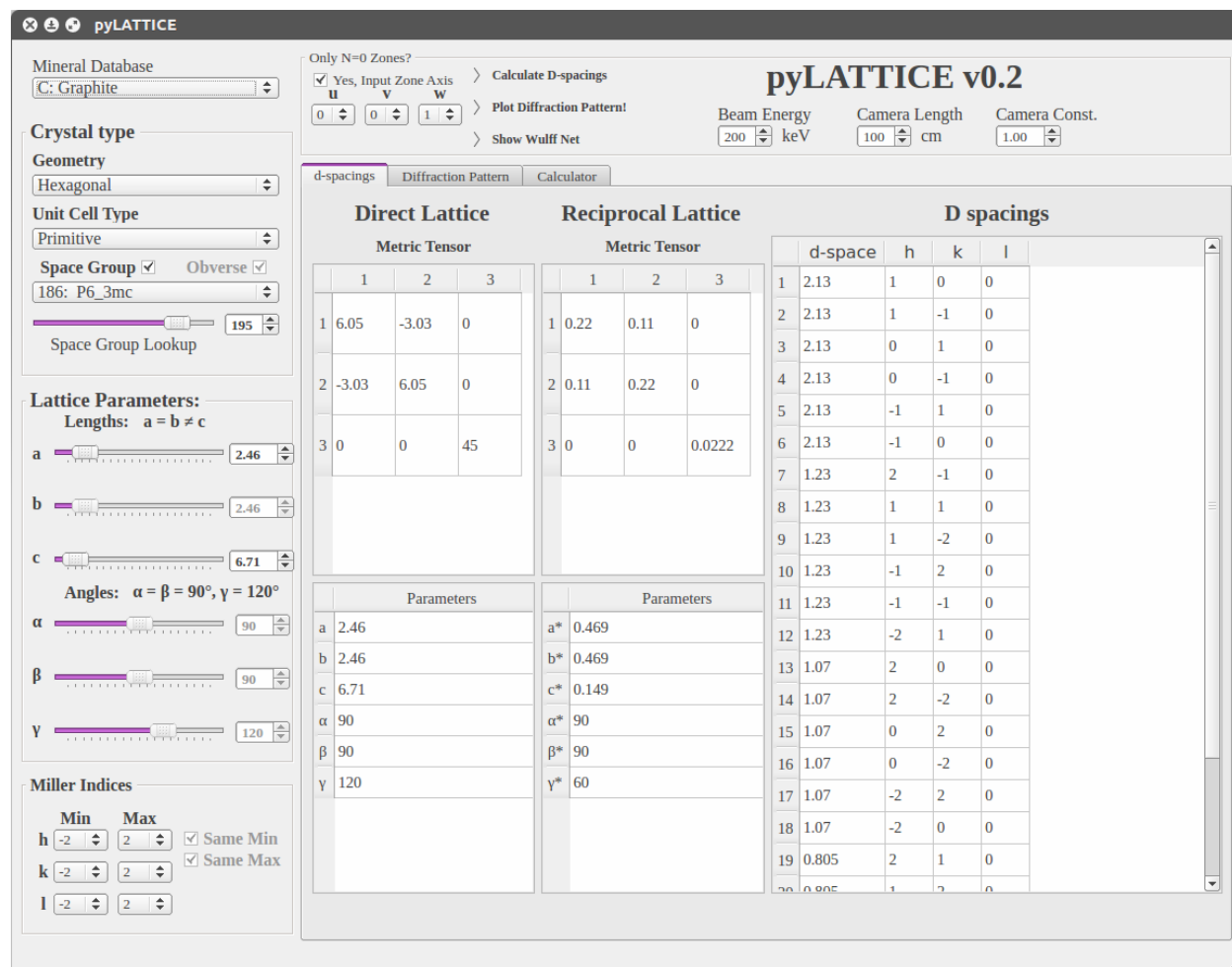
FIGURE 8.1: pyLATTICE main window. Crystal parameters are input in the combo boxes and spin boxes in the left column of the graphical user interface (GUI). The central region of the GUI contains an interface with tabs for displaying d-spacings, displaying the diffraction pattern, and for calculating angles between planes/axes directions.

To use **pyLATTICE**, the user must first select the desired crystal properties, beginning with a selection from the **Geometry** combo box under **Crystal Type** in the left column (see Figure 8.1), followed by a **Unit Cell Type** selection, and (optionally) a **Space Group** selection. There are seven possible options for the unit cell geometry:

- Cubic
- Tetragonal
- Orthorhombic

- Trigonal
- Hexagonal
- Monoclinic

- Triclinic

Selection of a unit cell **Geometry** subsequently limits the available **Unit Cell Type** selections. For instance, a *Cubic* **Geometry** selection limits the **Unit Cell Type** selections to *Primitive*, *Face Centered*, and *Body Centered*. Each **Unit Cell Type** stipulates certain general conditions for h, k, and ℓ, which must be satisfied for a given $(kh\ell)$ plane to be observed. The full list of **Unit Cell Types** and conditions is:

- (P) Simple Primitive [no conditions]

- (I) Body Centered [$h + k + \ell = n$]

- (A) (100) Faces centered [$h + k = 2n$]

- (B) (010) Faces centered [$h + \ell = 2n$]

- (C) (001) Faces centered [$k + \ell = 2n$]

- (F) (all) Faces Centered [h, k, ℓ all odd or all even]

- (H) Triply Primitive Hexagonal [no conditions]

- (R_O) Rhombohedral Lattice indexed on Hexagonal Axes: Obverse setting [$-h+k+\ell = 3n$]

- (R_R) Rhombohedral Lattice indexed on Hexagonal Axes: Reverse setting [$h - k + \ell = 3n$]

- (P_H) Primitive Hex. Lattice indexed on Rhombohedral Axes [$h + k + \ell = 3n$]

where n is an integer. One can see that for a Body Centered (I) crystal, (111) is not a valid diffracting plane since $(1 + 1 + 1)/2$ is not an integer. Planes that will result in diffraction spots include (211) and $(2\bar{2}2)$, however. The distinction between the obverse (R_O) and reverse (R_R) settings for rhombohedral lattices is primarily one of orientation, however it should be noted that certain planes may be visible in one setting and not in the other, e.g., (322) is valid in the reverse setting but not in the obverse. The **Obverse** check box becomes available in **pyLATTICE** when a rhombohedral unit cell is selected; it remains disabled otherwise.

From here, the user may (optionally) choose a valid **Space Group** for their desired crystal. The **Space Group** numbers are available for each **Geometry** (Table 8.2), while a **Unit Cell Type** selection will further limit the options in the **Space Group** combo box. By default **pyLATTICE** uses the most general conditions for each space group. The user may, however, manually enter special reflection conditions for specific multiplicities and site symmetries (see Section 8.6.3). The full set of General and Special conditions for each Space Group and origin selection can be found in the *International Tables for Crystallography* (Hahn, 1989). **pyLATTICE** also contains a Space Group Lookup feature, operated by the slider in the **Crystal Type** box or by its accompanying spin box. The crystal geometry and Patterson symbol will be displayed for any space group number.

TABLE 8.2: Space groups for each crystal geometry.

Geometry	Space Group Numbers	# Members
Triclinic	1–2	2
Monoclinic	3–15	13
Orthorhombic	16–74	59
Tetragonal	75–142	68
Trigonal	143–167	25
Hexagonal	168–194	27
Isometric (Cubic)	195–230	36

Lattice Parameters

The lattice parameters (a, b, c) and angles (α, β, γ) may subsequently be entered for the desired crystal. There are restrictions based upon the selected **Geometry**, however, which are displayed above the sliders and summarized in Table 8.3.

TABLE 8.3: Constraints on lattice parameters and angles based upon crystal geometry.

Geometry	Lattice Parameters	Angles
Cubic	$a = b = c$	$\alpha = \beta = \gamma = 90°$
Tetragonal	$a = b \neq c$	$\alpha = \beta = \gamma = 90°$
Orthorhombic	$a \neq b \neq c$	$\alpha = \beta = \gamma = 90°$
Trigonal	$a = b \neq c$	$\alpha = \beta = 90°; \ \gamma = 120°$
Hexagonal	$a = b \neq c$	$\alpha = \beta = 90°; \ \gamma = 120°$
Monoclinic	$a \neq b \neq c$	$\alpha = \gamma = 90°$
Triclinic	$a \neq b \neq c$	

The direct and reciprocal lattice metric tensors shown in the "d-spacings" tab are updated continuously as the user changes the lattice parameters. The user may copy or save these tables by highlighting selections and right-clicking, which will bring up a context menu.

Miller Indices and Zone Axis

The user may further select a range of Miller Indices for each h, k, and ℓ, which defines the set of planes for which **pyLATTICE** will calculate d-spacings. The user may also select

a zone axis $[UVW]$ and whether **pyLATTICE** should only display d-spacings for $N = 0$ Laue Zones (a typical requirement for plotting diffraction patterns). **pyLATTICE** will only calculate d-spacings that satisfy the Weiss Zone Law (Equation 8.24).

Mineral Database

pyLATTICE contains a useful feature where the parameters of various minerals may be stored in and loaded from HDF (.h5), EXCEL (.xls, xlsx), or CSV (.csv) databases. By default, **pyLATTICE** loads the file "MineralDatabase.h5" from the local "resources" directory. This database may be altered and appended to suit the user's needs; alternatively, new databases may also be created and loaded. The database contains the following information for each entry: Name; Chemical Symbol; Crystal Geometry; Unit Cell Type; Space Group Number; Lattice Parameters a, b, and c; and Special Reflection Conditions under the headers: "Name", "Chemical", "Crystal", "UnitCell", "SpaceGroup", "a", "b", "c", "SpecialConditions". Export the default database as a .csv or .xls file for some examples.

Once a mineral database is loaded, the user may select a mineral from the combo box in the upper left of the GUI (Figure 8.2). Minerals may be removed from the current list by selecting "Remove DB Minerals", keyboard shortcut (Ctrl+R), from the "Minerals" menu. New minerals may be appended to the current list by setting all of the input parameters to their desired values and selecting "Append mineral to DB" (Ctrl+A). The database must be saved to make changes permanent.
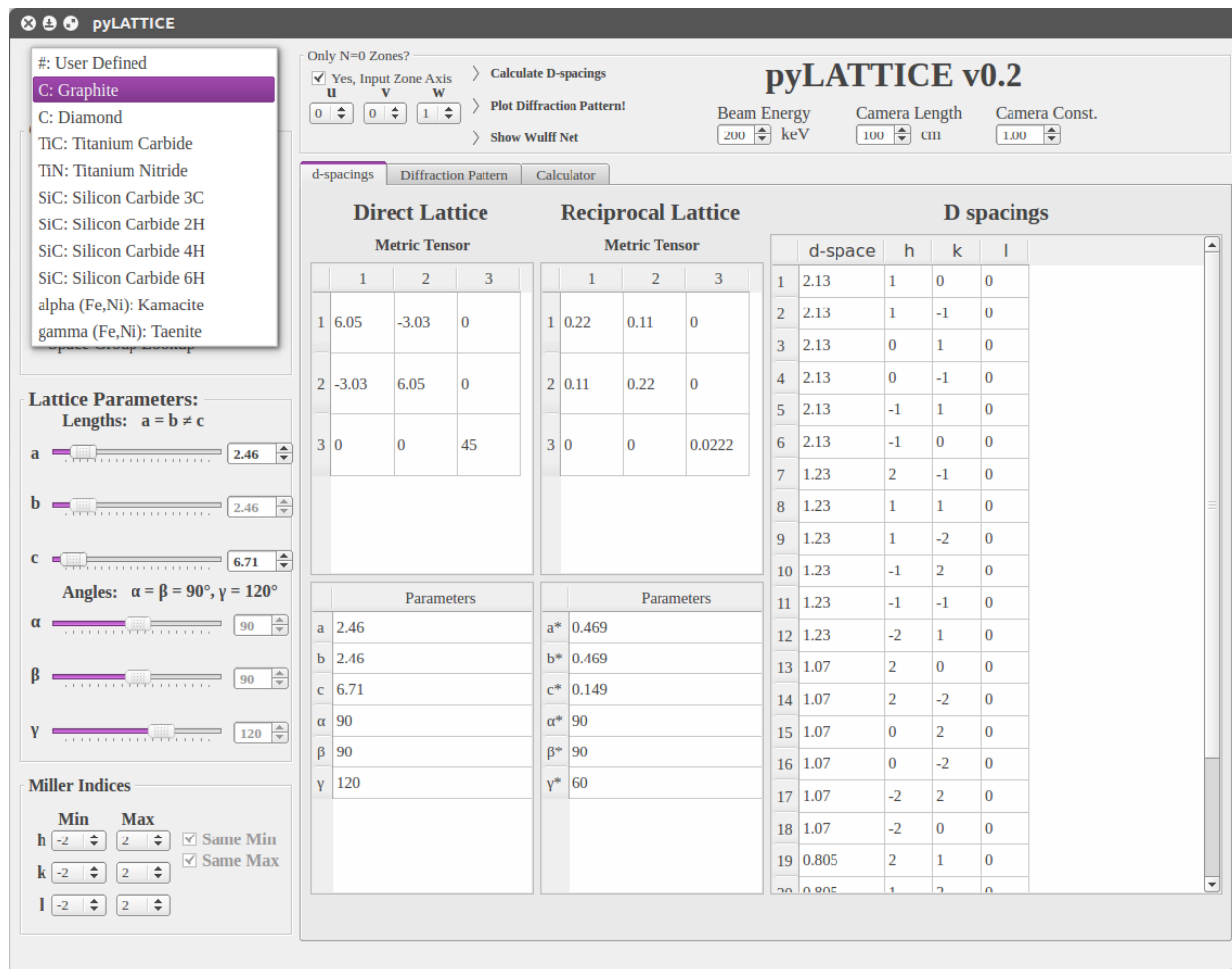
FIGURE 8.2: Menu to select pre-defined minerals.

8.6.2   Plotting

By clicking the "Plot Diffraction Pattern!" button, the diffraction spots corresponding the current d-spacings will be plotted on the "Diffraction Pattern" tab. The plot axes correspond to the reciprocal lattice spacings. Each diffraction spot is selectable; upon selecting two diffraction spots an arrow will be drawn between them and four pieces of information will be displayed to the left: the reciprocal lattice distance (Å^{-1}), the direct lattice distance

between the two sets of planes (Å), the distance on film (cm), and the angle between the two planes (°). The distance on film is dependent upon the parameters of the transmission electron microscope (TEM) including its operating energy (keV) and camera length (cm). These parameters may be adjusted in the spin boxes above the tabbed interface. This is useful for simulating how large a diffraction pattern will appear on film and which diffraction spots can be expected to be visible for a given camera length. Additionally, a camera constant factor may be adjusted, which is useful for diffraction patterns captured on a CCD camera above the plane of the TEM screen.

Measuring the distance between the central spot (000) and any other spot $(kh\ell)$ yields the d-spacing for the set of planes $\{kh\ell\}$. The vector to any point on the reciprocal lattice may also be constructed as the vector addition or subtraction of two or more different $[h_i, k_i, \ell_i]$ vectors. Take the case of FCC Diamond (Space Group 227, Wyckoff letter 8a) along the [101] zone axis (Figure 8.3). Let's say we wish to calculate the angle and d-spacing for (040) (the vector [0,4,0] from the origin): from inspection we can see that a summation of two other allowed reflections, $(13\bar{1})$ and $(\bar{1}11)$, will do the trick:

$$[0, 4, 0] = [1, 3, \overline{1}] + [\overline{1}, 1, 1] \tag{8.30}$$

$$\begin{cases} d^*_{(040)} \cos(\theta_{(040)}) = d^*_{(13\overline{1})} \cos(\theta_{(13\overline{1})}) + d^*_{(\overline{1}11)} \cos(\theta_{(\overline{1}11)}) \\[2mm] d^*_{(040)} \sin(\theta_{(040)}) = d^*_{(13\overline{1})} \sin(\theta_{(13\overline{1})}) + d^*_{(\overline{1}11)} \sin(\theta_{(\overline{1}11)}) \end{cases} \tag{8.31}$$

$$\therefore \theta_{(040)} = \arctan\left(\frac{d^*_{(13\overline{1})} \sin(\theta_{(13\overline{1})}) + d^*_{(\overline{1}11)} \sin(\theta_{(\overline{1}11)})}{d^*_{(13\overline{1})} \cos(\theta_{(13\overline{1})}) + d^*_{(\overline{1}11)} \cos(\theta_{(\overline{1}11)})} \right) \tag{8.32}$$

$$d^*_{(040)} = \left(d^*_{(13\overline{1})} \cos(\theta_{(13\overline{1})}) + d^*_{(\overline{1}11)} \cos(\theta_{(\overline{1}11)}) \right) / \cos(\theta_{(040)}) \tag{8.33}$$

$$d_{(040)} = 1/d^*_{(040)} \tag{8.34}$$

For $(13\overline{1})$, the reciprocal distance, real distance, and angle are 0.929 Å^{-1}, 1.080 Å, and 29.50°, respectively; for $(\overline{1}11)$ they are 0.485 Å^{-1}, 2.060 Å, and 109.47°. By substituting these values into the above equations we can solve for $d^*_{(040)} = 1.12$ Å^{-1}, $d_{(040)} = 0.89$ Å, and $\theta_{(040)} = 54.74°$, which match the measurement tool in **pyLATTICE**.

When **pyLATTICE** calculates the d-spacings for a range of Miller Indices on a zone axis, it simultaneously keeps track of forbidden reflections – atomic planes which would satisfy the most general conditions for a crystal geometry and unit cell type, but are precluded due to specific space group and other special conditions. These forbidden reflections will appear as holes in an otherwise periodic lattice of diffraction spots, such as in Figure 8.4, where the $(\overline{1}\overline{1}1)$ and $(11\overline{1})$ are forbidden along the [101] zone axis for graphite. Plotting these forbidden reflections may be toggled on using the check box "Show Forbidden Reflections". They will appear as smaller gray markers in the diffraction pattern. It should be noted that in practice
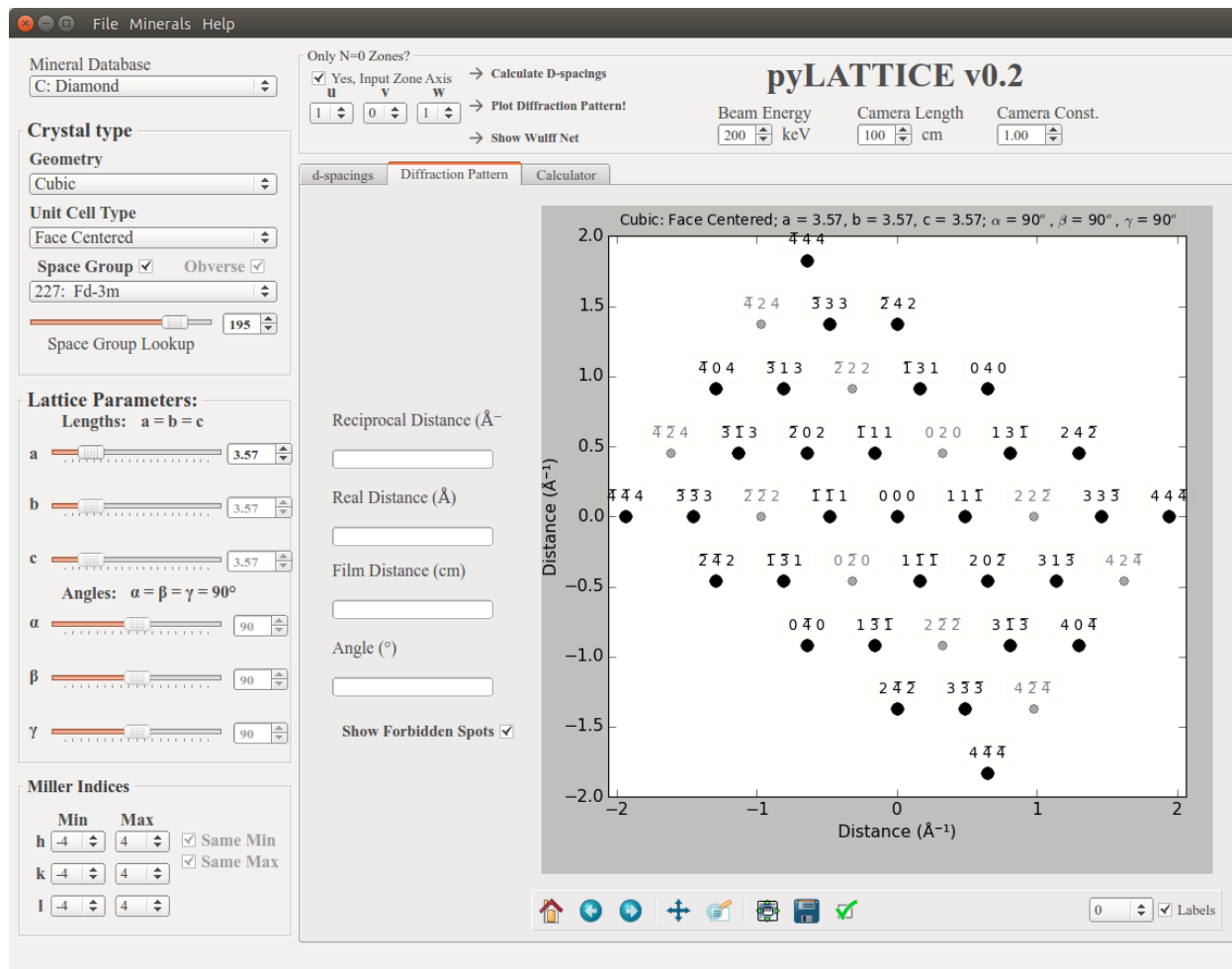
FIGURE 8.3: Diffraction pattern from FCC diamond, space group 227, along zone axis [101] with forbidden reflections.

forbidden reflections may appear weakly in diffraction patterns due to multiple scattering within the sample. **pyLATTICE** currently does not allow selecting forbidden (gray) spots for an interactive measurement, however d-space and angle information is available through use of the `IPython` console (see Section 8.6.4) or, as state above, may be calculated through vector addition of multiple other allowed diffraction spots.
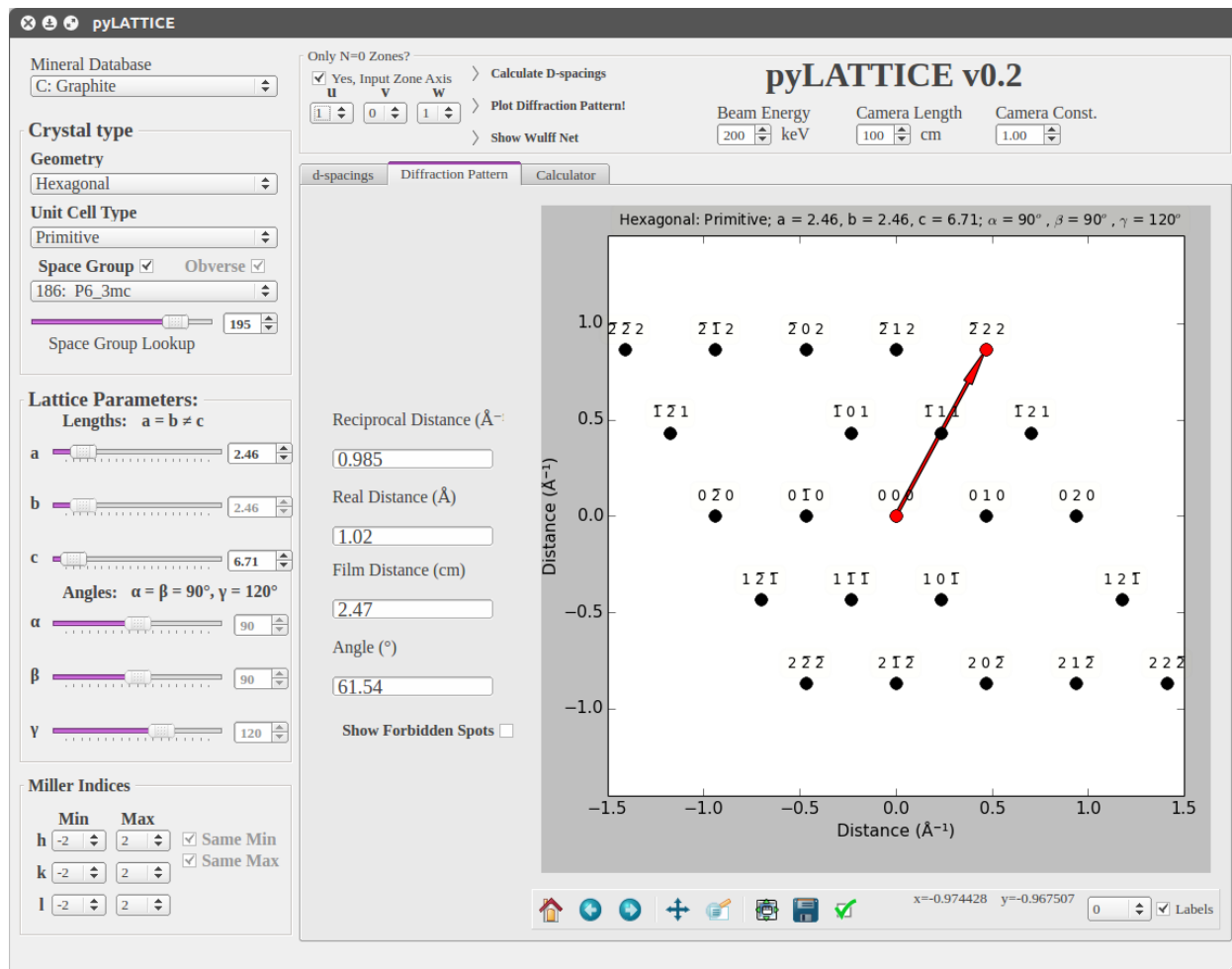
FIGURE 8.4: Example of plotting and measuring diffraction patterns for Graphite on the [101] zone axis.

8.6.3 Manually Specifying Special Reflection Conditions

By default, **pyLATTICE** only uses the most general reflection conditions for each Bravais lattice and space group. The user may, however, manually enter Special Conditions, which may be required for specific site symmetries of a space group. In the Special Conditions dialog (Figure 8.6) the user is supplied with the most basic building blocks of the Special Reflection conditions, phrased as *if : then* statements. The user may assemble com-

206
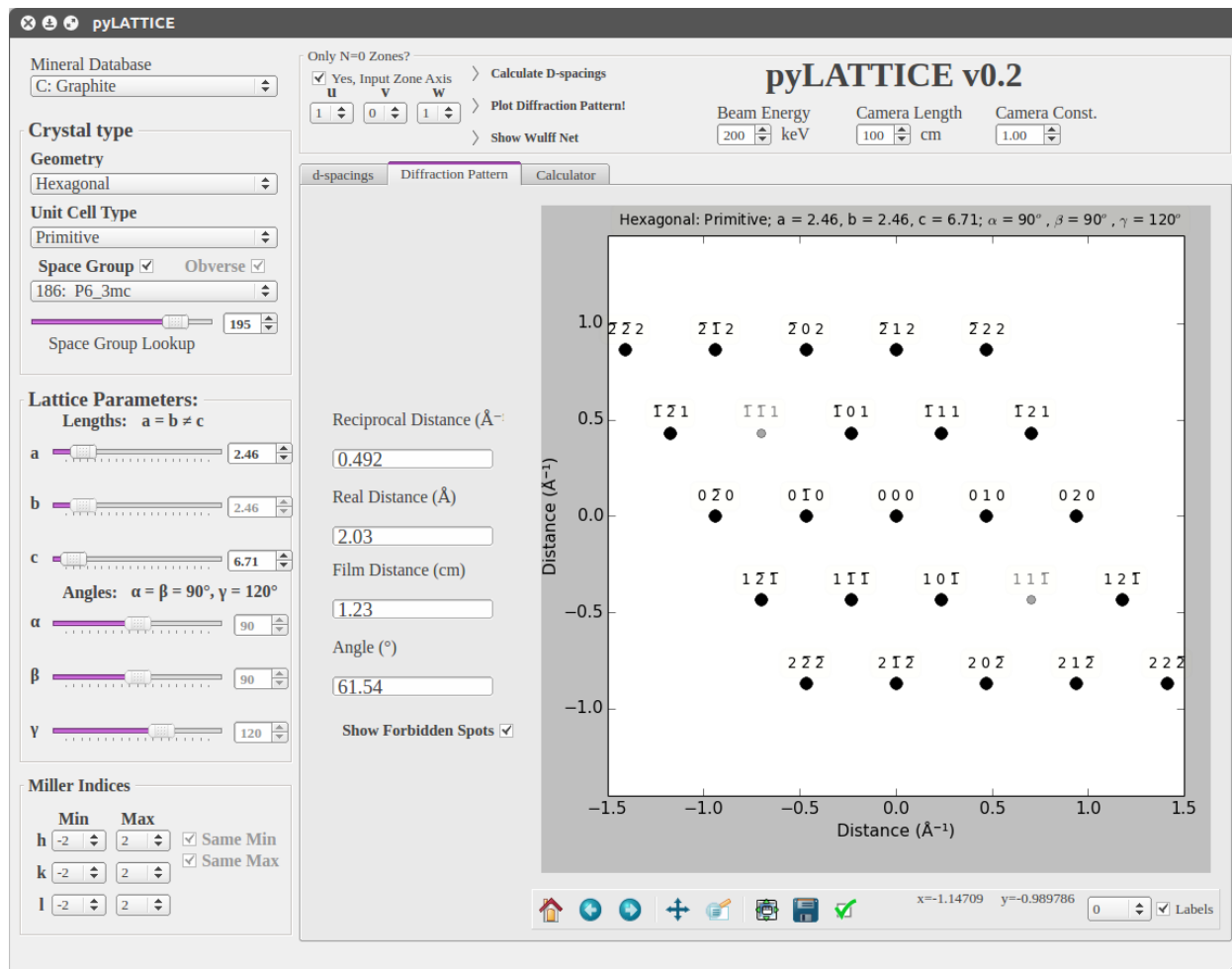
FIGURE 8.5: Example of plotting forbidden reflections for Graphite on the [101] zone axis.

binations of conditions and add them to the list where they will be displayed in the proper

`Python/Pandas` syntax. The `Python/Pandas` syntax is very important and should not be

disrupted. Double-clicking on a list selection on the right allows for manual editing. More ex-

amples of general space group conditions can be found in the "SpaceGroups.h5" file, though

it is imperative that this file not be altered.

An example involving General reflection conditions from space group 134:

$$hk0 : h + k = 2n \tag{1}$$
$$0k\ell : k + \ell = 2n \tag{2}$$
$$00\ell : \ell = 2n \tag{3}$$
$$h00 : h = 2n \tag{4}$$

Since these are General conditions, they are already implemented in **pyLATTICE**, however let us imagine that we must enter them manually. Firstly, there is clearly some redundancy in the conditions, which we may ignore. Condition (1), for instance, specifies that if $\ell = 0$, then $h + k$ must be an even integer, or $h + k$ modulo[1] 2 must be equivalent to 0. Clearly, Condition (4) always satisfies Condition (1) from the computer's standpoint. To implement Condition (1), the user should select ℓ from the first **If** combo box and set its corresponding spin box to 0. For the **Then** conditions the user should select h from the first combo box, check the check box in the second row (which enables the next combo boxes), select $+$ and k from the second row, and enter 2 in the n spin box. Once this condition has been added, it should read $if \ (l \ == \ 0) : (h + k)\%2 \ == \ 0$, where $\%$ is `Python`'s modular operator – we want $(h + k)$ modulo 2 to be equivalent to 0. Condition (3) is similarly a redundant statement of Condition (2). In the same fashion we will select h from the **If** combo box and set its corresponding spin box to 0, and set $k + \ell = 2n$ in the **Then** conditions. The second condition will now read, $if \ (h \ == \ 0) : (k + \ell)\%2 \ == \ 0$. Upon selecting "OK" from the dialog, the new special conditions will be saved, overwriting any previous Special conditions. "Cancel" discards any changes to the Special conditions.

An advanced example of Special reflection conditions from space group 227, f 2.mm

---

[1]Modulo: the remainder of division of one number by another, e.g., 5 modulo 2 = 1.

(FCC Diamond):

$$hk\ell : h = 2n + 1 \ \ \text{or} \ \ h + k + \ell = 4n$$

Since this condition allows for any permutable $kh\ell$ combination, the user would choose "True" in the first **If** combo box followed by selecting $h + k + \ell$ in the **Then** combo boxes and "4" in the n spin box. The only way to satisfy an "OR" condition (and a condition where e.g., $h = 2n + 1$) is to manually edit the special condition text. So far the text should read $if \ True : (h + k + l)\%4 == 0$. When adding a second or third condition on either the if or $then$ side of the statement, one must encapsulate each condition in parentheses (), otherwise `Pandas` will raise an ambiguity error. `Pandas` uses logical symbols in lieu of `Python`'s text operators – in this case, "OR" corresponds to "|". The final statement should read $if \ True : ((h + k + l)\%4 == 0) \ | \ (h\%2 == 1)$, where now the second condition requires h modulo 2 to be equivalent to 1.

8.6.4   Using the IPython Console

pyLATTICE also comes with a built-in `IPython` console for interacting with data and parameters via the command line (Figure 8.7). Being a full `IPython` console, however, the user may also interact with files, directories, and any other `Python` packages that the user may have installed, provided that they are compatible with the **pyLATTICE** `Python` version (Figure 8.10). An especially useful feature of the `IPython` console is the ability to use magic functions, which, among other things, allow the user to run python scripts to automate

209
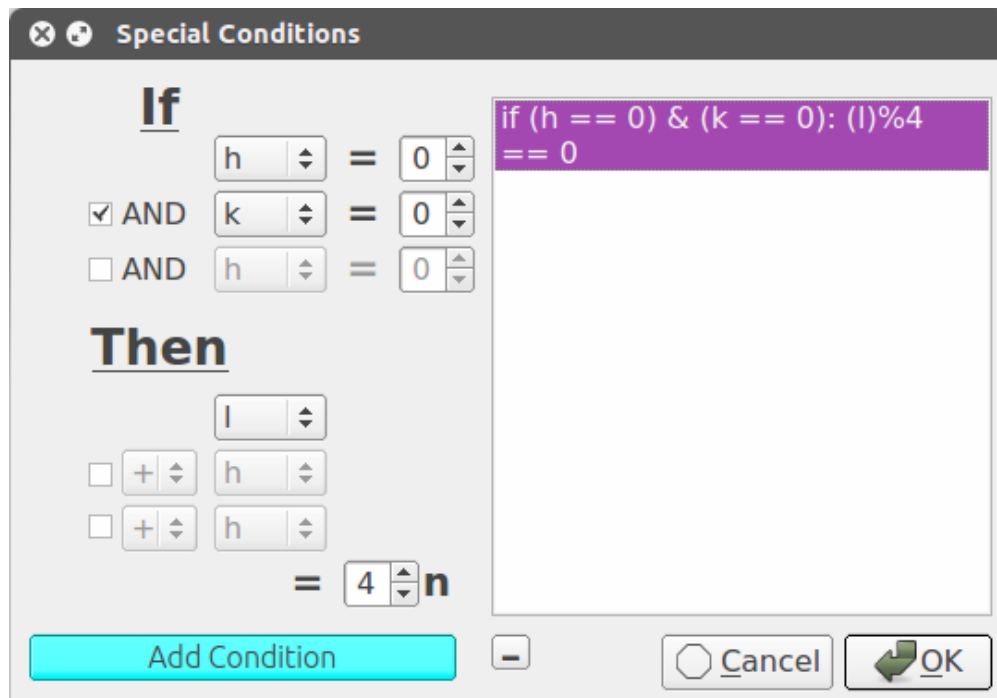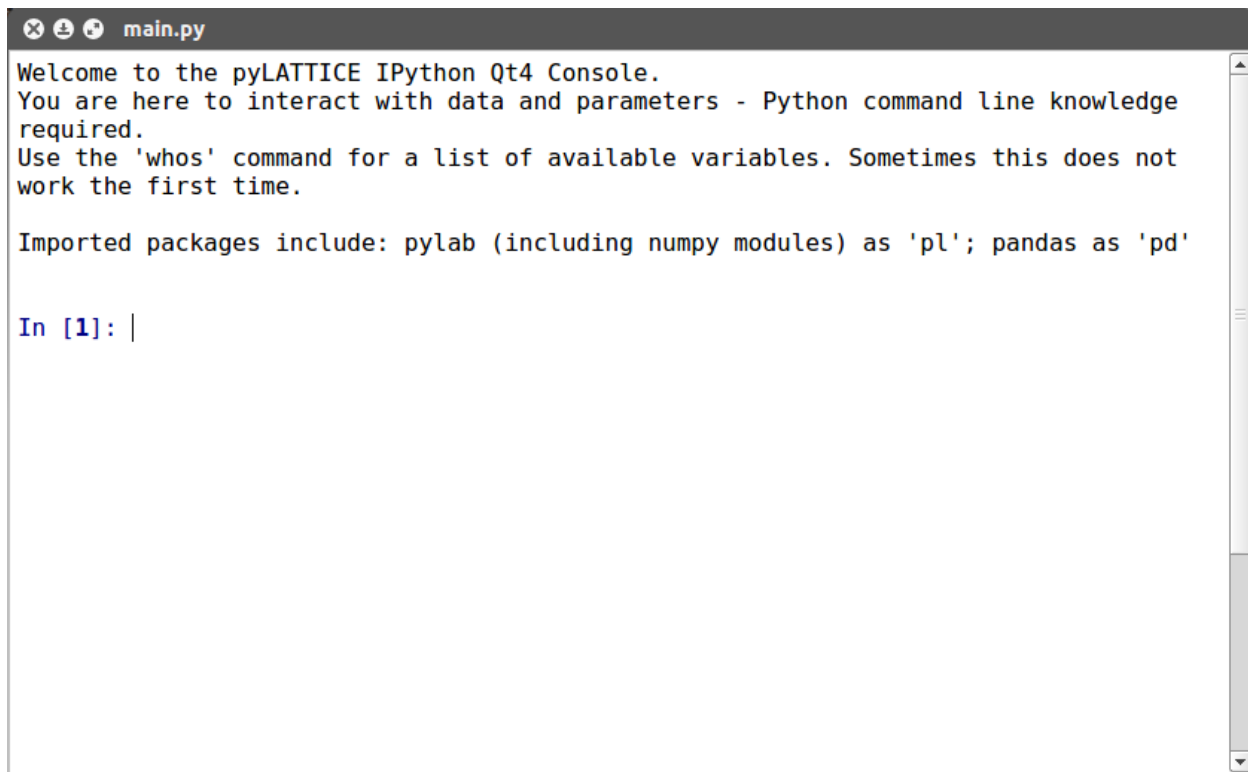
FIGURE 8.6: The user may manually enter special conditions in order to satisfy multiplicity, site symmetry, etc. These special conditions are stored in the mineral database. Conditions are inputted in the form of If:Then statements from the left panel and are displayed in `Python\Pandas` syntax on the right. Conditions on the right are manually editable.

pyLATTICE and/or save/load user-defined functions. Figure 8.11 shows two functions, functest1 and functest2, defined by the user on lines 1 and 2. The magic function %save is used to output the contents of lines 1 and 2 to the file "functest.py". The magic function %load will similarly populate the next line of the console with the contents of the specified file. (Note: As of this writing, automation for **pyLATTICE** is not full implemented via the console.)

```
⊗ ☺ ⊙  main.py

Welcome to the pyLATTICE IPython Qt4 Console.
You are here to interact with data and parameters - Python command line knowledge
required.
Use the 'whos' command for a list of available variables. Sometimes this does not
work the first time.

Imported packages include: pylab (including numpy modules) as 'pl'; pandas as 'pd'


In [1]: |
```

FIGURE 8.7: pyLATTICE contains a built-in IPython console for interacting with its data and parameters.
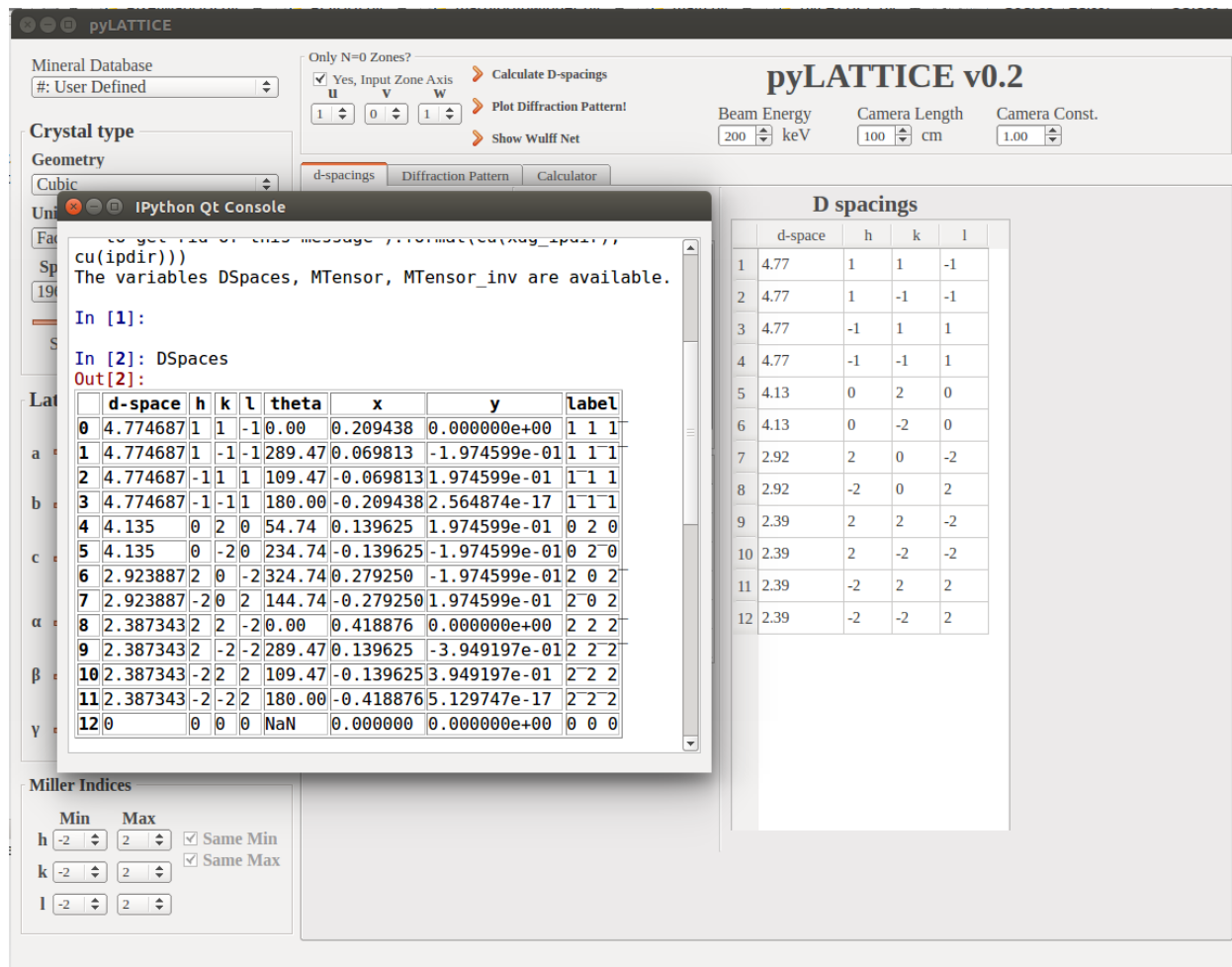
FIGURE 8.8: Example of parameters and data available in the `IPython` console. The d-spacings information is available via the variable "DSpaces", which is a `Pandas` DataFrame object. This object is shown to contain more information than what is visible in the GUI. Specifically, it includes the Cartesian coordinates and utf-8 labels used in the plotting tab. The command "whos" will print a list of available parameters and a summary of their values (see Figure 8.9).

```
● ● ▣  main.py                                                          ▲

In [2]: whos
Variable        Type            Data/Info
--------------------------------------
DSpaces         DataFrame               d-space   h   k  l\<...>n23  0.3535534  -2  -2  0
Forbidden       DataFrame       Empty DataFrame\nColumns:<...>pace, h, k, l]\nIndex: []
ZoneAxis        ndarray         3: 3 elems, type `int64`, 24 bytes
a               float           1.0
alpha           int             90
alphastar       float64         90.0
astar           float64         1.0
b               float           1.0
beamenergy      int             200
beta            int             90
betastar        float64         90.0
bstar           float64         1.0
c               float           1.0
camconst        float           1.0
camlength       int             100
cstar           float64         1.0
gamma           int             90
gammastar       float64         90.0
manualConds     list            n=0
mineraldb       DataFrame                       Name   <...>                     NaN
path            str             /home/eegroopm
pd              module          <module 'pandas' from '/u<...>ages/pandas/__init__.py'>
pl              module          <module 'pylab' from '/us<...>/dist-packages/pylab.py'>
sg              DataFrame               Patterson       G<...>n\n[230 rows x 5 columns]
sghex           DataFrame               Patterson  Geometr<...> if h==-k:l%3==0; if...
u               int             0
v               int             0
w               int             1
wavelength      float64         0.0250839647099

In [3]:                                                                ▼
```

FIGURE 8.9: Example of "whos" command run in the `IPython` console, which prints the available interactive data and parameters.

```
☒ ☻ ☺  main.py
In [7]: cd Documents/Research/Thesis/
/home/eegroopm/Documents/Research/Thesis

In [8]: ls
Abstract.tex                Chapter-pyLATTICE.aux
Acknowledgements.tex        Chapter-pyLATTICE.bbl
bibBackground.bib           Chapter-pyLATTICE.blg
bibChp3.tex                 Chapter-pyLATTICE.tex
bibFirstPaper.bib           Chapter-TiXANES.tex
bibFirstPaper.bib.bak       Chapter-XANES.aux
bibHDGraphite.bib           Chapter-XANES.bbl
bibHDGraphite.bib.bak       Chapter-XANES.blg
bibIntro.bib                Chapter-XANES.tex
bibMethods.bib              compilationscript.bash
bibMethods.bib.bak          compilationscript.bat*
bibNanocore.bib             deluxetable.sty
bibNanocore.bib.bak         demo.py*
bibNanocore.txt             Figs-FirstPaper/
bibpyLATTICE.bib            Figs-HDGraphite/
bibpyLATTICE.bib.bak        Figs-Intro/
bibtexAll.bash              Figs-Methods/
bibtexAll.bat*              Figs-NanoCore/
bibTiXANES.bib.bak          Figs-pyLATTICE/
bibXANES.bib                Figs-XANES/
bibXANES.bib.bak            front.bbl
Chapter-Background.aux      front.blg
```

FIGURE 8.10: The full `IPython` console allows for interaction with the user's system, not only with variables in pyLATTICE. The user may interact with files and directories, and may import any other `Python` packages installed on the user's system which are compatible with the `Python` version. This allows the user to augment pyLATTICE's capabilities and is especially useful for exporting data and variable values. `IPython` recognizes BASH commands, such as "cd" and "ls", whose output is shown in the figure.

```
 ⊗ ⊕ ⊙   main.py

In [1]: def functest(var):
   ...:         newvar = var**2
   ...:         print(newvar)
   ...:

In [2]: def functest2(var):
   ...:         newvar = var**3
   ...:         print(newvar)
   ...:

In [3]: %save functest.py 1 2

File `functest.py` exists. Overwrite (y/[N])?  y
The following commands were written to file `functest.py`:
def functest(var):
    newvar = var**2
    print(newvar)

def functest2(var):
    newvar = var**3
    print(newvar)


In [4]: %load functest.py

In [5]: def functest(var):
   ...:         newvar = var**2
   ...:         print(newvar)
   ...:
   ...: def functest2(var):
   ...:         newvar = var**3
   ...:         print(newvar)
   ...:


In [6]: |
```

FIGURE 8.11: IPython's magic functions (e.g., "%save", "%load", "%run") allow for the import/export of user-defined functions, as shown, or full automation of pyLATTICE from the command line through running a Python script.

Bibliography

Bernatowicz, T. (**1989**), "A User's Guide to LATTICE: A Crystallographic Utilities Program, v. 2", Unpublished.

Frank, F. C. (**1965**), "On Miller-Bravais Indices and four-dimensional Vectors", *Acta Crystallographica* **18**, 862–866, URL http://dx.doi.org/10.1107/S0365110X65002116.

Hahn, T. (Ed.) (**1989**), *International Tables for Crystallography*, volume A: Space Group Symmetry, Kluwer Academic Publishers for The International Union of Crystallography, Dordrecht.

Williams, D. B. & Carter, C. B. (**1996**), *Transmission Electron Microscopy: A Textbook for Materials Science*, Plenum Press, New York.

Chapter 9

Conclusions

"Where the telescope ends the microscope begins. Which of the two has the grandest view? Choose."

- Victor Hugo, *Les Misérables*, 1862

The laboratory study of presolar grains complements the astronomical observations and modeling of stellar and nebular processes. Many insights into stellar processes may be gleaned through the study of interstellar dust that either complement or are unavailable to telescopic observations, including: possible stellar sources for presolar grains; interstellar processes, such as galactic cosmic ray exposure; nucleosynthetic processes in stars; physical and chemical conditions in stellar ejecta; and processing in the early Solar System.

One of strongest features of the laboratory analysis of presolar grains is the ability to correlate isotopic, chemical, and microstructural studies of individual, unique grains, which is emphasized in this thesis. With such small and unique presolar samples, it is imperative to be able to perform as many correlated analyses as possible on each presolar grain. A

significant difficulty with performing population-based studies on presolar grains lies in the vast parameter space (e.g., nucleosynthesis, temperature, pressure, C/O ratio, stellar mass loss rate, radiation level, etc.) available for the production of dust in stellar ejecta. It remains nearly impossible to pinpoint whether isotopic/microstructural variations in similar presolar grains arose due to variations within the ejecta of one progenitor star, or were the results of differences between two different stars. Correlated studies of individual presolar grains do, however, provide a wealth of information regarding the specific environments in which they formed and may act to constrain models of grain formation and stellar evolution.

This thesis has emphasized the correlated isotopic, chemical, and microstructural study of presolar grains through NanoSIMS, TEM, and STXM/XANES, with a focus on connecting these data to astrophysical phenomena. Presolar graphite grains have been the predominant topic of this thesis. Compared to the $< 20,000$ presolar SiC grains analyzed with SIMS, only $\sim 2,200$ presolar graphite grains have been similarly studied. Of these, merely 50–70 grains have been additionally studied with TEM in a correlated fashion. Given their propensity for capturing small subgrains of different chemical composition, presolar graphite grains provide useful templates for characterizing the condensation sequences and thermodynamics within stellar ejecta. Graphite grains from SNe are especially interesting in this regard, as their heterogeneous isotopic compositions pinpoint different locations within the star from which the material that formed the grains originated. Coupled with the grains' inferred condensation sequences, a picture involving complex mixing within SN ejecta emerged, corroborated by telescopic observations and stellar models.

Continued TEM study of presolar graphite grains with extreme Ti and Ca isotopic

anomalies and AB SiC grains will help to shed light on their possible progenitors, currently posited to include Born-Again AGB stars. XANES study of presolar grains remains in its infancy, currently requiring higher quality data from standards. There have been numerous successes, however, including observations of various organic components within presolar graphite grains. Future investigations will also probe the effect of V in solid solution in TiC subgrains and thus infer properties of the progenitor stellar ejecta.

There remain many open questions in the field of presolar grains, many of which parallel the continuing work described in this thesis. The locus of continued stellar astrophysics lies at the intersection of stellar modeling, telescopic observations, and laboratory analysis of extraterrestrial materials.

Appendix

This appendix consists of tables containing NanoSIMS bulk-grain isotope data from low- and high-density presolar graphite grains from Orgueil mounts OR1d6m, OR1f4m, OR1g2m.

TABLE A.1: Bulk-grain isotope compositions for low-density (LD) presolar graphite grains from Orgueil mount OR1d6m. Grains G1, G3, G7, G14, G16, and G22 are likely insoluble organic material from Orgueil, containing excesses in ^{15}N, not presolar grains. Continued on next page...

Grain	Size (μm)	^{12}C/^{13}C	er.	^{16}O/^{18}O	er.	^{14}N/^{15}N	er.
OR1d6m-4 (G4)	6	7.5	0.1	486.0	9.2	236.0	18.3
OR1d6m-5 (G5)	10.5	45.9	0.3	323.5	5.7	248.0	10.7
OR1d6m-6 (G6)	5	113.2	0.8	163.2	2.8	145.3	5.4
OR1d6m-8 (G8)	8	127.8	0.9	280.4	5.0	145.0	9.3
OR1d6m-9 (G9)	5.5	8.0	0.1	338.5	8.5	233.8	12.0
OR1d6m-11 (G11)	7.5	22.0	0.2	297.7	6.0	232.2	10.3
OR1d6m-13 (G13)	5.5	66.0	0.4	170.1	3.2	263.0	5.8
OR1d6m-15 (G15)	12	13.4	0.1	471.8	10.5	240.2	16.4
OR1d6m-17 (G17)	18	306.1	2.1	306.3	6.4	215.1	10.4
OR1d6m-18 (G18)	12	121.0	0.8	432.9	9.2	148.8	14.6
OR1d6m-20 (G20)	4.5	74.3	0.5	501.6	10.3	273.9	16.9
OR1d6m-21 (G21)	7	140.7	1.0	140.1	2.6	267.6	4.8
OR1d6m-23 (G23)	6	73.7	0.5	394.4	7.2	214.4	13.1
OR1d6m-24 (G24)	13	13.1	0.1	479.2	9.4	236.3	16.5
OR1d6m-1 (G1)	12	91.5	0.6	482.0	9.2	132.4	16.0
OR1d6m-3 (G3)	8	91.3	0.6	485.2	12.9	179.7	16.3
OR1d6m-7 (G7)	9	89.8	0.6	475.6	9.5	153.1	15.8
OR1d6m-14 (G14)	5	86.1	0.6	484.5	9.8	135.6	16.1
OR1d6m-16 (G16)	5.5	89.6	0.6	487.7	10.4	172.5	16.2
OR1d6m-22 (G22)	6.5	90.1	0.6	490.9	9.4	276.8	16.4

Grain	δ^{30}Si/^{28}Si	er.	δ^{29}Si/^{28}Si	er.	δ^{41}K/^{39}K	er.
G4	62.4	13.40	39.1	10.60	16.8	16.5
G5	135.3	15.10	74.3	12.40	11.0	12.0
G6	59.5	15.70	13.0	12.70	-36.5	11.5
G8	29.1	12.80	48.10	10.20	-0.2	13.6
G9	158.60	54.70	36.8	40.40	25.1	28.2
G11	40.0	14.00	20.5	11.00	-4.2	17.8
G13	181.1	21.20	140.5	17.40	1145.8	57.5
G15	6.60	30.10	21.1	24.00	-23.6	25.5
G17	85.8	21.10	27.1	17.50	-10.8	17.8
G18	12.3	20.20	28.9	16.00	282.8	44.9
G20	32.0	18.10	37.2	14.30	51.5	22.0
G21	164.8	15.40	125.2	12.50	2.8	19.1
G23	167.8	9.80	133.9	7.50	33.2	19.1
G24	4.00	13.80	3.40	10.60	9.0	30.0
G1	28.8	21.40	2.70	17.40	-40.5	11.8
G3	94.3	22.10	76.8	17.90	2.8	13.8
G7	1.60	20.60	28.1	16.10	-35.5	39.1
G14	36.8	36.80	61.8	29.40	-18.8	27.5
G16	47.4	15.50	39.5	12.20	23.6	20.6
G22	26.1	18.30	21.9	14.60	-0.5	16.5

Table A.1 continued...
All delta values in permil (‰).

Grain	δ^{25}Mg/^{24}Mg	er.	δ^{26}Mg/^{24}Mg	er.	^{26}Al/^{27}Al[†]	er.
G4	–	–	–	–	–	–
G5	-42.6	17.5	230.9	19.9	1.77E-02	3.77E-04
G6	8.9	19.1	27596.5	272.3	4.46E-01	7.66E-03
G8	1.5	11.9	755.9	17.9	7.71E-02	9.08E-04
G9	-20.6	40.5	947.1	58.6	1.84E-02	8.60E-04
G11	-18.9	18.4	1681.9	35.2	7.36E-02	1.42E-03
G13	37.5	39.1	11665.7	217.0	2.31E-01	8.42E-03
G15	8.9	18.2	-4.9	17.6	–	–
G17	119.2	28.1	442.8	31.7	5.58E-02	1.69E-03
G18	-32.0	15.9	259.1	18.4	1.20E-02	2.26E-04
G20	-9.1	21.9	22.6	21.6	–	–
G21	125.8	55.0	23677.0	503.5	2.71E-01	1.26E-02
G23	18.7	15.2	1509.3	28.2	6.89E-02	1.03E-03
G24	-34.5	10.7	-2.7	10.8	–	–
G1	10.5	19.0	-10.8	18.2	–	–
G3	5.6	12.3	21.9	12.3	–	–
G7	-3.4	11.0	-24.2	10.7	–	–
G14	-17.3	15.6	-7.1	15.3	–	–
G16	19.5	18.1	-3.4	17.3	–	–
G22	4.8	8.6	5.5	8.8	–	–

Table A.1 continued...
[†] Inferred initial ^{26}Al/^{27}Al ratio based upon ^{26}Mg excess relative to solar isotopic composition.

Grain	δ^{42}Ca/^{40}Ca	er.	δ^{43}Ca/^{40}Ca	er.	δ^{44}Ca/^{40}Ca	er.
G4	-59.5	53.2	-175.1	108.0	26.9	32.0
G5	-9.5	28.9	-42.3	61.6	11.8	18.0
G6	72.8	20.5	108.3	45.6	35.6	13.7
G8	291.3	32.3	719.2	81.1	65.3	18.2
G9	-11.7	109.5	-285.8	196.2	25.4	61.2
G11	-39.4	79.1	90.4	183.1	28.3	46.4
G13	204.4	47.4	-42.3	91.3	24.0	25.5
G15	60.6	78.3	-108.0	155.0	-7.7	42.9
G17	183.0	64.1	381.3	149.6	98.4	35.4
G18	337.6	58.2	-8.8	108.1	-39.3	28.4
G20	-35.4	57.1	94.2	130.7	56.6	34.3
G21	80.6	24.2	80.7	52.9	-7.7	15.0
G23	6.1	41.1	80.7	91.5	18.1	24.1
G24	115.6	93.6	-119.1	178.0	45.9	51.2
G1	21.8	27.4	24.8	59.6	-22.3	16.7
G3	-40.0	35.9	-6.5	78.8	23.0	22.1
G7	-107.1	115.5	407.4	316.1	-48.1	66.6
G14	10.5	80.2	127.0	182.7	104.8	47.5
G16	32.7	25.2	-2.8	53.7	26.4	16.0
G22	112.7	70.1	-12.5	143.7	-11.1	37.5

Table A.1 continued...

Grain	δ^{46}Ti/^{48}Ti	er.	δ^{47}Ti/^{48}Ti	er.	δ^{49}Ti/^{48}Ti	er.	δ^{50}Ti/^{48}Ti	er.
G4	-66.3	68.4	97.7	79.2	-26.9	87.8	2566.7	548.2
G5	20.1	10.9	9.1	12.0	391.3	17.5	205.8	82.3
G6	39.4	26.4	29.1	27.5	467.2	39.5	747.5	341.7
G8	31.2	11.0	-4.6	11.9	1211.0	24.0	801.0	106.1
G9	–	–	–	–	–	–	–	–
G11	-15.3	16.4	-64.4	17.2	440.0	26.2	279.4	155.1
G13	–	–	–	–	–	–	–	–
G15	–	–	–	–	–	–	–	–
G17	-2.1	52.6	68.0	56.8	828.5	90.3	437.4	406.3
G18	10.4	17.0	-19.3	17.9	282.4	24.7	505.7	124.2
G20	–	–	–	–	–	–	–	–
G21	4.1	10.1	-36.7	11.0	383.3	16.5	109.7	160.5
G23	-26.2	26.8	-36.3	28.5	241.8	38.6	659.6	197.1
G24	0.5	74.6	109.0	82.7	-57.4	90.8	7093.7	753.7
G1	-51.5	25.7	18.4	28.4	-30.5	32.6	401.8	197.9
G3	–	–	–	–	–	–	–	–
G7	-85.5	56.4	30.7	64.0	128.3	79.1	2991.6	476.2
G14	–	–	–	–	–	–	–	–
G16	–	–	–	–	–	–	–	–
G22	–	–	–	–	–	–	–	–

Table A.1 continued...

[226]

TABLE A.2: Bulk-grain isotope compositions for high-density (HD) presolar graphite grains from Orgueil mounts OR1f4m and OR1g2m. All delta values in permil (‰). Continued on next page...

Grain	Size (μm)	^{12}C/^{13}C	er.	δ^{29}Si/^{28}Si	er.	δ^{30}Si/^{28}Si	er.
OR1f4m-1 (f1)	5.1	465.3	2.2	-55.9	28.5	-25.9	25.0
OR1f4m-2 (f2)	3.9	127.7	0.5	-98.6	48.1	-37.9	54.8
OR1f4m-3 (f3)	3.8	806.7	4.2	99.8	67.6	144.3	77.6
OR1f4m-4 (f4)	2.8	11.9	0.0	3.5	28.4	-19.9	22.6
OR1f4m-5 (f5)	3.9	474.2	2.3	15.3	26.4	9.7	18.8
OR1f4m-7 (f7)	3.2	89.5	0.3	-26.3	25.8	-22.9	19.1
OR1f4m-8 (f8)	4.2	98.0	0.3	14.6	31.6	-18.2	27.5
OR1f4m-9 (f9)	4	322.2	1.3	54.1	28.7	-17.6	21.0
OR1f4m-10 (f10)	2.9	559.1	2.5	-49.7	34.1	153.3	37.2
OR1f4m-11 (f11)	5	585.5	2.6	19.0	29.0	11.8	23.5
OR1f4m-12 (f12)	2.9	27.6	0.1	3.3	28.3	-6.8	22.6
OR1f4m-13 (f13)	3.7	445.0	2.1	-56.5	32.0	0.4	31.2
OR1f4m-14 (f14)	3.5	9.7	0.0	-69.3	23.8	-35.2	17.0
OR1f4m-15 (f15)	3.8	345.4	1.4	67.4	32.2	2.5	26.7
OR1f4m-16 (f16)	2.3	685.3	2.9	-59.4	50.8	-22.0	57.2
OR1f4m-17 (f17)	2.7	197.3	0.8	-16.2	39.4	6.1	40.8
OR1g2m-1 (g1)	5.1	146.5	0.5	36.8	28.7	49.0	22.7
OR1g2m-2 (g2)	3	652.7	3.3	-16.6	51.9	143.1	61.8
OR1g2m-3 (g3)	6.5	313.0	1.3	-56.3	36.2	-5.0	37.4
OR1g2m-4 (g4)	7.6	77.8	0.3	-67.4	28.6	-47.5	25.4
OR1g2m-5 (g5)	3.7	5.3	0.0	-50.1	31.7	22.3	30.9
OR1g2m-6 (g6)	6.4	89.5	0.3	-146.0	23.3	-15.8	19.8
OR1g2m-8 (g8)	3.0	396.5	1.6	93.4	40.4	239.3	42.8
OR1g2m-9 (g9)	4	462.8	2.0	22.1	26.8	-2.3	19.1
OR1g2m-11 (g11)	4.6	110.9	0.4	3.5	30.1	29.8	26.2
OR1g2m-12 (g12)	4.4	309.0	1.3	-27.7	27.2	8.2	22.3
OR1g2m-13 (g13)	4.6	287.7	1.3	-53.0	35.0	-73.0	34.2

Grain	δ^{41}K/^{39}K	er.	δ^{42}Ca/^{40}Ca	er.	δ^{43}Ca†	er.	δ^{44}Ca	er.
f1	-38.1	36.3	71.9	134.8	219.8	313.2	14.1	75.4
f2	113.5	29.7	98.1	94.9	76.8	206.1	155.9	57.4
f3	15.8	13.7	-40.9	125.9	27.1	283.9	94.4	77.7
f4	-47.2	31.1	435.7	89.8	296.1	184.2	58.6	45.8
f5	-3.2	17.0	45.8	59.7	-233.7	111.1	98.3	37.9
f7	-3.1	12.2	13.7	36.4	22.7	78.5	37.3	25.6
f8	-3.5	15.6	104.0	98.8	226.5	232.1	-15.4	54.3
f9	66.0	68.3	-205.7	143.2	-510.2	245.1	207.7	101.2
f10	-10.9	20.8	-145.7	125.7	302.8	335.1	-80.8	74.9
f11	-39.0	34.5	-189.6	70.5	-198.9	153.3	-52.7	45.0
f12	14.2	16.4	122.9	100.6	225.0	228.4	59.6	57.1
f13	-64.3	49.6	250.3	151.8	-47.7	286.0	238.7	86.8
f14	2.0	33.9	2242.6	180.7	2526.0	407.1	906.2	82.5
f15	55.7	21.6	-46.3	210.0	-772.1	223.5	190.8	133.4
f16	-12.7	15.3	38.7	43.2	-44.0	89.0	24.7	28.3
f17	2.7	14.8	21.9	38.4	190.2	89.9	42.2	26.5
g1	-51.2	45.3	71.9	89.8	-222.6	164.4	-7.7	50.6
g2	-7.5	16.0	-45.5	36.8	116.8	86.0	48.0	26.4
g3	-5.8	13.1	13.6	33.1	-24.0	69.4	10.2	23.6
g4	-5.5	13.0	41.9	31.7	53.8	67.9	27.2	23.1
g5	-11.7	15.1	-38.1	56.9	113.1	134.7	128.3	38.5
g6	-9.7	20.6	83.2	49.4	-16.6	102.5	22.3	30.7
g8	72.3	61.9	257.3	173.5	-18.1	343.3	-101.6	84.3
g9	3.7	13.3	16.8	28.1	-15.1	58.5	12.1	21.5
g11	8.7	49.0	41.6	117.1	7.9	250.8	8.3	66.4
g12	–	–	–	–	–	–	–	–
g13	12.7	14.5	60.5	74.4	365.8	184.0	-19.8	42.7

Table A.2 continued...
† δ^{43}Ca shorthand for δ^{43}Ca/^{40}Ca. All Ca delta values with respect to ^{40}Ca.

Grain	δ^{46}Ti†	er.	δ^{47}Ti	er.	δ^{49}Ti	er.	δ^{50}Ti	er.	††
f1	88.1	257.0	-436.8	199.7	624.9	197.6	-1966.9	-3303.4	102%
f2	301.7	305.7	175.0	320.6	922.4	230.7	9353.1	7480.3	45%
f3	2035.3	485.9	-18.8	254.3	1134.9	264.2	8889.7	4983.5	64%
f4	887.6	620.7	-620.4	270.5	5254.8	1219.6	14941.8	6098.7	50%
f5	668.0	102.8	135.2	87.7	1466.4	96.5	8341.5	1412.2	41%
f7	52.0	35.7	-14.8	36.2	-52.9	16.5	-263.7	816.7	85%
f8	-29.8	126.5	142.3	145.0	1110.7	133.5	351.7	3841.2	94%
f9	578.0	39.6	138.6	34.7	1391.6	36.8	2835.0	499.3	21%
f10	234.2	170.8	-21.5	159.6	290.5	97.4	5441.3	1723.5	95%
f11	241.7	118.4	-98.2	104.3	770.6	92.5	1388.2	1681.2	93%
f12	-38.2	12.6	-27.4	13.1	157.6	7.6	9.3	184.1	20%
f13	789.0	76.1	115.5	61.6	1056.2	58.1	4421.3	741.7	14%
f14	4309.6	634.1	1684.5	430.3	9813.7	1165.6	23,740.1	5933.3	37%
f15	606.7	273.1	474.3	275.8	-166.1	84.1	-175.5	2786.3	97%
f16	248.5	148.5	-254.0	117.4	-221.2	48.8	70,994.8	4463.5	54%
f17	770.6	255.5	1352.1	325.4	1798.6	251.5	303.3	2940.9	94%
g1	156.6	125.6	211.3	136.7	10.0	57.1	-1698.7	-854.5	100%
g2	-56.0	45.6	12.6	50.1	38.6	24.1	319.7	607.4	71%
g3	-21.3	5.5	-14.0	5.3	-1.9	3.0	17.6	587.5	4%
g4	242.9	65.5	32.0	63.5	2230.3	89.9	-460.9	505.2	98%
g5	479.8	216.3	469.7	225.5	156.4	88.2	-3561.8	-1195.8	102%
g6	54.8	45.9	74.0	48.8	-30.4	21.3	-922.0	366.3	100%
g8	-338.0	175.1	-122.6	220.6	221.4	133.8	-1651.6	-2705.1	103%
g9	612.6	101.0	177.5	90.4	901.7	69.9	4168.3	706.5	73%
g11	79.6	129.4	11.5	135.1	83.0	70.4	3811.4	1779.3	62%
g12	-43.1	139.9	-82.5	152.3	48.0	71.0	-2933.7	-1155.6	72%
g13	246.4	117.8	-94.8	103.7	161.5	57.4	1529.7	782.3	81%

Table A.2 continued...
† All delta values with respect to ^{48}Ti.
††Isobaric correction to ^{50}Ti from ^{50}V, ^{50}Cr; inferred from ^{51}V, ^{52}Cr signals, assuming solar isotopic composition.

Evan E. Groopman

Washington University in St. Louis
Physics Department
Laboratory for Space Sciences
One Brookings Drive
Campus Box 1105
Saint Louis, MO 63130

Email: eegroopm@physics.wustl.edu
Office: (314) 935-6243
Mobile: (410) 258-6928
http://presolar.wustl.edu/Laboratory_for_Space_Sciences/Evan_Groopman.html

Education

2015	Ph.D. in Physics, Washington University
	Advisors: Thomas Bernatowicz and Ernst Zinner
2011	A.M. in Physics, Washington University
	Advisors: Thomas Bernatowicz and Ernst Zinner
2009	B.A. in Physics, Washington University
	Advisor: Carl Bender

Research and Professional Experience

2010 – 2014	Graduate Student Researcher, Laboratory for Space Sciences, Washington University
Summer 2008	Undergraduate Researcher, Theoretical Division, Los Alamos National Laboratory
Summer 2007	Radiology Trainee, Division of Medical Imaging Physics, Johns Hopkins University
Summer 2006	Radiology Trainee, Division of Medical Imaging Physics, Johns Hopkins University

Teaching and Mentoring Experience

2010–2014	Graduate Student Mentor, Washington University
Sp. 2011	Teaching Assistant, Washington University
	Physics 322/422: Physical Measurements Laboratory
F. 2010	Teaching Assistant, Washington University
	Physics 360: Biophysics Laboratory
Sp. 2009	Teaching Assistant, Washington University
	Physics 117/118: General Physics Laboratory

Awards and Honors

2011–2014	NASA Earth and Space Sciences Fellowship (NESSF)
2014	Captain, CaSTLe (St. Louis' Premier Men's Club Ultimate Frisbee team)
2012	NASA Cosmochemistry Award, 75th Meteoritical Society Meeting, Cairns, AU
2012	Wiley-Blackwell Award, 75th Meteoritical Society Meeting, Cairns, AU
	(Outstanding student presentation)
2011	Student Travel Award, 74th Meteoritical Society Meeting, London, UK
2011	Franklin B. Shull Prize, Washington University
	(Outstanding Work as a Teaching Assistant)
2009–2010	University Fellowship, Washington University
2005–2009	Thomas Eliot Scholar, Washington University

Review Panels

2013   NASA Cosmochemistry, External Reviewer

Invited Talks

2013   Academy of Science of St. Louis Pioneering Science Seminar Series
                "Ancient Stardust: A Guide to the Hitchhikers of the Galaxy"

Publications

2014

E. Groopman, L. R. Nittler, T. J. Bernatowicz, E. Zinner. "NanoSIMS, TEM, and XANES Studies of a Unique Presolar Graphite Grain" (2014) *The Astrophysical Journal*, 790, 9 doi:10.1088/0004-637X/790/1/9

2013

T. K. Croat, T. Berg, T. Bernatowicz, E. Groopman, M. Jadhav. "Refractory metal nuggets within presolar graphite: First condensates from a circumstellar environment" (2013) *Meteoritics and Planetary Science*, 48, Nr 4, 686 doi:10.111/maps.12093

2012

E. Groopman, T. Bernatowicz, E. Zinner. "C, N, and O isotopic heterogeneities in low-density supernova graphite grains from Orgueil" (2012) *The Astrophysical Journal Letters*, 754, L8 doi:10.1088/2041-8205/754/1/L8

C.J. Olson Reichhardt, E. Groopman, Z. Nussinov, C. Reichhardt. "Jamming in Systems with Quenched Disorder" (2012) *Physical Review E*, 86, 061301 doi:10.1103/PhysRevE.86.061301

Conference Presentations (first author is presenter)

2014

E. Groopman, L. R. Nittler, T. J. Bernatowicz, T. K. Croat, E. Zinner, A. L. D. Kilcoyne. "Diversity in C K-edge XANES Among Presolar Graphite Grains". 45th Lunar and Planetary Science Conference, March 2014. [#1492]

2013

E. Groopman, T. Bernatowicz, E. Zinner. "An Unusual Low-Density Supernova Graphite Grain with a Nanocrystalline Core". 76[Th] Annual Meeting of the Meteoritical Society, August 2013. [#5072]

E. E. Groopman, E. K. Zinner, T. J. Bernatowicz. "C, Ca, and Ti Isotopes: On the Origins of High- and Low-Density Presolar Graphite Grains". 44th Lunar and Planetary Science Conference, March 2013. [#1757]

2012

E. E. Groopman, T. L. Daulton, L.R. Nittler, T. J. Bernatowicz, E. K. Zinner. "Ti-XANES and EELS of presolar TiC subgrains in low-density supernova graphite grains". 75[Th] Annual Meeting of the Meteoritical Society, August 2012. [#5225]

T. K. Croat, S. Amari, E. Groopman and T. J. Bernatowicz. "TEM Investigations into the Stellar Origins of the ^{13}C-rich graphite subgroup". 75[Th] Annual Meeting of the Meteoritical Society, August 2012. [#5242]

E. Groopman, B. Wopenka, T. Bernatowicz, E. Zinner. "Heterogeneous distributions of C, N, and O isotopes and Raman signatures in low-density supernova graphite grains from Orgueil" 43rd Lunar and Planetary Science Conference, March 2012. [#2126]

2011

E. Groopman, B. Wopenka, E. Zinner "Isotopic and Raman Analyses of Low-Density Orgueil Carbon Grains". 74[Th] Annual Meeting of the Meteoritical Society, August 2011. [#5031]

Nittler L. R., Groopman E., Bernatowicz T. J., Croat T. K., Zinner E. K. "X-Ray Absorption Near-Edge Spectroscopy of Supernova Carbonaceous Grains". 74[Th] Annual Meeting of the Meteoritical Society, August 2011. [#5361]

Wopenka B., Groopman E., Zinner E. "Orgueil Low-Density Presolar Carbon ain't Graphite but Glassy Carbon". 74[Th] Annual Meeting of the Meteoritical Society, August 2011. [#5032]

Charles Reichhardt, Evan Groopman, Zohar Nussinov, Cynthia Olson Reichhardt. "Jamming, Clogging, and Fragility in Frictionless Disk Systems with Quenched Disorder". American Physical Society, 2011 APS March Meeting, Vol. 56, No. 2; March 21-25, 2011. [#Q13.00012]

2010

Charles Reichhardt, Cynthia J. Olson Reichhardt, Evan Groopman, Zohar Nussinov. "The Jamming Transition and Crossover to Clogging for Disks with Quenched Disorder". American Physical Society, 2010 APS March Meeting, Vol. 55, No. 2; March 15-19, 2010. [#V13.00003]

2009

Cynthia Olson Reichhardt, Evan Groopman, Zohar Nussinov, Charles Reichhardt. "Quenched Disorder as a Fourth Axis to the Jamming Phase Diagram". American Physical Society, 2009 APS March Meeting, March 16-20, 2009. [#P9.004]

Posters (first author is presenter)

2015

E. Groopman, S. Amari, F. Gyngard, M. Jadhav, Y. Lin, Y. Xu, E. Zinner. "Isochrons and Al Contamination in Presolar Grains". 46rd Lunar and Planetary Science Conference, March 2015. [#1559]

2014

J. B. Lewis, D. Isheim, C. Floss, <u>E. Groopman</u>, F. Gyngard, D. N. Seidman. "Isotopic Composition and Trace Element Abundances of a Presolar SiC AB Grain Reconstructed by Atom-Probe Tomography". 77[Th] Annual Meeting of the Meteoritical Society, September 2014. [#5367]

<u>Other Qualifications</u>

<u>Technical Skills</u>: Secondary Ion Mass Spectrometry (SIMS/NanoSIMS); Transmission Electron Microscopy (TEM); Scanning Electron Microscopy (SEM); Diamond Ultramicrotomy; Micromanipulation

<u>Less Familiar Technical Skills</u>: Scanning Transmission X-Ray Microscopy (STXM/XANES); Focused Ion Beam (FIB-SEM); Auger Nanoscopy

<u>Computer Skills</u>: Python; Linux; Windows; LaTeX; Mathematica; Matlab; Microsoft Office; Google Sketchup

<u>Other</u>: PADI Rescue Diver (2002-present)

<u>Interests</u>

Ultimate Frisbee; Swing Dancing; Hockey; Backpacking; General History